METAL–SEMICONDUCTOR TRANSITIONS IN NANOSCALE VANADIUM DIOXIDE—THIN FILMS, SUBWAVELENGTH HOLES, AND NANOPARTICLES

By

Eugenii U. Donev

Dissertation

Submitted to the Faculty of the

Graduate School of Vanderbilt University

in partial fulfillment of the requirements

for the degree of

DOCTOR OF PHILOSOPHY

in

Physics

December 2008

Nashville, Tennessee

Approved:

Leonard C. Feldman

Richard F. Haglund, Jr.

Deyu Li

James H. Dickerson

Sharon M. Weiss

To Nicki,

for waiting this out.

ACKNOWLEDGEMENTS

First and foremost, I thank Prof. Len Feldman, my advisor and the chair of my Ph.D. committee, and Prof. Richard Haglund, Jr., who has been my co-advisor from the beginning of my graduate studies. I thank them, of course, for giving me the opportunity and resources to work at the forefront of experimental nanoscience, but above all for teaching me how to experiment, analyze, think, write, and speak like a physicist. It has been an honor for me to know them, both on a personal level and in the context of our common research endeavors.

I am also grateful to the other three members of my committee—Profs. Sharon Weiss, James Dickerson, and Deyu Li—for their contributions of time, guidance, and expertise, which can only improve the quality of my dissertation.

Special thanks go to my close collaborators and friends—René Lopez and Jae Suh—together with whom a lot of the experiments included in this work were brought to fruition. I hope my contributions to the "knowledgebase of VO_2" do them justice.

None of these experiments would have seen the light of day without the technical expertise and logistical support of Prof. Tony Hmelo. I thank him in particular for training me on what are now two of my favorite experimental tools—the focused ion beam and the ion accelerator.

I am much obliged to Prof. Ken Schriver for motivating me to become a better teacher and showing me in practice how to get there, as well as for his timely career advice.

For many invigorating discussions, whether scientific or not, I thank my colleagues and friends: John Rozen, Manoj Sridhar, Sriram Dixit, Stephen Babalola, Andrej Halabica, Stephen Johnson, Nicole Dygert, Joyeeta Nag, Davon Ferrara, Jed Ziegler, Kevin Tetz, Sarit Dhar, and Borislav Ivanov. I fully appreciate Davon's and Jed's direct contributions to my

research, in the form of gold nanoparticles and Raman-spectroscopy expertise, respectively. I owe Kevin my freedom from the limitations of Microsoft Excel, among other improvements in my data acquisition and analysis habits. I thank Borislav for the rare chance to talk science in my native tongue. And I am especially grateful to John for his expert help with various experimental setups, constructive criticism of my work, and countless yet absolutely necessary diversions, without which my graduate experience would have been much less enjoyable.

Finally, I thank my Bulgarian and American families for simply being (t)here to remind me that there are things in life more important than hystereses or even plasmons. And of course, I thank my wife Nicki for everything—for making many of the graphics on the pages that follow, for designing a professional website for me (www.geeno.com), for putting her ambitions on hold during my graduate years, for keeping me focused on the task at hand, for appreciating my interest in physics "for physics' sake"... Thank you.

TABLE OF CONTENTS

LIST OF FIGURES

PREFACE

Phase transformations hold a special significance in Nature, science, technology, and everyday life. From the ecologically essential melting, freezing and boiling of water to the theoretical and technological challenges of high-temperature superconductivity, phase transitions provide many views of core physical principles: the minimization of free energy to achieve stability, the role of energy barriers in metastability, the increase in entropy associated with disorder and higher symmetry, the stochastic nature of nucleation that gives birth to a new phase, the dissipation of energy through hysteresis, and so on. Even for a particular type of solid-solid transformation in one particular compound—the thermally-induced metal-insulator transition in vanadium dioxide (VO_2)—the richness and complexity of the phenomena involved have kept researchers busy for half a century, with no end in sight. For instance, the precise cause-and-effect pathway for the phase transition of VO_2 is still a vigorously debated subject, which revolves around a core issue of condensed-matter physics: the competition and cooperation between electron-electron correlation and electron-lattice interaction in determining the itineracy of electrons in narrow-band systems. A review of the above concepts in the context of the VO_2 phase transition, as well as some of the latest advances in understanding its intricate mechanism, are presented in **Chapter I**.

From a materials physics standpoint, the VO_2 transition appears to nucleate heterogeneously at "potent defect sites", but the microscopic nature of these sites remains unknown. Bulk VO_2 crystals and even thin films contain so many such sites as to make it virtually impossible to quantify their potency distribution, or perhaps even pinpoint the defect(s) responsible for nucleating the transition at a given temperature. Thus there is no substitute for observing the VO_2 phase transition in tiny quantities of the material, such as NPs of sub-100-nm sizes. Previous results from our group, which link the increased thermal hysteresis width for VO_2 NPs to the decreased availability of potent nucleating defects as the size of the transforming NPs shrinks, are briefly described in **Chapter I** (Section 1.3.2)

and **Chapter VI** (Section 6.1.1).

Size-dependent phenomena are an important aspect of phase transformations and manifest themselves in a great variety of nanoscale systems,[10] *e.g.*: reversible diffusion phase change in nanometer-sized alloy particles;[11] size-dependent surface energy of free Ag nanoparticles (NPs);[12] size-dependent spontaneous alloying of Au-Ag NPs;[13] size- and facet-dependent ferromagnetism in Pd NPs;[14] statistical polarization in a small ensemble of electron spin centers;[15] size-dependent melting of silica-encapsulated Au NPs;[16] unexpected decrease in the strength of materials upon on passing from micrometer into nanometer scale;[17] tunnelling in CdSe quantum rods;[18] size-dependent magnetism of iron clusters;[19] size-dependent electronelectron interactions in metal NPs;[20] size-dependent optical properties of implanted and lithographic VO_2 NPs.[5,9]

Nanostructured materials and improved optical probes have brought about in recent years the emergence and vigorous growth of "nanoplasmonics"—the study of active nanostructures that harness surface plasmons and other near-field electromagnetic phenomena to control light at subwavelength scales, with the promise of bridging the dimensional gap between photonic and electronic devices. Among those nanostructures are periodic arrays of subwavelength holes in noble metals, which transmit much more of the incident light than standard diffraction theory predicts. This so-called extraordinary optical transmission (EOT) and its origins in the electromagnetic coupling of light to surface-bound propagating modes, dominated by the surface-plasmon polariton (SPP), are explained in **Chapter IV** (Section 4.1.2). On the other hand, when the collective oscillations of the free electrons are spatially confined in ∼100-nm noble-metal NPs, they become a localized surface-plasmon resonance (LSPR), whose spectral position (energy) and width (lifetime) depend sensitively on NP size and shape, on incident-light polarization, and on the dielectric functions of the metal NP and, crucially for this work, of the surrounding medium. The LSPR is introduced in **Chapter III** (Section 3.1.1).

I find it convenient to divide my original contributions to some of the aforementioned

subjects in two loose categories, which "happen" to coincide with my affiliations with two closely integrated research groups at Vanderbilt University: the *Materials Physics* group of Professor Len Feldman and the *Applied Optical Physics* group of Professor Richard Haglund, Jr. Chapters V and VI fit in the first category because they deal with manifestations of the phase transition of VO_2, particularly the monoclinic $\leftrightarrow$ tetragonal structural transformations, in previously unexplored nanoscale forms of the material: individual VO_2 NPs and arrays of hybrid Au+VO_2 NPs, respectively. Chapters III and IV, on the other hand, fit in the second category because they describe ways of applying the significant change in the near-infrared dielectric properties of VO_2 across the phase transition to the modulation of plasmonic behavior in noble-metal nanostructures: the LSPR of Au NPs and the EOT effect of Au/Ag subwavelength hole arrays, respectively.

The phase transition of a single VO_2 NP had not been observed prior to the confocal Raman measurements presented in **Chapter V**, which constitute the altogether first characterization of nanoparticulate VO_2 by means of Raman spectroscopy. Very different hysteresis widths were obtained for two isolated VO_2 NPs of roughly the same volume but with rather dissimilar morphologies: one NP appearing round and homogeneous, and switching with the widest hysteresis documented for any form of VO_2 ($\Delta T_A = 56\pm5$ °C), while the other NP appearing "ruffled", as it were, and switching with a much narrower hysteresis ($\Delta T_B = 18\pm2$ °C), but still much wider than the hysteresis of the witness patch of VO_2 film on the same sample ($\Delta T_{film} = 2\pm1$ °C). These comparisons, albeit limited, provide an important first step towards unravelling the microscopic origins of the VO_2 phase transition, for example, by virtue of correlating the presence of likely nucleation sites (grain boundaries, protrusions, etc.) with the ease of Raman switching (hysteresis width) for a statistically significant number of individual VO_2 NPs. Particle size, it turns out, is not the only factor determining the extent of thermal driving needed to complete the transformation cycle.

However, obtaining *regular* Raman spectra from 50–100-nm NPs—the most interest-

ing size range for VO_2 NPs owing to the low number of stochastically anticipated potent defects—proved beyond our detection limits because the intrinsically weak Raman scattering efficiency was being further hampered by the small amount of analyte. The solution to this challenge, which became a project in its own right and is described **Chapter VI**, was to use surface-enhanced Raman scattering (SERS) to boost the signal from the VO_2 NPs. I implemented a new type of hybrid nanostructure consisting of 50–150-nm VO_2 NPs covered with 45–110-nm Au caps, which provided excellent signal enhancement and made it possible to measure the size-dependence of the structural transformation in VO_2 NPs through the hysteresis of the Raman intensity. The same set of data also revealed a plasmonic size-effect with regard to the Au caps, namely that the magnitude of SERS enhancement depends critically on the size of the field enhancer, thus evincing the dominant role of LSPR in boosting the scattered optical radiation.

Chapter III investigates another variation on the plasmonic–phase-transition hybrid system: arrays of Au NPs covered with a thin film of VO_2. The concept behind it is somewhat complementary to that of the arrays of Au-capped VO_2 NPs, in the sense that the latter nanostructure exploits the plasmonic properties of the Au caps to amplify the phase-transition behavior of the VO_2 NPs, whereas the former makes use of the permittivity-switching property of the VO_2 film to modulate the plasmonic behavior of the Au NPs. Although modulation of the Au LSPR by VO_2 had already been demonstrated, this work was the first to systematically explore the shift in resonant wavelength with Au-NP size and aspect ratio, as well as with polarization of the incident light.

Chapter IV presents a novel application of the transition-induced change in optical properties of VO_2. It turned out that arrays of subwavelength holes in a double-layer structures of Ag-on-VO_2 and Au-on-VO_2 exhibited not only the EOT effect arising from the perforated noble metal, but also a modulation of the EOT intensity depending on the phase of the perforated VO_2 layer. Even more surprising was the "direction" of the EOT modulation: higher overall transmission in the *metallic* phase of VO_2 as compared to the

semiconducting phase, quite the opposite to the transmission contrast of a plain VO_2 film of the same thickness. This counterintuitive "reverse switching" in Ag/Au-VO_2 hole arrays prompted me to explore the transmission behavior of a perforated single layer of VO_2, which was not expected to have EOT. Indeed, the VO_2-only hole array did not exhibit the characteristic spectral profile of the EOT effect, but it had another peculiar feature: a crossover in the near-IR wavelength range of the metallic-phase transmission spectra for perforated and plain VO_2, wherefrom the array of subwavelength holes begins to transmit more than the non-perforated film. With the help of numerical simulations, I proposed a simple heuristic model to account qualitatively for the transmission crossover and the reverse-switching effect, based on the idea that there are transmission losses inside the holes due to evanescent waves that leak into the plane of the VO_2 layer, in addition to diffuse scattering at the entrance and exit apertures, and that the magnitude of the losses increases with higher permittivity contrast between the interior (air) and exterior (VO_2) of the holes—brought about by the metal-to-semiconductor transition of the VO_2 layer. Thus far, the combination of phase-change and SPP properties realized in our perforated hybrid structures remains unique in the field of nano-optics.

Ultimately, none of the above contributions would have materialized without the expertise to grow, pattern, and probe the right material, vanadium dioxide. The tools and techniques of this trade form the subject of **Chapter II**, while **Appendix A** lists some of my preliminary results on the fabrication of thin films of vanadium sesquioxide, another material with a remarkable phase transformation.

CHAPTER I

INTRODUCTION

Abstract

This chapter is meant to familiarize the reader with vanadium dioxide (VO_2) and its phase transition, including some of the latest contributions to a decades-long debate: whether electron-electron correlations or lattice instabilities dominate the transition dynamics. The topics of hysteresis, nucleation, and size-effects in the VO_2 phase transition are treated in detail, in order to provide the basis for interpreting some of the experimental results of the current work.

1.1 Vanadium dioxide (VO_2): A primer

Vanadium dioxide (VO_2) is a transition-metal compound that has held the attention of researchers for half a century since 1959, when F. J. Morin[21] first observed its remarkable metal-to-insulator and insulator-to-metal transitions upon cooling and heating through a critical temperature of $T_c \approx 340$ K (67 °C). Figure 1.1 shows examples of the drastic changes in electrical and optical properties across the VO_2 transition, together with the phenomenon of hysteresis that generally accompanies first-order phase transformations (see Section 1.2). At or near T_c, VO_2 also undergoes a structural transformation of the crystal lattice, from a tetragonal/rutile (R) phase for the high-temperature metal to a monoclinic (M_1) phase for the low-temperature insulator (semiconductor);[22,23] the two crystallographic structures are depicted in Figure 1.2. In fact, it is the intricate interplay between electronic and structural degrees of freedom—between carrier localization due to electron-electron repulsion (Mott-Hubbard corellation[23,24]) and unit-cell–doubling due to lattice instability (Peierls distortion[23,24])—that has been at the heart of an enduring debate[1–3,22,25–32] about

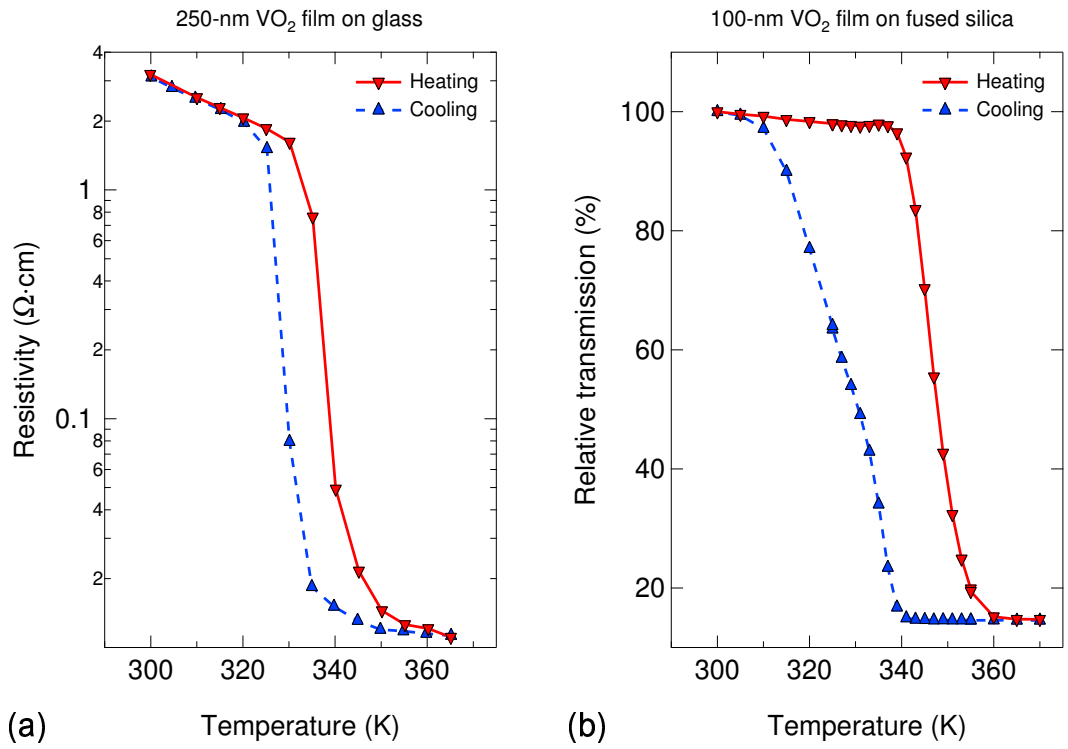

Figure 1.1: **(a)** Resistivity and **(b)** optical transmission (here, integrated response to white light in the range $\lambda = 800$–1700 nm) as a function of sample temperature for typical VO_2 films on typical substrates.

the precise cause-and-effect linkage in the mechanism of the VO_2 transition. Because of the nano-to-femtosecond timescales of its phase transition, VO_2 has recently been propelled to the forefront[1,3,33–36] of a rapidly developing research avenue, that of ultrafast pump-probe techniques, in the very realistic hope[3] that the delicate web of interactions among various degrees of freedom can be untangled in the time domain. On the other hand, materials physicists want to understand how such complex systems behave on the spatial nanoscale and, in particular, how phase transitions occur in nanocrystalline systems[10,16,37–42] and what are the microscopic sources of heterogeneous nucleation in small particles.[43,44] This goal has sparked an interest in making and probing nano-VO_2: from nanogranular thin films,[3,45–49] to ensembles of implanted or lithographic VO_2 nanoparticles[9,50–54] (NPs), up to the isolated VO_2 NPs (Chapter V), arrays of hybrid metal-VO_2 NPs (Chapter VI) and

perforated thin films (Chapter IV) presented in this work.

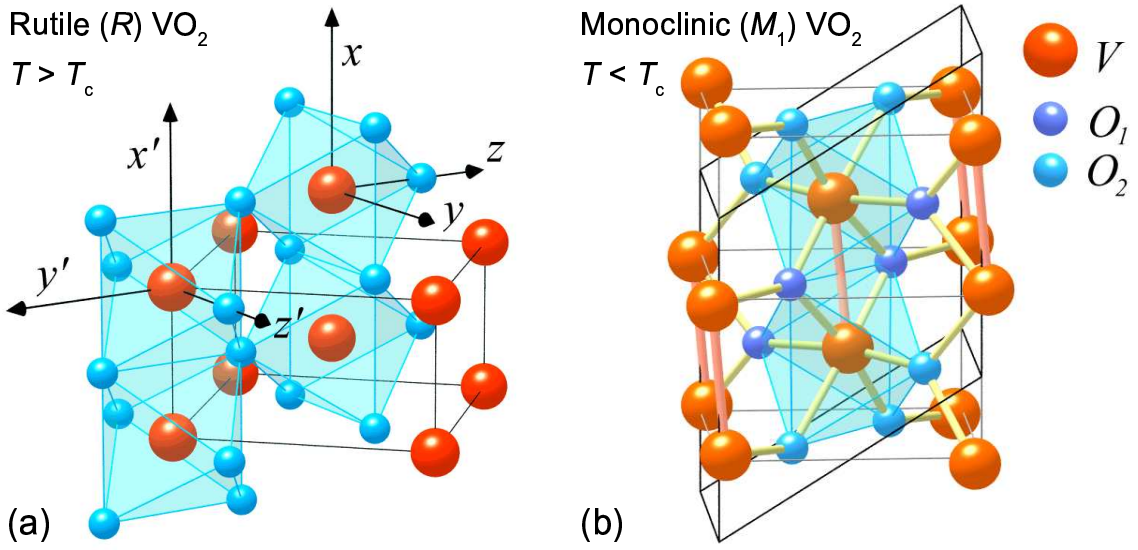

Figure 1.2: Crystallographic structures of vanadium dioxide (VO_2): **(a)** Tetragonal/rutile (R) above the transition temperature T_c, and **(b)** monoclinic M_1 below T_c. Large and small spheres denote vanadium (V) and (two different types of M_1) oxygen (O) atoms, respectively. Shaded regions outline edge- and corner-sharing oxygen octahedra; the two local coordinate systems in **(a)** reflect the different orientation of octahedra centered at corners and in the center of the R cell. In **(b)**, note the *V–V pairing and tilting* in the M_1 phase along the vertical direction, as well as the *doubling of the M_1 unit cell* (darker bounding lines) with respect to the R unit cell (lighter bounding lines and **(a)**). After Reference [55].

1.1.1 Lattice and electronic structures

Above the transition temperature T_c, the R phase of VO_2 exhibits the characteristics of a (poor[56]) metal and has a tetragonal body-centered unit cell of vanadium (V) atoms, each surrounded by an orthorhombically distorted octahedron of six oxygen (O) atoms. The octahedra stack by sharing edges that form chains along the c-axis, which are in turn coupled to each other by sharing corner O atoms. The closest V–V distance is 2.85 Å in chains along the c-direction (Figures 1.2a, 1.3, and 1.4a). Below T_c, the M_1 phase of VO_2 is a monoclinic

semiconductor with a ∼0.7-eV optical bandgap[22,33,57–59] and a distorted structure (Figures 1.2b, 1.3, and 1.4a): the V atoms *pair/dimerize* along the chain, resulting in *unit-cell doubling*, and also *tilt* transversely in a zigzag-like fashion; the V–V pairing and tilting also cause the O-octahedra to distort and twist slightly.[55]

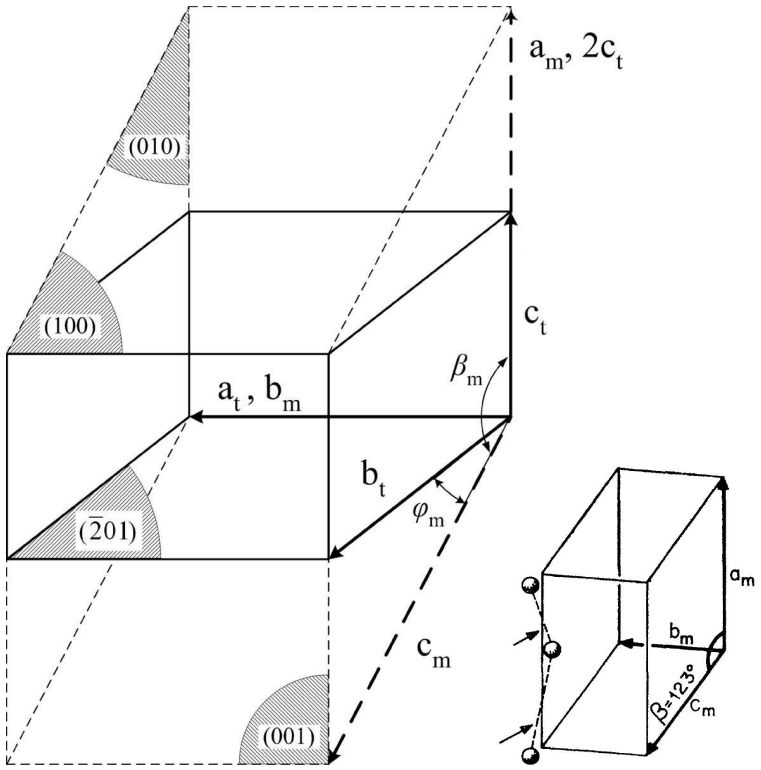

Figure 1.3: Orientation and dimensions of tetragonal/rutile R (solid lines, "t" subscripts) and monoclinic M_1 (dashed lines, "m" subscripts) unit cells of VO_2; several crystallographic planes for M_1 are also indicated. According to Eyert[55] (and references therein), the lattice parameters are: for the R phase, $a_t = b_t = 4.5546$ Å, $c_t = 2.8514$ Å, $\angle_{axial} = 90°$; for the M_1 phase, $a_m = 5.7517$ Å $\approx 2c_t$, $b_m = 4.5378$ Å, $c_m = 5.3825$ Å, $\angle\beta_m = 122.646°$. Note again the doubling of the monoclinic cell along the rutile c-axis, *i.e.*, $a_m \approx 2c_t$. **(inset)** *Metal-metal pairing and tilting* in the M_1 phase result in two different V–V distances along the monoclinic a-axis: 2.619 Å and 3.164 Å (see also Figure 1.2b). After Reference [60].

The essential structural and electronic details of both VO_2 phases, first proposed by Goodenough,[22] are neatly summarized by Cavalleri *et al.*[33] in Figure 1.4. The $[Ar]4s^23d^5$ V atoms, each bound to two $1s^22s^22p^4$ O atoms, cede four electrons to fill the O 2p shells, leav-

ing V^{4+} cations with a single valence electron near the Fermi level. The closed-shell O 2p electrons are now tightly bound and lie well below the Fermi level, not contributing significantly to the conductivity. The remaining one electron per V^{4+} cation occupies the lowest of the 3d levels, making VO_2 a $3d^1$ compound. The bands in transition-metal compounds form under the strong influence of anisotropic crystal fields. The fivefold energy-degenerate 3d levels of the isolated V^{4+} cation are split in VO_2 by the cubic and orthorhombic components of the octahedral field of the six surrounding oxygens,[25] resulting in a higher-energy two-level manifold (e_g) and a lower-energy three-level manifold (t_{2g}). The t_{2g} states, located near the Fermi energy, are split into a $3d_{//}$ state, which is directed along the rutile *c*-axis with good metal-metal bonding, and the remaining $3d_{\pi}$ states, as shown in Figure 1.4b. Thus, a single electron resides in the lowest vanadium d band, $3d_{//}$, which is the reason for *R*-phase VO_2 being metallic. In the monoclinic M_1 phase, V–V pairing within the chains parallel to the rutile *c*-axis causes splitting of the $3d_{//}$ band into filled bonding and empty antibonding states. In addition, the $3d_{\pi}$ bands move to higher energies due to increased overlap of these states with the O 2p states, caused by the zigzag-like tilting of the V–V dimers. As a result, a bandgap of ~0.7 eV opens between the bonding $3d_{//}$ band and the other t_{2g} bands (Figure 1.4c); the $3d_{//}$ band splitting amounts to ~2.5 eV, while the $3d_{\pi}$ band is raised by ~0.5 eV.[58]

1.1.2 Transition mechanism: Peierls or Mott-Hubbard?

The d^1 configuration of the V^{4+} cation allows a single electron to be shared by the $3d_{//}$ and $3d_{\pi}$ bands (Figure 1.4c). Because of their different widths and anisotropies ($3d_{//}$ is highly anisotropic while $3d_{\pi}$ is more spherical), these two bands are expected to respond in a different way either to electron-electron interactions (significant only for the narrow $3d_{//}$ band) or to a lattice distortion.[26] Within Goodenough's phenomenological model,[22] the lattice distortion (tilting) in the VO_2 M_1 phase raises the antibonding $3d_{\pi}$ band above the Fermi level and leaves the $3d_{//}$ band half filled. The point of contention as regards the

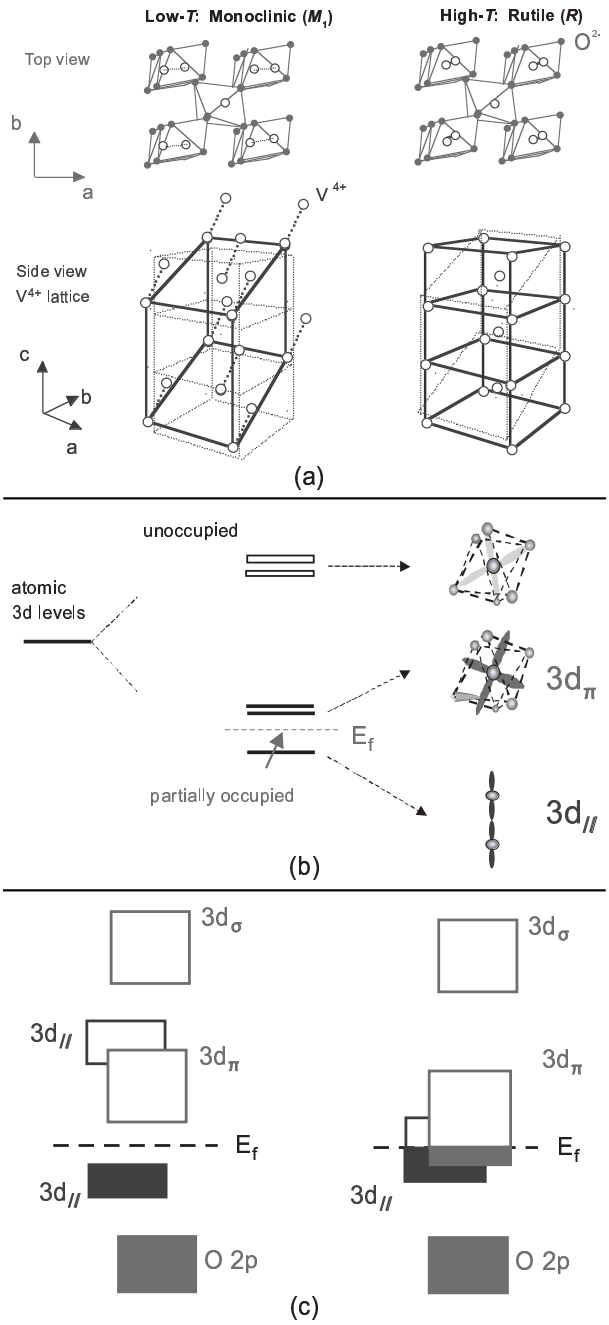

Figure 1.4: **(a)** Structure of VO_2: semiconducting monoclinic (M_1) phase for $T < T_c \approx$ 340 K and metallic rutile (R) phase for $T > T_c \approx 340$ K. **Side view:** Only the vanadium sublattice is shown, which undergoes *pairing and tilting* along the c-axis in the *cell-doubled* M_1 structure. **Top view:** Each V^{4+} cation lies within an octahedron of six oxygen atoms. **(b)** Diagram of the crystal-field-split V 3d states in VO_2: the fivefold degeneracy of 3d levels, found in isolated atoms, is lifted in the octahedral crystal field; the Fermi level falls within the three lower t_{2g}-like states, which form the valence and conduction bands. **(c)** Energy-level diagram of VO_2: each V atom is left with one valence electron, while ceding four to fill the O 2p shell, which becomes tightly bound; the near-Fermi level states are those of the t_{2g}-like manifold, where the $3d_{//}$ levels are split in the M_1 phase by unit-cell doubling (Peierls mechanism) *and/or* by Coulomb repulsion (Mott-Hubbard mechanism); the higher-lying $3d_\pi$ states shift in the M_1 phase due to the structural distortion. After Reference [33].

VO_2 transition mechanism is whether the additional splitting of the $3d_{//}$ band originates from V–V pairing along the rutile c-axis and unit-cell doubling (Figures 1.2b and 1.3), as in the Peierls mechanism,[22,27,29] *or* from the opening of a correlation gap due to carrier localization, as in the Mott-Hubbard mechanism.[25,26,28]

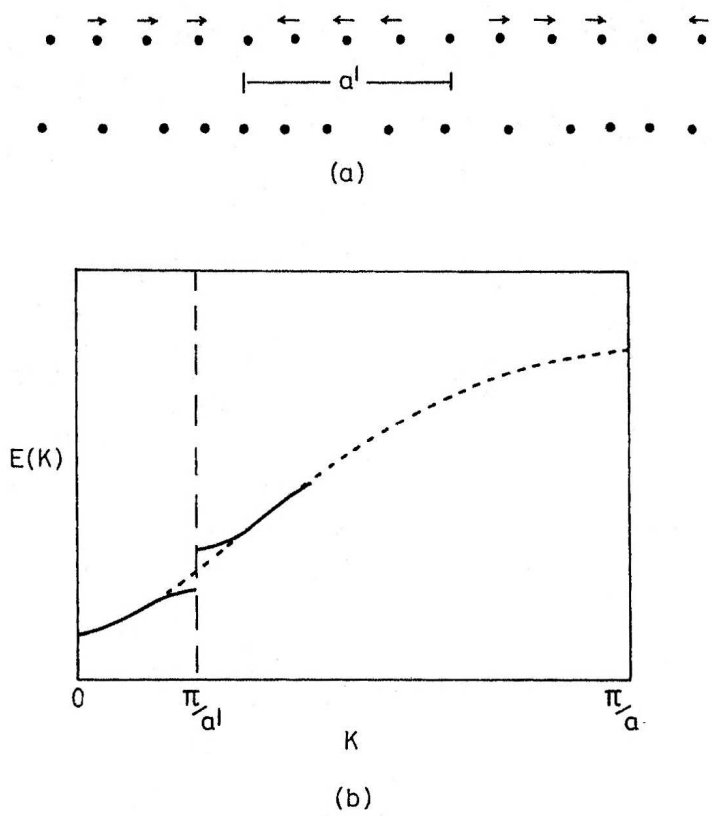

Figure 1.5: Sketch of Peierls mechanism. **(a)** Periodic lattice distortion of chain of atoms and **(b)** its effect on the band structure. New bandgaps appear in the energy-wavevector dispersion at $k = \pi/a'$, and at multiples of this value of k (not shown), where a' is the periodicity of the distortion. After Reference [24].

The **Peierls** mechanism refers to an instability in the normal Fermi surface of a one-dimensional metal, whereby an energy gap opens up at the Fermi surface due to periodic lattice deformations that change the periodicity of the crystal.[24,61] Figure 1.5 shows a generic band structure for a one-dimensional system, illustrating the effect of such a periodic

deformation on the energy-wavevector (E–k) dispersion. New Brillouin-zone boundaries appear in response to the enlarged "superlattice" periodicity a' and lead to new energy gaps at values of k that are a multiple of π/a'. If the Fermi surface of the unperturbed crystal ends up at one of the new zone boundaries, the deformation-induced bandgap will destroy the metallic properties of the conduction electrons. Opening a bandgap at the Fermi level lowers the energy of electrons below the gap (Figure 1.5b), and thereby leads to some stabilization of occupied electron states. It turns out that in a *one-dimensional* system a Peierls perturbation of the electronic levels is always energetically favorable, so that an appropriate periodic deformation of the crystal lattice will always prevail over the opposing short-range elastic forces and destroy the metallic ground state.[24]

The periodicity a' of the lattice deformation resulting from the Peierls instability is related to the Fermi-surface wavevector k_{F} by $a' = \pi/k_{\mathrm{F}}$. Depending on the value of k_{F}, a' may or may not be commensurate with the original lattice spacing a. An example of particular relevance to VO_2 is that of a half-filled band in one dimension: $k_{\mathrm{F}} = \frac{1}{2}\pi/a$, hence $a' = 2a$. Such periodic deformation can be described simply as "dimerization" of the original lattice, with electrons concentrating periodically in the "bonds" between the more closely spaced pairs of atoms—a situation referred to as a *charge-density wave*.[24] Considering the formation of metal-metal dimers, the doubling of the monoclinic unit cell, and the quasi-one-dimensional character of the $3d_{//}$ (formed by d orbitals oriented for overlap along the rutile c-axis; see Figure 1.4b), it seems only natural to attribute the VO_2 phase transition to a Peierls-type instability of the Fermi surface. In the metallic phase, the $3d_{//}$ band would be half-full, and the predicted Peierls deformation would indeed lead to an alternation of V–V distances, yielding a lower band filled by two electrons per vanadium pair.

Support for the Peierls-like influence of the lattice degrees of freedom on the VO_2 transition was furnished by electronic structure calculations[27,55] based on density functional theory within the local density approximation. Wentzcovitch *et al.*[27,29] used a variable cell-shape approach to allow for simultaneous relaxation of the atomic positions and the

primitive translations. As a result, starting from different intermediate structures, these authors obtained the monoclinic M_1 structure as the most stable one. The calculated lattice parameters for both cells were in good agreement with the experimental data. However, the calculations failed to yield the opening of the M_1-phase bandgap: the top of the bonding $3d_{//}$ band was found to overlap slightly (0.04 eV) with the bottom of the $3d_{\pi}$ band (only for a hypothetical structure with larger dimerizations would the band gap open). This result was attributed to the typical failure of the local density approximation to correctly reproduce measured optical bandgaps. Eyert[55] also found semimetallic behavior, with a band overlap of 0.1 eV rather than the observed optical bandgap. Since both types of 3d bands were found to be coupled by charge conservation rather than hybridization, the author interpreted the M_1 phase as arising from a Peierls-like instability of the $3d_{//}$ bands in an embedding reservoir of $3d_{\pi}$ electrons.

A different mechanism for the VO_2 phase transition was proposed by Zylbersztejn and Mott,[25] one based on the presence of strong electron-electron correlations in the $3d_{//}$ band, with the electron-lattice interaction playing an auxiliary role. In the metallic phase, the correlations appear to be efficiently screened by the $3d_{\pi}$ bands, but in the semiconducting phase the effect of screening on the $3d_{//}$ electrons is diminished, since the $3d_{\pi}$ bands experience an upshift in energy due to the zigzag displacement of the V atoms. As a consequence, the narrow $3d_{//}$ bands at the Fermi energy are susceptible to strong Coulomb correlations and undergo a Mott transition (see below), which opens the optical bandgap. In this scheme, the crystalline distortion (tilting of V atoms) serves to lift the band degeneracy, so that the correlation energy becomes comparable with the bandwidth, while the dimerization (V–V pairing) has only a minor effect on the bandgap.[25]

In general, d-electron systems, such as the transition-metal compounds, are characterized by very narrow bandwidths because:[23] **(i)** the relatively small radius of the d-electron wavefunction, as compared to the lattice constant in crystals, leads to a weak overlap between two such orbitals on two adjacent metal atoms; **(ii)** the overlap between d orbitals is

often mediated by indirect transfer through ligand p orbitals (*i.e.*, d-p hybridization), which shrinks the bandwidth even further; **(iii)** the 4s and 4p bands are pushed well above the d band, reducing the screening effectiveness of the 4s and 4p electrons, which makes the interactions among d electrons comparable or even larger than the bandwidth. Ultimately, the narrow bandwidths underpin the importance of electron-electron correlation in d-electron systems, the effects of which are unaccounted for in the band theory of solids.[23,24]

In band theory, it is assumed that repulsion between electrons can be represented by an average *effective* potential. This approximation works very well for "normal" metals (Figure 1.6a), and particularly for the states near the Fermi surface where the mobile electrons have good screening properties. However, it breaks down in systems with very narrow bands, such as many d-electron compounds, as well as when the concentration of conduction electrons is low. It is then that *electron-electron correlation* becomes important: this term refers to the tendency of electrons to alter their motion, so as to avoid each other more effectively than an "independent-electron" orbital wavefunction can describe.[24] An approximation often found useful for the treatment of correlation effects in transition-metal compounds is the so-called **Mott-Hubbard** model.[24,62,63] Mott[64] pointed out early on that if the Coulomb interaction between the electrons is sufficiently strong as compared to the band energy of the quasiparticles (which can be thought of as "single particles accompanied by a distortion cloud in the [interacting] electron gas"[61]), then electrons in a solid would have to localize on the atoms, with one electron per atom. This qualitative change in the nature of single-electron states from freely propagating (delocalized) to atomic-like (localized) constitutes a metal-insulator transition known as a Mott transition. In the reverse transition, as carriers are excited in the insulating phase of the solid, they will tend to screen out the Coulomb repulsion more effectively and the solid becomes a metal. The distinction between the normal metallic and Mott insulating systems is illustrated schematically in Figure 1.6.

Carrier motion in the Mott-Hubbard picture is depicted as follows: an empty state in the Mott insulator, that is, without electrons occupying it, will act as a mobile hole, and hence

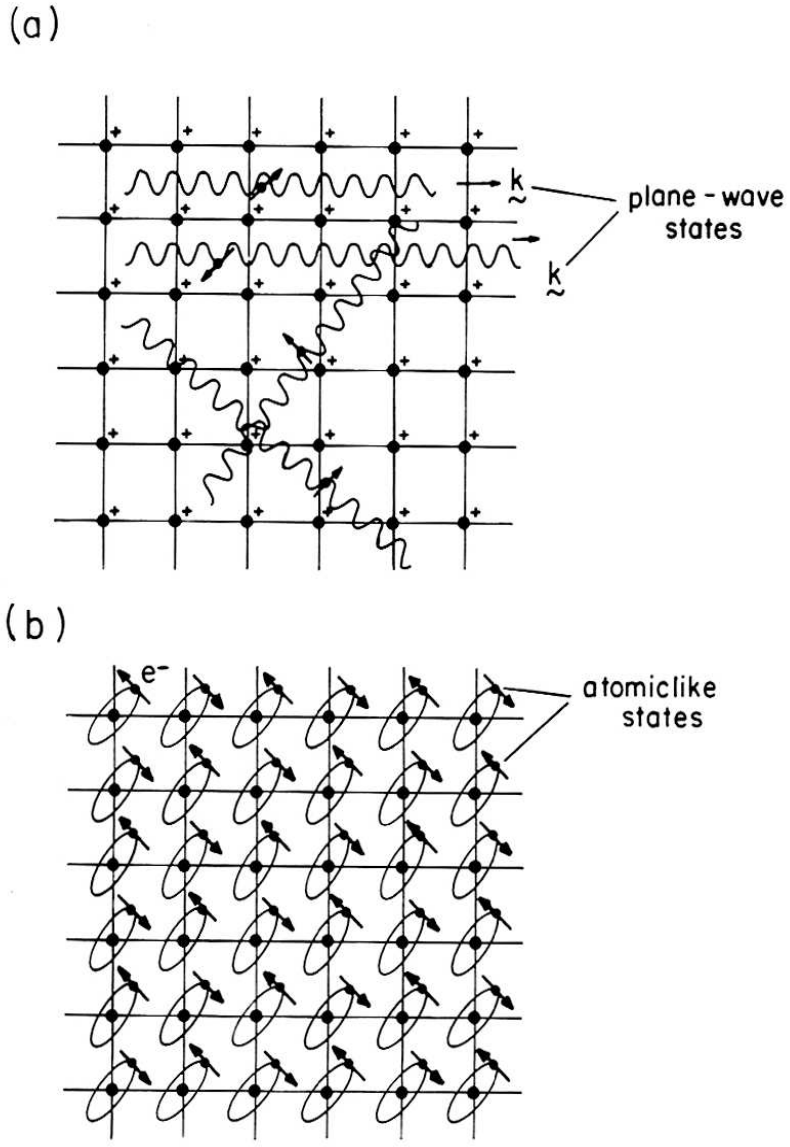

Figure 1.6: **(a)** Normal metal: lattice of ions and plane waves of wavevector $\vec{k}$ representing free-electron states. **(b)** Mott insulator: lattice of atoms with electrons localized on them (one per site). Note that the ground-state configuration of a Mott insulator is usually antiferromagnetic (*i.e.*, with spins antiparallel to each other), as in the low-temperature phase of V_2O_3, but not always: the low-temperature phase of VO_2 avoids magnetic ordering because of competing effects of charge ordering.[2,27] After Reference [62].

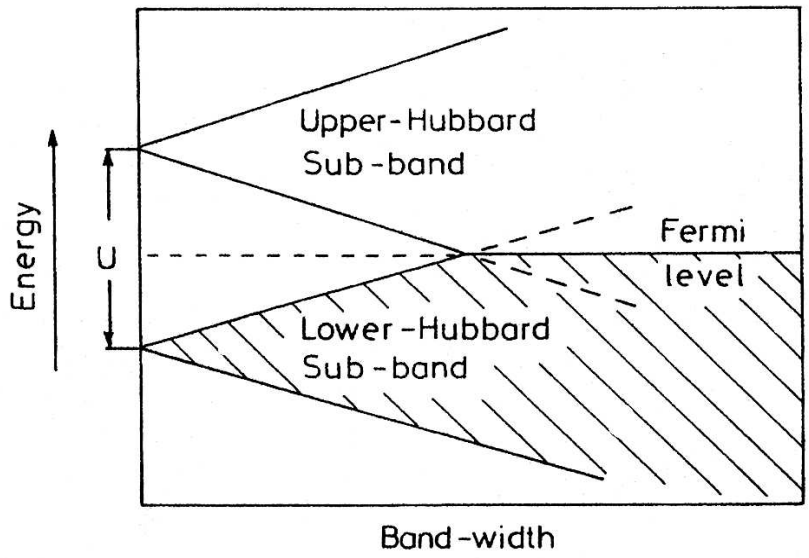

Figure 1.7: Schematic of band structure in Mott-Hubbard model. Hubbard subbands overlap to give a metallic state when the bandwidth W exceeds the *intra*atomic Coulomb interaction U. For larger values of U/W (*i.e.*, to the left of the band crossover), the lower subband is formed from electrons occupying an empty site and the upper one from electrons occupying a site already taken by another electron. With one electron per site, the lower band is full, and the system becomes a Mott insulator. After Reference [24].

charge transport occurs via the correlated hopping of electrons through such hole states. Hubbard[65] developed the description of the Mott insulator into a quantitative model, which in essence compares the relative strengths of the localization versus delocalization tendencies of electron states to determine whether and when a system of interacting electrons exhibits metallic or insulating behavior. According to the model, a metal-insulator transition occurs when the interaction strength of the electrons—characterized by the magnitude U of the *intra*atomic (same-site) Coulomb repulsion—increases and becomes comparable to the band energy per particle, which is in turn characterized by the bare bandwidth W. At the critical point, $U \sim W$, the original band of single-particle states splits into two halves, and the system becomes an insulator (Figure 1.7). In actual calculations, the ratio U/W is indeed what determines the localized versus itinerant behavior of the electrons in the solid,[62] although accurate estimates of U are often difficult to obtain.[24]

Returning to the specific case of VO_2, Paquet and Leroux-Hugon[26] pointed out some

deficiencies in the description of the transition in terms of the Mott-Hubbard model *alone*. One of these arises from the lattice distortion (zigzag tilting of vanadium atoms), which is required to lift the $3d_{//}$–$3d_{\pi}$ degeneracy and also implies, by symmetry arguments, V–V pairing—whereas a Mott-Hubbard mechanism generally cannot break any crystallographic symmetry. In addition, the vanishing magnetic susceptibility in the M_1 phase suggests some spin dimerization mechanism that also originates in V–V pairing, such as the magnetic analog of the Peierls instability known as a "spin-Peierls" transition.[66] Paquet and Leroux-Hugon thus concluded that "any theory attempting to account for the major features of the transition, namely, symmetry breaking, gap opening, and magnetic properties, and to give a quantitative thermodynamical analysis must incorporate both [Peierls and Mott-Hubbard] mechanisms on an equal footing".[26] Starting from experimentally derived parameters and a tight-binding representation for the $3d_{//}$ and $3d_{\pi}$ bands, but also including Mott-Hubbard-type interactions for both bands as well as a phonon contribution, the authors calculated that the VO_2 transition is primarily driven by electron-electron correlations, with the onset of lattice distortion being only a consequence of this primary mechanism though playing a crucial role in determining the first-order nature of the transition.[26] As seen below, however, the authors' prediction that their treatment "puts an end to a long-standing controversy" has proved somewhat overoptimistic.

1.1.3 VO_2: What's new

Outlined here in chronological order are some very recent theoretical and experimental advances regarding the nature of VO_2 and its phase transition.

⋆ **CAVALLERI** *et al.*[31] (2004): *Evidence for a Structurally-Driven Insulator-to-Metal Transition in VO_2: A view from the Ultrafast Timescale*

• Measured the transition time for changes in the reflectivity and transmission of thin-film VO_2, using ultrafast pump-probe spectroscopy in the range 15 fs–1.5 ps; measured continuous-wave Raman spectra.

• Uncovered a limiting timescale for the transition at 80 fs, where a "structural bottleneck" prevents further increase in transition speed.

• Attributed bottleneck timescale to coherently initiated structural motion due to optical phonons—because of spectral overlap between the coherent-phonon oscillations and two Raman-active modes (200 cm^{-1} and 226 cm^{-1}) associated with the pairing and tilting motions of the V–V dimers that map the monoclinic onto the rutile structure.

• Concluded that atomic arrangement of the rutile (high-temperature) unit cell is necessary for the formation of the metallic phase of VO_2, suggesting significant band-like, *i.e.*, **Peierls-like**, character for the semiconducting phase, but **not** ruling out electronic correlations through the formation of spin singlets.

⋆ **BIERMANN** *et al.*[30] (2005): *Dynamical Singlets and Correlation-Assisted Peierls Transition in VO_2*

• Calculated the electronic structures of metallic (R phase) and semiconducting (M_1 phase) VO_2, using: (i) a cluster extension of dynamical mean-field theory (C-DMFT) in combination with (ii) density functional theory within the local density approximation (DFT-LDA).

• Treated structural and correlation aspects on equal footing by choosing the V–V dimers as the fundamental unit of the calculation (hence, "cluster extension").

• Succeeded (unlike the standard single-site LDA+DMFT treatments) in correctly predicting the insulating nature of the M_1 phase, with a bandgap of ∼0.6 eV and a large charge redistribution in favor of the $3d_{//}$ band—both in good agreement with experiments.

• Concluded that *nonlocal* correlations effectively assist the Peierls-like transition, with dimerization in the M_1 phase causing the formation of molecular singlets within the $3d_{//}$ channel embedded in a bath.

• **Tomczak and Biermann**[67] (2007) added that: "... despite the undeniable presence of strong local correlations, the system retains the coherence of its excitations by means of intra-dimer fluctuations, to an extent that the physics of the compound is indeed dominated by the **Goodenough-Peierls** picture. The role of correlations consists in [refer to Figure

1.4c] (i) pushing the a_{1g} [$3d_{//}$] anti-bonding band beyond the top of the e_g^π [$3d_\pi$], consistent with the experimental findings, and, more importantly, in (ii) enhancing the a_{1g} [$3d_{//}$] bonding-e_g^π [bonding-$3d_\pi$] splitting due to an effectively reduced Coulomb repulsion in the a_{1g} [$3d_{//}$] bonding band, hence favouring the depopulation of the e_g^π [$3d_\pi$] bands. The latter results in the opening of the gap. Thus, as a matter of consequence it *is* the correlations that are responsible for the insulating state, albeit they cause it in a rather specific fashion."

⋆ **HAVERKORT** *et al.*[68] (2005): *Orbital-Assisted Metal-Insulator Transition in VO_2*

• Measured and simulated polarization-dependent X-ray absorption spectra (XAS) in both phases of single-crystal VO_2 at the V $L_{2,3}$ edges ($2p \rightarrow 3d$, $h\nu \approx 510$–530 eV).

• Observed "dramatic switching" of orbital occupation across the transition—from almost isotropic in the metallic R phase to almost completely $3d_\pi$-polarized in the insulating M_1 phase—"indicating the crucial role of the orbitals and lattice in the correlated motion of the electrons".

• Argued that (i) such change in orbital polarization reduces the effective bandwidths as well as transforms the electronic structure of VO_2 from three-dimensional (R phase) to one-dimensional (M_1 phase)—thus making the V ions in the chains along the rutile c-axis very susceptible to a Peierls transition—but that (ii) strong electron correlations are also needed to attain the dramatic change of the orbital occupation by bringing the narrow-band VO_2 system to the Mott regime.

• Concluded that the VO_2 phase transition is an "orbital-assisted 'collaborative' **Mott-Peierls** transition".

⋆ **KÜBLER** *et al.*[1,69] (2007): *Coherent Structural Dynamics and Electronic Correlations during an Ultrafast Insulator-to-Metal Phase Transition in VO_2*

• Measured directly the temporal evolution of (the change $\Delta\sigma_1$ in) the mid-IR ($\hbar\omega = 40$–110 meV) electronic conductivity σ_1 of thin-film VO_2, using: (i) 12-fs optical laser pulses centered at $\lambda_{\text{pump}} = 800$ nm to trigger the insulator-to-metal transition, and (ii) multi-THz probe pulses with a variable pump-probe time delay to map $\Delta\sigma_1$ both spectrally and

temporally.

• Obtained "direct and selective access" to the structural and electronic microscopic degrees of freedom (DoF), since ultrabroadband THz pulses couple directly to lattice polarizability as well as electronic conductivity, on a femtosecond timescale.

• By simultaneously resolving the spectral signatures of electronic ($\hbar\omega \geq 85$ meV, free of phonon resonances) and lattice (40 meV $< \hbar\omega <$ 85 meV) DoF, revealed fundamentally different dynamics of the electronic (E) and lattice (P) contributions to $\Delta\sigma_1$, namely (Figure 1.8):

◦ (i) quasi-instantaneous increase in E-σ_1 (maximum at $\tau = 130$ fs) due to directly injected mobile carriers (photoexcitation is over after 50 fs), with E-$\Delta\sigma_1$ promptly decaying within 0.4 ps for sub-threshold fluence ($\Phi < \Phi_c = 4.6$ mJ $\cdot$ cm^{-2})—but when $\Phi > \Phi_c$, executing *one* oscillation cycle in phase with the lattice (see below) and subsequently settling to a constant value for at least 10 ps, which indicates transition of the electronic system into a metallic state (Figure 1.8b); and

◦ (ii) long-lived phononic contribution (Figure 1.8a), red-shifted and superimposed on a "remarkable coherent modulation" of P-$\Delta\sigma_1$ along the pump-probe delay axis τ, with a 6-THz center frequency of modulation—related to but distinct from the 5.85-THz (195-cm^{-1}) and 6.75-THz (225-cm^{-1}) lattice modes, which are associated with the pairing and tilting motions of the V–V dimers that map the monoclinic onto the rutile structure—the oscillations persisting for $\tau > 130$ fs, unlike the E contribution.

• Proposed a "novel qualitative picture" (Figure 1.9) for the photoinduced insulator-to-metal transition in VO_2, inspired by the work of Biermann *et al.*[30] (see above): ultrafast photoexcitation of spin singlets, *i.e.*, the V–V dimers, into a conductive state followed either by a subpicosecond recovery of intradimer electron correlations causing a return to the insulating state when $\Phi < \Phi_c$, or by settling into a (near-)steady metallic state when $\Phi > \Phi_c$, with the lattice still undergoing coherent oscillations far from equilibrium.

⋆ **QAZILBASH** *et al.*[2] (2007): *Mott Transition in VO_2 Revealed by Infrared Spectroscopy*

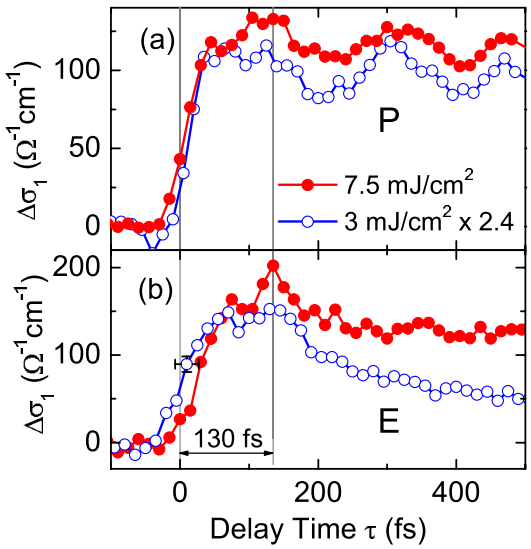

Figure 1.8: Contributions to the change $\Delta\sigma_1$ in mid-IR conductivity of VO_2 as a function of pump-probe delay time τ, due to **(a)** phononic ("P", photon energy $\hbar\omega = 60$ meV) and **(b)** electronic ("E", photon energy $\hbar\omega = 100$ meV) degrees of freedom. The traces taken at $\Phi = 3$ mJ $\cdot$ cm^{-2} are scaled by a factor of 2.4 in amplitude. After Kübler *et al.*[1]

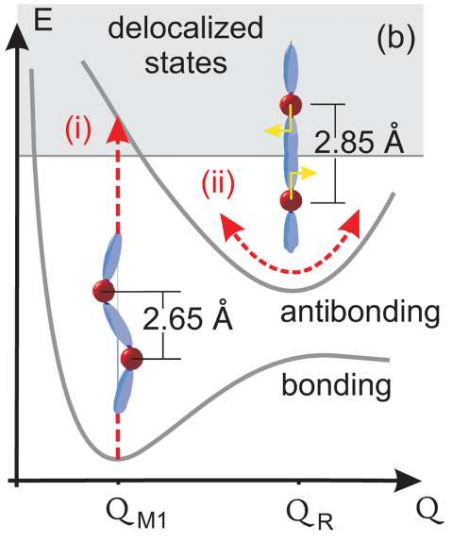

Figure 1.9: The minimum of the bonding energy surface defines the atomic position in the M_1 phase (Q_{M_1}). Absorption of a near-IR photon removes an electron from the bonding orbital, destabilizing the V–V dimer, while the lattice site is left in an excited state (marker (i)). In an isolated molecule, the energy surface of the excited state would lead to dissociation, but because of the repulsion by the nearest neighbors, an energy minimum of the antibonding orbitals is located near the R configuration by symmetry (Q_R). Ultrafast photoexcitation thus launches a coherent structural deformation of excited V–V dimers (marker (ii)), followed by oscillations at 6 THz around the new potential minimum. After Kübler *et al.*[1]

and Nano-Imaging

• Measured the electromagnetic response of a VO_2 film on a spatial scale of 20 nm, using scattering scanning near-field infrared microscopy (s-SNIM) in conjunction with far-field infrared spectroscopy.

• Imaged the appearance and temperature evolution of "nanoscale metallic puddles" in a narrow temperature range at the onset of the insulator-to-metal transition (Figure 1.10).

• Obtained the spectral and temperature response of the optical conductivity, scattering

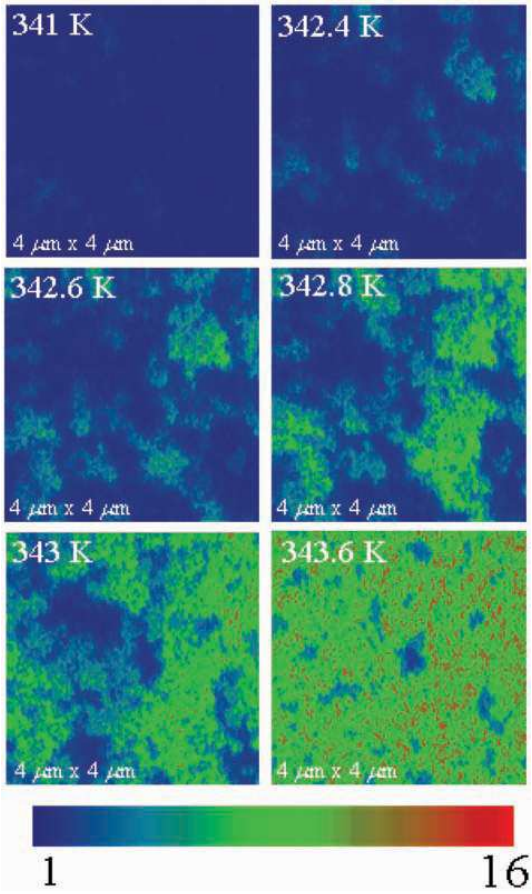

Figure 1.10: Images of near-field scattering amplitude over the same 4-μm-by-4-μm area obtained by s-SNIM operating at IR frequency $\omega = 930$ cm^{-1}. The images are displayed for representative temperatures in the VO_2 insulator-to-metal transition regime, showing percolation in progress. The metallic "nanopuddles" (light blue, green, and red colors) give higher scattering near-field amplitude compared with the insulating phase (dark blue color). After Qazilbash *et al.*[2]

rate, and optical effective mass of the nanoscale puddles, from a combination of near-field scattering amplitudes and far-field spectra within an effective medium theory (EMT).

• Revealed that the nanoscale metallic puddles have different characteristics from the rutile (R) metallic phase of VO_2, namely: (i) optical pseudogap in the electronic density of states, likely resulting from "a complex interplay between electronic correlations and charge ordering"; (ii) enhancement of the low-frequency effective optical mass at $T = 342$ K compared to the R-phase value (*e.g.*, at $T = 360$ K); (iii) crucially, divergent temperature-dependence of the low-frequency effective optical mass in the vicinity of the insulator-to-metal transition, arising from electronic correlations due to many-body Coulomb interactions—"an unambiguous attribute of the **Mott** transition".

• Concluded that the M_1 phase of VO_2 should be classified as a "Mott insulator with charge ordering", and that "the classic temperature-induced insulator-to-metal transition in VO_2 occurs from the monoclinic insulator [M_1 phase] to an incipient **strongly correlated metal (SCM)** in the form of nanoscale puddles" (Figure 1.11)—although the precise lattice structure of the SCM phase remains an open question, which can potentially be resolved using the nano-Raman technique described in Chapter V.

⋆ **BAUM** *et al.*[3] 2007: *4D Visualization of Transitional Structures in Phase Transformations by Electron Diffraction*

• Measured femtosecond-to-nanosecond changes in intensity of various electron-diffraction spots across the photoinduced transition in single-crystal VO_2, using 120-fs infrared (800 nm) laser pulses to initiate the transition and time-delayed electron packets to probe the structural dynamics via Bragg diffraction.

• Observed two distinct timescales—femtosecond and picosecond—corresponding to the temporal evolution of diffraction intensity of different Bragg spots, which "indicate stepwise atomic motions along different directions".

• Concluded that (i) the initial *femtosecond* motion occurs along the monoclinic a-axis, which is the direction of the V-V bond, and that (ii) the *picosecond* structural transforma-

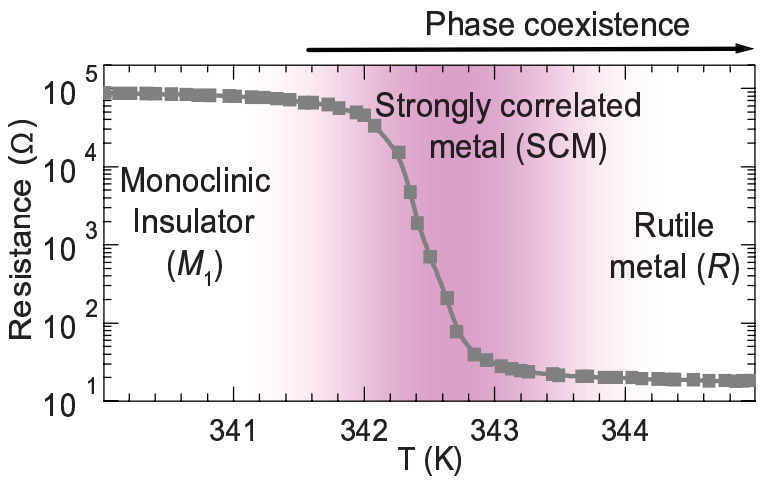

Figure 1.11: Phase diagram of VO_2 and resistance-temperature curve showing the insulator-to-metal transition. The shaded area highlights the region of the phase diagram where the strongly correlated metal (SCM) with divergent quasi-particle mass and an optical pseudogap exists in the form of "nanopuddles" (see Figure 1.10). After Qazilbash *et al.*[2]

tion projects along the c and b axes—because if the femtosecond motion had large components along b or c, it would show up in the dynamics of *all* investigated spots, contrary to the observations.

• Proposed a stepwise transformation path for the VO_2 transition on the atomic scale, as follows (see Figure 1.12): "The initiating excitation at 1.55 eV [800 nm] primarily involves the $3d_{//}$ band, which arises from bonding of the vanadium pairs. From a chemical perspective, the excitation is to an antibonding state, which instantly results in a repulsive force on the atoms, and they separate along the bond direction [initial fs-scale V–V dilation]. In sequence and on a slower timescale, the unit cell transforms toward the configuration of the rutile phase. Therefore, the observed stepwise atomic motions show that the phase transition proceeds by a nondirect pathway on the multidimensional potential energy surface and not by a direct structural conversion. [...] The coincidence of the thermal and photoinduced transition thresholds at different temperatures suggests the common pathway mechanism for the transition."

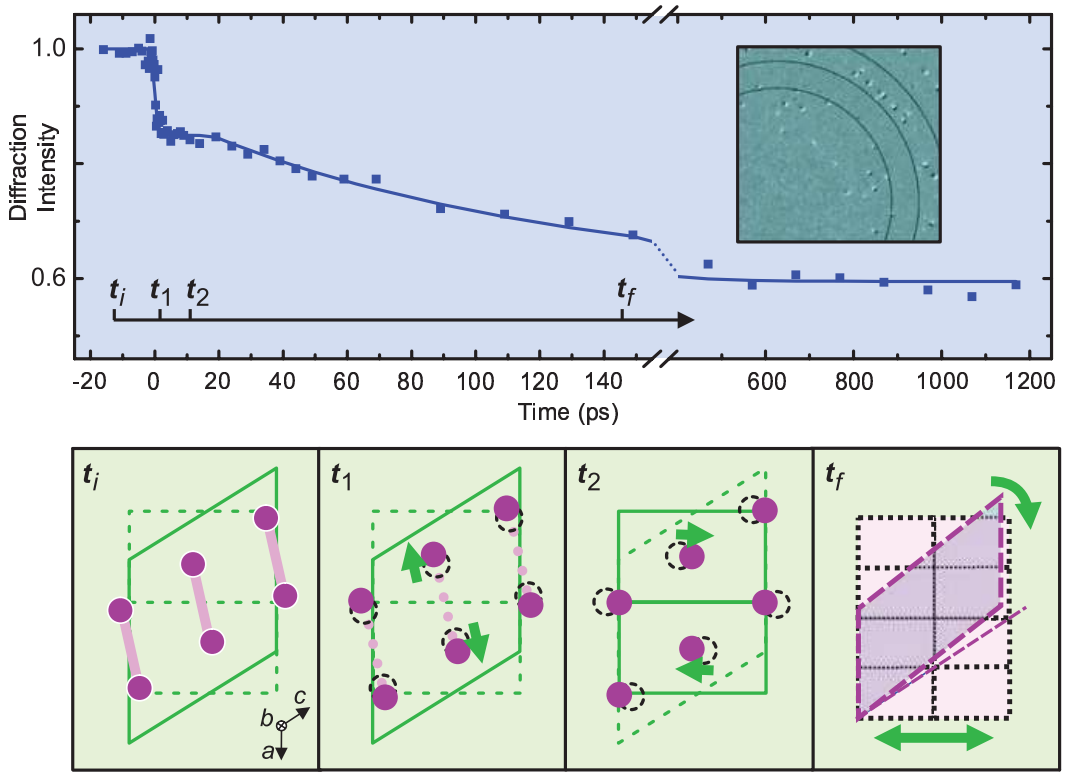

Figure 1.12: Transitional structures during ultrafast phase transformation of VO_2. **Top:** The experimental data from a particular Bragg diffraction spot reflects the stepwise atomic motion within the unit cell and, on larger length scales, the shear motion. **(inset)** The difference in static X-ray patterns between monoclinic M_1 (low-temperature) and rutile R (high-temperature) VO_2 suggests macroscopic shear (angular) displacement. **Bottom:** Frames at the corresponding times (t_i, t_1, t_2, and t_f) of structural changes, showing the t_1 ultrafast (fs, V–V dilation), t_2 fast (ps, atomic-scale shear), and t_f speed-of-sound (sub-ns, long-range macroscopic shear) movements that transform monoclinic into rutile VO_2. The axes refer to the monoclinic phase. After Baum *et al.*[3]

1.2 Thermodynamics and hysteresis

The phase transformation of VO_2 can be classified thermodynamically according to the relation between the discontinuous thermodynamic quantities and the free-energy function.[70] Thus, VO_2 undergoes a *first-order transition*, since the volume V (Reference [55]) and the entropy S (Reference [71]) change discontinuously at the equilibrium transition temperature T_c, with those two quantities being *first* derivatives of the Gibbs free energy G:

$$G \equiv H - TS = U + PV - TS \tag{1.1}$$

$$\left(\frac{\partial G}{\partial P}\right)_T = V, \quad \left(\frac{\partial G}{\partial T}\right)_P = -S \tag{1.2}$$

where H is the enthalpy, U is the internal energy, and P is the pressure; the subscripts indicate which quantities are held constant. Figure 1.13 represents schematically a two-phase

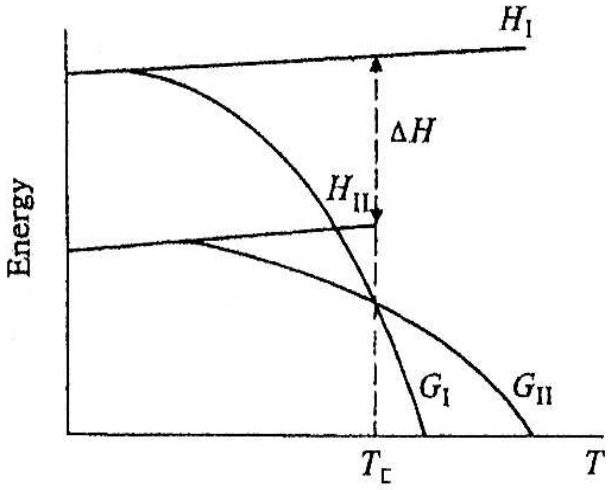

Figure 1.13: Sketch of variation of enthalpy (H) and Gibbs free energy (G) with temperature (T), for two-phase system (I and II) at constant pressure. The free-energy curves intersect at the point of thermodynamic equilibrium, *i.e.* the "true" transition temperature T_c. After Reference [70].

system undergoing a first-order transition as a function of temperature, with a discontinuous change in entropy ΔS, and hence a latent heat of transformation $\Delta H = T_c \Delta S$. Below T_c, phase II is stable because $G_{II} < G_I$, whereas phase I becomes stable for $T > T_c$. The two phases coexist at T_c and differ by their enthalpies, indicative of different structural details at the equilibrium point. As sketched in the figure, the free-energy curves G_I and G_{II} may be extrapolated, albeit to a limited extent, on either side of T_c, and the resultant situations would correspond physically to an undercooled (*i.e.*, supercooled) phase I and overheated (*i.e.*, superheated) phase II. Indeed, it is the persistence of a phase beyond the formal terminus (here, T_c) of its thermodynamic stability that constitutes the phenomenon

of *hysteresis*.

Experimentally, thermal hysteresis manifests itself as a difference in the transition temperatures for heating and cooling through T_c, indicating that the transformation does not occur at the point where the free energies of the two phases are exactly equal. Accompanying the lag in the system response to external driving are a dependence on the previous transformation history (forward or reverse direction, extent of completion) and energy dissipation. From a microscopic point of view, hysteresis marks the presence of multiple metastable two-phase configurations, dynamically linked along the transformation path.[72]

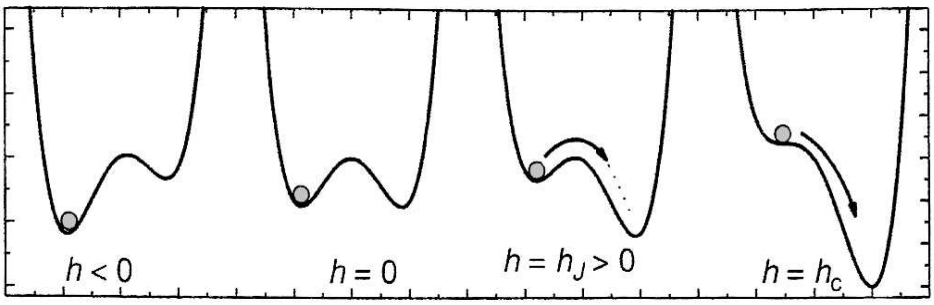

Figure 1.14: Generic double-well potential with linear tilt controlled by the driving field h. The dot represents the occupancy of either of two consecutive metastable minima within the transition region, with the arrow pointing to the more stable state. After Reference [72].

Figure 1.14 illustrates the occurrence of hysteresis in a simple intuitive model. Let us consider a bistable potential with a linear tilt controlled by an external driving field h, which may represent, for example, a temperature change with respect to the equilibrium point. The potential wells may correspond to two consecutive metastable minima within the transition region. Starting with $h < 0$ and the system initially occupying the lower well, the driving field is increased towards the phase equilibrium. Since there is an energy barrier separating the two wells, the system is still in the same well at $h = 0$. As the field is increased further, the energy barrier decreases but the system will remain in the metastable

upper well at least until $h = h_J > 0$, at which point a jump to the lower minimum *may* occur. The limiting value of the driving field is $h = h_c$, where the upper well and the energy barrier disappear, and the jump occurs with certainty.[72] By symmetry, the reverse transition terminates at $h = -h_c$, and the two limiting values mark the maximum hysteresis width.

This simple model leaves an open question: Given enough time, can thermal fluctuations assist in overcoming the energy barrier separating the two states, even at $h = 0$? The strict answer is "yes", and because of the randomness of thermal fluctuations, the control parameter $h = h_J$ is actually a random variable with a probability distribution characterized by its mean value $\langle h_J \rangle$ and standard deviation σ_J. However, the kinetics of the particular transition must enter into practical consideration. From a kinetic point of view, the passage of a system from a metastable to a more stable state under the influence of an external field (Figure 1.14) proceeds as a competition between the sweep rate τ_h^{-1} of the driving parameter (*e.g.*, temperature), the thermal decay rate τ_f^{-1} of the metastable state, and the nonthermal decay (relaxation) rate τ_r^{-1} from a locally unstable state to the next metastable state occurring at the limiting value (h_c) of the driving field. Such competition is at the origin of the hysteresis effect in many systems.[72]

A peculiar scenario occurs when $\tau_r \ll \tau_h \ll \tau_f$, that is, when the system spends the overwhelming majority of its time in a static situation. These transitions are called *athermal*, in the sense that thermal fluctuations do not play a relevant role, so the system needs continuous heating or cooling for the transformed fraction of the new phase to increase. Formally, if $\tau_h/\tau_f \to 0$, it can be shown[72] that $\sigma \to 0$ and $\langle h_J \rangle \to h_c$: thermal fluctuations are inoperative and the energy barrier can only be overcome when the limiting driving field h_c is reached. Thus at any temperature within the phase coexistence region, an athermal transition appears to be instantaneous on practical time scales and the transformed fraction increases only if the external temperature is changed.

Typical examples of athermal transitions are the so-called *martensitic* transformations,

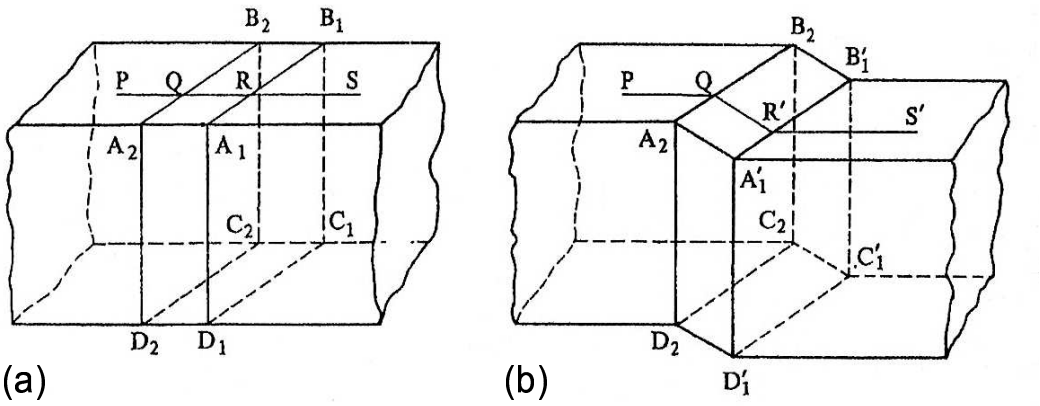

Figure 1.15: Schematic representation of **(b)** martensitic plate (middle section) formed from **(a)** rectangular block of the parent crystal. The letters indicate points of correspondence between the two phases. After Reference [70].

which have been observed in a variety of crystalline solids, ranging from simple metals to shape-memory alloys and even biological systems.[72,73] While variations on what exactly constitutes a martensitic transition abound in the literature,[74] certain characteristics are usually deemed pertinent and used by way of definition:[72,73] **(i)** structural distortion involving a shear-dominated lattice change; **(ii)** diffusion not required for the transformation; and **(iii)** strain energy dominates the kinetics and morphology during the transition. Figure 1.15 gives a schematic idea of the formation of martensite, clearly depicting the shear-type displacive deformation of the parent crystal. Since the above definition is not based on the structure, morphology, or properties of the specific transformation product, but rather on how the product forms,[73] the martensitic transformation can be used as a model to study the phenomenology of any crystalline solid that undergoes a fast, diffusionless, and shear-dominated first-order phase transition. As it turns out, the phase transition of VO_2 shares all those characteristics, in addition to a host of rather complex and still not fully understood hysteretic effects. An explicit empirical correspondence between the VO_2 phase transition and a model of martensitic transformation was established by Khakhaev *et al.* (see Reference [75] and several of the references therein).

Very recently, Sharoni *et al.*[4] have experimentally demonstrated the athermal nature

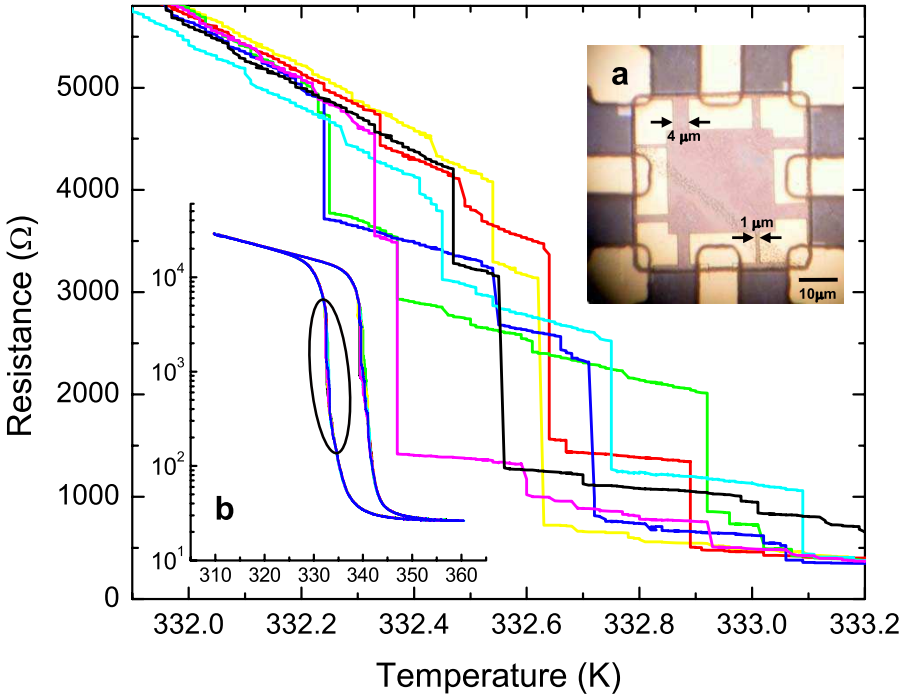

Figure 1.16: Discrete jumps (avalanches) in resistance R as a function of temperature T across the phase transition of nanoscale VO_2 junctions. **(main panel)** 8 consecutive R–T cycles (R in linear scale) for VO_2 device (1×6 μm^2), zoomed in on the region of the cooling curve marked by ellipse in **(b)** the full measurement (R in log scale). **(a)** Image of 8 devices on one sample showing VO_2 square (50×50 μm^2), on top of which are Au-on-V electrodes defining device lengths of 1, 2, 3, and 4 μm (2 devices of each) and width of 8 μm for all the devices; devices with length of 1 and 4 μm are marked. After Reference [4].

of the VO_2 transition, and, more intriguingly, its microscopic "jerkiness", which is another typical feature of martensitic transformations.[72] The authors measured the resistance of 90-nm-thick VO_2 nanostructures of various lengths (200 nm–4 μm) and widths (2–15 μm); a representative sample with eight such devices is imaged in Figure 1.16a. The jagged curves in Figure 1.16 correspond to several consecutive measurements of resistance as a function of temperature (on cooling) across one particular 1×6 μm^2 VO_2 device, while Figure 1.16b shows the full hysteresis cycle. Sharoni *et al.* observed that the resistance jumps occurred between two consecutive measurements even for the slowest temperature sweep rates, whereby adjacent data points were separated by (nominally) less than 0.5 mK, indicating that the timescale of each jump was much shorter than the response time

of the measurement apparatus, owing to the fast progression of the VO_2 transition. As the authors point out, this jerky behavior implies a discontinuous transition between the spatially separated but coexisting metallic and semiconducting VO_2 phases,[2,76] which takes place through a series of avalanches observed as resistance jumps in the measurements.[4] The authors also noted a particular distribution of jump magnitudes: fewer than ten large jumps, which may account for 50% of the resistance change, and numerous smaller jumps covering a wide range. They attributed this distribution to percolation effects[48] arising from the constrained device geometry and the phase coexistence of metallic and insulating VO_2; the largest observed jump in resistance was identified as the percolation threshold for each device.[4]

Avalanches connecting metastable equilibrium states are a general microscopic feature of martensitic transitions (*e.g.*, see Reference [77]), born of the "graininess" of the transforming material. At each step in the transition from the high- to the low-temperature phase, for example, elastic energy is stored in the system and, simultaneously, energy is released as latent heat and irreversible energy, with the system reaching thermoelastic equilibrium. Therefore, the external temperature must be lowered at each new metastable situation in order to restart the transformation,[72] leading to the macroscopically observed athermal behavior. As discussed by Ortín *et al.*,[72] the transformation usually involves differently oriented domains of the parent phase (grains), in which the martensite phase nucleates and grows in a number of different orientations (variants); even a single-crystal to single-crystal martensitic transition necessitates at least one interface separating the two phases. The interfacial energy of the domain boundaries contributes to the internal energy of the material. On the other hand, shape and volume differences between the two phases induce an extremely complex strain field among the differently oriented domains and variants. The strain energy dominates the transition kinetics and the morphology of the product phase. Because of the spatially inhomogeneous strain field, different regions in the sample transform at different levels of applied temperature.

To attain a more realistic description of the transition thermodynamics, two main points require consideration:[72] **(i)** the transformation takes place by a sequence of metastable states, rather than at equilibrium; and **(ii)** the passage between metastable states is a *dissipative* process, which gives rise to hysteresis. The energy balance for the passage from one metastable two-phase state to the next along the transformation path now includes two more contributions besides the driving-force term given by the Gibbs free-energy difference: **(i)** the elastic energy stored by the strain field within the material, and **(ii)** the energy dissipated irreversibly during the nonequilibrium process. The dominant mechanism of energy dissipation is the relaxation of elastic strain energy, released (at least partially) during avalanches in the form of ultrasonic transient elastic waves, known as acoustic emission. The crucial point is that the irreversible energy always makes a nonnegative contribution to the energy balance, regardless of the direction in which the transition progresses, reflecting the fact that the branching of transformation trajectories upon reversal of the transformation direction—the essence of hysteresis—stems from energy dissipation.[72]

The above concepts are illustrated in Figure 1.17, which shows the generic staircase microstructure of an avalanche-mediated thermal hysteresis. Along the horizontal segments, the two-phase system is blocked in a metastable state with the fraction of transformed material X remaining constant ($\delta X = 0$), while the driving force caused by the free-energy difference between the two phases builds up due to the change in external temperature δT. Along the (nearly) vertical segments, an abrupt transition, that is, an avalanche, takes place from one metastable state to the next, whereby the transformed fraction X changes by some amount $\delta X \neq 0$ (avalanche amplitude), and the corresponding free energy is partially stored in the elastic strain field and partially dissipated (*e.g.*, as acoustic emission or frictional heat). The passage between metastable states is almost instantaneous compared to typical driving rates, since the domain walls move at velocities close to that of sound in the material (*e.g.*, $\sim 4000\ \mathrm{m \cdot s^{-1}}$ in VO_2 according to Reference [78]). The transformation path can then be regarded as a dense sequence of metastable states, in which the system

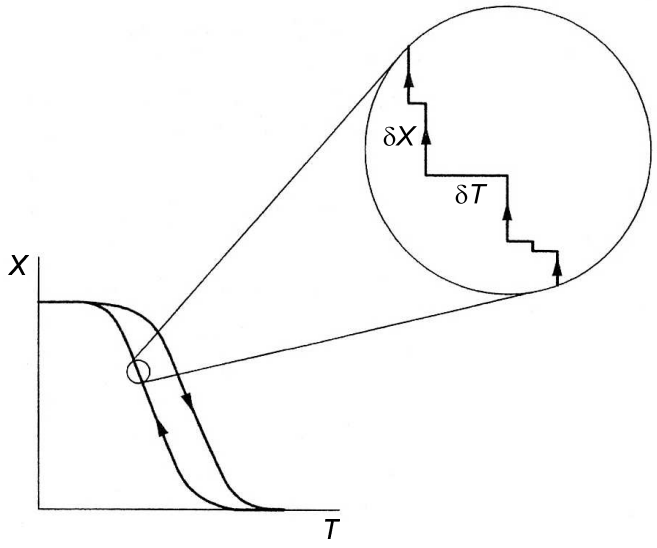

Figure 1.17: Schematic of avalanche-mediated transformation path as a function of temperature T, where X is (any property proportional to) the fraction of transformed material. The driving force, built up by the change in temperature δT (horizontal segments), is partially stored and partially dissipated in the transformation jumps (vertical segments). After Reference [72].

spends most of its time, thus allowing a quasi-static thermodynamic description, such as "athermal transition", despite the jerky character of the individual transformation events. In addition, the area enclosed by the macroscopic hysteresis loop is directly proportional to the total energy dissipated during the transformation cycle.[72] Figure 1.18 presents some examples of typical hysteresis cycles observed in thermally induced martensitic transitions.

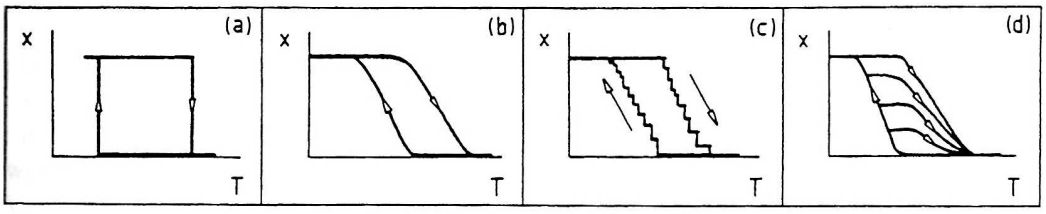

Figure 1.18: Schematic representation of some hysteresis loops encountered in thermally induced transitions: **(a)** single-interface transformation in single crystal; **(b)** transformation via multiple interfaces; **(c)** discontinuous jumps (avalanches); **(d)** partial cycles. After Reference [73].

Specifically for VO_2, a variety of hysteretic effects have been observed in bulk crystals, contiguous or perforated (see Chapter IV) thin films, nanowires (*e.g.*, see Figure 1.16 or Reference [48]), and nanoparticles (see Sections 1.3 and 6.1.1, and Chapters V and VI). Mostly qualitative discussions of hysteresis shape, inclination, amplitude, position, and width are scattered throughout the VO_2 literature (*e.g.*, see Reference [79]), but in some cases numerical[75,80] or analytical models[5,47,81] have been developed (see also Section 1.3.2). Among the factors believed to affect the transformation pathway in VO_2 are: synthesis and annealing conditions;[82,83] crystallographic orientation of film and/or substrate and type of substrate material;[79,84,85] film thickness;[86] degree of stoichiometry[87] and crystallinity;[45,88] doping[52,89–91] and irradiation;[92–96] grain size and microstructure;[45–47,97–100] nanoparticle size[5,9] (see also Chapter VI) and morphology (see Chapter V).

1.3 VO_2 nanoparticles: Nucleation and size-effects

Here we recall a striking manifestation of the hysteresis phenomenon in nanocrystalline VO_2, as demonstrated by Lopez *et al.*[5,50,51] Figure 1.19 shows electron micrographs of three ensembles of VO_2 nanoparticles (NPs) of different effective sizes (70, 130, 180 nm), prepared by implantation of vanadium and oxygen ions into fused silica and subsequent thermal annealing. Also presented for each ensemble is the optical transmission at $\lambda = 1.5$ μm across the VO_2 phase transition, normalized to the maximum transmission value in the semiconducting phase. What is striking about these thermal hysteresis loops are their anomalously large widths, ΔT up to 50 K, in comparison with the usual 1–15 K in bulk crystals or thin films of VO_2, as well as the apparent dependence of the anomalous ΔT on the size of the NPs. Below is a concise explanation of these effects, following the account of Lopez *et al.*[5]

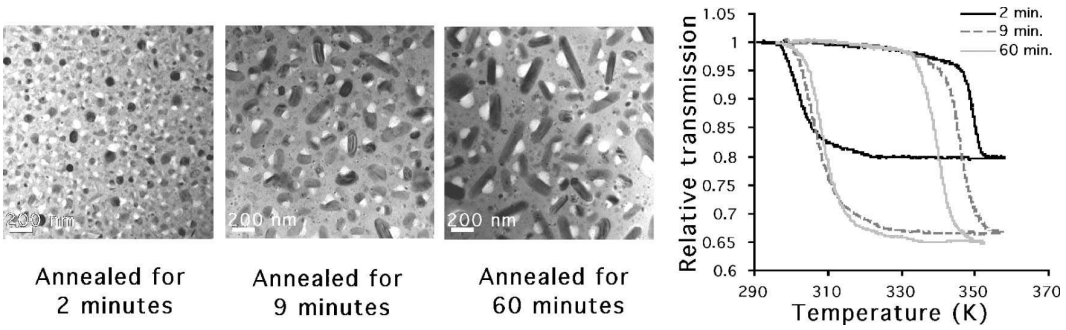

Figure 1.19: Transmission electron micrographs (TEMs) of VO_2 precipitates in SiO_2 and their optical transmission as a function of temperature at $\lambda = 1.5\mu$m. Shorter annealing times produced smaller precipitates (2 min: ∼70 nm; 9 min: ∼130 nm; 60 min: ∼180 nm), and shifted the heating and cooling transition temperatures to produce wider hysteresis loops. The samples were prepared by implanting SiO_2 with $1.5{\cdot}10^{17}$ V-ions/cm^2 at 150 keV and $3.0{\cdot}10^{17}$ O-ions/cm^2 at 55 keV, then annealing in argon at 1000 °C. After Reference [5].

1.3.1 Unviability of homogeneous nucleation for VO_2

Before discussing the model of heterogeneous nucleation that accounts for the wide hysteresis loops of the above VO_2 NPs, we first show that homogeneous nucleation of the VO_2 phase transition is highly improbable.[5] Assuming no difference between the specific volumes of the two phases and hence no strain at the phase boundary—which would actually enhance the barrier for nucleation—the change in free energy ΔG due to the formation of spherical nuclei consists of two terms: **(i)** the bulk free-energy *decrease* per unit volume, Δg_{ex}, also referred to as the *excess driving force* of the transition;[44] and **(ii)** the surface free-energy *increase* per unit area of the surface, γ. For a spherical "embryo" (*i.e.*, a tiny unstable region of the product phase) of radius r, ΔG may be written as

$$\Delta G = -\frac{4\pi}{3} r^3 \Delta g_{\text{ex}} + 4\pi r^2 \gamma \tag{1.3}$$

Embryos can evolve into stable nuclei only if the net free-energy change during their formation is negative; otherwise, the unstable embryo dissolves back into the parent phase. Since the positive second term in Equation 1.3 dominates over the negative first term at small values of r, embryos of such sizes are thermodynamically unstable and nucleation cannot

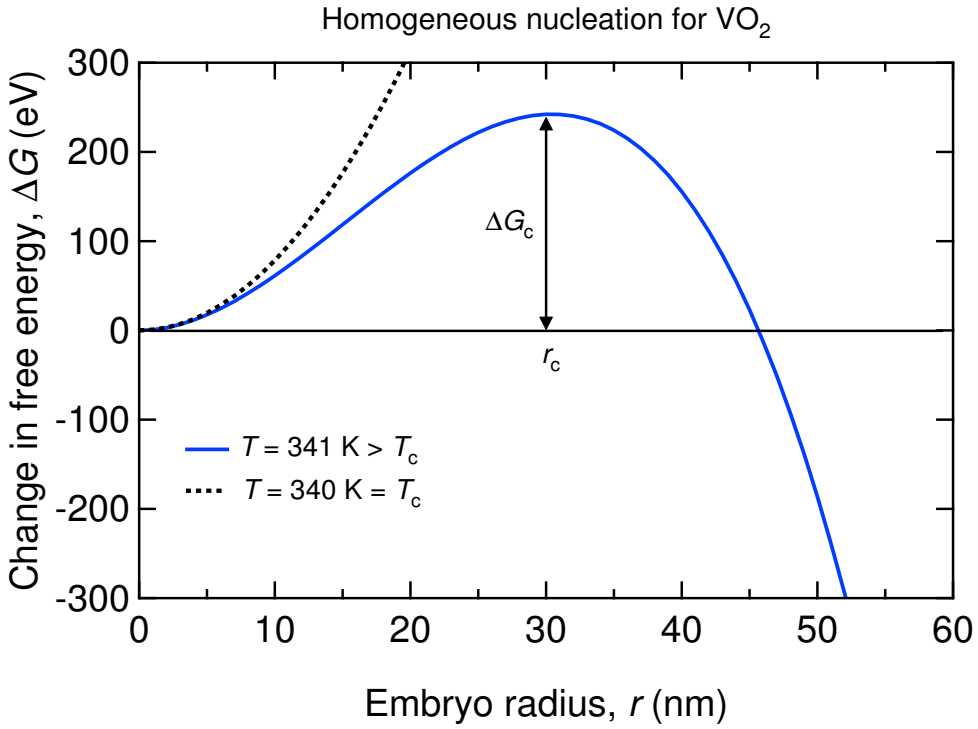

Figure 1.20: Variation of nucleation barrier ΔG as a function of embryo size, for two different temperatures, using VO_2 parameters from the literature. Note that no stable nucleus can form at T_c, since ΔG is then positive for all r. *Legend*: $T_c \equiv$ thermodynamic transition temperature; $\Delta G_c \equiv$ critical excess free energy; $r_c \equiv$ critical nucleus size.

proceed. However, if an embryo attains a critical size of radius r_c, ΔG will begin to decrease and further growth will be thermodynamically favorable.[70]

For VO_2, Figure 1.20 plots the dependence of ΔG on r using Equation 1.3, with an estimate of $\gamma = 10^{-2}$ J $\cdot$ m^{-2} (Reference [5]) and an expression for Δg_{ex} that exhibits the (approximately) linear dependence of the excess driving force on the amount of undercooling and overheating,[44,70] *i.e.*,

$$\Delta g_{ex} = \Delta s \, |T - T_c| \tag{1.4}$$

The proportionality constant Δs is determined by the entropy difference between the parent and product phases;[44] for VO_2, $\Delta s = 6.57 \cdot 10^5$ J $\cdot$ K^{-1} $\cdot$ m^{-3} (Reference [71]). For a given temperature other than T_c, which is defined as the "true" thermodynamic transition

temperature where the free energies of the two phases are exactly equal, the critical nucleus size r_c and the critical excess free energy ΔG_c can be obtained from the maximum of the free-energy curve (see solid line in Figure 1.20):

$$\left.\frac{\partial \Delta G}{\partial r}\right|_{r=r_c} = 0 \quad \Rightarrow \quad r_c = \frac{2\gamma}{\Delta g_{ex}} = \frac{2\gamma}{\Delta s\,|T - T_c|} \tag{1.5}$$

$$\Delta G_c = \frac{16\pi}{3}\frac{\gamma^3}{\Delta g_{ex}^2} = \frac{16\pi}{3}\frac{\gamma^3}{(\Delta s\,|T - T_c|)^2} \tag{1.6}$$

Precisely at the "true" transition temperature, $T = T_c$, no nucleation can occur because ΔG is always positive (see dotted line in Figure 1.20) and the nucleation barrier diverges: $\Delta G_c\,(T = T_c) \to \infty$. Therefore, since a phase transformation can never occur at the precise equilibrium temperature, some amount of undercooling and overheating—that is, excess driving forces—must be imposed to initiate the transition. This kinetic requirement justifies, at least formally, the existence of thermal hysteresis around the equilibrium transition temperature.[70]

The magnitude of the excess critical free energy ΔG_c in Figure 1.20 points to another important conclusion: *homogeneous* nucleation of the VO_2 phase transition is energetically very unfavorable because the energy barrier for this type of nucleation, $\Delta G_c \approx 250$ eV, is much larger than the energy involved in thermally inducing the transition, $k_B T_c = (8.61 \cdot 10^{-5}\ \text{eV} \cdot \text{K}^{-1})\,(340\ \text{K}) \approx 0.03$ eV. Therefore, the VO_2 phase transition must be initiated at special nucleation sites of "high potency", rather than uniformly throughout the volume, in a process referred to as heterogeneous nucleation.

1.3.2 Heterogeneous nucleation in VO_2 NPs

The nature of the special nucleation sites in VO_2 is practically unknown, but in principle they can consist of vacancies, impurities, various types of dislocations, untransformed embryonic regions, grain and interface boundaries, electronic defects due to the multivalent character of the vanadium ion, and so on.[5] Whatever their diverse origins, nucleation sites

capable of initiating the VO_2 transition must somehow reduce the local energy barrier for forming a stable nucleus of the product phase inside the parent phase, so that the transformation can begin even under such modest driving forces as are typically employed in thermally inducing the transition. In light of the unusual switching properties observed for nanoscale amounts of VO_2 (Figure 1.19), it seems reasonable to relate the hysteresis width, which represents the excess thermal driving forces necessary to cycle through the forward and reverse transitions, to the availability of potent nucleation sites within each confined volume of VO_2 material. In other words, a higher probability of finding potent defects at a given temperature entails smaller excess driving forces needed to complete the transition cycle, and hence results in a narrower hysteresis loop.

To explain the dependence of the hysteresis width on NP size, Lopez *et al.*[5] adopted a model based on the statistics of heterogeneous nucleation of martensitic transitions[43,44]—a class of high-speed, diffusionless, shear transformations that provide a general basis for understanding structural changes in many systems,[70] including vanadium dioxide.[75] According to this model, the probability F that a particle of volume V harbors at least one potent nucleation site is given by

$$F = 1 - \exp\left[-\rho \cdot V\right] \tag{1.7}$$

where ρ is the density of such sites per unit sample volume. If the transformation is nucleation controlled, then F directly represents the transformation probability of the particle itself. As the driving force imposed on the particle increases, for example, by increasing the extent of undercooling or overheating, defects of lower potency may become active. Since low-potency defects are likely to be more abundant than high-potency defects, ρ is expected to increase with the excess driving force, as in $\rho \propto (\Delta g_{\text{ex}})^m$, where m is a positive phenomenological exponent. The power-law dependence can be justified by a more detailed analysis of the statistical correlations between the size, potency, and abundance of generalized nucleating defects.[44] Using this relationship for the potency distribution ρ, as well as

the explicit expression for Δg_{ex} from Equation 1.4, the transformation probability becomes

$$F = 1 - \exp\left[-C \cdot \Delta g_{\mathrm{ex}}^{m} \cdot d^{3}\right] = 1 - \exp\left[-C \cdot (\Delta s\,|T - T_{\mathrm{c}}|)^{m} \cdot d^{3}\right] \tag{1.8}$$

where C is a proportionality constant and d is the diameter of the particle. The reference temperatures T_{c} can be obtained by extrapolation to the points where the forward and reverse transitions start for the bulk material (Figure 1.21).

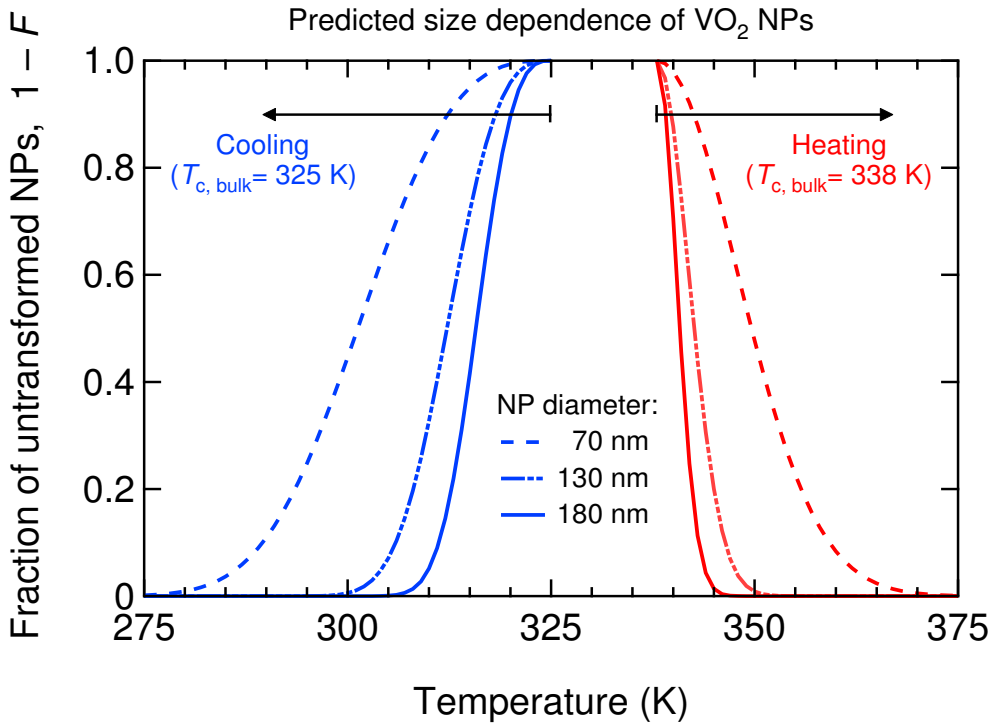

Figure 1.21: Predicted size dependence of the stability of VO_2 NPs against semiconductor-to-metal transformation on heating and metal-to-semiconductor transformation on cooling, according to the model of heterogeneous nucleation (see Equation 1.8). For VO_2, the specific values of parameters C and m were obtained by Lopez *et al.* from fits to their experimental data.[5]

Lopez *et al.* applied this model to the optical transmission data for ensembles of implanted VO_2 NPs of different effective sizes;[5] three of those ensembles were presented in

Figure 1.19. Identifying the probability of transformation F with the relative optical transmission, the authors were able to obtain good least-squares fits to the experimental data using Equation 1.8. Figure 1.21 plots the thus predicted dependence of the VO_2 phase transition on NP size. On average, smaller NPs need larger deviations from the bulk transition temperatures $T_{c,\ bulk}$ to complete their transformation cycle because they are less likely to contain suitable nucleating defects. A later experiment by Lopez *et al.*,[9] performed on arrays of lithographically patterned VO_2 NPs of well-controlled sizes, revealed the stochastic nature of the phase transition by demonstrating that NPs of a defined size do not have a unique T_c, but a probability of transformation centered at that temperature[9] (see also Section 6.1.1).

CHAPTER II

EXPERIMENTAL TOOLS AND TECHNIQUES

Abstract

This chapter describes some of the experimental techniques and instruments used to fabricate, characterize, and optically probe the nanostructures explored in the subsequent chapters.

2.1 Pulsed laser deposition (PLD)

Pulsed laser deposition (PLD) is an application of *laser ablation*, the generic process of laser-induced material removal, to the growth of thin films from elemental or compound targets. A powerful laser beam impinges on the target material, undergoes absorption, and vaporizes a thin surface region.[101] One of the most common PLD lasers, and the one used in this work, is the krypton fluoride (KrF) excimer (*exci*ted di*mer*) laser operating at an ultraviolet (UV) wavelength of $\lambda = 248$ nm ($\equiv 5$ eV). Short-wavelength photons are strongly absorbed by most materials and have sufficient energy to induce photochemical reactions and break molecular bonds.[102]

2.1.1 Excimer lasers and laser-induced vaporization

Figure 2.1a sketches the typical layout of an excimer laser. A high-voltage switching component (*e.g.*, thyratron or thyristor) delivers an electrical pulse of high energy density, on the order of 10^{-2} J $\cdot$ cm^{-3}, discharged homogeneously into the laser gases on a timescale of a few nanoseconds to create a high-pressure glow discharge.[102] The gas mixture inside the pressurized laser tube consists primarily of the discharge carrier, which is the buffer gas (mostly helium), and, with a much lower concentration, the reactant gases (*e.g.*, Kr

and F_2). The dominant reaction paths for the KrF system are shown in Figure 2.1b: The formation of the electronically excited $(KrF)^*$ molecule follows both a *neutral* channel, that is, a chemical exchange reaction, and an *ionic* recombination channel. Since third-body collisions with the buffer-gas atoms stabilize these processes, high pressures of a few bars are usually utilized. The buffer gas also provides fast relaxation to the lowest vibrational state of $(KrF)^*$, followed by a radiative transition ($\lambda = 248$ nm) to the electronic ground state within a few nanoseconds.[102]

The rare-gas–halide systems typically have two electronic ground states, correlating with the electronic ground states of the rare-gas and halogen atoms, which combine to a molecular Σ and a Π state (Figure 2.1c). While the Π state is strongly repulsive, the Σ state exhibits a shallow potential-energy minimum (only a few hundred cm^{-1} in depth), so that thermal energy causes the molecule to dissociate within a few picoseconds. The first electronically excites states correlate with the positive rare-gas and negative halogen ions (see the right-hand-side branch in Figure 2.1b), and hence show a deep minimum. The higher states correlate with the electronic excitations of the neutrals (see the left-hand-side branch in Figure 2.1b), and their potential is shallower, as is expected of covalent bonding.[102]

Pulsed laser deposition is a "flash evaporation" method. In order to avoid shadowing by the evaporant plume, the laser beam is fired at an angle to the target normal, resulting in an elliptical beam spot of typical area $\delta A = 0.1$ cm^2 on the surface (Figure 2.2a). During each of the pulses in the laser waveform (Figure 2.2b), with a typical duration $\delta t = 25$ ns and repetition rate $f = 50$ Hz, part of the incident energy is reflected from the target surface and the rest is absorbed, followed by fast heat conduction downward from the surface to a depth determined by the thermal diffusion length L_t of the target material (Figure 2.2c); this heat conduction occurs on the time scale of the laser pulse.[101] For strongly absorbing materials, such as metals (*e.g.*, vanadium) and narrow-bandgap semiconductors (*e.g.*, vanadium oxides), $L_t \gg L_{abs}$, where the optical absorption length L_{abs} is the inverse of the optical absorption coefficient at the laser wavelength, $L_{abs} = 1/\alpha(\lambda)$. For metal

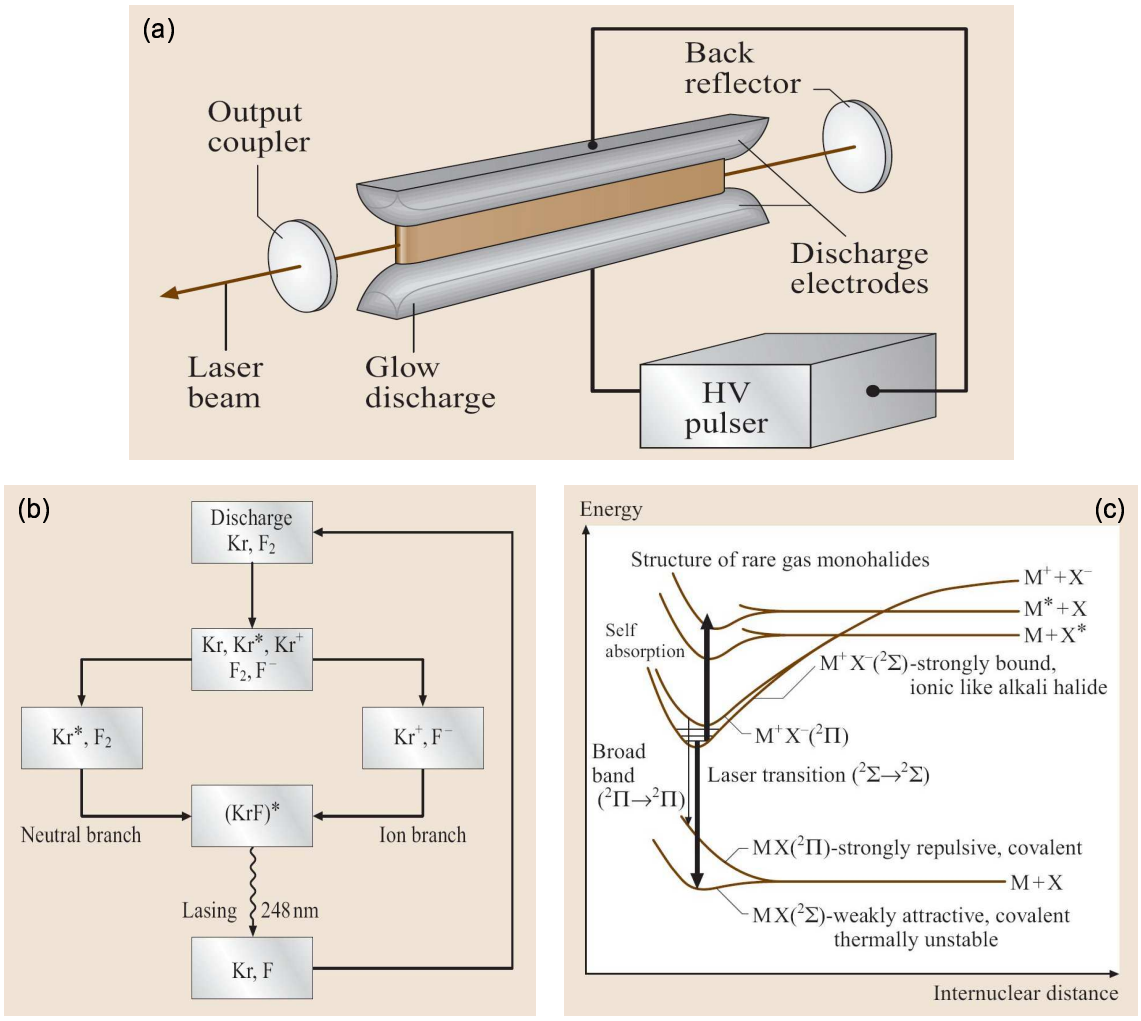

Figure 2.1: **(a)** Excimer laser layout: resonator cavity with UV optics (typically CaF_2), discharge electrodes, and high-voltage (HV) switching circuit for generating transverse electrical discharges with duration of several nanoseconds; the gas mixture inside the laser tube is pressurized to a few bars. **(b)** Flowchart of dominant reaction paths in KrF excimer laser; asterisk denotes electronic excitation. **(c)** Typical potential-energy diagram as a function of internuclear distance for rare-gas halide molecule. *Legend*: M ≡ rare-gas atom (*e.g.*, Kr); X ≡ halogen atom (*e.g.*, F); Σ, Π ≡ molecular states. After Reference [102].

targets, L_{abs} is on the order of 10 nm at UV wavelengths, whereas L_{t}, which scales as $\sqrt{\delta t}$, is on the order of 2–3 μm. The solid material within the heated volume $\delta A \cdot L_{\mathrm{t}}$ melts and a fraction of the atoms also receive the heat of evaporation. A large pressure gradient causes this initial layer to expand out of the shallow crater, mainly along the target normal. As the vapor expands adiabatically, its temperature greatly decreases while its flow velocity

increases, giving rise to a conical plume of evaporant (Figures 2.2c and 2.3b). The adiabatic expansion ceases when the plume density drops sufficiently, and the vapor particles continue travelling towards the substrate in free molecular flow, whereby the mean free path of a particle is long compared to the dimensions of the plume. In reality, the plume is very complex, consisting of ground- and excited-state atoms, molecules, ions, electrons, and atom clusters, its adiabatic expansion may not be complete before reaching the substrate, and it may tilt towards or away from the laser beam depending on surface morphology.[101]

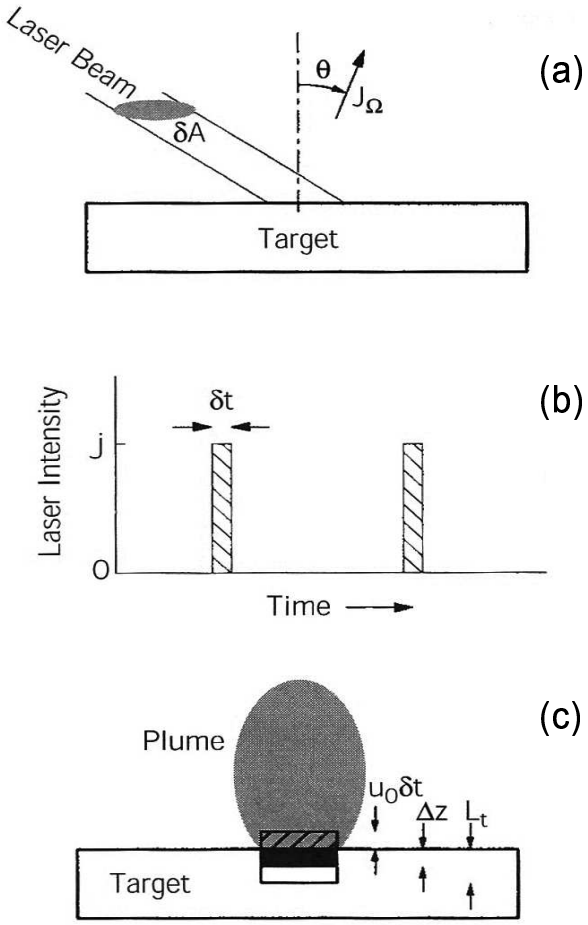

Figure 2.2: Pulsed-laser deposition (PLD) process: **(a)** laser-target arrangement; **(b)** ideal laser waveform, with pulse duration δt; **(c)** heated volume $\delta A \cdot L_\mathrm{t}$, vaporized layer $\delta A \cdot \Delta z$, initial vapor volume $\delta A \cdot (\Delta z + u_0 \delta t)$, and plume of evaporant. After Reference [101].

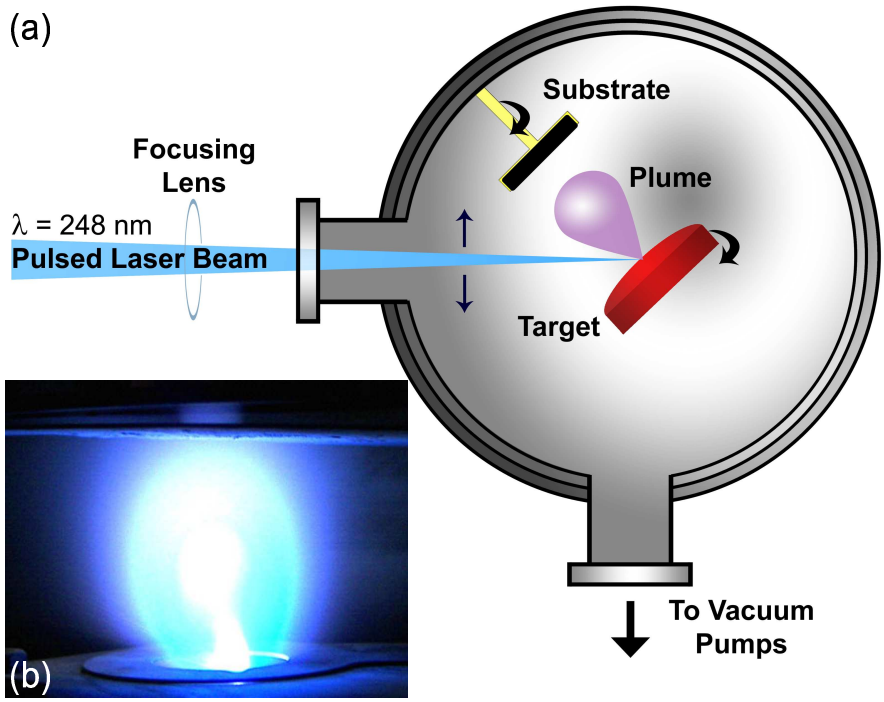

Figure 2.3: **(a)** Schematic of PLD chamber; up-down arrows indicate beam rastering on target surface. **(b)** Photograph of vapor plume.

In addition to the excimer laser, a PLD system includes external optics for beam focusing and rastering, and a processing chamber connected to a vacuum manifold (Figure 2.3a). The laser beam is scanned off-center across the rotating target using a raster mirror, in order to prevent drilling a hole or a trench in the target disc. The substrate rotates to improve the uniformity of the film being deposited. The larger the target-to-substrate distance, the better the film thickness uniformity, but the deposition rate drops off rapidly and, for compound materials, the deviations in film stoichiometry from the composition of the target becomes more pronounced, since different elements in the plume can have different angular distributions.[101] Higher pulse fluence ($J \cdot cm^{-2}$) enhances the deposition rate but also the rate of undesirable expulsion of particulates (micrometer-sized solid particles and liquid droplets). Introducing a background gas in the chamber can cause the vapor plume to thermalize to the temperature of the gas, and simultaneously lead to a reduction of the incident flux at the substrate and an improvement in film thickness uniformity.[101] In

addition, the background gas can take part in chemical reactions at the substrate, as is essential, for example, in the case of depositing vanadium oxide films from a vanadium metal target. Finding the optimum deposition conditions for a particular material is often a lengthy and frustrating task, but it can be facilitated by employing combinatorial PLD, whereby one or more of the growth parameters are varied without breaking vacuum; an example of using this technique with a simple substrate-masking aperture is reported in our Reference [103].

2.1.2 Specifications of our PLD system

The vanadium dioxide (VO_2) films and nanoparticles studied in the subsequent chapters were prepared via a one-step PLD process at a temperature of 550 °C, or via a two-step process consisting of room-temperature PLD followed by a thermal anneal at 450 °C in oxygen (O_2) background gas. The typical PLD parameters used in this work are listed below:

• **PLD system**: Epion 3000 from PVD Products, Inc., with COMPex 205 excimer laser from Lambda Physik, Inc. (now part of Coherent, Inc.).

• **Software**: User-modifiable control interface, implemented as LabVIEW virtual instruments.

• **Laser**: KrF, $\lambda = 248$ nm, $\delta t \approx 25$ ns, $p_{\text{buffer}} = 3.2$ bar, $E_{\text{pulse}} = 300$–450 mJ, $\delta A \approx 0.1$ cm^2, fluence = 3–4.5 J $\cdot$ cm^{-2}, $f = 25$ Hz.

• **Deposition**: V-metal disc target from Cerac, inc., or V_2O_3 pressed-powder disc target from Vin Karola Instruments, $p_{\text{base}} \approx 5 \cdot 10^{-6}$ mtorr, $p_{O_2} = 5$–12 mtorr (flowing), $T = 25$ °C (for two-step process) or 550 °C (for one-step process), $p_{\text{pulses}} = 10^4$–$2 \cdot 10^5$ (depending on desired film thickness), target-to-substrate distance = 5–10 cm.

• **Anneal (applies to two-step processing)**: $p_{\text{base}} \approx 10^{-5}$ mtorr, $p_{O_2} = 250$ mtorr (static), $T = 450$ °C (measured by thermocouple on substrate surface), $t = 30$–60 min.

The vanadium oxide, VO_x, films deposited at room temperature are amorphous and

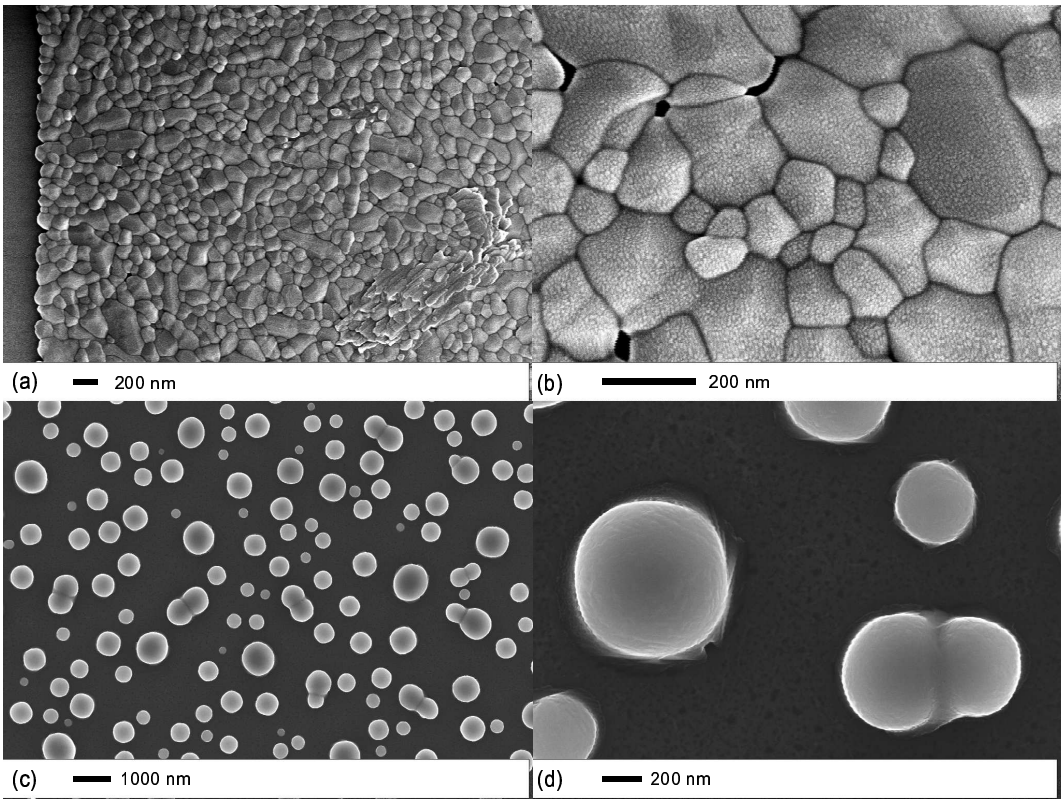

Figure 2.4: Scanning electron micrographs (SEMs), at different magnifications, of two PLD-grown and thermally annealed VO_2 films on **(a, b)** fused-silica and **(c, d)** silicon substrate. The film on fused-silica was coated with 2–3 nm of gold to prevent charging during imaging.

sub-stoichiometric, with $x \approx 1.7$. The subsequent thermal anneal both compensates for the oxygen deficiency and causes the film to crystallize into "switchable" material, that is, a VO_2 film that exhibits the reversible and reproducible metal-semiconductor phase transition. Depending on the initial VO_x thickness and/or the underlying substrate and/or the overlying material, a crystalline VO_2 film can form interconnected grains of various sizes and orientations or break up into isolated particles. Examples of these morphologies are shown in Figure 2.4.

2.2 Focused ion beam (FIB)

The focused ion beam (FIB) instrument served a dual purpose in this work: **(i)** as a sputter tool for milling periodic and randomized arrays of sub-micrometer holes in VO_2 and Ag/Au-VO_2 films (Chapter IV), and **(ii)** as a lithography tool for patterning arrays of Au and VO_2 nanoparticles (Chapters III and V), used in lieu of the yet-unavailable electron-beam writer (see Section 2.3).

2.2.1 Ion-solid interactions and the FIB instrument

The FIB microscope is analogous to a scanning electron microscope (SEM), except that the beam that scans across the sample surface consists of positively charged ions rather than electrons. Secondary electrons, generated by the interaction of the ion beam with the sample material (Figure 2.5), can be used to obtain images of high spatial resolution. The tight focusing and precise spatio-temporal control of the primary ion beam can be used to pattern samples on the nanoscale by local exposures of a suitable polymer (*e.g.*, PMMA), similarly to electron-beam lithography (EBL). The unique property of the FIB, however, comes from its ability to remove (sputter) atoms from the sample with nanoscale precision, leading to a host of applications in the nano- and micromachining of solids.

The following description of ion-solid interactions is taken from the review article of Volkert and Minor[104] on FIB microscopy and micromachining. When an ion impinges on a solid, it loses kinetic energy through interactions with the sample atoms. This transfer of energy from the ion to the solid results in a number of different processes (Figure 2.5): ion reflection and backscattering, electron emission, electromagnetic radiation, atomic sputtering and ion emission, sample damage, sample heating. Kinetic energy and momentum are transferred from the incident ion to the solid through both inelastic (electronic energy loss) and elastic (nuclear energy loss) interactions. In *inelastic* interactions, ion energy is lost to the electrons in the sample, resulting in ionization and the emission of electrons and electromagnetic radiation from the sample. In *elastic* interactions, ion energy is lost via

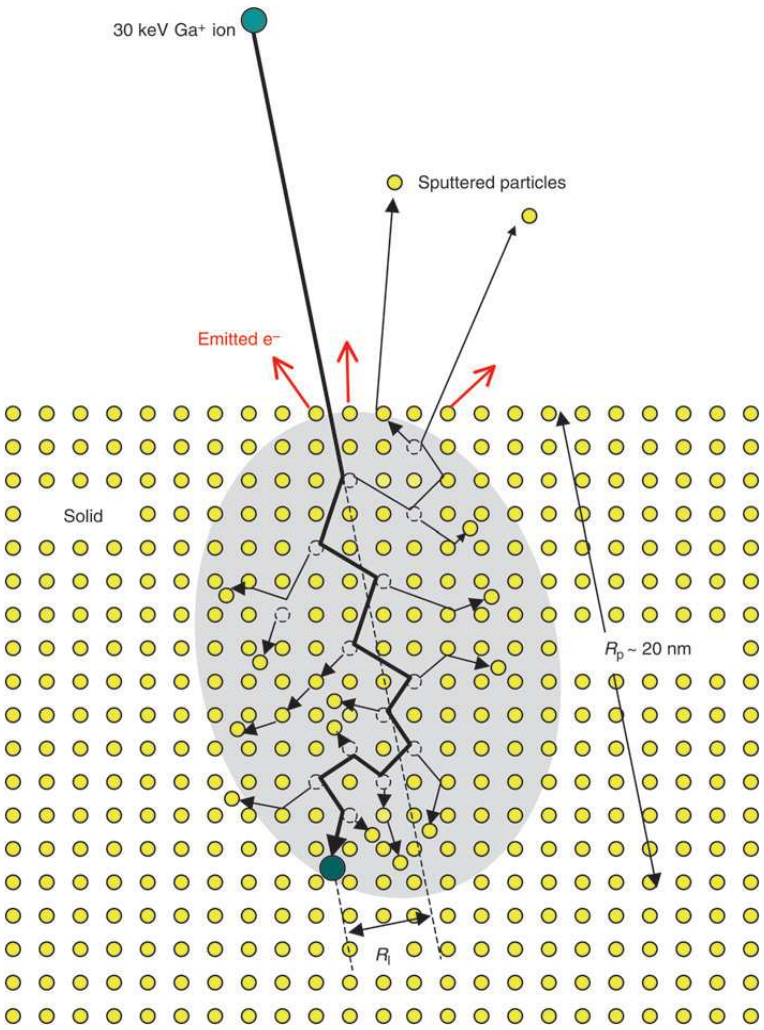

Figure 2.5: Schematic of collision cascade generated by 30-keV Ga^+ ion incident on crystal lattice, showing damage created in the collision cascade volume, with projected range R_p and lateral range R_l of the implanted ion. After Reference [104].

translational transfer to screened target atoms, which can result in displacement of sample atoms from their initial sites (*i.e.*, sample damage) and sputtering from the sample surface. After approximately 10^{-11} s, the 5–30 keV Ga ion comes to rest in the solid and the energies of all particles participating in the cascade have decreased below the displacement energy, at which point the collision cascade terminates and the Ga ion becomes implanted in the solid. Monte Carlo simulations for 30-keV Ga^+ into elements from Li to Bi show that roughly twice as much of the incident-ion energy is converted to nuclear energy losses than to electronic losses. Most of the nuclear energy loss occurs through atom vibrations

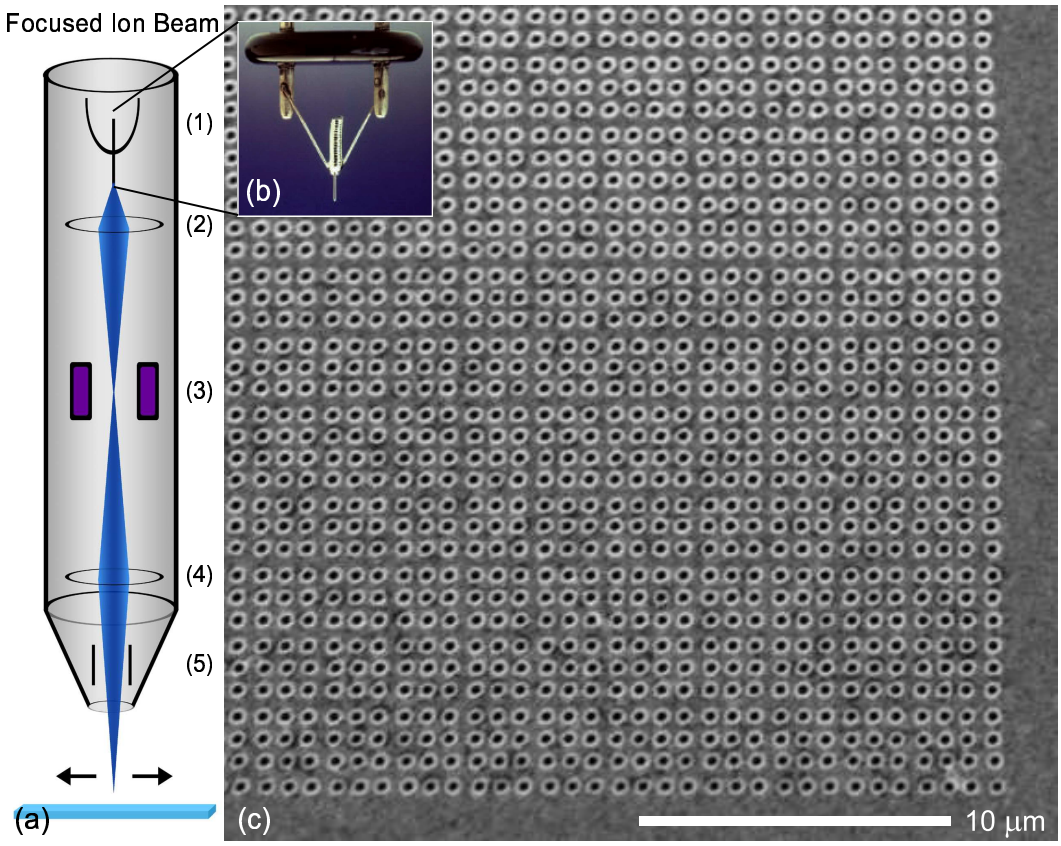

Figure 2.6: **(a)** Schematic of FIB column: **(1)** Ga^+ liquid-metal ion source (LMIS), **(2)** electrostatic condenser lens, **(3)** octupole for alignment, **(4)** electrostatic objective lens, **(5)** octupole for stigmation and scanning. **(b)** Photograph of Ga^+ LMIS, including reservoir; from http://www.fei.com. **(c)** FIB micrograph of FIB-milled periodic hole array in silver-VO_2 double layer on glass. *Parameters*: $d \approx 300$ nm, $a_0 = 750$ nm, $t_{Ag} = 160$ nm, $t_{VO_2} = 200$ nm.

or heating rather than through vacancy formation.

The FIB instrument (Figure 2.6a) requires, of course, a tightly focused ion beam of high brightness, which in turn entails the use of a field-ionization source with a size on the order of 5 nm. Most FIB systems available today use a liquid-metal ion source (LMIS), which provides the brightest and most focused beam. The gallium-ion (Ga^+) source (Figure 2.6b) is the most commonly used LMIS because of the combination of low melting temperature (30 °C), low volatility, and low vapor pressure of Ga compared to other LMIS metals. Focusing and steering of the ion beam are performed using electrostatic components, rather than the electromagnetic components used for electrons, since the focusing strength of an

electromagnetic lens is directly related to the charge-to-mass ratio of a particle, so it is impractical to build electromagnetic lenses for ions.[104]

2.2.2 Specifications of our FIB system

Listed below are the main parameters for the FIB instrument used to drill the hole arrays and lithographically pattern some of the nanoparticles studied in later chapters:

• **FIB system**: FIB-200 from FEI Company.

• **Software**: Proprietary interface for hardware control and pattern processing, FEIxP; user-created algorithms for pattern generation, True BASIC language; non-commercial program for Monte Carlo simulation of ion-solid interactions, SRIM/TRIM.

• **FIB column**: 30-keV Ga^+, emission current = 2.2 μA, magnification = 5.0 kX, beam spot $\approx$ 10 nm, beam current $\approx$ 10 pA (for lithography) or 90 pA (for milling), dwell time = 30–100 μs/pixel (for lithography) or 1–2 s/hole (for milling).

Figure 2.6c shows a periodic array of sub-micrometer holes in a silver-VO_2 double layer, milled and imaged by this FIB instrument.

2.3 Electron beam lithography (EBL)

Electron beam lithography (EBL) refers to a serial patterning technique, whereby a focused beam of keV electrons is selectively scanned across a sample surface coated with a special polymer, called a "resist", allowing a subsequent chemical removal ("developing") of either the exposed (for positive resists) or unexposed (for negative resists) material. The e-beam modifies a positive resist by breaking the polymer chains, whereas it promotes cross-linking in negative resists. The result is a sacrificial mask of nano- and/or microscale features in the resist, which (or whose complementary pattern) can be transferred into the underlying substrate by etching or into an overlying layer by film deposition, to be followed by subsequent removal of the excess material(s). The main advantage of EBL over photolithography is the nanoscale resolution of the former, while the latter, being a parallel-

processing technique, wins over at throughput. The smallest controlled size achievable with today's research-grade EBL instruments is around 15–20 nm for isolated features, and somewhat larger for closely packed features due to the proximity effect, that is, the unintended additional exposure of a region of the resist due mainly to backscattered electrons from adjacent regions and, to a smaller extent, to fast secondary electrons with energies on the order of 1 keV. In general, it is the much slower 2–50 eV secondary electrons, generated as the primary electrons slow down, that cause the bulk of the actual resist exposure and set the maximum practical resolution of the EBL technique, even though the primary e-beam can be focused to a spot smaller than 5 nm. A comprehensive review of e-beam interactions, instrumentation, and resists can be found in Reference [105].

2.3.1 Nanolithography steps

In the current work, EBL was used to fabricate the gold-VO_2 hybrid nanoparticles (NPs) described in Chapter VI. A common positive resist, poly(methyl-methacrylate), or PMMA, dissolved in a liquid solvent, was deposited by spin-coating on a 1-cm^2 silicon (Si) substrate and patterned according to the protocol outlined below (see also Figure 2.7). As mentioned in Section 2.2, the same protocol was applied to the fabrication of Au and VO_2 nanoparticles by FIB lithography, except that in the Au-NPs case the insulating glass substrate was precoated with a conducting indium-tin-oxide (ITO) film in order to reduce charging during ion-beam exposure.

⋆ **Protocol for charged-beam nanolithography:**

• Substrate: conducting (*e.g.*, Si) or insulating (*e.g.*, glass or sapphire), the latter covered with conducting film (*e.g.*, ITO) to reduce charging; cleaned using solvents (TCE, acetone, methanol/IPA, deionized water) and/or UV-ozone treatment.

• Spin-coating and baking of *positive* resist: *e.g.*, PMMA of 950K molecular weight in anisole, spun at 4000 rpm for 50 s and hot-plate–baked at 180 °C for 60–90 s, typically yields 100-nm-thick resist layer.

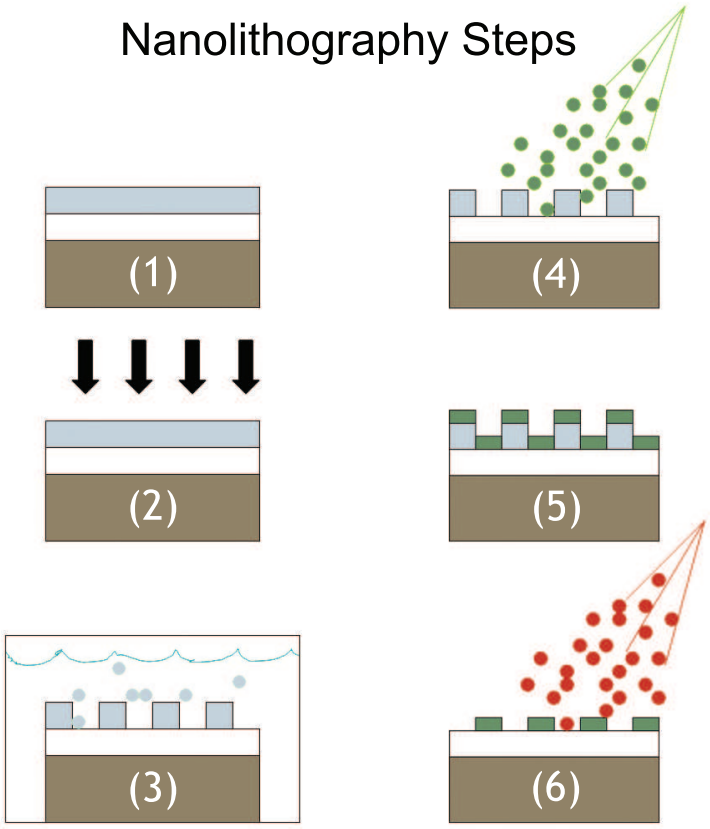

Figure 2.7: Charged-beam nanolithography steps: **(1)** spin-coating and baking of positive resist on substrate covered with conducting layer (or simply on conducting substrate); **(2)** patterning of resist by selective exposure to nanometer-size electron or ion beam; **(3)** developing of resist pattern by chemical removal of exposed regions; **(4)** deposition of material(s) to be patterned; **(5)** lift-off of remaining resist and overlying excess material by chemical removal in stronger solvent; **(6)** optional deposition of additional overlayer(s).

• Patterning of resist: selective exposure to tightly focused electron beam (10–30 keV) or ion beam (30-keV Ga^+); for FIB exposure, resist thickness is limited to about 50 nm due to short projected range of ions (see Figure 2.5).

• Developing of patterned resist: removal of exposed regions by immersion and agitation for 30 s in chemical solvent, such as 1:3 mixture of MIBK:IPA, which preferentially dissolves regions of fragmented polymer, followed by rinsing in pure IPA and blow-drying with nitrogen or air.

• Deposition of material(s) to be patterned: film growth done at (near-)ambient temperature

due to presence of resist mask; more than one film can be deposited but total thickness should not exceed 1/2 the resist thickness (the smaller the fraction, the better the chances of success in the next step).

• Lift-off: removal of remaining resist and overlying excess material(s) by soaking and agitation for 10–20 min in acetone or specialized solvent (*e.g.*, methylene chloride or Remover PG), followed by IPA rinse and blow-drying.

• Optional: deposition of additional overlayer(s) and/or thermal annealing of $VO_{1.7}$ material (see Section 2.1).

Further details on the general nanolithography steps can be found in Reference [105].

2.3.2 Specifications of our EBL system

Below are some of the operational parameters of the e-beam writer used to pattern the Au+VO_2 NPs of Chapter VI:

• **EBL system:** e_LiNE from Raith USA, Inc., with microscope column from Carl Zeiss, Inc.

• **Software**: Proprietary dual interface for hardware control, pattern generation and processing, e_LiNE + SmartSEM.

• **E-beam:** accelerating voltage = 30 kV, magnification = 1.0 kX, working distance = 10 mm, beam spot ≈ 2 nm, beam current ≈ 0.04 nA, charge dose = 10–50 fC/dot (for single-pixel exposures) or 200 $\mu C \cdot cm^{-2}$ (for area exposures).

Two examples of EBL-patterned arrays of vanadium-oxide NPs are shown in Figure 2.8; the images were obtained with the same EBL instrument operated in SEM mode. With an average diamter of about 35 nm, the particles in Figure 2.8a are among the smallest lithographically produced VO_2 NPs to date.

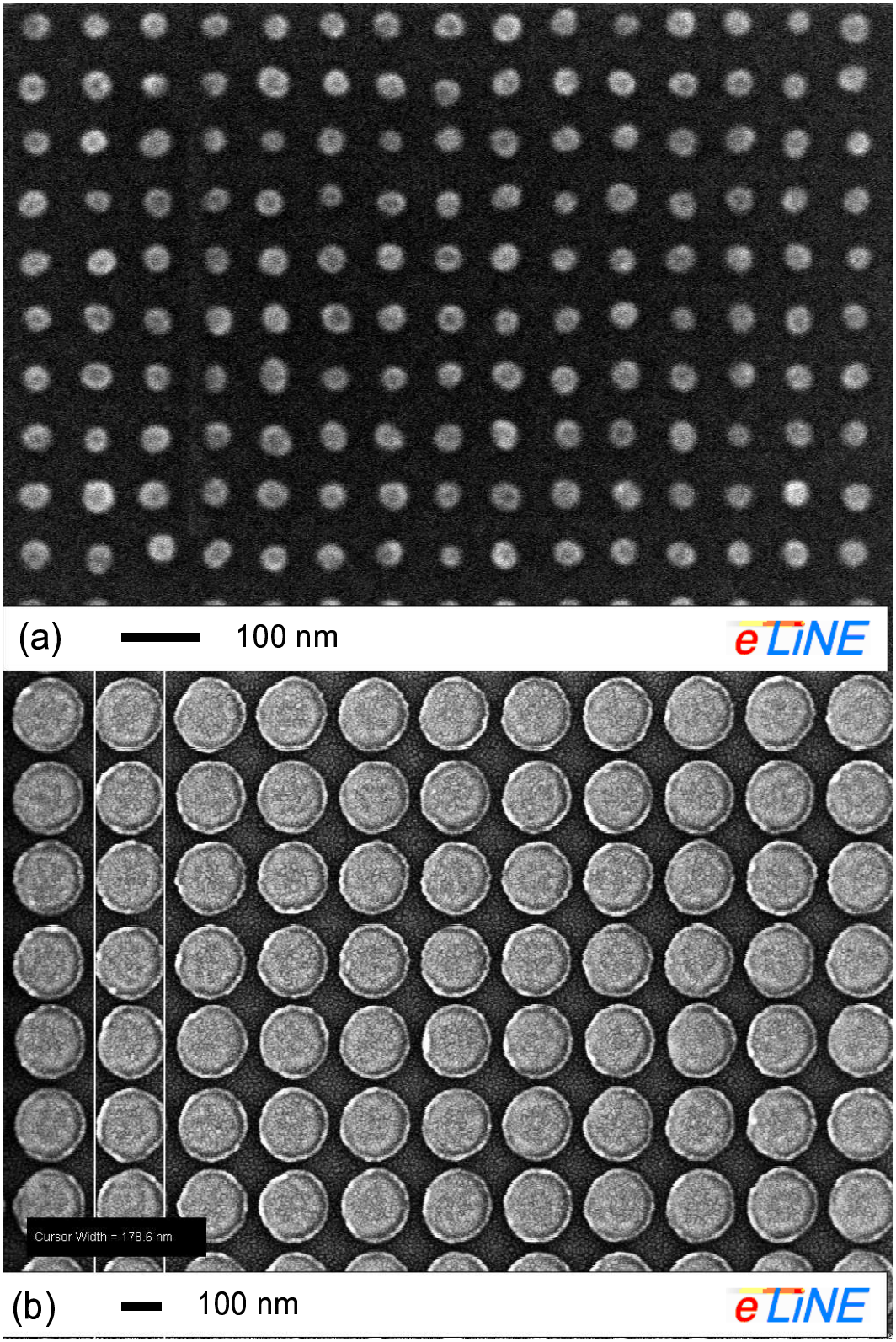

Figure 2.8: SEM images of EBL-patterned arrays of **(a)** 35-nm-diameter VO_2 (annealed) NPs on Si substrate and **(b)** 180-nm-diameter $VO_{1.7}$ (non-annealed) NPs on glass substrate. The sample in **(b)** was coated with 2–3 nm of gold to prevent charging during imaging.

2.4 Rutherford backscattering spectrometry (RBS)

Rutherford backscattering spectrometry (RBS) is an analytical technique for determining the elemental composition (stoichiometry), isotope abundance, thickness, and depth profile of a material through the large-angle scattering of light fast ions by more massive stationary atoms. Historically, this technique was born in the very experiments by Rutherford (1904), and by Geiger and Marsden (1911–1913), that gave rise to the picture of the atom as a positively charged nucleus surrounded by orbiting electrons. In a typical RBS setup, a beam of 2-MeV helium ions ($^4He^+$) from a linear Van de Graaff accelerator impinges on the sample, and a fraction of the backscattered $^4He^+$ projectiles are collected in a solid-state surface-barrier detector, where they generate voltage pulses through the creation of electron-hole pairs. The pulses are then sorted and stored in a multichannel analyzer according to their heights, which are proportional to the energy of the backscattered projectiles. Since the scattering process is governed by the well-known Coulomb repulsion between the positively charged nuclei of the projectile ion and the target atom, RBS provides highly quantitative measurements that are insensitive to electronic configuration or chemical bonding.[106]

2.4.1 Kinematic factor and scattering cross-section

The kinematics of the elastic ion-atom collisions can reveal the identity of the target atom. Applying conservation of energy, parallel and transverse momentum to two isolated particles, one obtains the ratio of scattered-to-incident energy of the projectile ion, the *kinematic factor* K_{M_2}:

$$K_{M_2} \equiv \frac{E_1}{E_0} = \left[\frac{\left(M_2^2 - M_1^2 \sin^2\theta\right)^{1/2} + M_1 \cos\theta}{M_2 + M_1} \right]^2 \tag{2.1}$$

The scattering geometry and notation in the laboratory coordinate system are given in Figure 2.9b. Equation 2.1 shows that the energy after collision depends only on the incident energy, the masses of the projectile and target particles, and the scattering angle, which

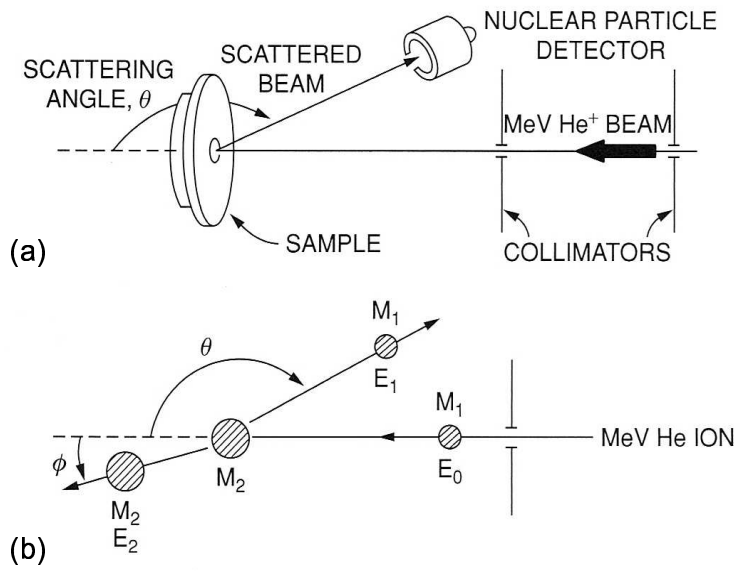

Figure 2.9: Schematics of **(a)** setup and **(b)** collision geometry for Rutherford backscattering spectrometry (RBS). *Legend*: $M_1 \equiv$ mass of projectile ion; $M_2 \equiv$ mass of target atom; $E_0 \equiv$ incident energy of projectile ion; $E_1 \equiv$ scattering energy of projectile ion; $E_2 \equiv$ recoil energy of target atom; $\phi \equiv$ recoil angle; $\theta \equiv$ scattering angle. After Reference [106].

allows the possibly unknown target atom to be identified by calculating its mass M_2. For a target material that contains two types of atoms that differ in their masses by a small amount ΔM_2, the larger the difference ΔE_1 in the corresponding energies of the scattered projectiles, the better the ability of the system to resolve the two target atoms. Since the greatest change in ΔE_1 for a given change in ΔM_2, with a fixed projectile mass $M_1 < M_2$, occurs when $\theta = 180°$, direct *backscattering* is the preferred experimental geometry; scattering angles around 165–175° are used in practice due to the finite size of the detector. For given projectile mass and scattering angle, the mass resolution of RBS deteriorates with increasing target mass as the kinematic factor asymptotically approaches unity, but the sensitivity of the technique improves for heavier target atoms because the cross-section for scattering scales as the square of the target-nucleus charge, as seen below. Thus, heavy elements (*e.g.*, Ag and Au) on a lighter substrate (*e.g.*, Si or SiO_2) can be analyzed at coverages well below a monolayer.[106]

While the kinematic factor of the scattering process (Equation 2.1) serves to identify the

target atoms, the scattering cross-section provides quantitative information on the number N_s of atoms per unit area in the target material, which is in turn related to the thickness t of a thin-film target of N atoms/cm^3 as $t = N_s/N$. Fundamentally, the scattering cross-section σ is defined through the probability P for scattering, that is, the ratio of the number of interaction events to the number Q of incident particles: $P \equiv \sigma Q N_s/Q = \sigma N_s$.

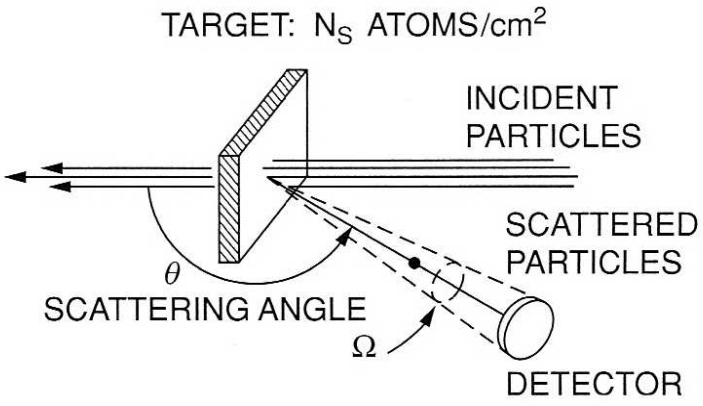

Figure 2.10: Simplified layout of RBS experiment. Only projectiles scattered within the solid angle $d\Omega$ of the detector are counted. After Reference [106].

For the RBS geometry depicted in Figure 2.10, Equation 2.2 gives the *differential scattering cross-section* $d\sigma/d\Omega$ of a target atom for scattering an incident particle through an angle θ into a detector centered around θ and spanning a differential solid angle $d\Omega$:

$$\frac{d\sigma(\theta)}{d\Omega} d\Omega \cdot N_s = \frac{\text{Number of particles scattered into } d\Omega}{\text{Total number of incident particles}} \tag{2.2}$$

Since an RBS detector of area A and at distance l from the target usually spans a small solid angle, $\Omega = A/l^2 \cong 10^{-2}$ steradians or less, an *average* differential scattering cross-section $\sigma(\theta)$, simply called the *scattering cross-section*, is used for practical RBS analysis:

$$\sigma_{\text{avg}}(\theta) \equiv \sigma(\theta) = \frac{1}{\Omega} \int_{\Omega} \frac{d\sigma}{d\Omega} \cdot d\Omega \tag{2.3}$$

Thus, the scattering cross-section is the link between the areal density N_s of the target material, in atoms/cm^2, and the number of detected particles, the *yield* Y, collected in a 100%-efficient detector of solid angle Ω:

$$Y = \sigma(\theta) \cdot \Omega \cdot Q \cdot N_s \tag{2.4}$$

The total number of particles in the incident beam, Q, is determined by the integration with respect to time of the measured current of charged particles impinging on the target. In order to obtain an analytical expression for the scattering cross-section $\sigma(\theta)$, the force that acts during the projectile-target collision must be specified explicitly. For most RBS situations, the distance of closest approach during the collision falls deep within the electron orbit, so the force can be described well as an unscreened Coulomb repulsion between two positively charged nuclei, with the electron screening treated as a small correction. Equation 2.5 gives the final result from the derivation of the unscreened scattering cross-section:[106]

$$\sigma(\theta) = \left(\frac{Z_1 Z_2 e^2}{4E}\right)^2 \left(\frac{4}{\sin^4\theta}\right) \frac{\left(\left\{1 - [(M_1/M_2)\sin\theta]^2\right\}^{1/2} + \cos\theta\right)^2}{\left\{1 - [(M_1/M_2)\sin\theta]^2\right\}^{1/2}} \tag{2.5}$$

where Z_1 and Z_2 are the atomic numbers (*i.e.*, number of charges $Z_1 e$ and $Z_2 e$) of the projectile and target nuclei, respectively, and E is the projectile energy. The $\sigma \propto Z_2^2$ scaling reflects the increased sensitivity of RBS for heavier elements.

2.4.2 Examples of RBS analysis

In our RBS system, typical backscattering spectra such as those shown in Figures 2.11 and 2.12 are performed using 1.8-MeV $^4He^+$ ions that impinge on the target after passing through a central aperture in an *annular* Au-coated Si surface-barrier detector, aligned collinearly with the incident beam, with the backscattered projectiles collected in the active area of the same detector at an angle $\theta \approx 175°$.

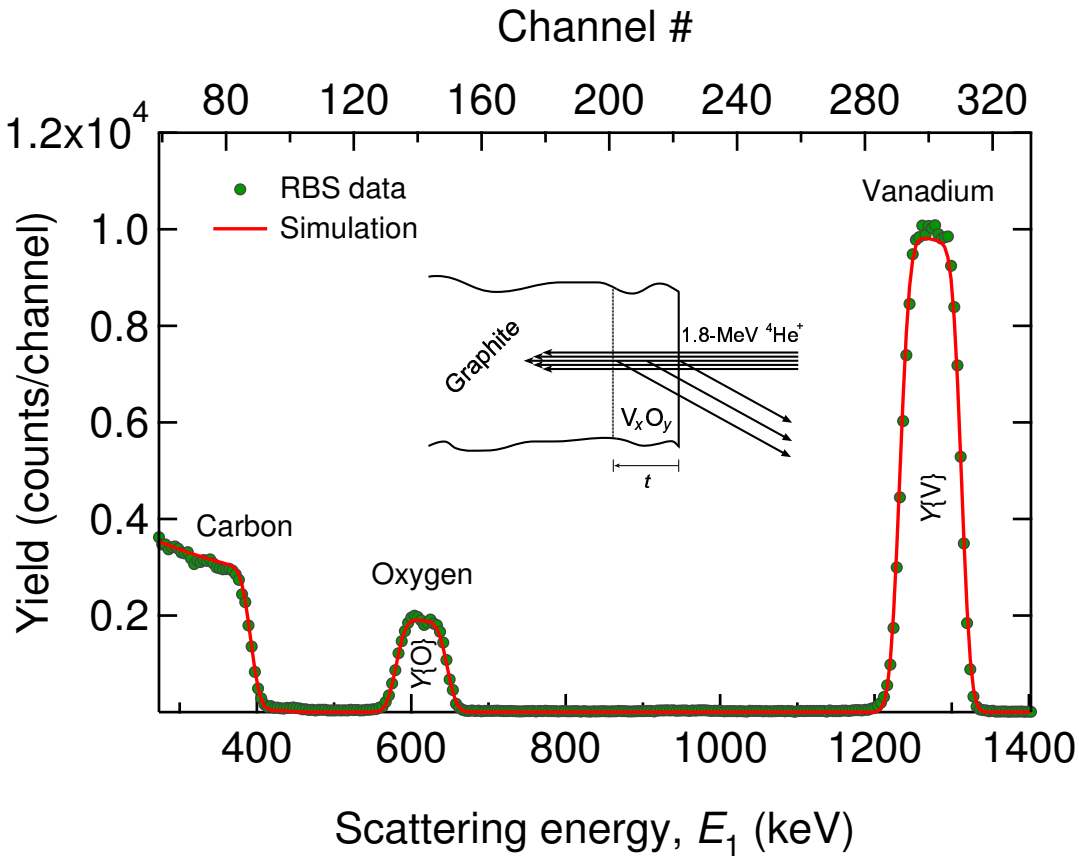

Figure 2.11: Example of experimental (circles) and simulated (line) RBS spectra for as-deposited vanadium-oxide film on graphite (C) substrate. The V_xO_y film was deposited by PLD from a V_2O_3 pressed-powder target in base vacuum, aiming for pre-anneal stoichiometry x/y as close to 2/3 as possible. The simulation was performed using the SIMNRA program.[107] *Analysis*: $V_2O_{2.99\pm0.02}$, $t \approx 83$ nm.

According to Equation 2.4, the number of counts (yield) accumulated in a given channel of the multichannel analyzer is related to the areal density of atoms in a thin slice within the target material. Thus, for a thin-film target, the cumulative yield Y from all the channels spanned by an isolated spectral peak, minus the counts due to background noise, is directly proportional to the amount N_s of a given element in the target material. For example (see Figure 2.11), the stoichiometry of a vanadium-oxide (V_xO_y) thin film on a graphite (C) substrate can be obtained from the ratio of the measured elemental yields for vanadium (V) and oxygen (O), after background subtraction and normalization by the inverse ratio

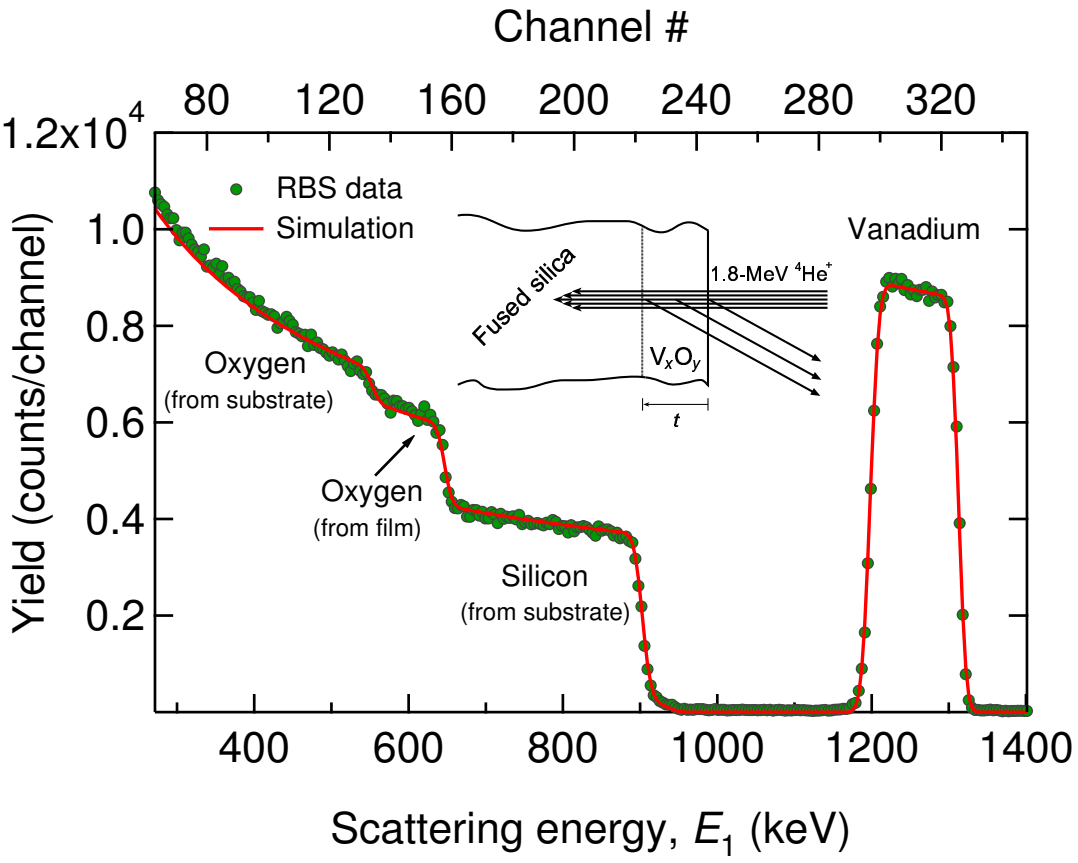

Figure 2.12: Example of experimental (circles) and simulated (line) RBS spectra for as-deposited vanadium-oxide film on fused-silica (SiO_2) substrate. The V_xO_y film was deposited by PLD from a V-metal target in 5 mtorr O_2 background gas—but at a larger target-to-substrate distance than the usual 5–10 cm used for VO_2 precursor films, aiming for pre-anneal stoichiometry x/y as close to 2/3 as possible. The simulation was performed using the SIMNRA program.[107] *Analysis*: $V_2O_{3.03\pm0.01}$, $t \approx 118$ nm.

of the calculated (see Equation 2.5) scattering cross-sections $\sigma(\theta)$, as shown below:

$$\mathrm{V}_x\mathrm{O}_y: \quad \frac{Y\{\mathrm{V}\}}{Y\{\mathrm{O}\}} = \frac{\sigma(\theta)\{\mathrm{V}\}\cdot\Omega\cdot Q\cdot N_\mathrm{s}\{\mathrm{V}\}}{\sigma(\theta)\{\mathrm{O}\}\cdot\Omega\cdot Q\cdot N_\mathrm{s}\{\mathrm{O}\}} = \frac{\sigma(\theta)\{\mathrm{V}\}\cdot N_\mathrm{s}\{\mathrm{V}\}}{\sigma(\theta)\{\mathrm{O}\}\cdot N_\mathrm{s}\{\mathrm{O}\}} \tag{2.6}$$

$$\Rightarrow \quad \frac{x}{y} \equiv \frac{N_\mathrm{s}\{\mathrm{V}\}}{N_\mathrm{s}\{\mathrm{O}\}} = \frac{Y\{\mathrm{V}\}}{Y\{\mathrm{O}\}}\cdot\frac{\sigma(\theta)\{\mathrm{O}\}}{\sigma(\theta)\{\mathrm{V}\}} \tag{2.7}$$

The absolute values of $N_\mathrm{s}\{\mathrm{O}\}$ and $N_\mathrm{s}\{\mathrm{V}\}$, and hence the thickness of the V_xO_y film, can be calculated by a comparison with the experimental yield of a standard sample of known

areal density. The most commonly used is the commercially available *bismuth (Bi) standard*, prepared by 30-keV implantation of nominally $5 \cdot 10^{15}$ Bi-atoms/cm^2 to a depth of about 20 nm beneath the surface of a silicon wafer. A round-robin of RBS measurements at a number of labs around the world has established a more precise value of $4.77 \cdot 10^{15}$ Bi-atoms/cm^2 for this calibration standard.

Alternatively, the stoichiometry and thickness of the target film can be obtained from simulation routines, such as the popular SIMNRA program,[107] that iteratively search for a least-squares fit to a given experimental RBS spectrum, subject to the equations of scattering and energy loss of ions penetrating a solid. Such simulations really prove their merit when the experimental RBS spectra have overlapping peaks, which prevents easy integration of elemental yields: for example (see Figure 2.12), a vanadium-oxide film on an oxygen-containing substrate such as glass or sapphire.

2.5 Scanning near-field optical microscopy (SNOM)

When an object is interrogated using optical radiation, information about spatial variations that are longer than about half the wavelength of the probing light is carried by the propagating portion of the field, while the evanescent portion of the field contains information about the smaller-scale variations.[108] Therefore, "tapping into" the evanescent near-field presents a way to overcome the limitations imposed by diffraction on conventional optical elements such as lenses and micro-objectives. The scanning near-field optical microscope (SNOM) does just that. Figure 2.13 depicts the general layout of a SNOM instrument, along with an example of a SNOM probe made from a metallized "heated-and-pulled" optic fiber. The surface of the sample can be illuminated by radiating (propagating) laser light from above, underneath, or both. The amplitudes of the radiating and evanescent fields that arise from interaction of the laser light with the sample are collected with a 50-200-nm diameter probe at a distance of 10-60 nm from the sample surface. Since the evanescent field decays exponentially with distance away from the surface, information

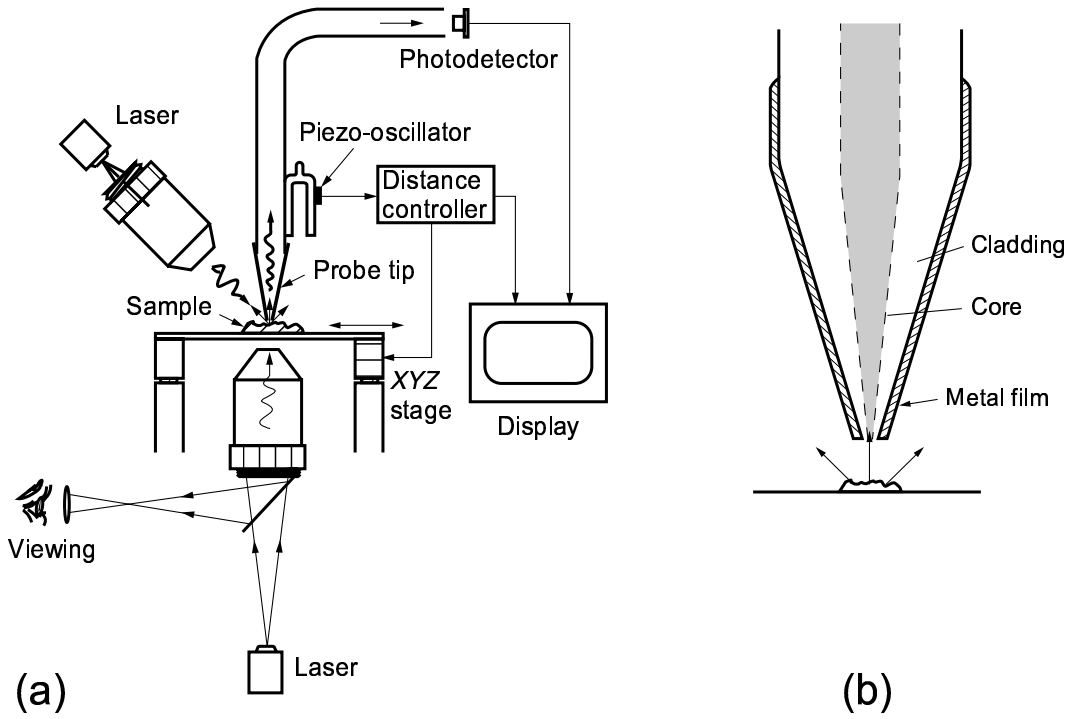

Figure 2.13: Schematics of **(a)** scanning near-field optical microscope (SNOM) and **(b)** fiber-based SNOM probe. The sample can be illuminated by radiating (propagating) laser light from above, underneath, or both. After Reference [108].

about the sub-diffraction surface variation is lost as soon as the probe is outside the very near-field.[108] The SNOM instrument can be operated in several different modes: collection (Figure 2.14a), illumination/transmission (Figure 2.14b), reflection, apertureless, fluorescence. In transmission mode, the sample is illuminated point-by-point as the probe or the sample stage is scanned, analogous to shining a flashlight spot on a large object, except for the largely evanescent nature of the fields emanating from the subwavelength SNOM aperture; the advantage of this mode is the minimization of the background light.[108]

2.5.1 Layout of our SNOM instrument

We used a near-field microscope in transmission mode (Figure 2.14b) to probe the subwavelength hole arrays in VO_2 and Ag/Au-VO_2 described in Chapter IV, one hole at a time. A SNOM image scan of a portion of a Ag-VO_2 hole array is given in Figure 2.15.

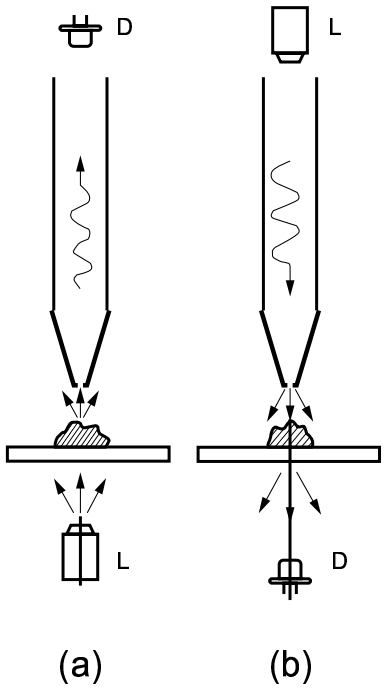

Figure 2.14: SNOM operation in **(a)** collection and **(b)** illumination/transmission mode. *Legend*: L ≡ laser; D ≡ photodetector. After Reference [108].

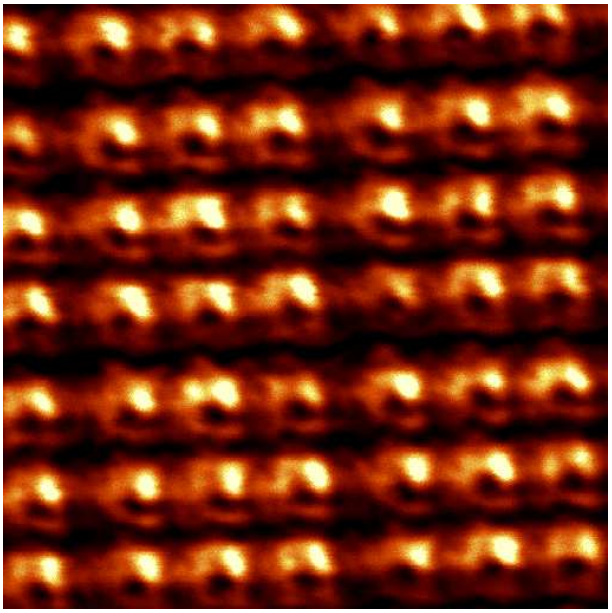

Figure 2.15: SNOM transmission image of 5-by-5 μm^2 portion of hole array in silver-VO_2 double layer on glass.

This method clearly revealed the role of perforated VO_2 in preferentially "funnelling" near-infrared ($\lambda_{\text{laser}} = 980$ nm) rather than visible ($\lambda_{\text{laser}} = 532$ nm) excitation light through the subwavelength holes (see Section 4.3.4). The layout of our Alpha*SNOM* instrument from WITec GmbH is shown in Figure 2.16. The cantilever sensor consists of a Si arm with a hollow SiO_2 tip in the shape of an inverted pyramid. Typical dimensions of the cantilever arm are 150-μm width, 700-μm length, and 5-μm thickness, while the pyramid has a typical base of 10 μm and height of 8 μm. The cantilever is Al-coated and has a nanoscale hole of $\sim$100-nm diameter at the center of the pyramid, which acts as the near-field aperture. The excitation laser (green in Figures 2.16 and 2.17) is focused into the backside of the cantilever pyramid, and a small portion of the light tunnels through the subwavelength aperture and illuminates with an optical near-field a correspondingly small area of the sample. Distance control between the tip of the pyramid and the surface of the sample is accomplished using the beam-deflection method familiar from atomic force microscopy (AFM); in fact, the Alpha*SNOM* instrument can acquire both optical (SNOM) and topographical (AFM) information during a single scan. As shown in Figure 2.17, a second laser (drawn in red) with a different wavelength from the excitation source is focused onto the back of the cantilever, and the reflected signal is detected with a segmented photodiode. The force on the sample is proportional to the bending of the cantilever, so if the bending changes, the position of the laser beam on the photodiode changes, which is registered by the electronics and used in a feedback loop to keep the tip-sample separation fixed via vertical adjustments to the sample stage.[109]

2.6 Raman spectroscopy

Raman scattering is a manifestation of the general phenomenon of *inelastic light scattering*, whereby an incident optical beam of a given frequency interacts with material excitations and emerges as scattered light of a different frequency. In *Raman scattering*, the incident light interacts with the optical phonons of the material, and its frequency ω in-

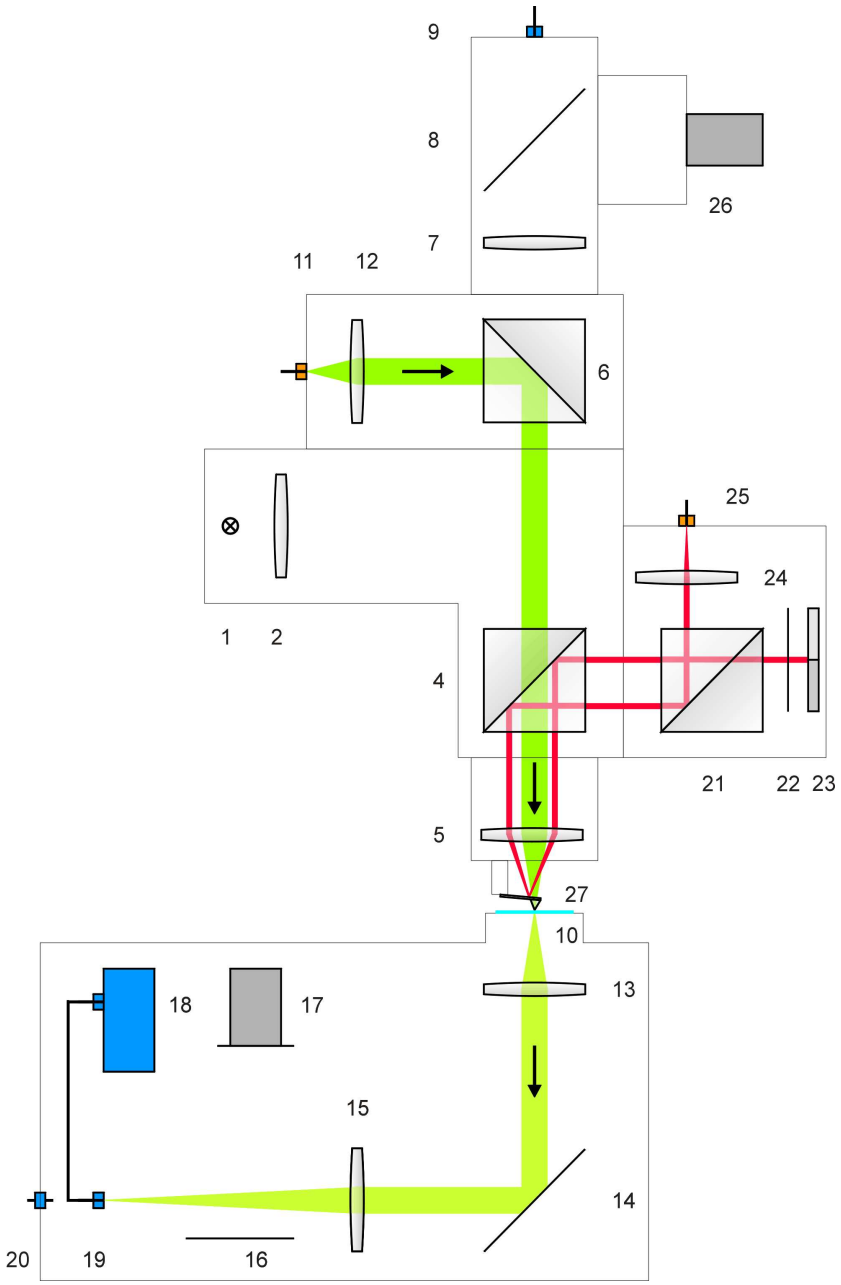

Figure 2.16: Layout and beam paths for Alpha*SNOM* instrument in near-field transmission mode. *Components*: **(11)** input fiber connector for incident laser (*e.g.*, $\lambda = 532$ nm); **(12)** achromatic lens assembly; **(6)** beamsplitter cube (50:50); **(4)** dichroic mirror (Transmittance $> 90\%$ @ $\lambda = 450$–700 nm; Reflectance $> 90\%$ @ $\lambda > 750$ nm); **(5)** near-field objective lens assembly (8 X) with magnetically affixed **(27)** cantilever sensor and subwavelength aperture probe (see Figure 2.17); **(10)** sample on piezoelectrically scanned stage; **(13)** collection micro-objective lens assembly (10, 20, 40 X); **(14)** mirror; **(15)** tube lens ($f = 125$ mm); **(19)** output fiber connector for transmitted light; **(18)** single-photon detector (APD $\equiv$ avalanche photodiode detector, Efficiency $> 10\%$ @ $\lambda = 410$–1020 nm); **(25)** input fiber connector for distance-feedback laser ($\lambda = 980$ nm); **(24)** achromatic lens assembly; **(21)** beamsplitter cube (50:50); **(22)** edge filter; **(23)** segmented photodiode for feedback on cantilever bending (see Figure 2.17). After Reference [109].

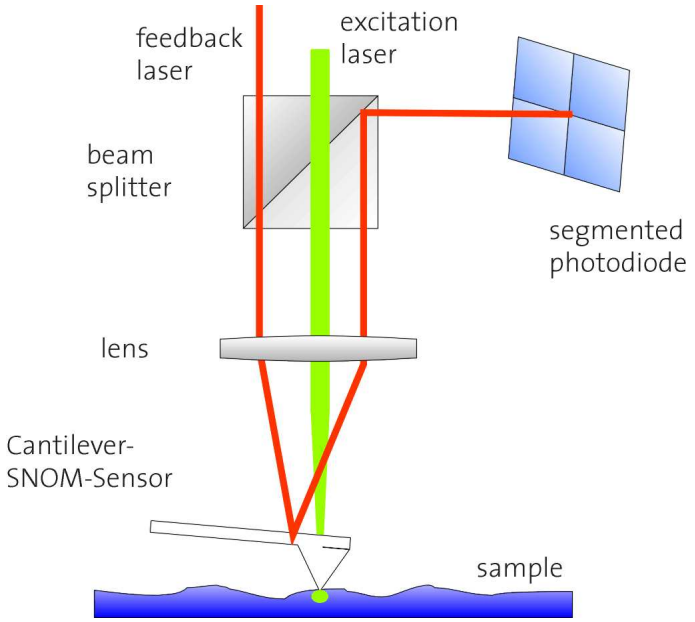

Figure 2.17: Distance feedback with cantilever sensor, maintaining fixed probe-sample separation and providing both optical (SNOM) and topographical (AFM) information. After Reference [109].

creases (blue-shifts) or decreases (red-shifts) depending on the type of interaction. For anti-Stokes scattering, the Raman-scattered light emerges with a frequency $\omega_{\mathrm{R}} = \omega + \omega_{\mathrm{vib}}$ (Figure 2.18a), and for Stokes scattering—with a frequency $\omega_{\mathrm{R}} = \omega - \omega_{\mathrm{vib}}$ (Figure 2.18b). The spectrum of frequency shifts ω_{vib} corresponds to specific vibrational frequencies of the probed molecules, originating from oscillations between their constituent atoms. Therefore, (anti-)Stokes Raman scattering involves the absorption and re-emission of an incident photon, mediated by the (absorption) emission of an optical phonon. At a given temperature, anti-Stokes processes occur with a much lower probability than their Stokes counterparts, as determined by the Boltzmann factor at the vibrational frequency.[110] Since the phonon spectrum of a solid depends on the particular molecular and lattice structure, Raman scattering provides a characteristic fingerprint of the probed material. Specifically for VO_2, the vibrational spectrum changes dramatically across the structural phase transition, with the complete vanishing of the monoclinic (low-temperature) modes in the rutile (high-temperature) phase. Thus Raman scattering provides an unambiguous probe of the lattice

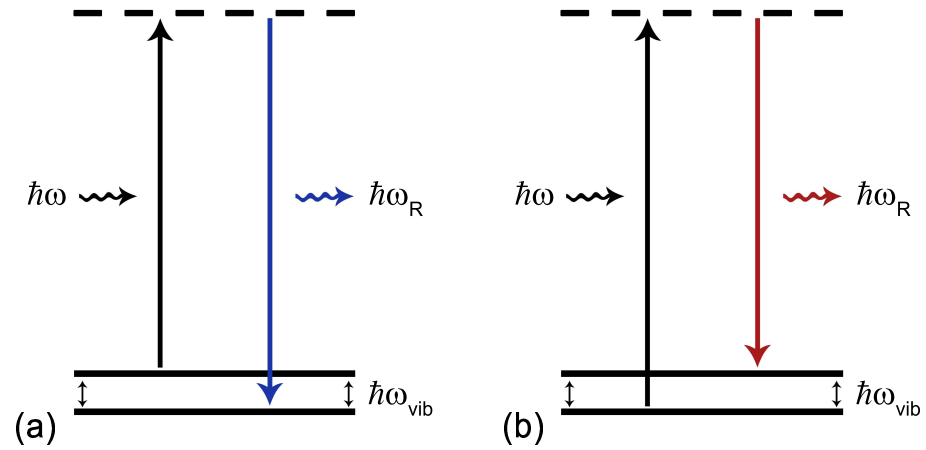

Figure 2.18: Molecular energy levels involved in **(a)** anti-Stokes ($\omega + \omega_{\text{vib}}$) and **(b)** Stokes ($\omega - \omega_{\text{vib}}$) Raman scattering. The molecule absorbs an incident photon of frequency ω, becomes excited to a virtual state, *i.e.*, a vacuum state that does not match any molecular level, and then relaxes by re-emitting a blue-shifted or red-shifted photon to a vibrational state that is lower (anti-Stokes, blue-shift) or higher (Stokes, red-shift) than the starting vibrational state; hence, the scattering process involves the absorption (anti-Stokes) or emission (Stokes) of an optical phonon.

configuration of the VO_2 material that falls within the interrogation volume of the incident light beam.

2.6.1 Confocal Raman microscopy

Confocal Raman microscopy, also called Raman microprobe, combines the material specificity of Raman spectroscopy with the spatial selectivity of confocal microscopy, making it possible to probe in a non-invasive manner the molecular and lattice structure of a material on a sub-micrometer scale. This is the technique used in Chapter V to study the phase transition of individual VO_2 nanoparticles.

The confocal microscope extends the conventional optical microscope by employing the scanning technique familiar in electron microscopy. Rather than forming an all-at-once, "parallel" image of the object, a confocal microscope acquires many point-images by serially scanning the diffraction-limited illumination spot across the object, and successively collecting the reflected/scattered light from each illuminated object point. At each pixel the

system samples either the number of counts per integration time or the output voltage of a photmultiplier tube; the brightness of an image pixel is thus defined by the sampled detector value. At the end of the scan, a composite image of the object is reconstructed from the brightness values of all the pixels.[111,112] The basic layout of a confocal reflection setup is

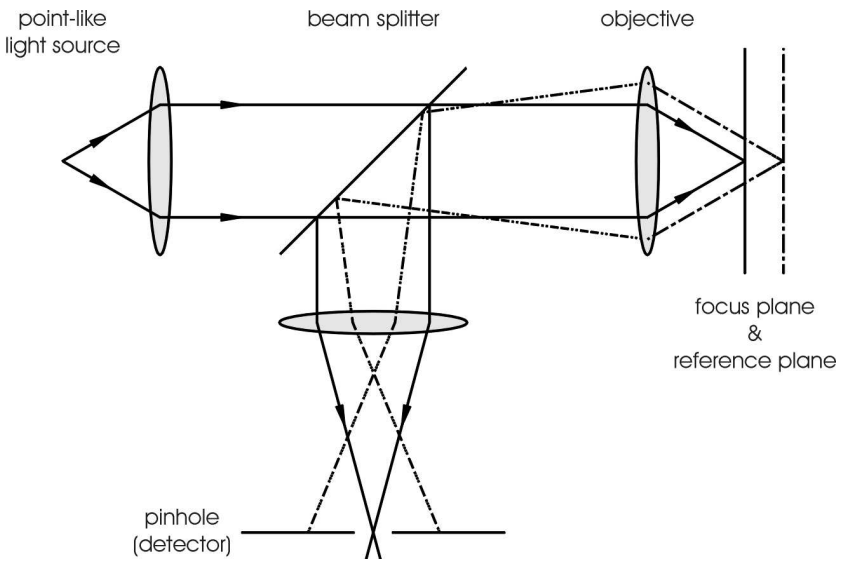

Figure 2.19: Basic layout of confocal reflection microscope. Image contrast is strongly enhanced because only rays from the image focal plane reach the detector. After Reference [109].

sketched in Figure 2.19. Confocal microscopy requires a point source (*e.g.*, a fiber-coupled laser), which is focused onto the sample using a micro-objective. The reflected/scattered light is usually collected with the same objective and focused into a pinhole in front of the detector (*e.g.*, the core of an optic fiber). Confocal detection benefits from the fact that only light originating from the focal area is able to pass through the output pinhole and reach the detector. Laterally displaced beams will miss the output pinhole, and beams originating from points displaced along the optical axis will not be focused in the detection plane and will therefore suffer strong attenuation by the pinhole.[112] These properties of confocal microscopy lead to a marginal increase in the lateral resolution over conventional far-field

microscopy, by reducing the full-width at half-maximum of the Airy diffraction pattern by a factor of 1.3. More importantly, the side lobes of the pattern are largely suppressed, which results in significant enhancement of the image contrast and allows the detection of weak signals in close spatial proximity to strong ones.[112] The improved image contrast, both lateral and axial, and the diffraction-limited sample addressing are the main properties of confocal microscopy that make the Raman microprobe well suited to the study of nanoscale materials.

2.6.2 Layout of our confocal microscope

The Alpha*SNOM* instrument described earlier (Section 2.5.1) can also operate as a confocal microscope; the confocal reflection light path is shown in Figure 2.20. The laser light is delivered via a single-mode optic fiber with a core diameter of about 5 μm, which transmits only a single transversal mode (Gaussian beam) that can be focused to a diffraction-limited spot. The core of the multi-mode collection fibre acts as the detector pinhole of Figure 2.19. Instead of scanning the illumination spot, the sample stage is raster-scanned in two dimensions along the focal plane, and the image is acquired line by line.

Inserting three additional filters converts the confocal microscope in Figure 2.20 into a Raman microprobe. The first extra filter (not shown) sits between the input achromat (component 12) and the top beamsplitter (component 6), and serves to eliminate any Raman signal that can arise from the input-fiber material, since confocal Raman spectroscopy often requires high laser powers. The second and third extra filters (not shown) are stacked between the output tube lens (component 7) and the output fiber connector (component 9), and are meant to reject as much of the elastically (Rayleigh) scattered light as possible, since the long acquisition times can easily cause the intense laser line to overwhelm the nearby Raman peaks in the accumulated spectrum. Examples of Raman spectra obtained with this instrument can be found in Chapters V and VI; note that those spectra were indeed acquired in confocal reflection mode but from single illumination spots, that is,

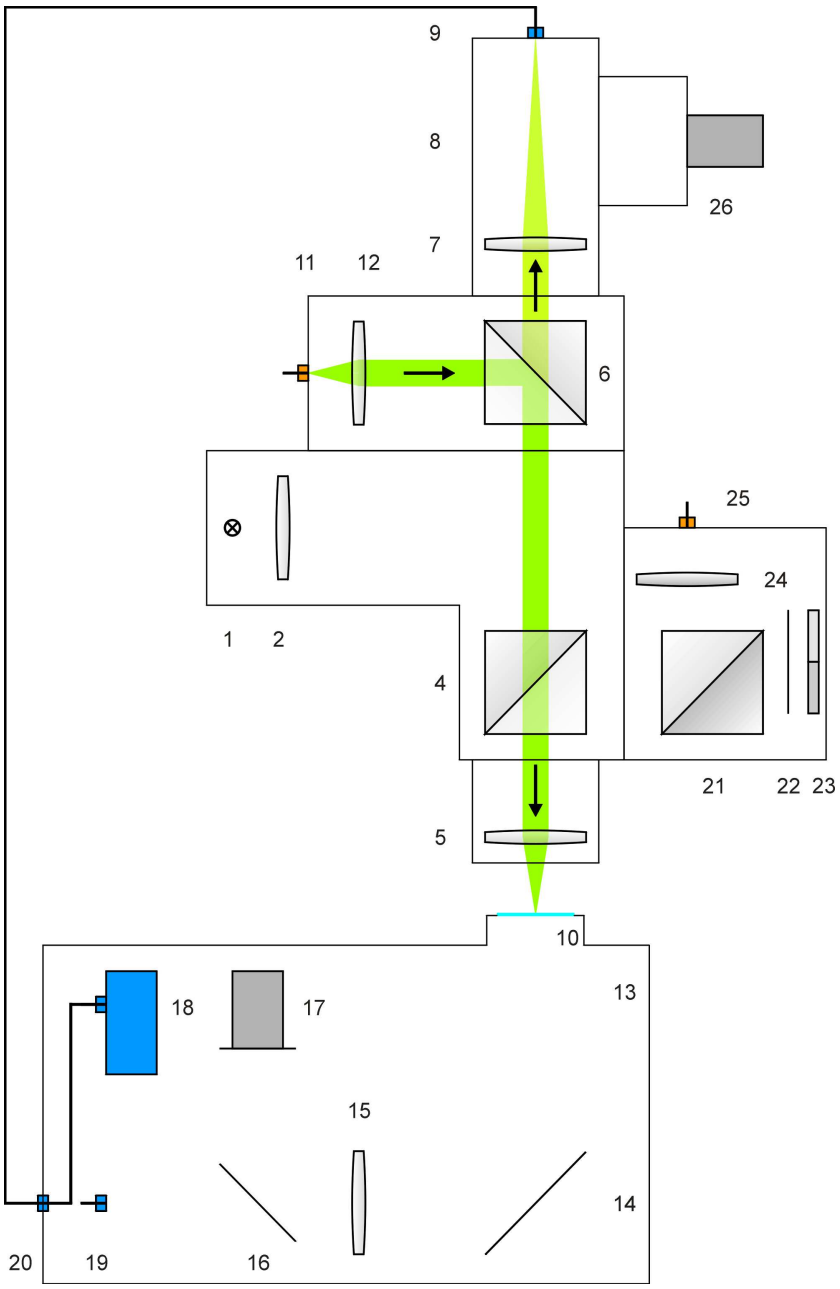

Figure 2.20: Layout and beam path for Alpha*SNOM* instrument in confocal reflection mode. *Components*: **(11)** input fiber connector for incident laser (for Raman, $\lambda = 633$ nm), also serving as the "point-like light source" (see Figure 2.19); **(12)** achromatic lens assembly; **(6)** beamsplitter cube (50:50); **(5)** micro-objective lens assembly (for Raman, 60 X); **(10)** sample on piezoelectrically scanned stage; **(7)** tube lens assembly ($f = 160$ mm); **(9)** output fiber connector for reflected/scattered light, also serving as the "detector pinhole" (see Figure 2.19); **(20)** optical fiber feedthrough; **(18)** single-photon detector (for Raman, spectrometer). After Reference [109].

without scanning the sample.

2.6.3 Surface-enhanced Raman scattering (SERS)

Raman scattering is inherently an extremely weak process, with cross-sections per molecule that are typically 14–15 orders of magnitude smaller than fluorescence cross-sections ($\approx 10^{-16}$ cm^2).[112] Fortunately, the electromagnetic field enhancement associated with the *collective* oscillations of the free electrons—the surface plasmons—of noble metals can be harnessed to greatly increase the interaction strength between an analyte and optical radiation. This notion finds its most prominent realization in the technique of surface-enhanced Raman scattering (SERS). In SERS, the analyte, which may even consist of single molecules, is placed within a few nanometers or in contact with the signal enhancer, which can be a roughened metal substrate, granular metal film, colloidally dispersed or lithographically patterned metal nanoparticles, usually silver or gold. Although a comprehensive theory explaining the fundamental origin of the SERS effect is still lacking, it is generally accepted that most of the signal enhancement comes from enhanced electric fields near curved or rough metal surfaces.[112,113]

Following Novotny,[112] let us place a metal nanostructure (*e.g.*, Ag particles) at $\vec{r}_1$, near the analyte molecule located at $\vec{r}_0$; see Figure 2.21. The electric field E_0 of the incident light, oscillating at an angular frequency ω, interacts with the molecule to give rise to a dipole moment μ associated with Raman scattering:

$$\mu(\omega_R) = \alpha(\omega_R, \omega)\,[E_0(\vec{r}_0, \omega) + E_s(\vec{r}_0, \omega)] \tag{2.8}$$

where $\omega_R = \omega \pm \omega_{vib}$ is a specific vibrationally shifted frequency. The molecular polarizability α is modulated at the frequency ω_{vib} of the molecular vibration and gives rise to the frequency mixing process that is Raman scattering. The molecule is interacting with the combined local field $E_0 + E_s$, where E_0 is the local field in the absence of the field-enhancing metal nanostructures and E_s the enhanced scattered field that originates from the interac-

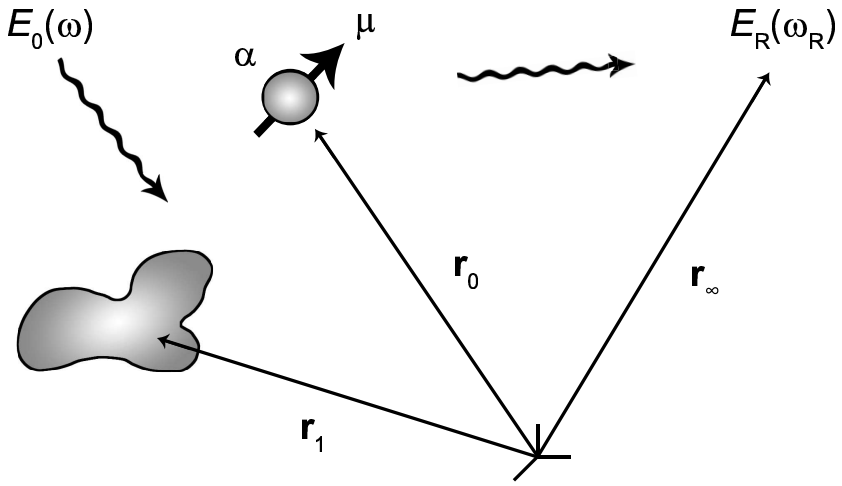

Figure 2.21: General configuration encountered in surface-enhanced spectroscopy. The incident electric field E_0, of angular frequency ω, interacts with a molecule of polarizability α and dipole moment μ to generate a scattered field E_{R} at frequency ω_{R}. Placing metal nanostructures (coordinate $\mathbf{r}_1$) near the molecule enhances both the incident and the scattered fields. After Reference [112].

tion of the incident light with the nanostructures. The scattered field can be expressed in terms of an enhancement factor $f_1(\omega)$, linear in the frequency, and the incident field:

$$E_{\mathrm{s}} = f_1(\omega) E_0 \tag{2.9}$$

The electric field E radiated by the induced dipole μ can be written as

$$E(\vec{\mathrm{r}}_\infty, \omega_{\mathrm{R}}) = \frac{\omega_{\mathrm{R}}^2}{\varepsilon_0 c^2} \left[G_0(\vec{\mathrm{r}}_\infty, \vec{\mathrm{r}}_0) + G_{\mathrm{s}}(\vec{\mathrm{r}}_\infty, \vec{\mathrm{r}}_0) \right] \mu(\omega_{\mathrm{R}}) \tag{2.10}$$

where the free-space Green's function G_0 represents the molecule's response in the absence of the metal nanostructures, while the scattered Green's function G_{s} accounts for the interaction of the radiated light with the nanostructures. Similarly to the scattered electric field, the scattered Green's function can be expressed as a second enhancement factor $f_2(\omega_{\mathrm{R}})$ times the free-space Green's function:

$$G_{\mathrm{s}} = f_2(\omega_{\mathrm{R}}) G_0 \tag{2.11}$$

Recalling that $I \propto |E|^2$, and using the relations from Equations 2.9 and 2.11, the Raman-scattered intensity I becomes

$$I(\vec{r}_\infty, \omega_R) = \frac{\omega_R^4}{\varepsilon_0^2 c^4} \left|[1 + f_2(\omega_R)] \cdot G_0(\vec{r}_\infty, \vec{r}_0) \cdot \alpha(\omega_R, \omega) \cdot [1 + f_1(\omega)]\right|^2 I_0(\vec{r}_0, \omega) \tag{2.12}$$

where I_0 is the incident (excitation) intensity, ε_0 is the vacuum permittivity, and c is the speed of light in vacuum. Hence, the Raman intensity scales as

$$I(\vec{r}_\infty, \omega_R) \propto \left|[1 + f_2(\omega_R)] \cdot [1 + f_1(\omega)]\right|^2 \tag{2.13}$$

Without any nanostructures, the scattered intensity is obtained by setting $f_1 = f_2 = 0$. In the presence of the "right" metal nanostructures, $\{f_1, f_2\} \gg 1$ and the overall Raman enhancement factor becomes

$$f_{\text{Raman}} \simeq |f_2(\omega_R)|^2 \, |f_1(\omega)|^2 \tag{2.14}$$

Therefore, provided that $|\omega_R \pm \omega|$ is smaller than the spectral response of the metal nanostructure, the bulk of the Raman scattering enhancement scales approximately with the *fourth power* of the electric field enhancement. An additional enhancement mechanism, the short-range "chemical effect", stems from modification of the molecular polarizability α when the molecule is in direct contact with the metal nanostructure.[112,113]

CHAPTER III

MODULATION OF THE GOLD PARTICLE-PLASMON RESONANCE BY THE METAL-SEMICONDUCTOR TRANSITION OF A VO_2 THIN FILM

Abstract

Reported here are experimental observations of relative blue-shifts in the particle-plasmon resonance of gold nanoparticles (Au NPs) covered with a vanadium dioxide (VO_2) film as the VO_2 material undergoes a semiconductor-to-metal transition at approximately 67 ^{o}C. Although the extinction spectra of the Au NPs exhibit significant red-shifts in the presence of the surrounding VO_2 film as compared to the same particles in air, the key result of this work is the dynamically controlled blue-shift of the Au-NP dipolar plasmon resonance upon thermal switching of the VO_2 overlayer from the semiconducting to the metallic state. We also report on the size and polarization dependence of the extinction spectra in both states, and present Mie-theory calculations that confirm in a qualitative way the observed trends in the VO_2-induced modulation of the Au-NP plasmon resonance, and their origin in the VO_2 dielectric function.

3.1 Introduction

Metal nanoparticles (NPs) exhibit characteristic absorption and scattering bands in the visible range due to electromagnetic interaction of light with oscillating surface charges, the so-called localized surface-plasmon resonance or simply the particle-plasmon.[114] The existence of surface plasmons, either localized or propagating, is peculiar to the interaction of metal nanostructures with optical radiation. Similar behavior cannot be simply reproduced by scaling because the material parameters, embodied in the dielectric function, change significantly with frequency. Therefore, model experiments, say with microwaves and corre-

spondingly larger metal structures, cannot substitute for experiments with metal nanostructures at optical frequencies. The study of the optical response of metals on subwavelength scales—and how to control it—is now often referred to as *plasmonics* or *nanoplasmonics*.[112]

3.1.1 Localized surface-plasmon resonance (LSPR)

When optical radiation encounters a small metallic sphere, the oscillating electric field sets up a coherent oscillation of the conduction-electron charge cloud, as depicted in Figure 3.1. The displacement of the electron cloud with respect to the positively charged lattice leads to the buildup of polarization charges on the NP surface, which provide a Coulombic restoring force between electrons and nuclei, thus giving rise to specific resonances in the surface charge-density oscillations. The localized surface plasmon resonance (LSPR) is distinct from the surface-plasmon polariton (SPP), in that the former is spatially confined within a particle, while the latter propagates along an extended metal-dielectric interface. The resonant electromagnetic response of noble-metal NPs is thus a consequence of the confinement of the conduction electrons to the small particle volume.[112,113,115] Inside the NP, a resonantly enhanced field builds up, which in turn generates a strong near-field in the immediate vicinity of the NP surface and boosts the absorption and scattering cross-sections for electromagnetic waves.

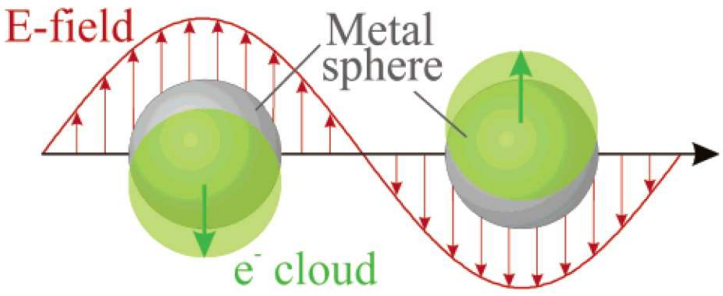

Figure 3.1: Schematic of the simplest mode of *collective* oscillation of the conduction electrons relative to the nuclei of a metal NP, the dipolar particle-plasmon. After Reference [115].

In general, the spectral position, damping, and magnitude of the plasmon resonances of individual metal NPs depend on the particle material, size, geometry, and the dielectric function of the surrounding host.[113] It is relatively straightforward to relate the lowest-order LSPR, the dipolar particle-plasmon, to the dielectric functions (permittivities) of the metal and the host medium within the framework of the so-called *quasi-static approximation*, which assumes that all points of an object respond simultaneously to the incoming light (*i.e.*, neglects retardation effects). For a small spherical NP of diameter $2a \ll \lambda$, where λ is the wavelength of the incident light in the surrounding medium, the conduction electrons inside the NP all move in phase upon plane-wave excitation, exhibiting a resonant response at a specific frequency (wavelength) where the electron motion has a phase lag of $\pi/2$ with respect to the driving field. In the small-particle limit ($2a \ll \lambda$), the field is homogeneous inside the NP and dipolar at a short distance r outside the NP surface (near-field zone: $2a \ll r \ll \lambda$), since the latter can be approximated as the electrostatic field of a point dipole of moment $\vec{\mathrm{p}}$, located at the NP center (origin) and oscillating in time with the angular frequency ω of the excitation light (hence the term *quasi*-static):[112,116]

$$\vec{\mathrm{E}}_{\mathrm{q.s.}}(r\hat{\mathrm{n}}_r, t) = \frac{1}{4\pi\varepsilon_0}[3\hat{\mathrm{n}}_r(\hat{\mathrm{n}}_r \cdot \vec{\mathrm{p}}) - \vec{\mathrm{p}}]\frac{1}{r^3}\mathrm{e}^{\mathrm{i}\omega t} \tag{3.1}$$

where $\varepsilon_0 = 8.854 \times 10^{-12}\ \mathrm{F \cdot m^{-1}}$ is the vacuum permittivity and $\hat{\mathrm{n}}_r$ is a unit vector directed from the origin (O) to the observation point (O_1). To see how this comes about, let us place an uncharged spherical nanoparticle (radius a, relative permittivity $\varepsilon_{\mathrm{NP}}$) in a host medium (relative permittivity $\varepsilon_{\mathrm{host}}$), and apply an electric field (magnitude E_0) directed along the x-axis, $\vec{\mathrm{E}}_0 = E_0\hat{\mathrm{n}}_x$, where $\hat{\mathrm{n}}_x$ is a unit vector; refer to Figure 3.2. The task is now to find how the presence of the particle alters the applied electric field inside and immediately outside the NP. In the scalar approximation, the electric potential Φ obeys the Laplace equation of electrostatics, $\nabla^2\Phi = 0$, which in spherical coordinates becomes

$$\frac{1}{r^2 \sin\theta}\left[\sin\theta\frac{\partial}{\partial r}\left(r^2\frac{\partial}{\partial r}\right) + \frac{\partial}{\partial\theta}\left(\sin\theta\frac{\partial}{\partial\theta}\right) + \frac{1}{\sin\theta}\frac{\partial^2}{\partial\varphi^2}\right]\Phi(r,\theta,\varphi) = 0 \tag{3.2}$$

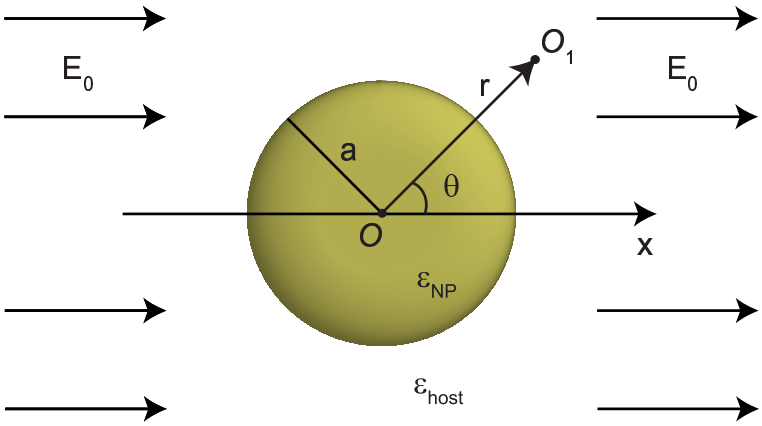

Figure 3.2: Small particle in host medium and under the applied electric field of x-polarized plane wave.

The axial symmetry of the problem suggests a solution of the type[116]

$$\textit{Inside of NP}: \qquad \Phi_{\text{in}} = \sum_{l=0}^{\infty} A_l r^l P_l(\cos\theta) \tag{3.3}$$

$$\textit{Outside of NP}: \qquad \Phi_{\text{out}} = \sum_{l=0}^{\infty} [B_l r^l + C_l r^{-(l+1)}] P_l(\cos\theta) \tag{3.4}$$

$$\begin{aligned} P_0(\cos\theta) &= 1 \\ P_1(\cos\theta) &= \cos\theta \\ P_2(\cos\theta) &= \tfrac{1}{2}(3\cos^2\theta - 1) \\ P_3(\cos\theta) &= \tfrac{1}{2}(5\cos^3\theta - 3\cos\theta) \\ P_4(\cos\theta) &= \tfrac{1}{8}(35\cos^4\theta - 30\cos^2\theta + 3) \\ &\ldots \end{aligned} \tag{3.5}$$

where A_l, B_l and C_l are constant coefficients to be determined from the boundary conditions; $P_l(\cos\theta)$ is a Legendre polynomial of order l. The boundary conditions far away from the NP, where the potential must approach that of the applied field, and at the surface of the NP ($r = a$), where the "in" and "out" tangential electric fields and normal components of

the electric displacements must be continuous, dictate that

$$\begin{aligned} &\textit{At infinity}: && \Phi_\infty \rightarrow \Phi_0 = -E_0 x = -E_0 r P_1(\cos\theta) = -E_0 r\cos\theta \\ &\textit{Tangential } E: && \left[\partial\Phi_{\text{in}}/\partial\theta\right]_{r=a} = \left[\partial\Phi_{\text{out}}/\partial\theta\right]_{r=a} \\ &\textit{Normal } D: && \varepsilon_{\text{NP}}\left[\partial\Phi_{\text{in}}/\partial r\right]_{r=a} = \varepsilon_{\text{host}}\left[\partial\Phi_{\text{out}}/\partial r\right]_{r=a} \end{aligned} \tag{3.6}$$

Evaluating the above boundary conditions for the series in Equations 3.3 and 3.4 yields the following solution for the potential inside (Equation 3.7) and outside (Equation 3.8) the particle:

$$\Phi_{\text{in}} = -E_0\left(\frac{3\varepsilon_{\text{host}}}{\varepsilon_{\text{NP}} + 2\varepsilon_{\text{host}}}\right) r\cos\theta \tag{3.7}$$

$$\Phi_{\text{out}} = \Phi_0 + \Phi_{\text{scatt}} = -E_0 r\cos\theta + E_0\left(\frac{\varepsilon_{\text{NP}} - \varepsilon_{\text{host}}}{\varepsilon_{\text{NP}} + 2\varepsilon_{\text{host}}}\right)\frac{a^3}{r^2}\cos\theta \tag{3.8}$$

The potential outside consists of the potentials of the incident (Φ_0) and scattered (Φ_{scatt}) fields; there is no φ-dependence owing to the azimuthal symmetry. The electric field can be calculated by taking the gradient of the potential, $\vec{\text{E}} = -\nabla\Phi$, and the resulting expressions for the electric field inside (Equation 3.9) and outside (Equation 3.10) the particle are

$$\vec{\text{E}}_{\text{in}} = E_0\left(\frac{3\varepsilon_{\text{host}}}{\varepsilon_{\text{NP}} + 2\varepsilon_{\text{host}}}\right)(\cos\theta\hat{\text{n}}_r - \sin\theta\hat{\text{n}}_\theta) = E_0\left(\frac{3\varepsilon_{\text{host}}}{\varepsilon_{\text{NP}} + 2\varepsilon_{\text{host}}}\right)\hat{\text{n}}_x \tag{3.9}$$

$$\vec{\text{E}}_{\text{out}} = E_0(\cos\theta\hat{\text{n}}_r - \sin\theta\hat{\text{n}}_\theta) + E_0\left(\frac{\varepsilon_{\text{NP}} - \varepsilon_{\text{host}}}{\varepsilon_{\text{NP}} + 2\varepsilon_{\text{host}}}\right)\frac{a^3}{r^3}(2\cos\theta\hat{\text{n}}_r + \sin\theta\hat{\text{n}}_\theta) \tag{3.10}$$

where the second equality for $\vec{\text{E}}_{\text{in}}$ makes use of the relation between unit vectors in the spherical ($\hat{\text{n}}_r$ and $\hat{\text{n}}_\theta$) and Cartesian ($\hat{\text{n}}_x$) bases:

$$\hat{\text{n}}_x = \cos\theta\hat{\text{n}}_r - \sin\theta\hat{\text{n}}_\theta \tag{3.11}$$

As stated earlier, the field inside the NP is homogeneous (Equation 3.9), while the field outside consists of the incident field (first term in Equation 3.10), $E_0(\cos\theta\hat{\text{n}}_r - \sin\theta\hat{\text{n}}_\theta) = E_0\hat{\text{n}}_x$, and the scattered near-field (second term in Equation 3.10). To show that the

latter is indeed identical to the electrostatic field of an electric dipole $\vec{\mathrm{p}}$ along the x-axis, $\vec{\mathrm{p}} = |\vec{\mathrm{p}}|\,\hat{\mathrm{n}}_x = p(\cos\theta\hat{\mathrm{n}}_r - \sin\theta\hat{\mathrm{n}}_\theta)$, we expand the expression in the square brackets of Equation 3.1:

$$[3\hat{\mathrm{n}}_r(\hat{\mathrm{n}}_r \cdot \vec{\mathrm{p}}) - \vec{\mathrm{p}}] = p(2\cos\theta\hat{\mathrm{n}}_r + \sin\theta\hat{\mathrm{n}}_\theta) \tag{3.12}$$

Now, comparing Equations 3.1, 3.12 and 3.10 (second term), and expressing the dipole induced by the incident electric field as $p = \varepsilon_{\mathrm{host}}\alpha(\omega)E_0$, we finally relate the dipolar particle-plasmon resonance to the dielectric properties of the two materials involved. The link is the frequency-dependent polarizability of the induced dipole:

$$\alpha(\omega) = 4\pi\varepsilon_0 a^3 \left(\frac{\varepsilon_{\mathrm{NP}}(\omega) - \varepsilon_{\mathrm{host}}}{\varepsilon_{\mathrm{NP}}(\omega) + 2\varepsilon_{\mathrm{host}}}\right) \tag{3.13}$$

The response of the dipole becomes resonant at the oscillation frequency (ω_{res}) of the incident field where the denominator in Equation 3.13 has a minimum, limited by the imaginary part of $\varepsilon_{\mathrm{NP}}$ describing Ohmic heating losses within the particle,[113] *i.e.*:

$$\Re\mathrm{e}\left[\frac{\varepsilon_{\mathrm{NP}}(\omega_{\mathrm{res}})}{\varepsilon_{\mathrm{host}}}\right] = -2 \tag{3.14}$$

In a medium with a real-valued $\varepsilon_{\mathrm{host}}$, the cross-section ($\sigma$) and efficiency ($Q$) for scattering, absorption and extinction of the incident radiation by the particle is obtained from the polarizability (Equation 3.13) as follows:[112]

$$Q_{\mathrm{scatt}} \equiv \frac{\sigma_{\mathrm{scatt}}}{\pi a^2} = \frac{k^4}{6(\pi a\varepsilon_0)^2}\,|\alpha(\omega)|^2 \tag{3.15}$$

$$Q_{\mathrm{abs}} \equiv \frac{\sigma_{\mathrm{abs}}}{\pi a^2} = \frac{k}{\pi a^2\varepsilon_0}\Im\mathrm{m}\,[\alpha(\omega)] \tag{3.16}$$

$$Q_{\mathrm{ext}} = Q_{\mathrm{scatt}} + Q_{\mathrm{abs}} \tag{3.17}$$

where $k = 2\pi\sqrt{\varepsilon_{\mathrm{host}}}/\lambda$ is the magnitude of the incident wavevector in the host medium. The

above quantities constitute the spectral response of the NP to the incident radiation, and their maxima result from the resonant condition in Equation 3.14, within the framework of the quasi-static approximation.

The polarizability in Equation 3.13 adequately describes only the near-fields and cross-sections, which nevertheless dominate the optical response of small particles when $2a \ll r \ll \lambda$. For larger particles, however, the dipolar resonance shifts to longer wavelengths (lower frequencies) and the plasmon peak broadens substantially.[113,115] The red-shift stems from retardation effects due to the finite ratio of NP size to wavelength—the conduction electrons no longer all move in phase, which reduces the depolarization field generated at the NP center by the surrounding polarized matter. Moreover, the radiative losses that were neglected in the quasi-static treatment begin to contribute to the plasmon damping (peak broadening), dominating the total damping for larger-than-100-nm Au and Ag NPs.[113] In fact, both the retardation and depolarization effects become equally important for NP sizes comparable to $\lambda/2\pi$, whereas the quasi-static treatment contains no dependence of the LSPR on NP size.[115]

Corrections can be made to the quasi-static approximation, in particular to the polarizability in Equation 3.13, that account not only for radiation damping and retardation, but also for higher-order plasmon resonances (*e.g.*, electric quadrupole oscillations where half of the electron cloud moves parallel and the other half antiparallel to the applied field[115]), as well as for particle shapes other than spherical (by including geometrical depolarization factors[113,115]). Such corrections form the basis of the so-called modified long-wavelength approximation (MLWA).[115,117] On the other hand, Maxwell's equations can be solved exactly in the case of a spherical particle of arbitrary size, as Gustav Mie[118] did in 1908, and in Section 3.3.1 we use a modified version[119] of what is now known as *Mie theory*[120] to validate the predictions of the quasi-static approximation for the shift of the Au-NP plasmon resonance with the change in $\varepsilon_{\text{host}}$ across the VO_2 phase transition.

3.1.2 Vanadium-dioxide–metal nanocomposites

As pointed out by Cortie *et al.*,[121] an important current issue in plasmonics is the possibility of a "self-regulating" LSPR of composite metallic NPs; for instance, under a sufficiently intense light irradiation, the dynamic functionality of such NPs could be used as a probe in photothermal therapy or optical sensing applications.[122,123] Vanadium-dioxide–gold (VO_2–Au) composite material is a practical candidate for enabling the modulation of plasmonic behavior, as was shown in the case of extraordinary optical transmission through subwavelength hole arrays.[124,125] VO_2 is a transition-metal oxide that exhibits a semiconductor-to-metal phase transition upon heating through a bulk critical temperature $T_c \approx 67$ °C, and the reverse transition upon cooling. The transition is accompanied by changes in the crystalline structure, large transmission contrast in the (near-)infrared range, and hysteresis. VO_2 possesses its own plasmonic resonance, albeit heavily damped, around 1.1 μm,[54,126] while Au NPs are known to have a relatively strong extinction cross-section at visible or near-infrared wavelengths.[127]

There are two recent experimental studies on metal NPs in a VO_2 matrix. In one case, Xu *et al.*[128] sputtered silver (Ag) on top of a VO_2 thin film; the resulting Ag NPs had a rather broad size distribution of particle diameters ($|\Delta(2r)| = 15$–55 nm), which generally manifests itself as a broadening of the LSPR peaks.[129] Such inhomogeneous broadening of the resonance peak was also observed by Maaza *et al.*[130] in a VO_2–Au nanocomposite made by pulsed-laser deposition (PLD), again due to the broad size distribution of the embedded Au NPs. Moreover, closely-spaced NPs—typically found in self-assembled or PLD-grown nanoparticulate films—can give rise to particle-particle interactions, and thus cause significant peak shifts[131] in addition to those due to the change in the dielectric environment.

In this report, based on our publication in Reference [132], we systematically explore the modulation of the LSPR in lithographically fabricated arrays of Au NPs by means of the reversible metal-semiconductor transition of VO_2. In particular, we demonstrate the

dependence of this modulation on nanoparticle size, shape, and light polarization. The Au LSPR peaks blue-shift in the metallic state of VO_2 ($T > T_c$) with respect to the semiconducting state ($T < T_c$) by as much as 80 nm for symmetric and 200 nm for asymmetric Au NPs (including polarization effects for the latter). The relative blue-shift is qualitatively predicted by a Mie calculation, modified to take into account the imaginary part of the complex permittivity of the VO_2 medium. For the asymmetric Au NPs, we observe a strong dependence of the plasmon resonance on polarization of the incident light with respect to the major (long) and minor (short) NP axes, complemented by subtler peak shifts with varying aspect ratios at a fixed polarization.

3.2 Experimental details

Using focused-ion-beam (FIB: 30-keV Ga^+) lithography[53,133] in a layer of poly(methylmethacrylate) (PMMA: 50-nm thickness), followed by thermal evaporation of gold (Au: 15-nm thickness) and chemical lift-off, we patterned arrays of Au NPs of various sizes and shapes, ranging from elliptical cylinders (2:1 aspect ratio in the plane parallel to the substrate) to circular cylinders. In order to prevent over-exposure of the PMMA, which would have resulted in cross-linking and enhanced resistance to chemical processing,[134] the dwell time was reduced to approximately 30 μs per FIB pixel. The substrate was a glass slide coated with a transparent layer of indium-tin oxide (ITO) to reduce charging during FIB exposure.

Scanning-electron micrographs (SEMs) of typical arrays, before deposition of the vanadium-oxide overlayer, are shown in Figure 3.3a and 3.3b. Pulsed-laser deposition (PLD) and subsequent thermal oxidation were performed to make a 50-nm VO_2 layer atop the Au-NP arrays: First, the beam from a KrF excimer laser (λ = 248 nm) was focused onto a vanadium-metal target at a fluence of about 4 J·cm^{-2} to deposit a sub-stoichiometric vanadium oxide ($VO_{1.7}$), then the sample was annealed at 450 ^{o}C under 250 mtorr of oxygen gas for 40 minutes, in order to convert the amorphous film into stoichiometric, crystalline VO_2.

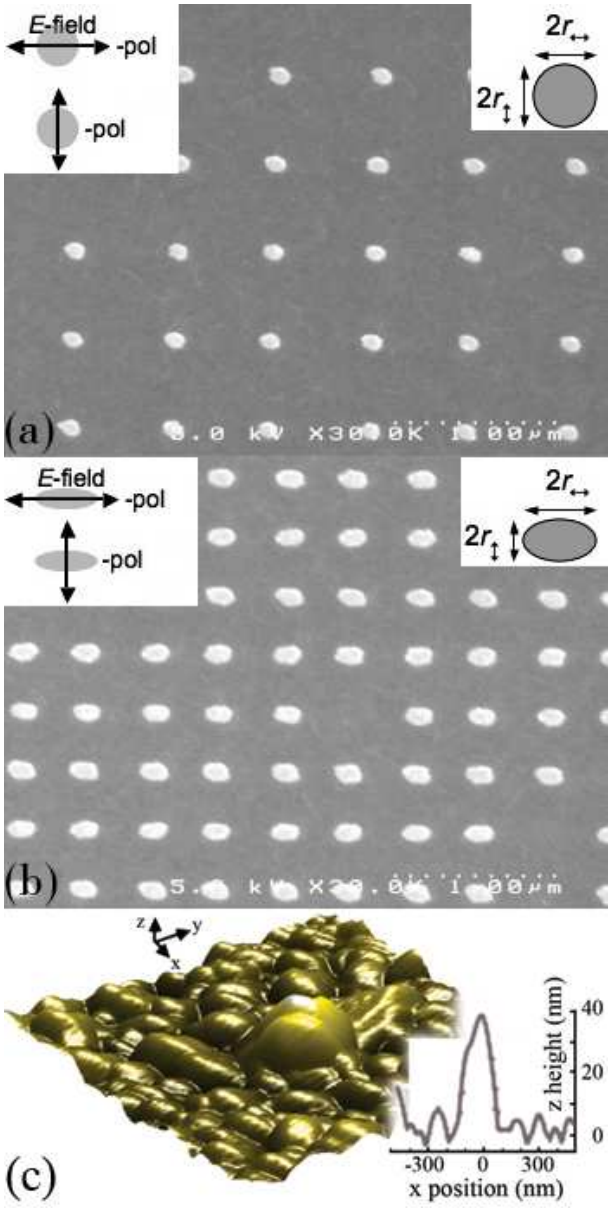

Figure 3.3: SEMs of **(a)** circular and **(b)** elliptical Au NPs on ITO-coated glass. **(c)** Atomic-force micrograph (AFM) and **(inset)** line scan of single Au NP covered with crystalline grains of PLD-grown VO_2 film. The schematic insets in **(a)** and **(b)** show the conventions used throughout the text for incident-light polarization (left) and Au-NP geometry (right).

This procedure has been demonstrated by multiple tests of stoichiometry, structure and switching properties to produce VO_2 rather than any of the multiple competing vanadium oxides.[45] Figure 3.3c shows an atomic-force micrograph (AFM) of one Au NP covered with the annealed VO_2 film. The VO_2 phase transition was confirmed by measuring the thermal hysteresis for infrared transmission ($\lambda = 1330$ nm). The sample was heated and cooled during the transmission measurement using a thermoelectric element, which was mounted on a translation-rotation stage equipped with a precision thermocouple. Optical transmission spectra of the different Au-NP arrays were acquired using linearly polarized white light at normal incidence to the sample surface. The incident-beam spot and array locations were monitored by dark-field scattering. The transmitted light was fiber-fed to a spectrometer with a cooled charge-coupled-device (CCD) detector, and normalized to transmission through the bare VO_2 film (*i.e.*, an area with no Au NPs). The resulting transmittance spectra were noise-filtered and converted to extinction spectra of the Au NPs. The optical setup is sketched in Figure 3.4.

3.3 Results and discussion

3.3.1 Qualitative predictions of environment-induced LSPR shift

The strong electric-field localization near a metal NP ensures that particle size and shape,[115,135,136] inter-particle spacing,[131,137] and dielectric environment[138,139] all have substantial effects on the extinction spectra. Therefore, the controlled geometrical parameters of lithographically fabricated NPs offer several distinct ways of modulating the particle-plasmon resonance, some of which are demonstrated below for the VO_2–Au nanocomposite.

The spectral shifts of the LSPR can be understood qualitatively within the framework of the quasi-static approximation for spherical particles. The polarizability α of a small ($r \ll \lambda$) metal sphere (here, Au NP) immersed in a host medium (here, VO_2 film) can be obtained by solving the Laplace equation;[112,115] in the simplest case of only dipolar

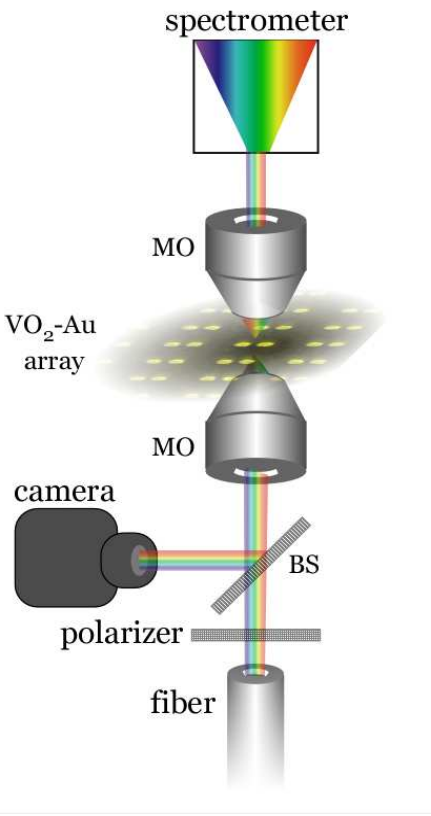

Figure 3.4: Schematic of the optical setup. *Legend*: MO ≡ micro-objective; BS ≡ beam-splitter.

excitations, α incorporates the complex-valued, wavelength-dependent permittivities $\tilde{\varepsilon}$ of the two materials as follows:

$$\alpha\{\text{Au sphere in VO}_2\} \propto \frac{\tilde{\varepsilon}_{\text{Au}}(\lambda) - \tilde{\varepsilon}_{\text{VO}_2}(\lambda)}{\tilde{\varepsilon}_{\text{Au}}(\lambda) + 2\tilde{\varepsilon}_{\text{VO}_2}(\lambda)} \tag{3.18}$$

The dipolar resonance condition for the Au particle requires that the real part of the denominator in Equation 3.18 vanish, *i.e.*:

$$\Re\text{e}\left[\tilde{\varepsilon}_{\text{Au}}/\tilde{\varepsilon}_{\text{VO}_2}\right] = -2 \tag{3.19}$$

Consequently, the LSPR peak occurs in the near-infrared region of the spectrum because there the real part of the Au permittivity (Figure 3.5b) becomes negative enough to cancel

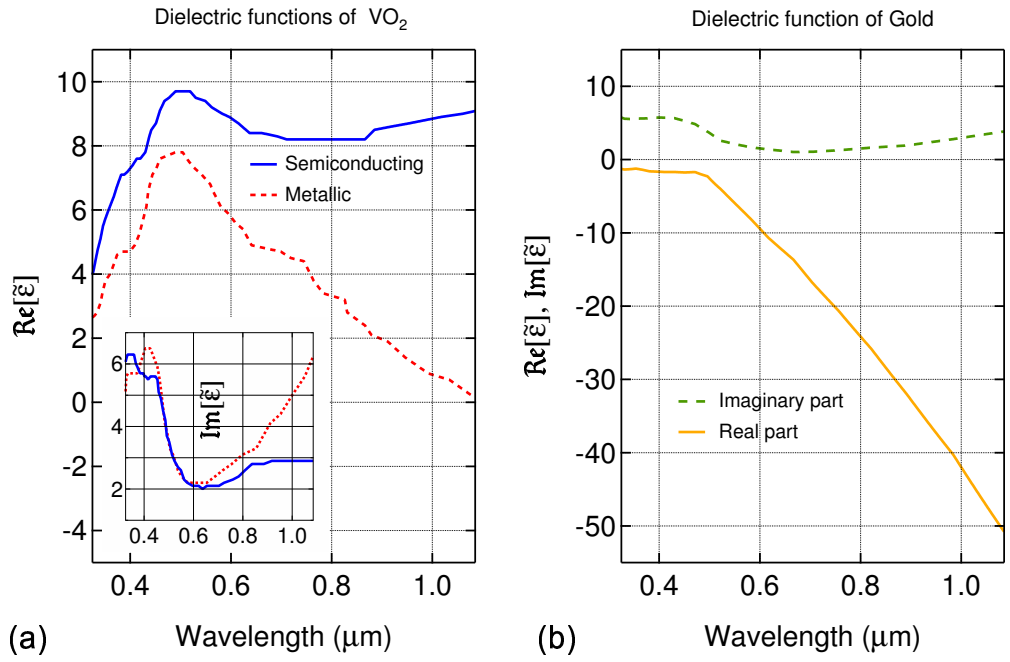

Figure 3.5: Real and imaginary parts of relative permittivities (dielectric functions) in the visible to near-infrared region for **(a)** VO_2 (data extracted from Reference [57]) and **(b)** Au (data extracted from Reference [140]).

its VO_2 counterpart in the oxide's semiconducting state, which varies between 8 and 10 at visible to near-infrared wavelengths (Figure 3.5a). In the metallic state of VO_2, however, the real part of the permittivity is considerably lower than that in the semiconducting state, which necessitates a less negative Au permittivity to satisfy the dipole resonance condition (Equation 3.19); hence, the LSPR peak should appear at shorter wavelengths when the surrounding VO_2 has switched into its metallic state. That is, the peak will be blue-shifted with respect to the semiconducting state.

Figure 3.6 shows the extinction efficiencies calculated by Mie theory for spherical Au NPs of different radii embedded in VO_2. The standard Mie formalism was amended as proposed in Reference [119], in order to account for fact that absorption in the host medium (VO_2) results in different incident intensity at different locations on the NP surface. The permittivities of VO_2 (Figure 3.5a) and Au (Figure 3.5b) were obtained from References [57] and [140], respectively; the effect of temperature on the Au permittivity is negligi-

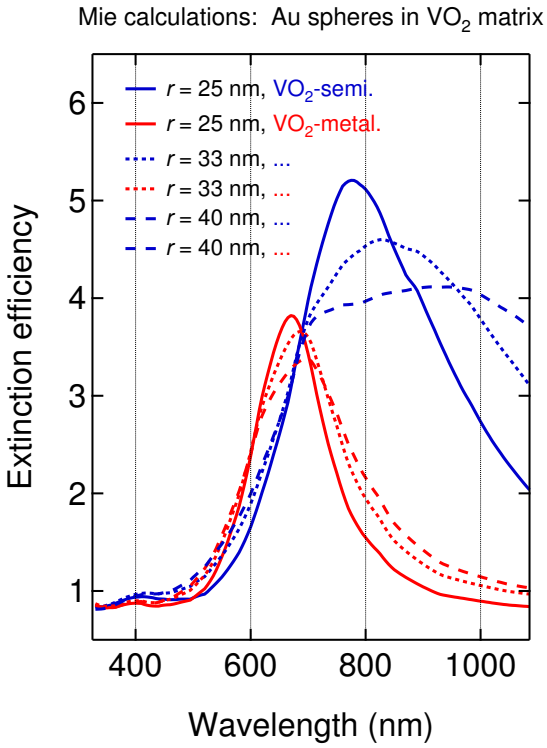

Figure 3.6: Mie calculations of extinction efficiencies for Au spheres (radii r = 25, 33, 40 nm) in VO_2 as a function of wavelength and state (semiconducting or metallic) of VO_2 host. Blue lines refer to the semiconducting phase, red lines to the metallic state of VO_2.

ble.[141] Although these Mie calculations lend support to the predictions of the quasi-static approximation for the spectral shifts of the Au LSPR, they cannot be compared directly to the experimental peak positions because of the different particle shape (*i.e.*, discs rather than spheres) and the presence of the ITO-coated glass substrate in our experiments. Crucially, however, Mie theory confirms qualitatively the observed blue-shift of the Au particle-plasmon resonance upon switching of the VO_2 matrix from semiconducting to metallic, as evidenced by the experimental spectra below (Figures 3.7 and 3.8).

3.3.2 Extinction spectra of symmetric Au NPs

Figure 3.7 shows extinction spectra of arrays of symmetric Au NPs of three different sizes, with inter-particle spacings of 600 nm. We first note that the Au-NP extinction peaks

at room temperature (20 °C) are significantly red-shifted with respect to those taken in the absence of the VO_2 overlayer (not shown). At a high enough temperature (95 °C)—so that the VO_2 layer has already transformed into its metallic state—the spectra move by more than 60 nm towards shorter wavelengths for either polarization direction. Comparing the peak shifts in Figure 3.7a and 3.7b, we observe that the LSPRs move further to the blue with decreasing particle size, as confirmed by Mie theory. Since these Au NPs are nearly symmetrical around an axis normal to the surface, the spectra in the two polarization directions are almost identical; slight differences between the two polarizations are likely due to a small, systematic asymmetry in the particle shapes originating from stigmation misalignment of the FIB. This asymmetry is somewhat evident in the planar-view SEM in Figure 3.3a, which shows an array of nearly circular NPs slightly skewed in a common, arbitrary direction.

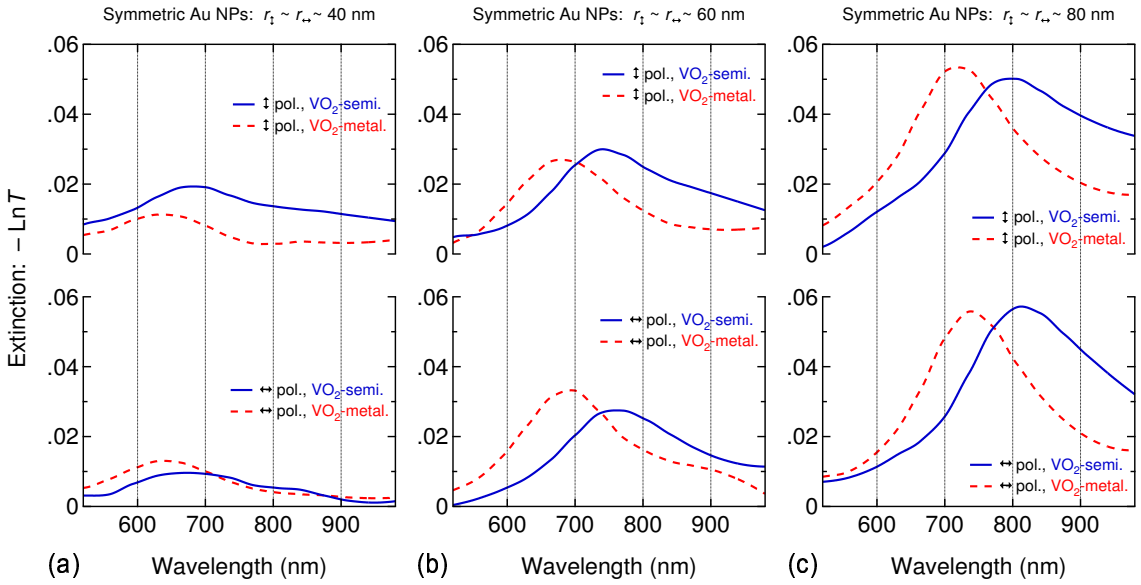

Figure 3.7: Extinction spectra as a function of wavelength, incident-light polarization, and state of the VO_2 overlayer for arrays of circular (*i.e.*, symmetric) Au NPs of three different diameters ($2r$): **(a)** 80 nm, **(b)** 120 nm, **(c)** 160 nm. *Transmittance*: T = *Intensity*{VO_2 + Au NPs + substrate} / *Intensity*{VO_2 + substrate}.

3.3.3 Extinction spectra of asymmetric Au NPs

The extinction spectra for three arrays of intentionally asymmetric Au NPs, covered with the same VO_2 layer, are shown in Figure 3.8. Besides LSPR shifts induced by the VO_2 phase transition and similar to those seen for the symmetric NPs, a strong dependence on polarization is also observable in the asymmetric case. When the electric field of the incident light lies parallel to the long axes of the NPs ($\leftrightarrow$-polarization), the transition-induced blue-shift of the LSPR peaks is more pronounced than when the electric field is parallel to the particles' short axes ($\updownarrow$-polarization). These asymmetric NPs give differences of more than 30 nm in the maximum resonant wavelength for the different polarizations, while there is hardly any shift between the two polarizations for the symmetric NPs. Thus, when compared to the LSPR position for a symmetric Au NP of $r = 60$ nm (Figure 3.7b), the resonance peaks of an asymmetric particle of $r_{\leftrightarrow} = 70$ nm and $r_{\updownarrow} = 50$ nm (Figure 3.8b) exhibit a red-shift for $\leftrightarrow$-polarization but a blue-shift for $\updownarrow$-polarization, in either state of the VO_2 overlayer.

3.3.4 Resonance shifts

Figure 3.9a summarizes our data on the shifts of the LSPR extinction peak for the symmetric Au NPs. The linear fits to the data for the semiconducting and metallic phases of VO_2 yield slightly different slopes. This divergence in resonant wavelengths stems from the permittivity difference between the two phases of the VO_2 film, which monotonically increases towards longer wavelengths (Figure 3.5a) where larger Au NPs have their resonances. For the largest of our symmetric NPs ($2r = 160$ nm), the transition-induced blue-shift of the resonant wavelength is about 80 nm (Figure 3.9a). On the other hand, our most asymmetric Au NPs ($r_{\leftrightarrow}$ / $r_{\updownarrow} = 1.80$) can yield blue-shifts as large as 200 nm (Figure 3.9b) under the combined effects of the VO_2 phase transition and the direction of the incident electric-field vector. The red-shift in resonant wavelength with increasing aspect ratio for $\leftrightarrow$-polarized light (see the positive-slope lines in Figure 3.9b) is brought

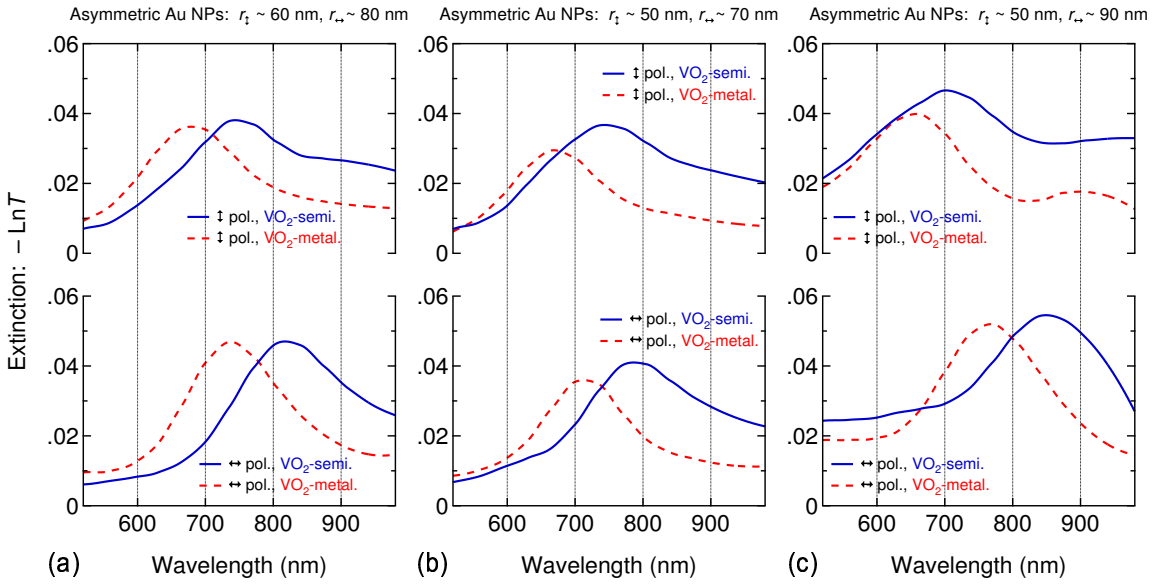

Figure 3.8: Extinction spectra as a function of wavelength, incident-light polarization, and state of theVO_2 overlayer for arrays of elliptical (*i.e.*, asymmetric) Au NPs of three different aspect ratios ($r_{\leftrightarrow}$ / $r_{\updownarrow}$): **(a)** 80 nm / 60 nm = 1.33 and **(b)** 70 nm / 50 nm = 1.40, **(c)** 90 nm / 50 nm = 1.80. *Transmittance*: T = *Intensity*{VO_2 + Au NPs + substrate} / *Intensity*{VO_2 + substrate}.

about by depolarization of the radiation across the particle surface due to the finite ratio of particle size to wavelength, as can be shown by applying electrodynamic corrections to the quasi-static treatment,[115,117] as in the modified long-wavelength approximation (MLWA) mentioned earlier (Section 3.1.1). Conversely, when the incident electric field oscillates along the short NP axes (↕-polarization), the resonance peaks blue-shift with increasing aspect ratio (see the negative-slope lines in Figure 3.9b), and the MLWA treatment also reproduces this trend.[115,117]

3.4 Summary and outlook

We have demonstrated a method to modulate the spectral features of the localized surface-plasmon resonance of Au nanoparticles by means of the metal-semiconductor transition of VO_2, by dynamically and reversibly changing the dielectric properties of the material

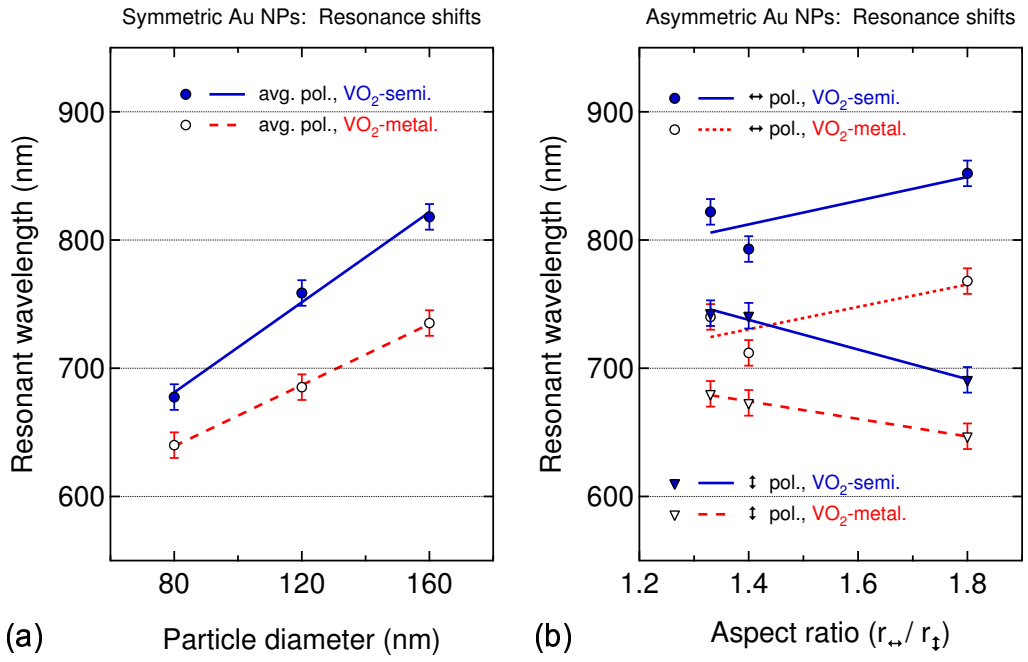

Figure 3.9: **(a)** Peak resonant wavelengths (from Figure 3.7), averaged over both incident-light polarizations, as a function of particle size ($2r$ = 80, 120, 160 nm) and state of the VO_2 overlayer for the circular (*i.e.*, symmetric) Au NPs. **(b)** Peak resonant wavelengths (from Figure 3.8) as a function of particle aspect ratio ($r_{\leftrightarrow}$ / $r_{\updownarrow}$ = 80 nm / 60 nm, 70 nm / 50 nm, 90 nm / 50nm), incident-light polarization, and VO_2 state for the elliptical (*i.e.*, asymmetric) Au NPs.

that covers the Au NPs. The modulation can be thermally controlled, as here, or initiated by a laser pulse on an ultrafast timescale.[54] As predicted by electromagnetic theory, the extinction spectra of the Au NPs exhibit a marked dependence on particle size and shape, incident-light polarization, and, of course, on the dielectric environment—semiconducting or metallic VO_2. The spectral shift of the Au LSPR across the VO_2 phase transition is caused by the different dielectric properties of VO_2 in each state: The transition-induced change in the VO_2 permittivity determines the spectral shift of the LSPR wavelength for the VO_2–Au nanocomposite. Invariably, a relative blue-shift of the LSPR peak follows the switching of the VO_2 host from semiconducting to metallic.

We speculate that an improved sample structure, one better suited to quantitative comparisons with Mie-theory calculations, would be an array of metal NPs fully embedded

in a VO_2 matrix: for example, a "sandwich" of two 100-nm-thick VO_2 films with Au NPs in between. Another possible extension of the work presented here may involve laser switching, that is, using high-powered laser pulses to launch the LSPR of metal NPs and the metal-semiconductor transition of VO_2 simultaneously. In any case, the VO_2 phase transition emerges as a promising mechanism for dynamically controlling the plasmonic behavior of metal nanoparticles.

CHAPTER IV

USING THE METAL-SEMICONDUCTOR TRANSITION OF VO_2 TO CONTROL OPTICAL TRANSMISSION THROUGH SUBWAVELENGTH HOLE ARRAYS

Abstract

This chapter describes a novel configuration in which the extraordinary optical transmission effect through subwavelength hole arrays in noble-metal films can be switched by the metal-semiconductor transition in an underlying thin film of vanadium dioxide. In these experiments, the transition is brought about by thermal heating of the double-layer film. The surprising reverse hysteretic behavior of the transmission through the subwavelength holes in the vanadium-dioxide layer suggest that this modulation is accomplished by a dielectric-matching condition rather than plasmon coupling through the double-layer film. The results of this switching, including the wavelength dependence, are qualitatively reproduced by a transfer matrix model. The prospects for effecting a similar modulation on a much faster time scale by using ultrafast laser pulses to trigger the metal-semiconductor transition are also discussed.

4.1 Introduction

4.1.1 Motivation

Ever since its initial description in a much-cited letter by Ebbesen *et al.*,[6] the phenomenon of *extraordinary optical transmission* (EOT) has generated intense interest regarding both the fundamental physics of the transmission mechanism as well as potential applications. In brief, the EOT effect refers to the observations that light transmission through periodic arrays of subwavelength holes in opaque thin films can be much larger

than the combined transmission for isolated holes predicted by standard diffraction theory,[142,143] and that the spectral profile of the transmission follows a sequence of dips and peaks peculiar to the materials involved and the detailed geometry of the hole array. This effect has been described predominantly in terms of light waves coupled to collective oscillations of the free electrons, the so-called propagating surface plasmons or surface-plasmon polaritons (SPPs), although recent theoretical developments have identified another surface-wave contribution to the EOT effect in addition to SPPs.[144]

Numerous applications of EOT have been proposed and, in some cases, realized in practice. Specific applications of subwavelength holes[8] include SPP-activated lithographic masks, bright point sources, SPP couplers/decouplers, near-field optical storage heads, molecular sensors, and so on. Recent work[145] has shown that the electroluminescence efficiency of an organic light-emitting diode (OLED) can be significantly enhanced by use of a perforated anode, which allows for light emission from both the back and the front of the device. Control of EOT through a hole array could make it possible, for example, to modulate selectively in wavelength and time the light emitted by an OLED or other sources, or the propagation of light in a waveguide, in effect serving as a subwavelength optical switch. However, there are few reports on methods for post-fabrication modulation of the EOT at visible and near-infrared wavelengths, and both involve varying the refractive index of the input side dielectric. In one case, the authors[146] used different index-matching liquids to vary the degree of asymmetry between the dielectric layer above a perforated gold film and the quartz substrate. The other scheme[7] entailed sandwiching a layer of liquid crystal between a transparent indium-tin-oxide electrode and a perforated chromium film on quartz, then varying the applied electric field. Ultrafast switching of THz signals through metallic subwavelength hole arrays has also been reported.[147]

Here we recount another recently demonstrated method to control the amount of light transmitted through perforated double-layer thin films on transparent substrates, as described in our publications in References [124,125,148]. The structures consist of an optically

opaque silver (Ag) or gold (Au) film on top of a vanadium dioxide (VO_2) film deposited on a glass substrate, with a periodic array of subwavelength holes penetrating the double layer. The intensity of transmitted light is controlled by means of a reversible metal-semiconductor phase transition, thermally induced in the VO_2 layer, which undergoes drastic changes in its electrical and optical properties.

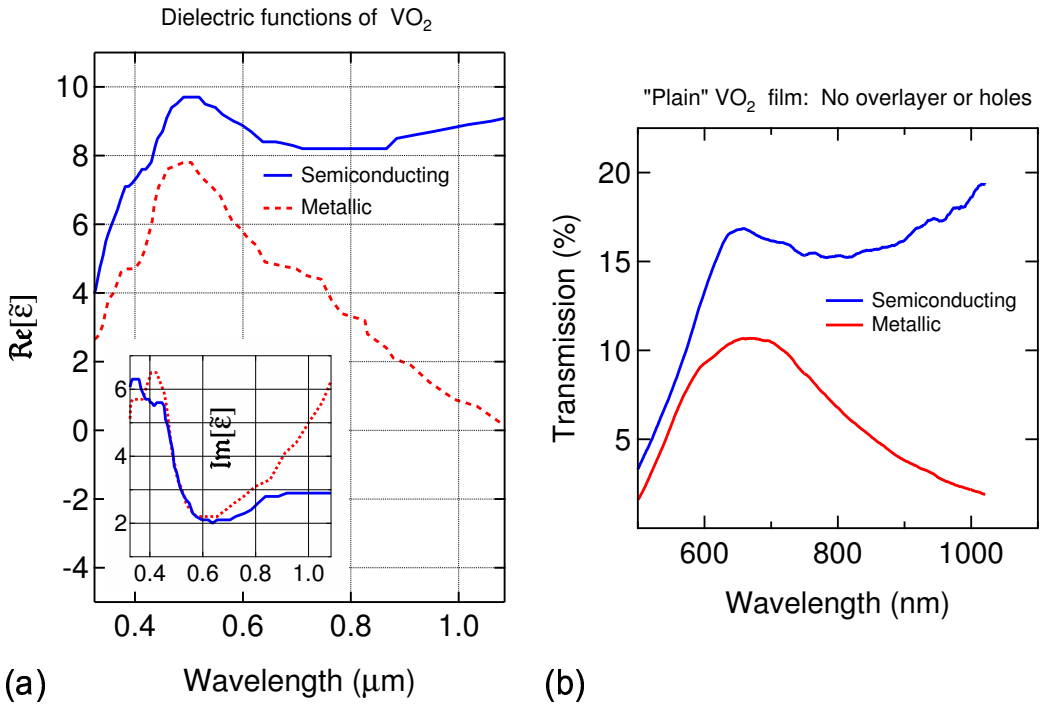

Figure 4.1: **(a)** Real and imaginary parts of relative permittivity of VO_2 (data extracted from Reference [57]). **(a)** Experimental normal-incidence transmission spectra of non-perforated 200-nm thick VO_2 film on glass.

Briefly, the phase transition of VO_2 is a first-order transformation that occurs at a critical temperature $T_c \approx 67^oC$, from a high-temperature metallic phase to a low-temperature semiconducting phase.[21] The precise mechanism of the phase transition has long been a topic of controversy,[25–29] and the cause-and-effect debate over the relative roles of lattice distortion and electron-electron correlations in triggering the VO_2 phase transition has

lately received renewed theoretical[30] and experimental[1–3,31,32] attention. The presence of thermal hysteresis, attributed to variations in the phase-equilibrium temperatures for film grains of different sizes,[81] allows for potential applications in memory devices and optical data storage, while the speed of the transition—about 80 fs according to Cavalleri *et al.*[31]—makes VO_2 a candidate for applications in ultrafast optical switching.[54] Above T_c, VO_2 exhibits metallic character with relatively high opacity in the infrared (IR) wavelength range. Below T_c, the dimerization and tilting of the V–V pairs result in the opening of a narrow band-gap;[22] in this semiconducting phase, films thicker than 100 nm are markedly more transparent in the (near-)IR range with respect to the metallic phase (Figure 4.1). Surprisingly, however, our metal-VO_2 structures exhibit larger near-IR transmission with the VO_2 layer in the metallic state as compared to transmission in the semiconducting state—quite the opposite of the conventional behavior of a "plain" (*i.e.*, no metal overlayer or holes) VO_2 film of the same thickness. This *reverse switching* can be understood in terms of a simple model that takes into account the losses due to *leaky evanescent waves* in the plane of the VO_2 layer and *diffuse scattering* from the holes at the entrance and exit apertures. Numerical simulations based on the transfer matrix formalism for photonic crystals[149] provide qualitative support for the experimental findings.

4.1.2 Extraordinary optical transmission (EOT) and the surface-plasmon polariton (SPP)

A short account of the EOT phenomenon follows in this section. One of Ebbesen *et al.*'s initial EOT results[6] is reproduced in Figure 4.2. It shows a typical zero-order (*i.e.*, the incident and detected light beams being collinear) transmission spectrum for a Ag film perforated by a square array of cylindrical subwavelength holes. Ebbesen and his colleagues termed the transmission "extraordinary" partly because of the very large enhancements at the observed IR peaks over the theoretical prediction for the transmission efficiency of a very small circular aperture in a thin screen of a perfect conductor. The theory, first developed by Hans Bethe[142] in 1944 and later extended by others,[143,150] circumvents

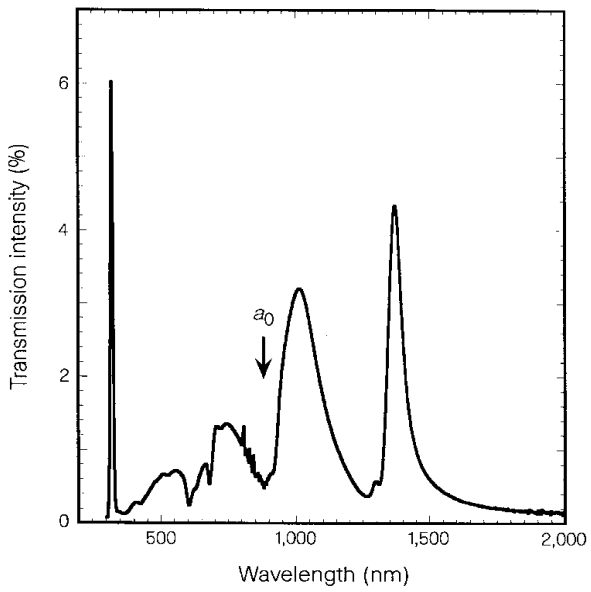

Figure 4.2: EOT spectrum, at normal incidence, from square array of subwavelength holes in Ag film. *Parameters*: periodicity, $a_0 = 900$ nm; hole diameter, $d = 150$ nm; film thickness, $t = 200$ nm; hole coverage, $f \equiv \pi(d/2)^2 \Big/ a_0^2 = 2.2\%$. After Reference [6].

the fundamental inconsistencies in Kirchhoff's formulation of diffraction[116] by treating the transmitted radiation as if originating from two virtual dipoles: an electric dipole normal to the aperture and a magnetic one in the plane of the aperture. This distribution of "fictitious magnetic charges and currents" in the diffracting hole ensures the fulfillment of the boundary conditions on the opaque screen and in the aperture itself. The influence of Bethe's calculation in coining the phrase "extraordinary optical transmission" can be easily appreciated by considering in Figure 4.2 the maximum observed transmission at λ = 1370 nm (neglecting the sharp leftmost peak for now)—about $4.5\%/f$, where f is the areal coverage of the holes—and comparing that to the very weak transmission predicted by the Bethe's theory for an aperture of the same diameter and at the same wavelength. The enhancement factor speaks for itself:

$$\frac{T_{\text{observed per hole}}}{T_{\text{Bethe}}} = \frac{T_{\text{observed}}/f}{\frac{64\pi^2}{27}\left(\frac{d}{\lambda}\right)^4} = \frac{T_{\text{observed}}}{\frac{\pi}{4}\left(\frac{d}{a_0}\right)^2 \times \frac{64\pi^2}{27}\left(\frac{d}{\lambda}\right)^4} = \frac{0.045}{\frac{16\pi^3}{27}\frac{(150\text{ nm})^6}{(900\text{ nm})^2(1370\text{ nm})^4}} \approx 614 \tag{4.1}$$

Transmission enhancements like the one in Equation 4.1 were one of the reasons to call the phenomenon "extraordinary". The other was the peculiar spectral profile of the observed transmission, which typically consists of a series of peaks separated by valleys of low transmission. For instance, the sharp leftmost peak in Figure 4.2 corresponds to the *bulk plasmon* of the silver metal and disappears with increasing film thickness.[6] The bulk or volume plasmon in a metal is the quantum of collective longitudinal oscillations of the conduction electron gas.[61] The energy of the bulk plasmon, characteristic of the given metal, can be calculated from the Drude model for the response of the free-electron gas to an applied electric field, extended to account for the polarizability of the bound electrons by a constant offset (ε_∞) to the dielectric function of the metal[61,112] and leading to an expression for the plasma frequency ω_p (or wavelength λ_p) of the collective oscillation:

$$\omega_\mathrm{p} = \sqrt{\frac{Ne^2}{\varepsilon_\infty \varepsilon_0 m_e^*}}\,, \quad \lambda_\mathrm{p} = \frac{2\pi c}{\omega_\mathrm{p}} \tag{4.2}$$

Substituting in Equation 4.2 for the density[110] ($N = 5.86 \cdot 10^{28}$ m^{-3}) and effective mass ($m_e^* \approx m_e$) of the free electrons in Ag, as well as for the background dielectric constant[151] ($\varepsilon_\infty \approx 6$) and the remaining natural constants ($e = 1.602 \cdot 10^{-19}$ C, $m_e = 9.109 \cdot 10^{-31}$ kg, $c = 3 \cdot 10^{17}$ nm $\cdot$ s^{-1}), yields the theoretical bulk-plasmon wavelength for Ag: $\lambda_\mathrm{p} = 338$ nm. This value matches reasonably well the observed position, 326 nm, of the leftmost peak in Figure 4.2.

However, what really intrigued Ebbesen and colleagues about an EOT spectrum like the one in Figure 4.2—and continues to occupy many researchers a decade since the original EOT report—were the other high-transmission peaks, especially those at wavelengths greater than the array periodicity. Based partly on the lack of extraordinary transmission from a hole array in nonmetallic germanium, and partly on angle-dependent EOT measurements for noble-metal samples, Ebbesen *et al.*[6] attributed the EOT effect to the excitation of *propagating* surface plasmons, which arise from the coupling between optical radiation and the collective longitudinal oscillations of the free-electron charge density at the bound-

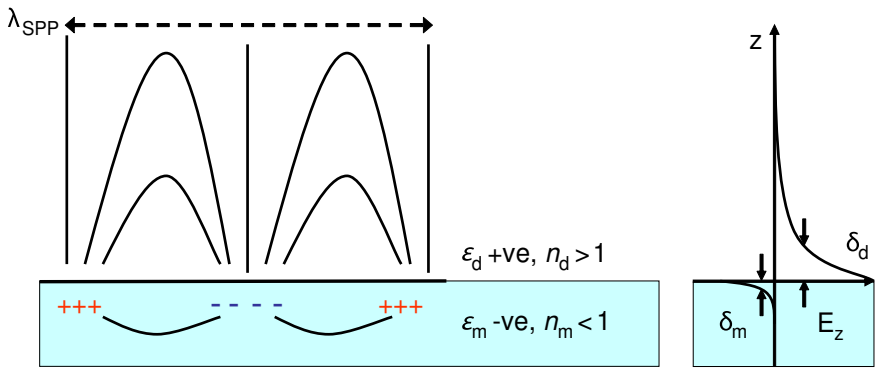

Figure 4.3: Left: Surface-plasmon polaritons (SPPs) at the interface between a metal of relative permittivity ε_{m} and a dielectric of relative permittivity ε_{d} have a combined electromagnetic-wave and surface-charge character, which causes the electric-field component perpendicular to the surface (E_z) to become enhanced near the surface and decay exponentially with away from it. **Right:** The E_z-field is evanescent, reflecting the bound nature of SPPs on a flat surface, so power does not propagate away from the interface. In the dielectric medium above the metal, typically air or glass, the decay length δ_{d} of the field is of the order of the wavelength of the excitation light, whereas the decay length δ_{m} into the metal is determined by the skin depth (*e.g*, about 25 nm for Ag). After Reference [152].

ary between a metal and a dielectric.[153] When an electromagnetic wave impinges on a good metal, it penetrates only a short distance into the material[127] ($\delta_{\mathrm{m}} < 50$ nm for Au or Ag at optical wavelengths) because of the high absorption coefficient, which results in high reflectivity; therefore, only the free electrons very close to the surface can interact with the incident wave. Such interaction of surface electrons with the electric field of the incident light can lead to a collective displacement of the free electrons with respect to the lattice of fixed positive ions and give rise to a charge-density wave propagating across the surface, known as a *surface-plasmon polariton* (SPP) (Figure 4.3a). Conceptually, SPPs can be thought of as "light waves that are trapped on the surface because of their interaction with the free electrons of the conductor".[154]

Surface-plasmon polaritons are surface-bound modes: SPP waves can propagate along the metal-dielectric interface for tens or even hundreds of micrometers for noble metals, limited only by the low Ohmic losses embodied in the imaginary part k''_{SPP} of the SPP

wavevector, but suffer strong attenuation away from the surface (Figure 4.3b). The dispersion relation between the angular frequency ω and the in-plane wavevector k_{SPP} of the surface waves for a flat metal-dielectric interface can be obtained by seeking surface-mode solutions of Maxwell's equations under appropriate boundary conditions. Continuity of the normal component of the displacement field $D_z = \varepsilon E_z$ requires that the real part of the relative permittivity of the metal $\varepsilon'_{\mathrm{m}}$ and the relative permittivity of the dielectric $\varepsilon'_{\mathrm{d}}$ have opposite signs, in order to allow for charges to be sustained at the metal surface.[152] In other words, materials surrounded by dielectrics can support SPP modes only in those spectral regions where $\Re\mathrm{e}\left[\varepsilon_{\mathrm{m}}(\omega)\right] \equiv \varepsilon'_{\mathrm{m}}(\omega) < 0$. The SPP dispersion relation is then derived as:[112,153]

$$k_{\mathrm{SPP}} = \frac{\omega}{c}\sqrt{\frac{\varepsilon_{\mathrm{d}}\varepsilon_{\mathrm{m}}}{\varepsilon_{\mathrm{d}}+\varepsilon_{\mathrm{m}}}}, \quad \text{with} \quad k_{\mathrm{SPP}} \equiv k'_{\mathrm{SPP}} + \mathrm{i}k''_{\mathrm{SPP}} \tag{4.3}$$

The relative permittivity of the metal can be approximated using a Drude-model expression for the frequency dispersion:[112]

$$\varepsilon_{\mathrm{m}}(\omega) \equiv \varepsilon'_{\mathrm{m}}(\omega) + \mathrm{i}\varepsilon''_{\mathrm{m}}(\omega) = 1 - \frac{\omega_{\mathrm{p}}^2}{\omega^2 + \mathrm{i}\Gamma\omega} \tag{4.4}$$

where ω_{p} is the plasma frequency of the metal (Equation 4.2) and Γ is the rate of dissipation of the electron motion through scattering (for silver,[152] $\Gamma_{\mathrm{Ag}} = 1.45 \cdot 10^{-13}$ s^{-1}). For weak damping, $|\varepsilon''_{\mathrm{m}}| \ll |\varepsilon'_{\mathrm{m}}|$, the SPP wavelength λ_{SPP} (Figure 4.3) can be obtained from the real part of the SPP wavevector k'_{SPP}:

$$k'_{\mathrm{SPP}} \approx \frac{\omega}{c}\sqrt{\frac{\varepsilon_{\mathrm{d}}\varepsilon'_{\mathrm{m}}}{\varepsilon_{\mathrm{d}}+\varepsilon'_{\mathrm{m}}}} \quad \Rightarrow \quad \lambda_{\mathrm{SPP}} = \frac{2\pi}{k'_{\mathrm{SPP}}} \approx \lambda\sqrt{\frac{\varepsilon_{\mathrm{d}}+\varepsilon'_{\mathrm{m}}}{\varepsilon_{\mathrm{d}}\varepsilon'_{\mathrm{m}}}} \tag{4.5}$$

where λ is the wavelength of the excitation light in the dielectric medium. In Figure 4.4, the SPP dispersion curve for a flat metal-air interface (solid line), when compared to the light line in air (dotted line), reveals a crucial characteristic of SPPs that reflects their bound nature on a flat, undecorated interface: a wavevector mismatch between the SPP mode and light, that is, the surface-plasmon polariton always carries greater momentum

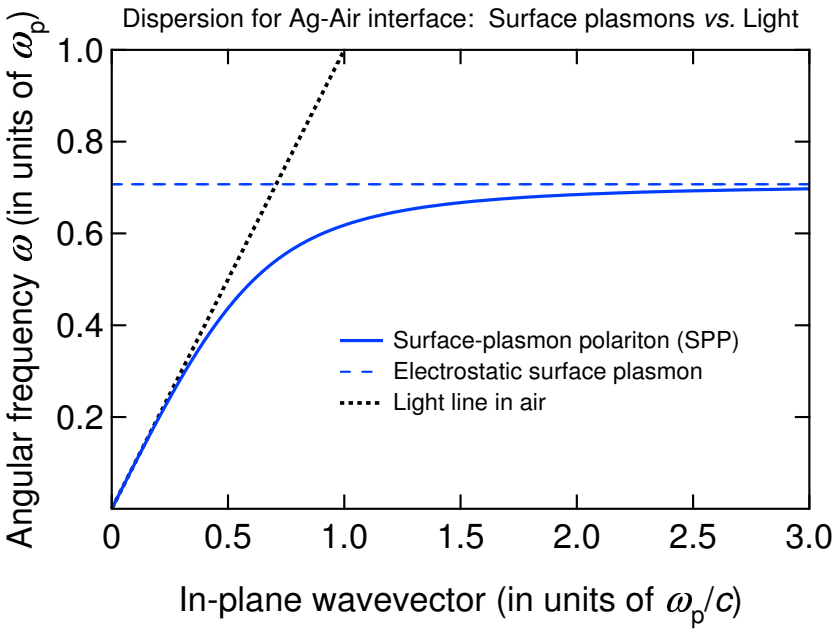

Figure 4.4: Frequency dispersion of SPP wavevector k'_{SPP} at Ag-air interface (see Equation 4.5), with asymptotic SP frequency $\omega_{\mathrm{sp}} = \omega_{\mathrm{p}}/\sqrt{2}$, *vs.* "light line" $k_0 = \omega/c$ in air. Note the wavevector (momentum) mismatch, $k'_{\mathrm{SPP}} > k_0$.

than a free-space (air) photon of the same frequency.[153,154] The physical reason for the increased momentum of the SPP is that the light field has to "drag" the electrons along the metal surface.[112] For large values of the wavevector, the SPP dispersion relation approaches the asymptotic frequency ω_{sp} of the *non-propagating* plasma oscillations at the interface, the electrostatic *surface plasmon* (SP): $\omega_{\mathrm{sp}} = \omega_{\mathrm{p}}/\sqrt{1+\varepsilon_{\mathrm{d}}}$. At the opposite limit of small wavevectors, SPPs are more "light-like", hence the designation "polaritons". Nevertheless, light of any frequency impinging from a dielectric medium onto a flat metal surface cannot directly excite the SPP modes at the same interface, unless the missing wavevector mismatch is somehow compensated. This is precisely where the periodic structuring of a hole array begins to shine.

According to the model of SPP-mediated EOT, the periodic surface structure of the hole array serves a triple purpose (Figure 4.5): **(i)** coupling of the incident light into surface-plasmon excitations, via scattering/diffraction at the input interface, to produce bound

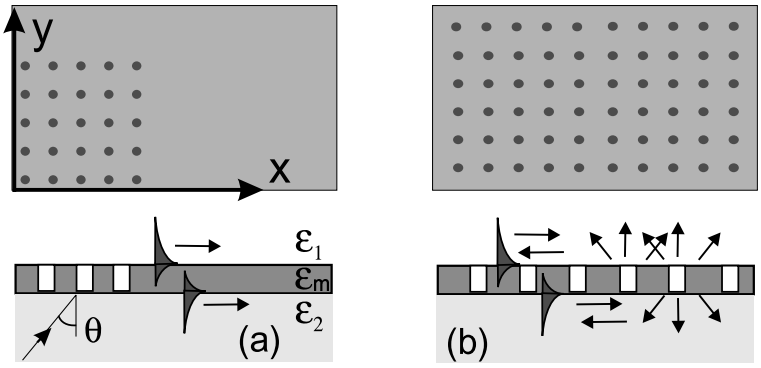

Figure 4.5: Schematics of light-SPP-light coupling. **(a)** SPP excitation by diffraction of incident light from perforated surface region and subsequent surface-bound propagation on smooth region; **(b)** SPP excitation, propagation, interference, and eventual scattering back into light from perforated surface region. After Reference [155].

SPP modes; **(ii)** selecting the wavelengths of allowed SPP modes via SPP-SPP interference; and **(iii)** scattering/diffraction of the bound SPPs at the output interface into propagating light, whose zeroth diffraction order becomes the observed transmission.[155] For a structured metal film bounded by dielectrics, light readily interacts with the surface charges because the structure can bridge the photon-SPP momentum gap through scattering/diffraction (Figure 4.5). Conservation of momentum for a square-lattice hole array of periodicity a_0 takes the following form:[155,156]

$$\vec{\mathrm{k}}_{\mathrm{SPP}} = \vec{\mathrm{k}}_{xy} \pm p\vec{\mathrm{G}}_x \pm q\vec{\mathrm{G}}_y \ , \quad \text{with} \tag{4.6}$$

$$\vec{\mathrm{k}}_{xy} = \hat{\mathrm{u}}_{xy}\sqrt{\varepsilon_{\mathrm{d}}}\left(\frac{\omega}{c}\right)\sin\theta \quad \text{and} \quad \left|\vec{\mathrm{G}}_x\right| = \left|\vec{\mathrm{G}}_y\right| \equiv \frac{2\pi}{a_0} \tag{4.7}$$

where $\hat{\mathrm{u}}_{xy}$ is the unit vector in the direction of the in-plane wavevector k_{xy} of the light of frequency ω incident at an angle θ; $\varepsilon_{\mathrm{d}} = \{\varepsilon_1,\ \varepsilon_2\}$ is the relative permittivity of either dielectric medium; pG_x and pG_y are the magnitudes of the reciprocal-lattice vectors, with integers $(p,\ q)$ designating the different SPP modes. At normal incidence ($\theta = 0°$), combining Equations 4.5 and 4.6 yields a first approximation for the spectral positions $\lambda_{\max}$ of

the EOT peaks:

$$\lambda_{\max}(p,\ q) \approx \frac{a_0}{\sqrt{p^2+q^2}} \sqrt{\frac{\varepsilon_{\mathrm{d}}\varepsilon'_{\mathrm{m}}}{\varepsilon_{\mathrm{d}}+\varepsilon'_{\mathrm{m}}}} \tag{4.8}$$

Figure 4.6 illustrates the use of Equation 4.8 for peak designation, whereby transmission peaks are attributed to different SPP modes corresponding to different substrates and four-fold degenerate $(\pm p,\ \pm q)$ pairs.[7] The peak widths, although partly due to inhomogeneous broadening from irregularities in the holes,[7] are mostly governed by the lifetime of the SPP modes before they scatter back into light.[157]

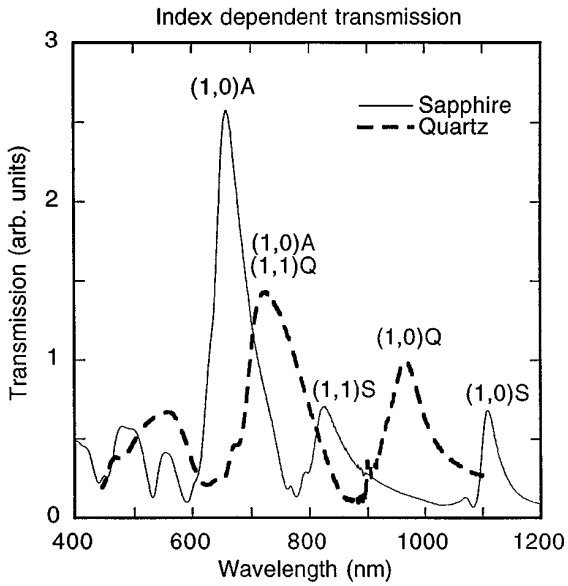

Figure 4.6: Peak designation according to SPP model for experimental EOT spectra of perforated Ag films on quartz (Q) and sapphire (S) substrates, with air (A) on opposite side. *Parameters*: $a_0 = 600$ nm, $d = 150$ nm. After Reference [7].

Matching the resonant wavelengths on both sides of a perforated metal film presents one way to control the EOT effect.[146] In general, two sets of resonances appear in the transmission spectra because each surface of the hole array borders on a different dielectric, typically the solid substrate and air, each with a different permittivity ε_{d}. Replacing air, for instance, with various index-matching liquids allows for tuning of the transmission

spectra, as varying the dielectric environment on one side of the structure influences the SPPs associated with both interfaces. The apparent coupling between the two interfaces is a form of evanescent Fabry-Perot resonances that re-circulate energy inside the holes and thus serve to amplify to an "extraordinary" extent the inherently weak transmission in the sub-wavelength regime, where cylindrical cavities cannot sustain propagating modes.[146,158–160] A key result of this resonant interaction is that minimizing the energy difference between SPP modes on opposite sides of the perforated metal film maximizes the peak transmission intensity (Figure 4.7); numerical simulations also confirm the experimental observations.[146] Therefore, within the framework of the surface-plasmon model, the EOT effect arises owing to a combination of SPP resonances at either or both interfaces and evanescent Fabry-Perot resonances inside the holes.[158]

Many authors[146,156,161–164] have elaborated on the initial explanation given by Ebbesen *et al.*[6] that the excitation of surface-plasmon polaritons at either or both metal-dielectric interfaces mediates the EOT effect. A small group of researchers had previously dismissed the role of SPPs and put forth a model of non-resonant generation and interference of composite diffracted evanescent waves (CDEWs);[165] however, a recent exchange of articles,[166–170] comments,[171,172] and responses to comments[173,174] between proponents of the SPP and CDEW models has led to a tacit consensus that surface plasmons must be involved in the extraordinary transmission at visible and near-infrared wavelengths. Although most workers in this field now regard the excitation of SPP modes as the dominant mechanism for mediating the EOT effect, some very recent theoretical work[144] has given further evidence of another contribution to the EOT, namely a "quasi-cylindrical wave creeping along the interface over several wavelength distances"; in fact, in the thermal-IR region, where SPPs are only weakly excited by the array of holes, the cylindrical wave dominates the scattering process.[144] Moreover, other recent studies[158,175] have also identified an additional plasmonic contribution to the observed transmission: the *localized surface-plasmon resonances*[153] (LSPRs) that originate on the metallic ridge of each aperture. Revealing

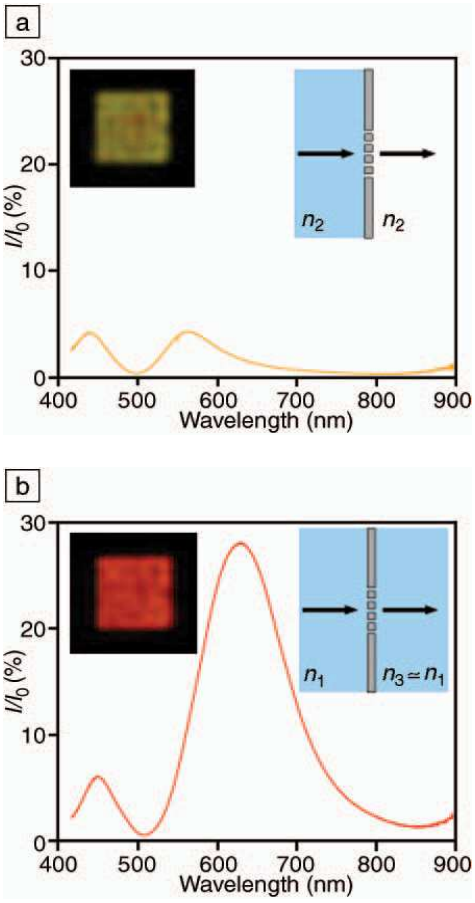

Figure 4.7: EOT effect in asymmetric *vs.* symmetric dielectric environment. Transmission spectra and **(left insets)** optical images of the same hole array in Ag film on quartz substrate ($n_1 \equiv \sqrt{\varepsilon_1} = 1.46$), with **(a)** air ($n_2 = 1$) and **(b)** glycerol ($n_3 = 1.47 \approx n_1$) as the output-side dielectric. *Parameters*: $t_{\mathrm{Ag}} = 200$ nm, $a_0 = 250$ nm, $d = 130$ nm. After Reference [8].

the role of LSPRs in the EOT phenomenon may also help to explain why hole arrays in good metals such as Ag and Au invariably exhibit the largest EOT effects.[175] Other researchers[176–178] interpret the EOT effect in a purely phenomenological fashion—in terms of Fano-type spectral profiles that result from the interference of two distinct contributions: a resonant channel (*e.g.*, SPPs and/or other surface modes) and non-resonant scattering—and account for the observed spectral shapes without explicitly specifying the nature of the resonant channel.

4.2 Experimental details

The nanostructures investigated in this work were: **(i)** hole array in a plain VO_2 film (Figure 4.8a); **(ii)** hole arrays in Au-on-VO_2 and Ag-on-VO_2 double layers (Figure 4.8b); **(iii)** plain VO_2 film. All the VO_2 layers were prepared simultaneously on fused-silica ("glass") substrates in a pulsed-laser deposition system (PLD: KrF excimer laser at $\lambda =$ 248 nm, fluence ≈ 4 J·cm^{-2}) by ablating a V-metal target in a 12-mtorr O_2 atmosphere at 550 °C. The resulting film thickness was 200 nm, as determined by Rutherford backscattering spectrometry (RBS). The Ag and Au overlayers were deposited in a bell-jar thermal evaporator. The RBS-measured thickness was 160 nm for Ag and 230 nm for Au. The hole arrays, consisting of 60-by-60 circular apertures of 250-nm nominal diameter and 750-nm pitch, were milled down to the substrates using a focused ion beam (FIB: 30-keV Ga^+, 90-pA beam current). Figure 4.9 shows a FIB micrograph of the VO_2 array (structure (i) above), while Figure 4.8c shows a portion of the same array imaged in transmission with a scanning near-field optical microscope (SNOM: $\lambda = 532$ nm, aperture ≈ 100 nm); a schematic of the SNOM setup is given in Figure 4.10a. We note here that the air-filled holes in the SNOM image of the VO_2 hole array (Figure 4.8c) appear darker—that is, transmit less—than the surrounding VO_2 film, whereas the contrast is reversed in the case of holes in Ag-VO_2 (Figure 4.8d) or Au-VO_2 (not shown) double-layer hole arrays. We shall return to this observation shortly. Spectral measurements at normal and oblique incidence were performed using nearly collimated white light delivered through a multimode optic fiber to a stopped-down micro-objective (Figure 4.10b). The incident-beam spot was slightly smaller than the size of the array, with a beam divergence of about $\pm 1^o$. The transmission spectrum through each sample was collected in the zero-diffraction-order (*i.e.*, detected beam collinear with incident beam) by another micro-objective, stopped down to reduce outgoing-beam divergence to about $\pm 1^o$, and coupled to another multimode fiber. The fiber was fed into a spectrometer equipped with a cooled charge-coupled-device (CCD) detector. The substrates were attached to a resistor-heated sample holder, mounted on a

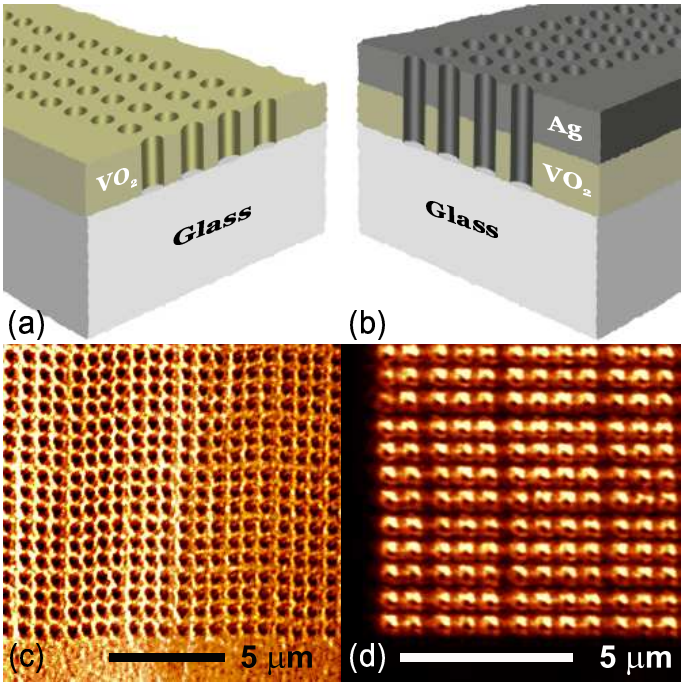

Figure 4.8: Schematics of hole arrays in **(a)** single VO_2 layer and **(b)** Ag/Au-VO_2 double layers. SNOM transmission images (λ = 532 nm) of hole arrays in: **(c)** single layer of VO_2 (semiconducting phase) and **(d)** Ag-VO_2 double layer. All nanostructures are on fused-silica ("glass") substrates.

translation-rotation stage, with a precision thermocouple placed in contact with the top surface of the sample. The position of the hole array with respect to the incident-beam spot was monitored in reflection via a CCD camera connected to a video display.

4.3 Results and discussion

4.3.1 Periodic double-layer hole arrays: EOT modulation and reverse hysteresis

Figure 4.11 presents the main experimental results of our work in Reference [125]: **(i)** controlled switching of the EOT effect through periodic arrays of subwavelength holes via the temperature-induced metal-semiconductor transition of VO_2; and **(ii)** counterintuitive transmission behavior of the VO_2 layer in these nanostructures. Figure 4.11a shows the transmission spectra for a hole array in a silver-VO_2 double layer on glass, at two different temperatures that correspond to the two phases of the VO_2 layer. It is immediately obvi-

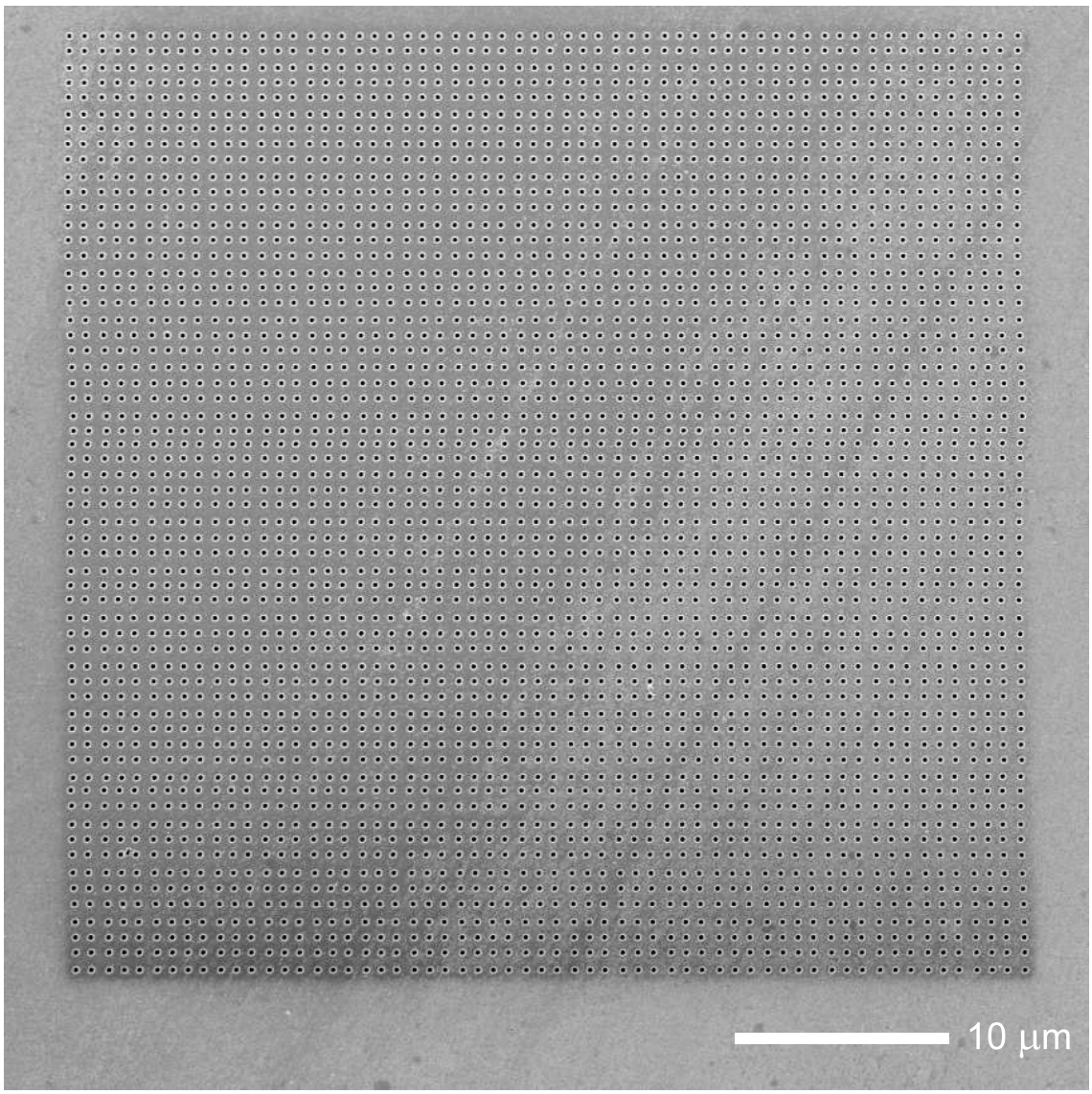

Figure 4.9: FIB micrograph of periodic array of 3600 circular holes in single layer of VO_2 on glass. *Parameters*: $d = 250$ nm, $a_0 = 750$ nm, $t_{VO_2} = 200$ nm.

ous that, for wavelengths greater than about 600 nm, the high-temperature, metallic-phase transmission dominates. The transmission contrast in the visible range is rather small, at some points even slightly in favor of the low-temperature, semiconducting-phase transmission, since the optical properties of the two VO_2 phases only begin to differ significantly in the near-IR range, as evidenced by the spectral dependence of the complex permittivity (Figure 4.1a) and transmission (Figure 4.1b). Figure 4.12a shows the EOT intensity for the

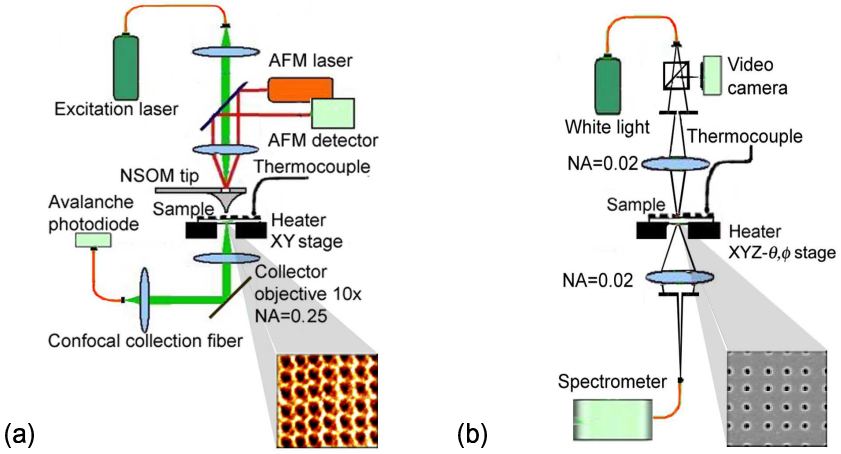

Figure 4.10: Schematics of **(a)** SNOM setup and **(b)** optical setup for transmission spectra.

Ag-VO_2 hole array as a function of temperature at a wavelength of 800 nm. Comparing the shape of this hysteresis curve to that of a plain VO_2 film (Figure 4.12b), it becomes clear why we call our observation *reverse switching* of VO_2. As explained later on, it is the permittivity contrast between the content of the holes (air) and the surrounding material (VO_2) that brings about this effect.

The controlled switching of EOT in the near-IR range stands out even more prominently in the case of a perforated gold-VO_2 double layer on glass (Figure 4.11b)—for example, the high-temperature, metallic-phase transmission at 800 nm exceeds the low-temperature, semiconducting-phase transmission by an order of magnitude. The magnitude of the EOT effect through the gold-VO_2 hole array is smaller than the magnitude in the corresponding phase of the silver-VO_2 nanostructure, partly because of the larger metal-layer thickness[179] and smaller hole diameter[180] for the gold-VO_2 structure, and partly due to gold being more dissipative than silver. The relative sharpness of the maximum transmission peak for the Au-VO_2 structure may also be related to hole size: Smaller holes, being less efficient scatterers of surface modes into far-field light, diminish the radiative damping and hence increase the lifetime of these modes, which in turn reduces the width of the peak.[157] Overall, the key observation holds for both types of structures, namely that EOT in the metallic

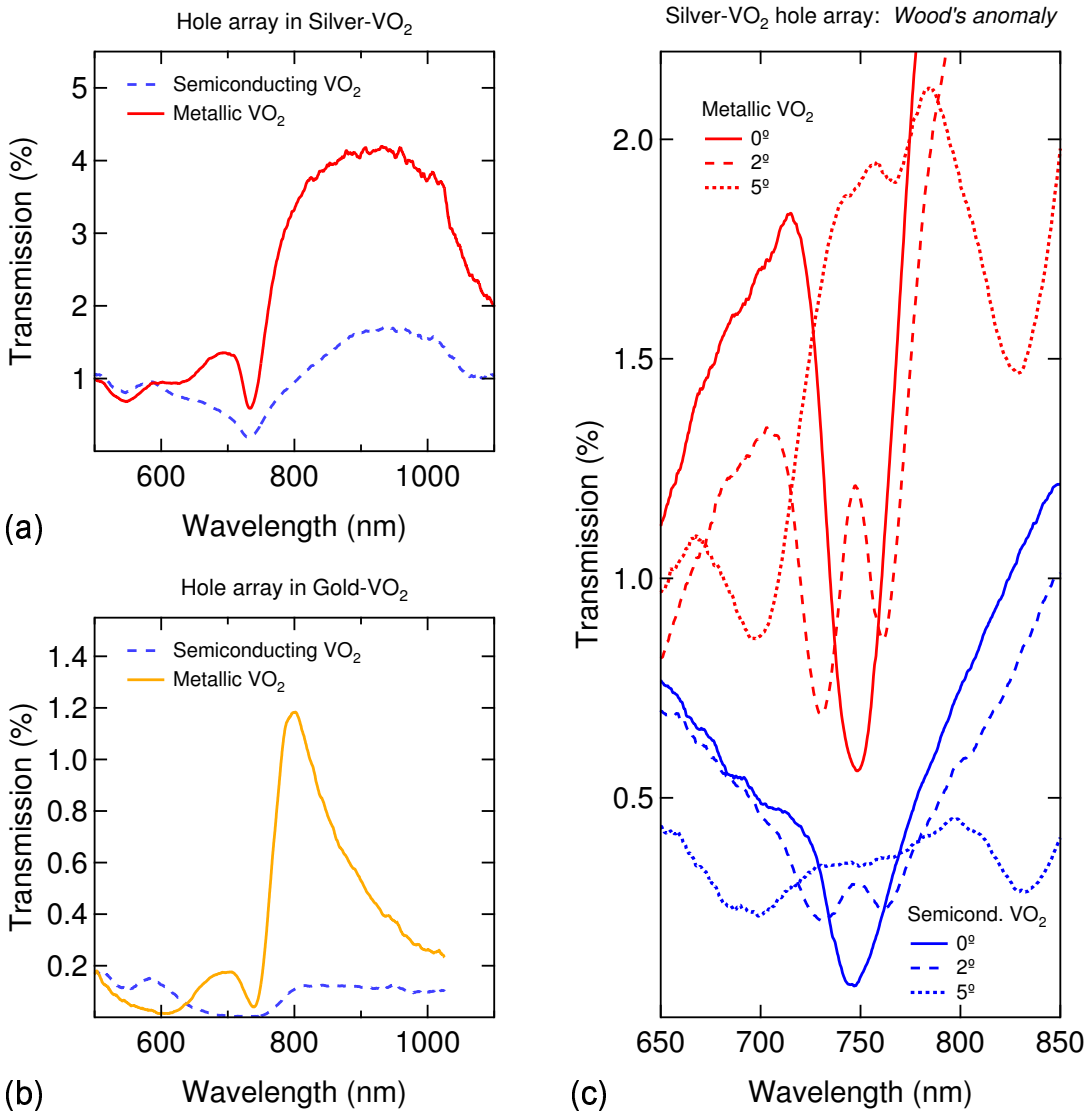

Figure 4.11: Experimental zero-order, normal-incidence transmission spectra for periodic hole arrays in **(a)** Ag-VO_2 and **(b)** Au-VO_2, in each phase of the VO_2 layer. **(c)** Demonstration of spectral splitting of Wood's anomaly minima with deviation from the normal (0^o) angle of incidence (lower/upper set of three curves corresponds to the semiconducting/metallic phase of the VO_2 layer in the Ag-VO_2 nanostructure). Note the *reverse switching* trend, whereby transmission is higher in the metallic phase of the VO_2 layer, contrary to the regular switching of a plain VO_2 film of the same thickness.

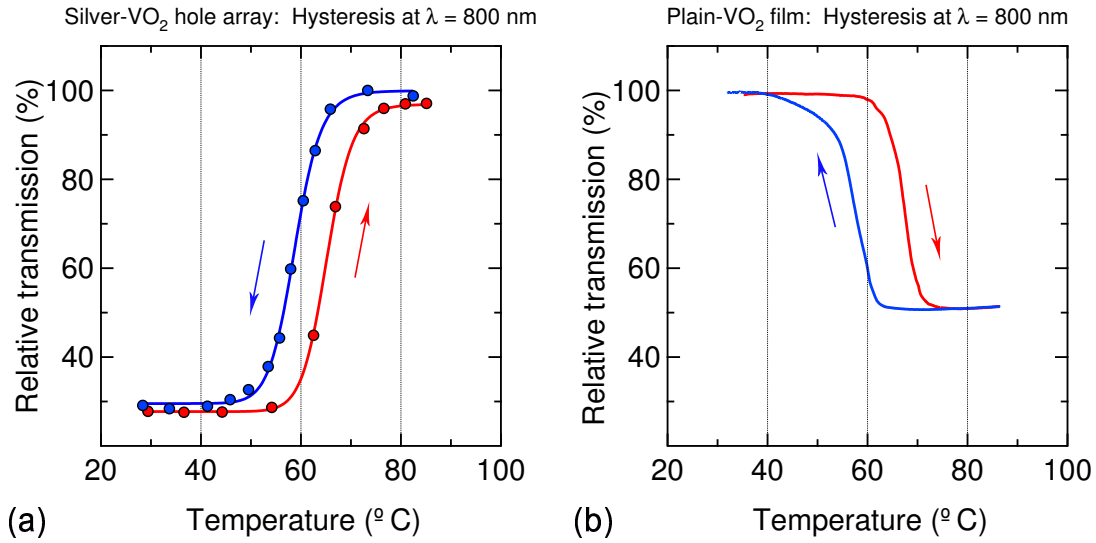

Figure 4.12: **(a)** *Reverse hysteresis* for periodic Ag-VO_2 hole array, normalized to highest transmission in metallic phase of VO_2 layer; upward/downward arrow denotes heating/cooling branch of thermal cycle. **(b)** *Regular hysteresis* for plain VO_2 film, normalized to highest transmission in semiconducting phase; downward/upward arrow denotes heating/cooling branch of thermal cycle.

phase of VO_2 is enhanced over EOT in the semiconducting phase.

Most EOT spectra exhibit sharp minima in the transmission profile, usually preceding the transmission peaks. These minima have routinely been attributed to the so-called *Wood's anomaly* for diffraction gratings,[181] which amounts to the disappearance of a diffracted order as it becomes tangent to the plane of the grating, caused by the accumulation of in-phase scattering events.[182] The spectral positions of the minima are also known as Rayleigh wavelengths. At normal incidence, the first-order Rayleigh wavelength (λ_R) coincides with the grating spacing,[183] that is, with the periodicity of the array. The sharp normal-incidence minima for our samples occur close to 750 nm (Figure 4.11a and 4.11b), which corresponds to the nominal lattice spacing of the hole arrays. As the angle of incidence is increased, the Rayleigh wavelengths for grazing orders should become longer on one side of the sample normal and shorter on the other side.[183] Consequently, we expect the sharp minimum at λ_R to split into two separate minima: one occurring at $\lambda_{R-} < \lambda_R$ and the other at $\lambda_{R+} > \lambda_R$. The experimental observations confirm this prediction. Figure

4.11c shows the splitting of the normal-incidence Wood's anomaly as the sample plane is rotated with respect to the optic axis. The incident light was polarized with the electric field oscillating parallel to the rows of the Ag-VO_2 hole array. Both VO_2 phases exhibit two sharp dips in each of their transmission curves for nonzero angles of incidence (θ_{inc}): for instance, the zero-order transmission at $\theta_{\text{inc}} = 2^{\text{o}}$ has one dip at 730 nm and another at 760 nm, as opposed to the single dip at 750 nm for zero-order transmission at $\theta_{\text{inc}} = 0^{\text{o}}$. In addition, we find once again that EOT in the metallic state of the VO_2 layer exceeds, for all pairs of curves, EOT in the semiconducting state.

4.3.2 Numerical simulations

Numerical simulations of the relevant optical quantities (transmission, reflection, scattering) were undertaken to gain some insight into the origin of the observed reverse switching of the EOT effect. The simulated zero-order transmission spectra for perforated Ag-VO_2 and Au-VO_2 structures are given in Figure 4.13, and those for a perforated single layer of VO_2 (see Section 4.3.4) are given in Figure 4.14(c, d).

The computational scheme used here stems from a numerical method for modelling the properties of patterned photonic crystal slabs, and is described in the work of Tikhodeev *et al.*[149] We also used the complex frequency-dependent permittivity of VO_2 from Reference [57] (Figure 4.1a), and those of Ag and Au from Reference [184]. The *transfer-matrix formalism* employed in the simulations contains the following basic elements:[149] **(i)** in-plane periodicity of the hole array is represented as a Fourier decomposition of the piecewise complex permittivity within each layer in terms of reciprocal square-lattice vectors; **(ii)** the solution of Maxwell's equations in each layer is decomposed into sets of eigenvectors propagating in both directions along the normal to the surface of the structure; **(iii)** *transfer matrices* connect the amplitudes of partial waves at different planar slices of the structure inside the same layer; **(iv)** *interface matrices* connect the partial-wave amplitudes across successive layers of the structure (*e.g.*, crossing from Au into VO_2) by imposing continuity

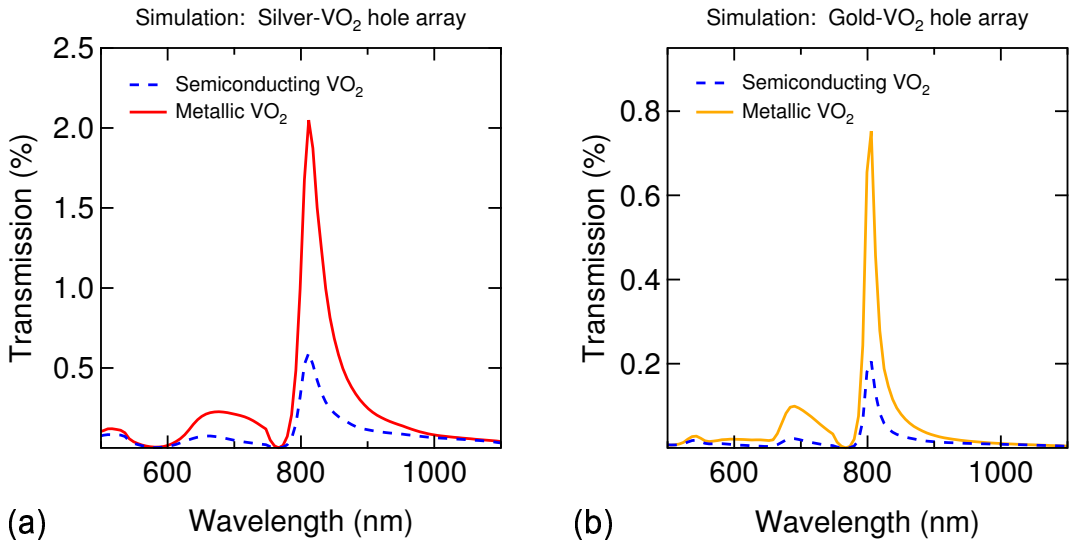

Figure 4.13: Numerical simulations of zero-order, normal-incidence transmission spectra for periodically perforated **(a)** Ag-VO_2 and **(b)** Au-VO_2 double layers on glass, in each phase of the VO_2 layer. The simulated spectra also exhibit the surprising trend of *reverse switching* of VO_2 observed in the experiments.

conditions on the in-plane components of the electric and magnetic fields at the interface; **(v)** *material matrices* convert the partial-wave amplitudes at a given point into in-plane components of electric and magnetic fields at that point. In essence, the goal is to construct a *total transfer matrix* that connects the field amplitudes at different dielectric planes. From knowledge of the total transfer matrix at a given frequency of the incoming light, the reflection, transmission, scattering, and absorption can be computed from the output electromagnetic field components; the computation is then repeated throughout the spectral range of interest.

Despite several simplifications to the model, such as square instead of circular apertures, infinite instead of finite arrays, and a limited number of Fourier components used in representing the in-plane dielectric variation, the simulation results show reasonable qualitative agreement with the corresponding experimental findings. Crucially, the simulations corroborate the key experimental observation of this work, namely, that EOT through perforated Ag-VO_2 and Au-VO_2 nanostructures receives a further enhancement in the near-IR range

when the VO_2 layer becomes metallic. Even though the simulated spectra differ in shape and absolute magnitude from the corresponding experimental curves, they unequivocally demonstrate the effect of *reverse switching* of VO_2.

4.3.3 Why is transmission higher in the metallic phase?

Regarding the reverse-switching effect, we propose the following heuristic explanation. Since the Ag and Au films are optically thick, the incident light cannot traverse the non-perforated areas in the metal-VO_2 hole arrays, as evidenced, for example, by the black regions in Figure 4.8d. Therefore, transmission can only occur through the holes in the metal layer, in the form of evanescent waves generated by diffraction of the incident light at the metal-air interface and mediated mostly by SPPs. The waves emanating from the holes in the metal overlayer undergo additional scattering at the metal-VO_2 interface and must then travel through the perforated VO_2 layer, where they become *leaky evanescent waves*, that is, surface-bound waves that lose intensity as they propagate.[108] The VO_2 material acts as a lossy medium: The evanescent waves penetrate the side walls of the air-filled holes and "leak" into the plane of the VO_2 layer, where partial absorption occurs. As a result, the leakage channels a portion of the light away from the zero-order transmission path and thus renders it undetected in the far field. As discussed in Section 4.3.4 below, the amount of light that penetrates into the VO_2 material between the holes evidently depends on the optical constants of metallic or semiconducting VO_2 and, in particular, on the permittivity contrast between the hole content (air) and its surroundings (VO_2). Besides mitigating the leakage of evanescent waves into the VO_2 layer, a lower permittivity contrast also seems to reduce the diffuse scattering from the holes at the air and glass interfaces;[185] conversely, higher permittivity contrast increases those losses. In the near-IR wavelength range, the permittivity of metallic VO_2 differs considerably from its semiconducting counterpart (Figure 4.1a): at $\lambda = 850$ nm, for example, $\tilde{\varepsilon}\{VO_2{-}\text{met.}\} = 2.67 + 2.98\text{i}$, while $\tilde{\varepsilon}\{VO_2{-}\text{semi.}\} = 8.17 + 2.65\text{i}$. Therefore, because the permittivity contrast between the

air interior and the VO_2 exterior of the holes is lower in the case of metallic VO_2, the high-temperature EOT receives an enhancement over the low-temperature EOT.

4.3.4 Periodic single-layer hole array: Role of perforated VO_2

In order to bring out the significance of the VO_2 layer for the metallic-phase enhancement of EOT in the Ag-VO_2 and Au-VO_2 hole arrays, we also examined the optical properties of a hole array in a single VO_2 film on glass (Figure 4.8a), that is, without a noble-metal overlayer, as described in our Reference [124]. It must be noted that transmission observed through this type of structure is not *extraordinary* in the sense used thus far, owing to the insufficient opacity of the VO_2 layer for direct transmission and its inability to support SPP modes in the wavelength region of interest, since $\Re\mathrm{e}\,[\tilde{\varepsilon}_{\mathrm{met.}}(\lambda < 1.2\ \mu\mathrm{m})] > 0$ (Figure 4.1a).

Figure 4.14a compares the zero-order transmission of a hole array and a non-perforated (plain) area nearby, in the *semiconducting phase* of the same VO_2 film. The hole array transmits less than the intact film throughout the wavelength range because the array diffracts some of the incident intensity away from the detector path, which then cannot contribute to the zero-order transmission. Similarly to the loss mechanisms discussed above (Section 4.3.3), a portion of the diffracted field becomes trapped as leaky waves in the plane of the VO_2 layer, while some of the light that persists in the zero order inside the holes undergoes additional diffuse scattering at the glass interface. Also, since direct transmission through the partially transparent VO_2 film overwhelms the transmission emerging from the holes, the exit apertures appear darker than their surroundings in the aforementioned SNOM image of semiconducting-phase transmission through the VO_2 array (Figure 4.8c).

Figure 4.14b presents the corresponding transmission curves for the *metallic phase* of the VO_2 layer. Here, something intriguing happens in the near-IR range: Despite diffraction/scattering, the zero-order transmission through the hole array exceeds the direct transmission through the plain film. This subtle observation prompted further exploration of the optical behavior of perforated VO_2.

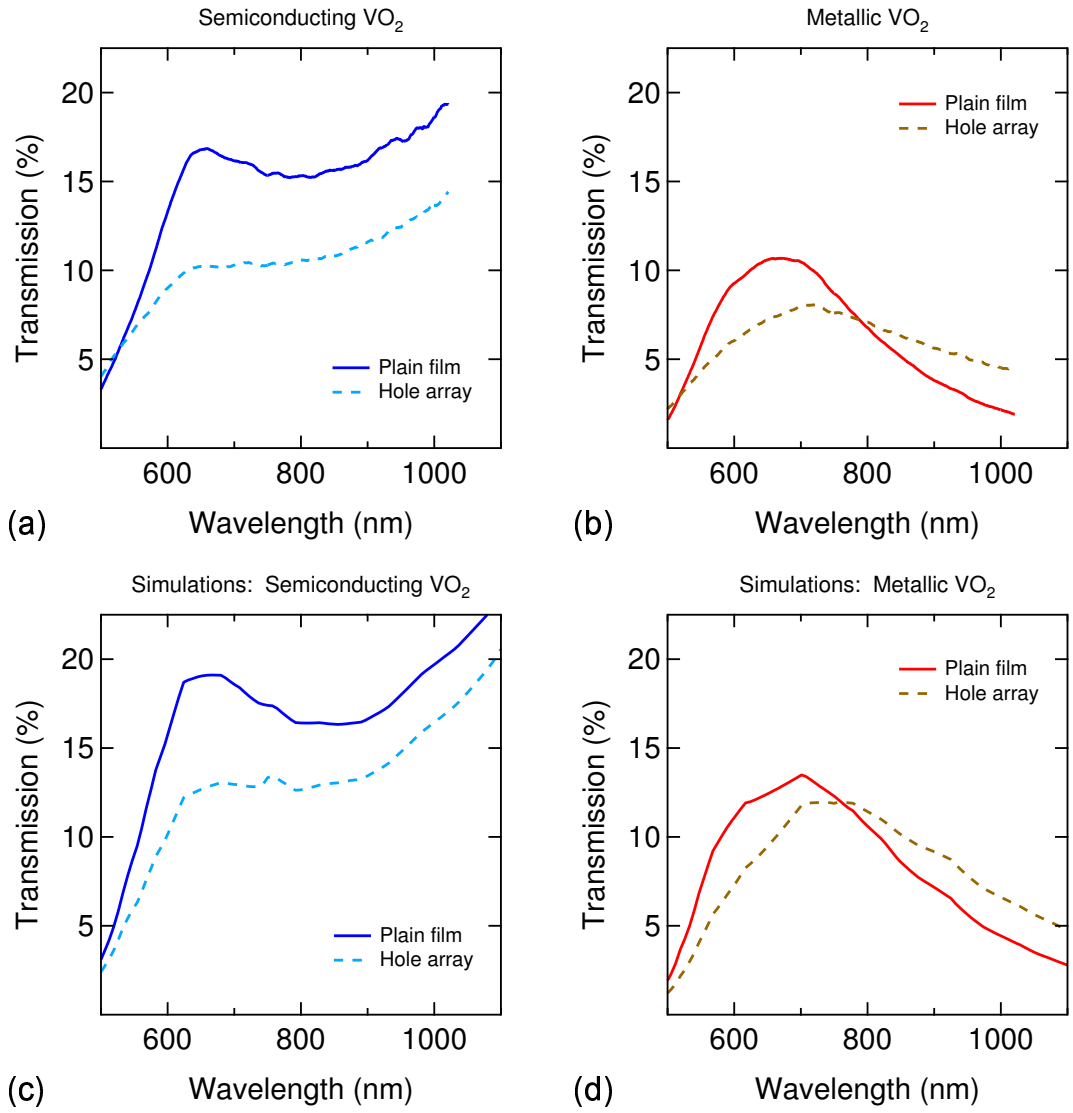

Figure 4.14: **(a, b)** Experimental and **(c, d)** simulated zero-order transmission spectra for plain and periodically perforated single layer of **(a, c)** semiconducting and **(b, d)** metallic VO_2 on glass. Note the crossover region in the metallic-phase spectra.

Using the numerical technique described earlier (Section 4.3.2), we also performed simulations of transmission, reflection, scattering, and absorption for a perforated as well as plain VO_2 film. The zero-order transmission spectra are shown in Figure 4.14c for the semiconducting phase and 4.14d for the metallic phase of the VO_2 film. The simulations reproduce the experimental data quite well; in particular, the simulated curves for the metallic phase show the characteristic crossover in the near-IR region, where the perforated

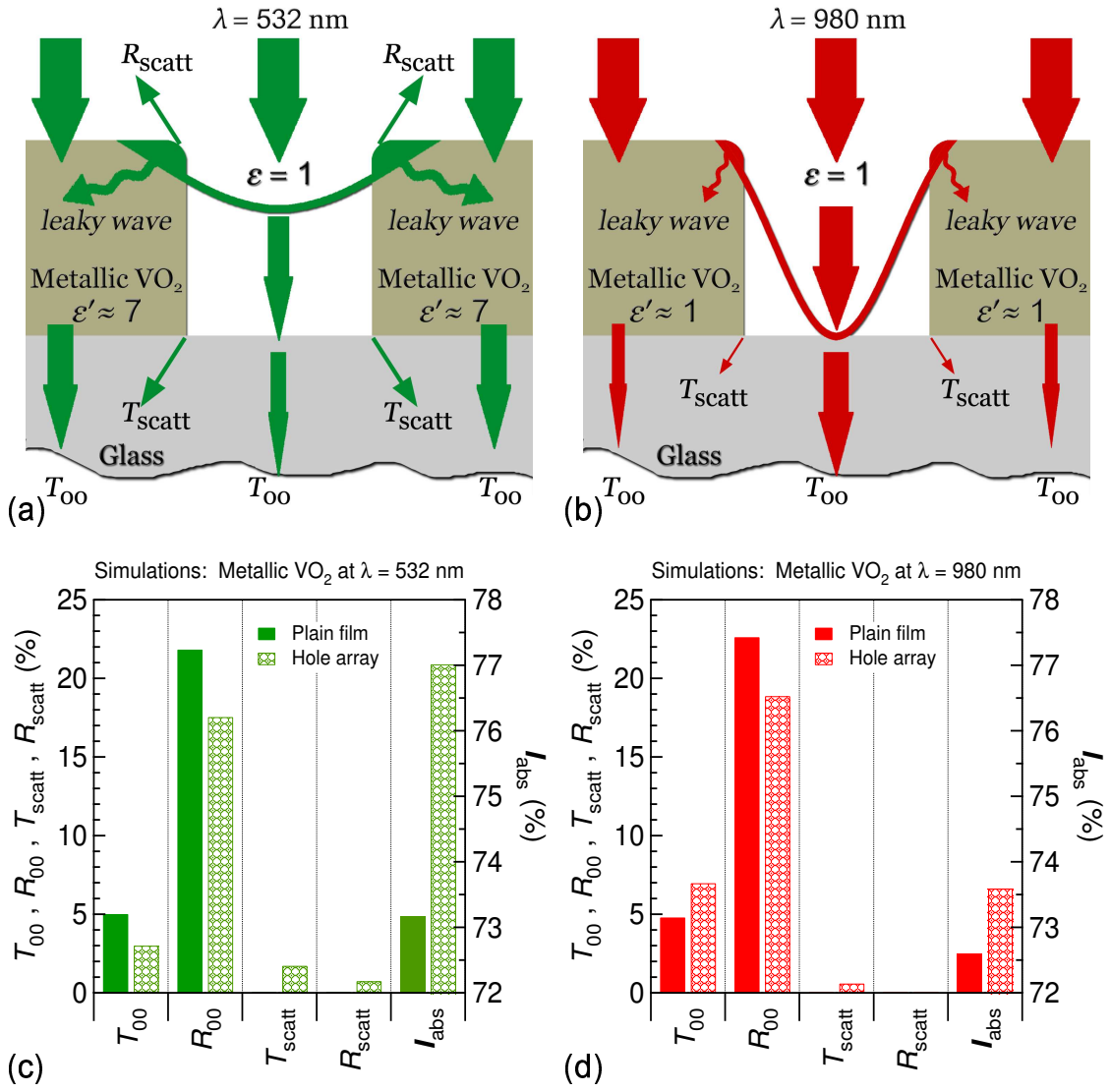

Figure 4.15: Schematics of **(a)** green (λ = 532 nm) and **(b)** near-IR (λ = 980 nm) light propagation through a hole in metallic-phase VO_2 film on glass. Simulated optical quantities for perforated (hatched bars) and plain (solid bars) metallic-phase VO_2 film for **(c)** green and **(d)** near-IR light. According to our model, lower dielectric contrast between the interior (air, $\varepsilon = 1$) and exterior (VO_2, $\varepsilon' \approx 1$) of each hole for metallic VO_2 in the near-IR range reduces the losses from leaky-waves absorption (part of I_{abs}) and diffuse scattering ($T_{\text{scatt}} + R_{\text{scatt}}$), to the extent that T_{00} through the array exceeds T_{00} through the film (direct transmission). *Legend*: $T_{00} \equiv$ zero-order transmission; $R_{00} \equiv$ specular reflection; $T_{\text{scatt}} \equiv$ forward diffuse scattering; $R_{\text{scatt}} \equiv$ backward diffuse scattering; $I_{\text{abs}} \equiv$ absorption (right-side scale) = $100\% - T_{00} - R_{00} - T_{\text{scatt}} - R_{\text{scatt}}$.

VO_2 film transmits more per unit area than the plain film. In fact, it was these simulations for perforated *vs.* plain VO_2 that led us to the explanation (Section 4.3.3) that the reverse switching of the EOT effect results from the permittivity contrast ($\Delta\varepsilon$) between the air-filled hole interiors and the surrounding VO_2 material, which differs considerably not only for the two VO_2 phases but also for different wavelengths in the metallic phase alone (Figure 4.1a).

Thus, higher $\Delta\varepsilon$ brings relatively large losses due to scattering ($T_{\text{scatt}} + R_{\text{scatt}}$) from the apertures[185] and leakage of evanescent waves[108] into the plane of the VO_2 layer (part of I_{abs}), as depicted schematically in Figure 4.15a for metallic-phase VO_2 at a visible wavelength (λ = 532 nm). Conversely, lower $\Delta\varepsilon$ reduces these losses—hence the smaller leaky-wave and scattering arrows in Figure 4.15b, which refers again to metallic-phase VO_2 but at a near-IR wavelength (λ = 980 nm). Therefore, when surrounded by a material of similar real-part permittivity, such as metallic VO_2 in the near-IR, the air-filled holes tend to "funnel" light along the forward direction by reducing the losses due to undetected components of the total optical field, namely leaky waves and diffuse scattering, all to the benefit of the detected zero-order transmission (T_{00}). Furthermore, in comparison with the plain film, the hole array experiences smaller specular reflection (R_{00}) and smaller *direct* absorption (the rest of I_{abs}) in either phase, since a portion of the incident light encounters apertures instead of VO_2 material. Ultimately, when the scattering and absorption losses for the hole array have decreased enough with respect to those for the plain film, T_{00} through the holes prevails over T_{00} through the non-perforated area of the film, and a crossover occurs in the transmission spectra (Figure 4.14(b, d)).

The relative magnitudes of T_{00}, R_{00}, T_{scatt}, R_{scatt}, and I_{abs} (right-side vertical axes) are charted in Figure 4.15(c, d) for plain and perforated VO_2 in the metallic phase, each at the visible and near-IR wavelengths mentioned above. As also noted above, R_{00} for the plain film exceeds R_{00} for the hole array. Conversely, I_{abs} for the array is appreciably greater than I_{abs} for the plain film at the visible wavelength (Figure 4.15c), while in the near-IR the

two absorption magnitudes are very similar (Figure 4.15d) because the effect of the leaky waves is reduced. In the latter case, since the plain film reflects specularly (R_{00}) more than the hole array and since the total diffuse scattering of the array is rather small (T_{scatt} only, as $R_{\text{scatt}} = 0$ for $\lambda \geq 750$ nm), conservation of energy requires that the hole array transmit *more* in the zero order than the plain film (cf, T_{00} bars in Figure 4.15d).

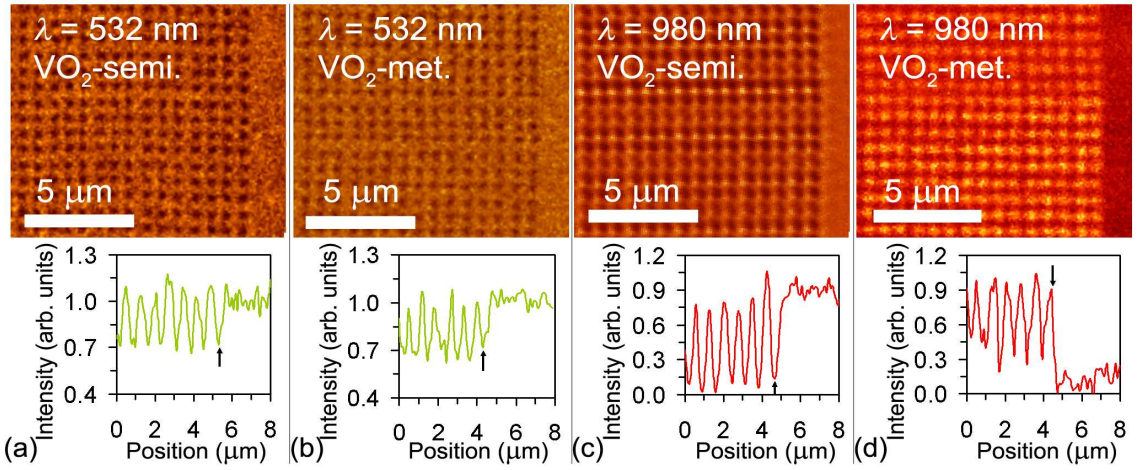

Figure 4.16: Top half: SNOM images of far-field transmission through VO_2 hole array under near-field illumination with **(a, b)** green ($\lambda = 532$ nm) and **(c, d)** near-IR ($\lambda = 980$ nm) laser, during **(a, c)** semiconducting and **(b, d)** metallic phase of VO_2. **Bottom half:** For each image above, plot of intensity as a function of position along part of a row of holes and extending into non-perforated area; rightmost hole indicated by arrow in each plot. Note that it is only in **(d)** that the holes "light up", that is, transmit more than the surrounding areas.

Perhaps most revealing of all are the SNOM image scans (Figure 4.16) of far-field transmission through individual holes and non-perforated areas, obtained under near-field incident illumination with green ($\lambda = 532$ nm) and near-IR ($\lambda = 980$ nm) laser light. Below each image in Figure 4.16 is a plot of the detected intensity along part of a row of apertures and extending outside the array into the plain, non-perforated film. The relative position of the rightmost aperture is marked by an arrow in each plot. For *semiconducting* VO_2 (Figure 4.16(a, c)), the intensity reaches local minima within the apertures relative to the intensity

through the plain film, indicating a leakage path through the film at both wavelengths. These observations corroborate the spectral measurements and simulations of T_{00} for semiconducting VO_2 (Figure 4.14(a, c)) by demonstrating that the air-filled holes transmit *less* than the plain film for both visible and near-IR illumination. For *metallic* VO_2, the holes transmit less than the surrounding film only under visible-light illumination (Figure 4.16b). In the near-IR range, however, the intensity contrast is reversed, so that more light emerges from each hole than from an equal-area spot on the intact film (4.16d). The overall effect of this behavior manifests itself in the transmission spectra for metallic-phase VO_2, discussed earlier in reference to Figure 4.14(b, d), where the crossover signifies that T_{00} through the hole array exceeds the direct transmission through a non-perforated area of the film.

4.3.5 Randomized double-layer hole array

Finally, we return to one of the perforated double-layer structures (Section 4.3.1), but with a twist: *randomly* distributed holes in gold-VO_2 (Figure 4.17), with the same nominal hole diameter and areal hole coverage as in the periodic Au-VO_2 array (Figure 4.9). The purpose of measuring the transmission of a randomized hole array was to reinforce our claim that the reverse switching we observed in the case of periodic metal-VO_2 arrays was caused by reduction in the permittivity contrast *inside* the holes and not between the two interfaces of the noble-metal film. The effect of the latter was discussed earlier in connection with Figure 4.7, where matching the refractive indices of the input and output interfaces produced a stronger EOT effect. On the other hand, a randomized hole array cannot sustain coherent surface modes due to the lack of periodicity, and hence no extraordinary transmission is expected as the EOT effect relies on in-phase multi-scattering and interference processes between neighboring rows in a periodic hole array.[144] Indeed, the transmission spectra of our randomized Au-VO_2 holes (Figure 4.18) differ qualitatively from the EOT spectra of the periodic array in the same double-layer film (Figure 4.11b). Instead of a sequence of relatively sharp dips and peaks, the random-holes spectra exhibit

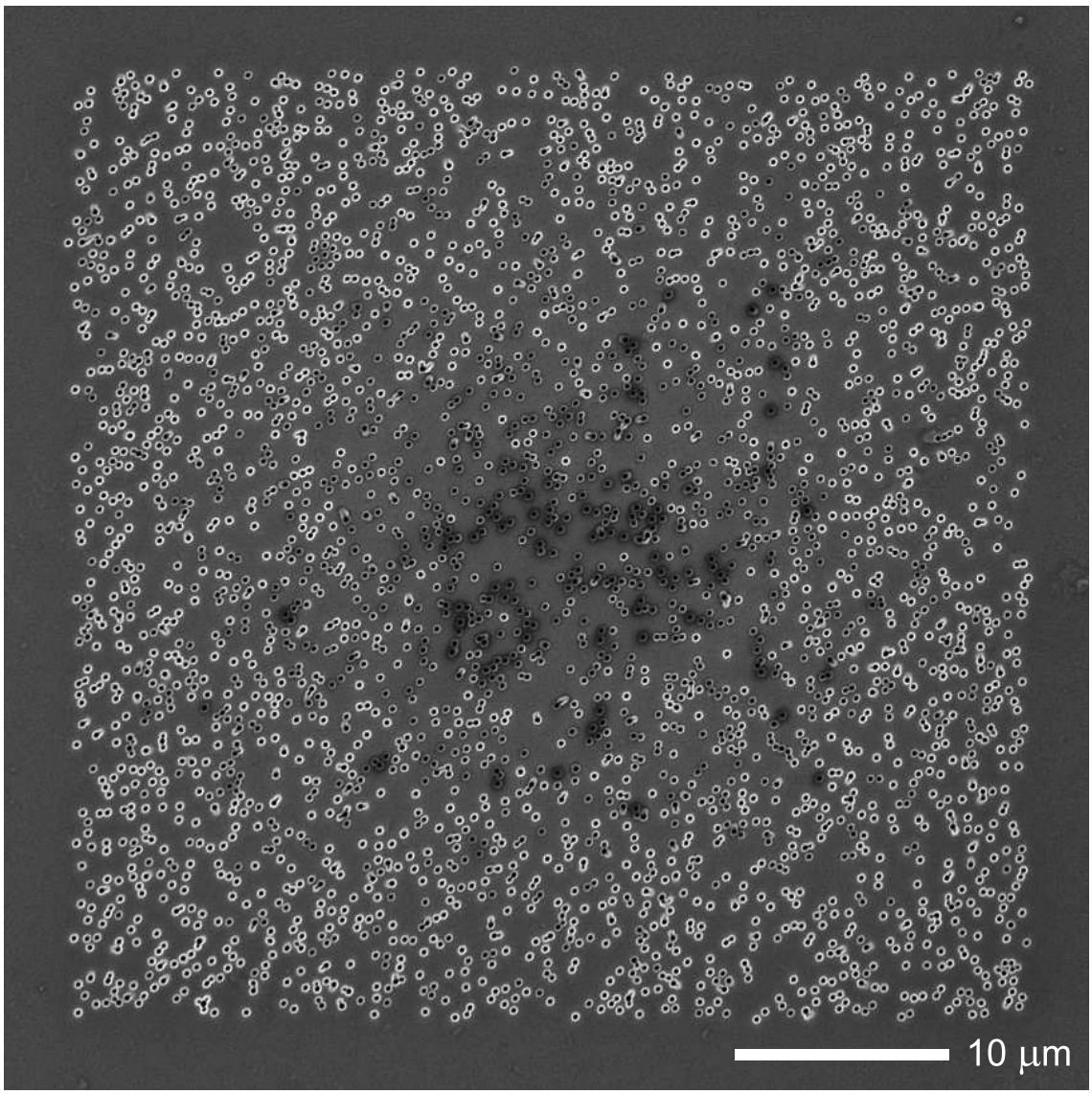

Figure 4.17: FIB micrograph of randomized array of 3600 circular holes in Au-VO_2 double layer on glass. *Parameters*: $d = 250$ nm, $t_{Au} = 230$ nm, $t_{VO_2} = 200$ nm.

a rather broad peak reminiscent of the transmission of an isolated hole in a metal film, which can be attributed to the excitation of a localized surface-plasmon resonance (LSPR) at the aperture ridge.[175,186] The crucial finding here is that the random-holes transmission is also reversed—the holes transmit more in the metallic phase of the VO_2 layer (Figure 4.18), independently of the EOT phenomenon. To recapitulate, our model attributes this reversal to the *reduction of losses* from diffuse scattering and leaky waves for metallic-phase

VO_2 at near-IR wavelengths, by virtue of the lower permittivity contrast between air and VO_2 (Figure 4.19).

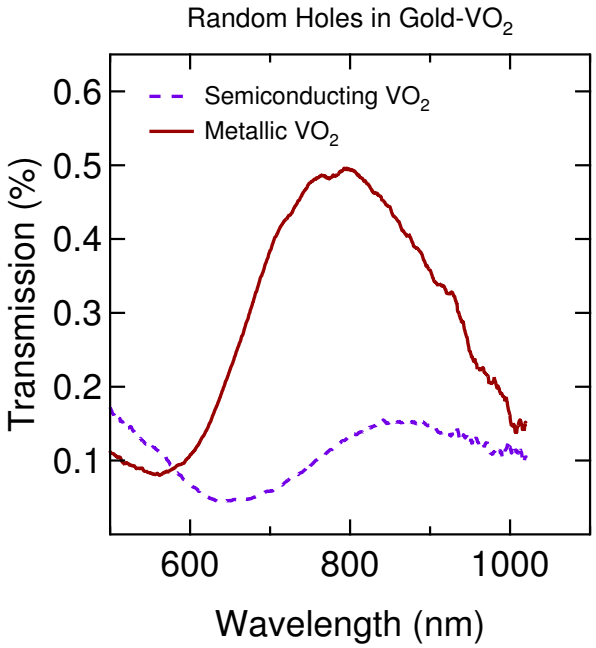

Figure 4.18: Experimental zero-order, normal-incidence transmission spectra, in each VO_2 phase, for randomized hole array in Au-VO_2 double layer. Note that the random holes also exhibit the *reverse switching* effect.

4.3.6 Prospects for all-optical modulation of EOT

Since the electronic response of the plasmonic material in these structures is fast on the femtosecond timescale, it is logical to ask whether the EOT effect can likewise be modulated on an ultrafast timescale. Experiments by Cavalleri *et al.* on VO_2 films show that hole doping effected by a femtosecond laser pulse can initiate the semiconductor-to-metal transition (SMT) within a few hundred femtoseconds.[187] The details of the ultrafast response, however, are dependent on the thickness of the film. More recent X-ray studies seem to indicate that for 800-nm incident laser light, the turn-on response of the film is

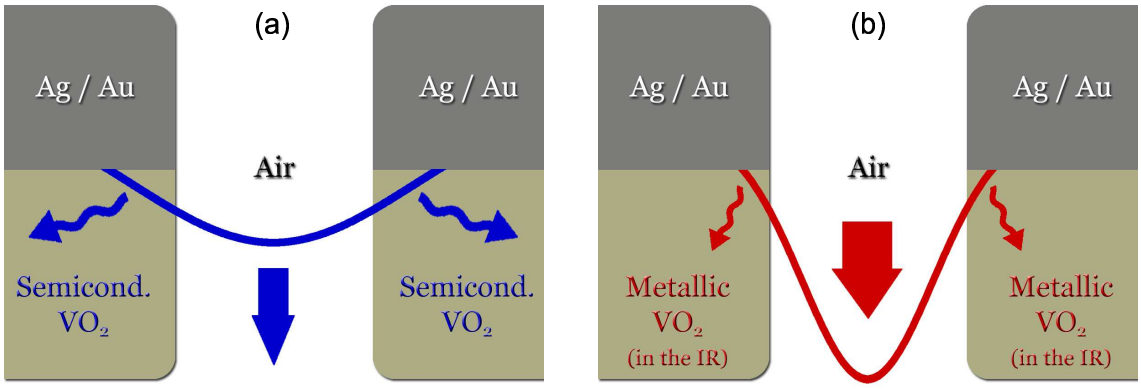

Figure 4.19: Schematics of transmission through hole in Ag/Au-VO_2 structure during the **(a)** semiconducting and **(b)** metallic phase of the VO_2 layer. The zero-order transmission is higher in the metallic-phase of the VO_2 layer because of the lower permittivity contrast between the hole interior ($\varepsilon_{\text{air}} = 1$) and the surrounding VO_2 (*e.g.*, $\varepsilon'\{met.\ VO_2 @ 980\ \text{nm}\} \approx 1$ *vs.* $\varepsilon'\{semi.\ VO_2 @ 980\ \text{nm}\} \approx 9$).

extremely fast for film thicknesses of 70 nm or less, but diffusive after that.[31] This ultrafast response depth is, of course, a function of the excitation wavelength, and it is possible that a laser wavelength with greater penetration depth in VO_2 could achieve ultrafast SMT initiation for thicker films. The response time also appears to be a function of fluence, with important dynamical features showing a differentiated response below the 100-fs timescale.[69]

The more challenging question for ultrafast modulation is whether or not the SMT can be turned off at a fast timescale. Evidence so far indicates that the return from the metallic to the semiconducting phase occurs on nanosecond or sub-nanosecond time scales, governed essentially by thermal diffusivity.[188,189] While the metallic state relaxes on a sub-picosecond timescale for near-threshold densities of photo-initiated electron-hole pairs, the relaxation times increase significantly with increasing electron-hole plasma density, even for rather thin VO_2 films on diamond substrates.[1] In the case of our double-layer plasmonic structures, it is nevertheless plausible that the thermal conductivity of the noble metal would assist the cooling transition back to the semiconducting state. Hence the question of possible ultrafast turn-on *and* turn-off of plasmonic effects remains open.

4.4 Summary

In generic terms, the future of optoelectronic devices relies on the ability to manipulate light on a subwavelength scale, where diffraction-limited optical components lose their utility. Here we have presented a novel way to control the *extraordinary optical transmission* through subwavelength hole arrays in structures composed of a VO_2 thin film sandwiched between an opaque metal layer and a transparent substrate. The control mechanism relies on the thermally induced metal-semiconductor transition of VO_2, but the transition can take place on a sub-picosecond timescale if triggered by a laser pulse, which opens the possibility for ultrafast switching devices. The present work has uncovered a counterintuitive trend in the near-IR transmission properties of the perforated VO_2 layer when compared to a continuous VO_2 film of the same thickness, which we call *reverse switching*. Under these conditions, the zero-order transmitted intensity from perforated Ag-VO_2 or Au-VO_2 double layers on glass is, in fact, considerably higher during the metallic phase of the VO_2 material than it is during the semiconducting phase. A simple heuristic model seems sufficient to account qualitatively for this effect, based on the idea that the losses in the zero-order transmission are caused by evanescent waves with varying leakage into the VO_2 layer, depending on the VO_2 state; in addition, diffuse scattering at the entrance and exit apertures also contributes. The magnitude of these losses increases with higher permittivity contrast between the interior and exterior of the holes. The role of metallic VO_2 in further enhancing the EOT from perforated silver or gold films has been emphasized by comparing measurements on perforated and non-perforated areas of the same VO_2 film, which showed that the zero-order high-temperature transmission through a VO_2 hole array can exceed the direct transmission through the flat film. A major point in the qualitative model is that the holey films with nanoscale dimensions, with or without the metal, constitute a very large effective interfacial area for the incident photons. The observed effects are thus directly related to the ability to construct such nanoscale structures.

CHAPTER V

CONFOCAL RAMAN MICROSCOPY ACROSS THE STRUCTURAL PHASE TRANSITION OF SINGLE VO_2 NANOPARTICLES

Abstract

The first Raman scattering measurements on nanoparticulate vanadium dioxide (VO_2) are presented here, as well as the first observations of the temperature-induced phase transition in *individual* VO_2 nanoparticles (NPs). We compare the Raman response of two VO_2 NPs and a companion VO_2 film undergoing their monoclinic-tetragonal-monoclinic transformations, and offer qualitative explanations for the large observed differences in hysteresis width. While bulk crystals and contiguous films contain numerous "potent" nucleation sites, individual NPs likely harbor only a few, which may make it possible to correlate detectable defects (*e.g.*, grain boundaries, dislocations) with the "ease" of switching phases as quantified by the width of the thermal hysteresis.

5.1 Introduction

Vanadium dioxide (VO_2), a transition-metal compound, has intrigued researchers for almost five decades since Morin[21] first discovered its temperature-driven metal-insulator transition ($T_c \approx 67$ °C). Accompanying the electronic transition is a change in crystallographic structure, from monoclinic (insulator/semiconductor) below T_c to tetragonal/rutile (metal).[22,23] The long-standing debate[25–29] over the relative roles of lattice distortion and electron-electron correlation in the mechanism of the VO_2 phase transition has lately been reinvigorated, both theoretically[30,55] and experimentally.[1–3,31,32] Furthermore, the overall scientific drive towards understanding how materials behave on the nanoscale and, specifically, how phase transitions occur in nanocrystalline systems,[10,16,37–39,41] has sparked in-

terest in making and probing nano-VO_2: thin films of nanosized grains[3,45–49] or intertwined nanorods;[190,191] thin films structured on silica microspheres[100] or perforated by nanoholes;[148] nanocrystalline powders;[192,193] ensembles of implanted,[50–52,54] grown,[194] or lithographically patterned nanoparticles (NPs).[9,53] In the present work, we cross the next frontier by investigating the structural phase transition of *individual* VO_2 NPs, which paves the way to pinpointing the elusive sources of the VO_2 phase transition—those "potent" defect sites deemed responsible for nucleating the new phase inside the old.

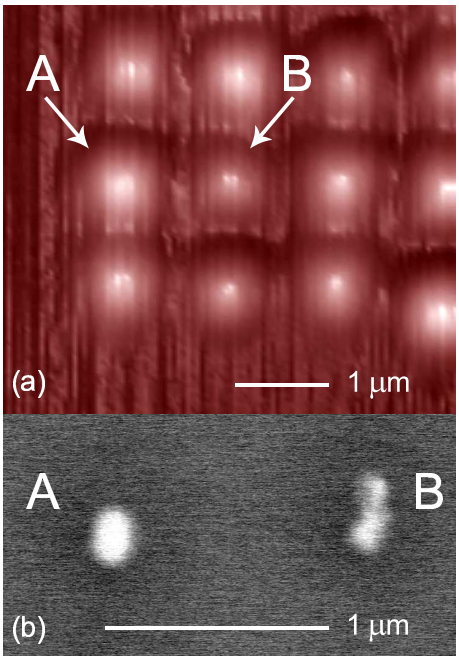

Figure 5.1: **(a)** Confocal image scan acquired at $\lambda = 633$ nm and **(b)** scanning electron micrograph (SEM) of VO_2 nanoparticles (NPs) on Si. Note the different morphologies of NP "A" and "B".

Using confocal microscopy, we probed as a function of temperature the Raman response of two single VO_2 NPs (Figure 5.1) and a companion ("witness") patch of contiguous VO_2 film, all on the same silicon (Si) substrate. This technique is well suited to interrogating structural changes in submicron particles because confocal scanning allows high-contrast imaging of an isolated NP, while Raman scattering identifies the lattice configuration of the

NP via the spectral signature of vibrational excitations. The Raman peaks of monoclinic and tetragonal VO_2 have been reported for bulk crystals and thin films;[31,195–201] we present here the first Raman measurements on NPs of VO_2 (Figure 5.3). Monitoring the evolution of the Raman intensity with temperature furnished the hysteresis loops characteristic of the first-order phase transition of VO_2, which proved much wider for the NPs than for the witness film (Figure 5.4). To explain the three different hysteresis widths observed in this study, we recall the model of heterogeneous nucleation of the VO_2 phase transition[5] that accounted for the size-dependence of the hysteresis in ensembles of VO_2 NPs[9,50] (see also Section 1.3.2).

5.2 Experimental details

We fabricated our VO_2 NPs on a Si substrate by means of: **(i)** focused-ion-beam lithography (FIB: 30-keV Ga^+, 1-pA beam current, 100-μs dwell time per NP) in a spin-coated layer of poly(methyl-methacrylate) (PMMA: 50-nm thickness), followed by chemical removal of the exposed areas;[9,53] **(ii)** pulsed-laser deposition (PLD: KrF excimer laser at $\lambda = 248$ nm, fluence ≈ 3 J·cm^{-2}, V-metal target, O_2 gas at 5 mtorr) of amorphous, sub-stoichiometric vanadium oxide ($VO_{1.7}$, 30-nm thickness); **(iii)** chemical lift-off of the remaining PMMA and its $VO_{1.7}$ overlayer; **(iv)** thermal anneal (450 °C, O_2 gas at 250 mtorr) of the resulting arrays of $VO_{1.7}$ clusters to crystalline VO_2 NPs. This procedure has been demonstrated by multiple tests of stoichiometry, structure and switching properties to produce VO_2 rather than any of the multiple competing vanadium oxides.[45] The lattice constant of the NP array was chosen large enough, about 1 μm, to ensure that individual NPs could be resolved in a confocal image scan at the laser wavelength to be used for Raman measurements. One such scan is shown in Figure 5.1a, with arrows pointing to the two VO_2 NPs later probed as a function of temperature. Those NPs were selected because a scanning electron micrograph (SEM) had revealed clear differences in their morphology (Figure 5.1b), which we suspected might lead to different phase-transition behaviors. For comparison, we also measured the

Raman response of a "witness" patch of non-patterned VO_2 film on the same sample.

The sample was excited with a continuous-wave laser light (He-Ne: $\lambda = 633$ nm, 45 mW output power), fed through a monomode fiber into a scanning near-field optical microscope (SNOM) operating in confocal-reflection mode, then focused onto the sample with a micro-objective (60 X, NA = 0.80, $1/e^2$ beam spot ≈ 0.5 μm). The light scattered from the VO_2 NPs or witness film and the Si substrate was collected by the same micro-objective (backscattering geometry), filtered to reduce the elastic-scattering component, and sent through a multimode fiber to a spectrometer equipped with a cooled charge-coupled-device (CCD) detector. In order to minimize laser heating of the sample, the incident beam was attenuated before entering the microscope. The external sample temperature was controlled (± 0.5 ^{o}C) via a thermoelectric heater and a thermocouple attached to the substrate surface.

Raman measurements were performed at several fixed temperatures as follows: **(i)** the sample was manually positioned using micrometers to bring the approximate area of interest into the laser beam spot, as imaged onto a CCD camera under concurrent white-light illumination; **(ii)** the focus was visually adjusted by vertical displacement of the microscope head; **(iii)** the setup was then switched to confocal mode, whereby the piezoelectric sample stage would be scanned at increasing resolution and fine-adjusted laterally until the NP of interest occupied the center of a 2x2-μm^2 image scan; **(iv)** as needed, the focus was also fine-tuned to yield a better object-to-substrate contrast; **(v)** finally, a 10-min Raman spectrum was collected. The sample was then heated up or cooled down, and the measurement sequence repeated at the next temperature point.

5.3 Results and discussion

5.3.1 Raman spectra

Figure 5.3 shows Raman spectra collected from the three VO_2-on-Si objects under investigation: witness film patch, misshapen particle "B", and spheroidal particle "A". The complete spectra (*e.g.*, see Figure 5.2) contain several peaks that match Stokes lines as-

signed in the literature to monoclinic VO_2 (*e.g.*, see Reference [201]), along with peaks belonging to the Si substrate (305 and 520 cm^{-1}). The peaks near 195 cm^{-1} and 225

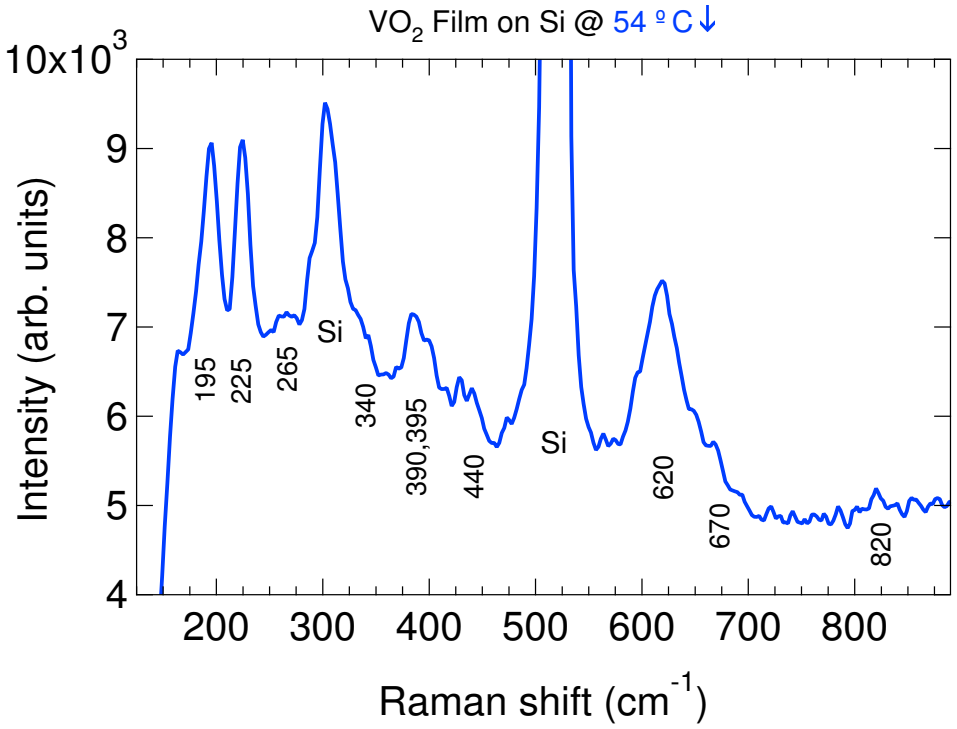

Figure 5.2: Representative Raman spectrum of the witness film in the monoclinic (low-temperature) phase, showing several characteristic VO_2 peaks and two Si-substrate peaks.

cm^{-1} correspond to characteristic A_g-symmetry vibrational modes of the monoclinic (low-temperature) structure of VO_2, which vanish upon transition into the tetragonal (high-temperature) phase.[195–197,201] These phonon modes play a crucial role in the structural transition of VO_2, since they are associated with the pairing and tilting motions of V–V dimers that map the monoclinic onto the tetragonal lattice configuration.[31] In addition, the complete disappearance of the 195 cm^{-1} peak at sufficiently high temperatures indicates that our VO_2 material does not contain measurable amounts of the V_2O_5 phase,[198] the terminal oxidation state of vanadium, which has a distinctive Raman line at 196 cm^{-1}.

Figure 5.3a presents snapshots of the temperature evolution of Raman intensity collected from each VO_2 object during heating of the sample towards the tetragonal phase. Only 2 °C above the bulk transition temperature of VO_2 (67 °C), the witness film no longer exhibits the monoclinic structure, as evidenced by the vanishing of the two A_g-peaks (top trace), which were present at room temperature (not shown). Similarly, NP "B" has also changed its structure, but not until a higher temperature of 75 °C (middle trace). Nanoparticle "A", however, has retained the monoclinic signature even at 75 °C (bottom trace)—a clear thermal delay in the onset of its monoclinic-to-tetragonal transition with respect to the transitions of NP "B" and the witness film.

Raman spectra representative of the cooling half-cycle for each VO_2 object are shown in Figure 5.3b. The temperature was ramped down from a high-enough value to ensure completion of each object's forward (monoclinic-to-tetragonal) transition. At 54 °C, the witness film has already reverted to the monoclinic phase (top trace), while the A_g-peaks for either NP have not yet reappeared (not shown). For NP "B", they reappear by 46 °C (middle trace), but NP "A" remains tetragonal down to at least 33 °C (bottom trace). Thus, the onset of the reverse (tetragonal-to-monoclinic) transition of NP "A" is also delayed in temperature compared to the transitions of NP "B" and the witness film.

We note in passing that the Si peak at 305 cm^{-1} diminishes slightly above the VO_2 phase transition, most likely because of the vanishing of an underlying peak of monoclinic VO_2, usually reported around 310 cm^{-1}.[195,197–201]

5.3.2 Thermal hystereses of the Raman intensity

For each of the three VO_2 objects, Figure 5.4 reveals the full temperature evolution of the Raman response through the thermal hysteresis that accompanies the first-order phase transition. The data points correspond to the total Raman intensity in the spectral interval containing both VO_2 peaks, summed between 165 and 255 cm^{-1} after background subtraction. The background was removed using an algorithm implementing a rolling-circle

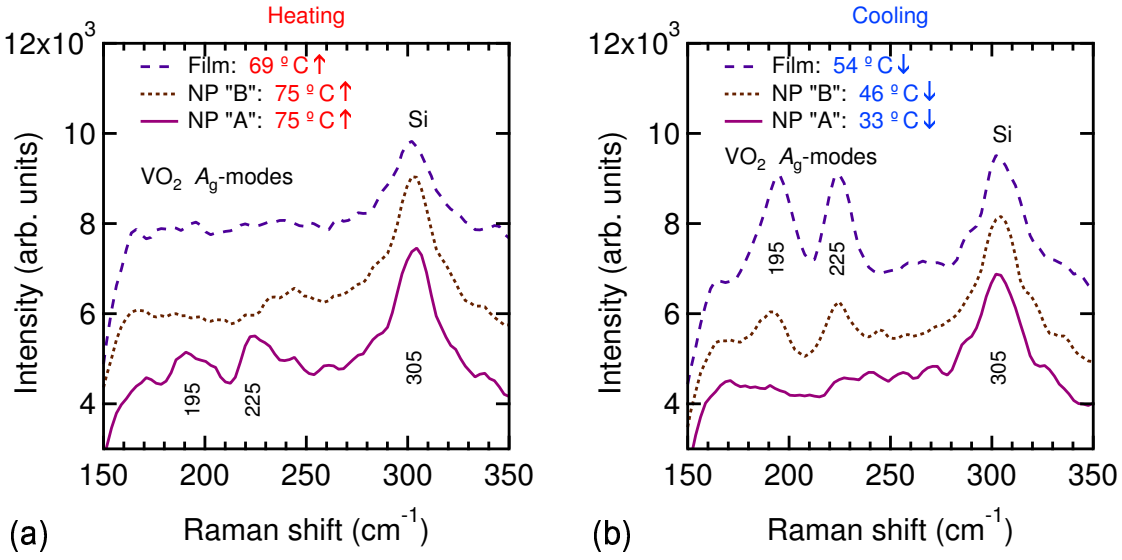

Figure 5.3: **(a)** During heating (↑) towards the tetragonal (high-temperature) phase, the witness film and NP "B" complete the structural transition (A_g-modes vanish) before 69 and 75 °C, respectively, while NP "A" remains at least partly untransformed at 75 °C. **(b)** During cooling (↓) from the high-temperature phase, NP "A" again lags thermally behind the film and NP "B" in switching back to the monoclinic phase.

spectral filter, which distinguishes between peaks and baselines according to their radii of curvature.[202] The comparatively large scatter in Figure 5.4b likely stems from a variable overlap between the laser beam spot and the irregular shape of NP "B" (Figure 5.1b) during different measurement sequences. The smooth lines through the data, used to estimate the transition mid-points (T_{half}) for the heating and cooling branches of each hysteresis loop, were obtained by least-squares fitting of an empirical sigmoidal function, the so-called Hill's equation:

$$I(T) = I_{\text{base}} + (I_{\text{max}} - I_{\text{base}}) \Big/ 1 + \left(\frac{T_{\text{half}}}{T}\right)^{\text{rate}}. \tag{5.1}$$

This function is used for convenience, and is not meant to imply a physical significance.

The most striking features of the three hysteresis loops are their very different widths: from 2±1 °C for the witness film (Figure 5.4a) to 18±2 °C for NP "B" (Figure 5.4b) and 56±5 °C for NP "A" (Figure 5.4c). In general, a first-order phase transformation requires

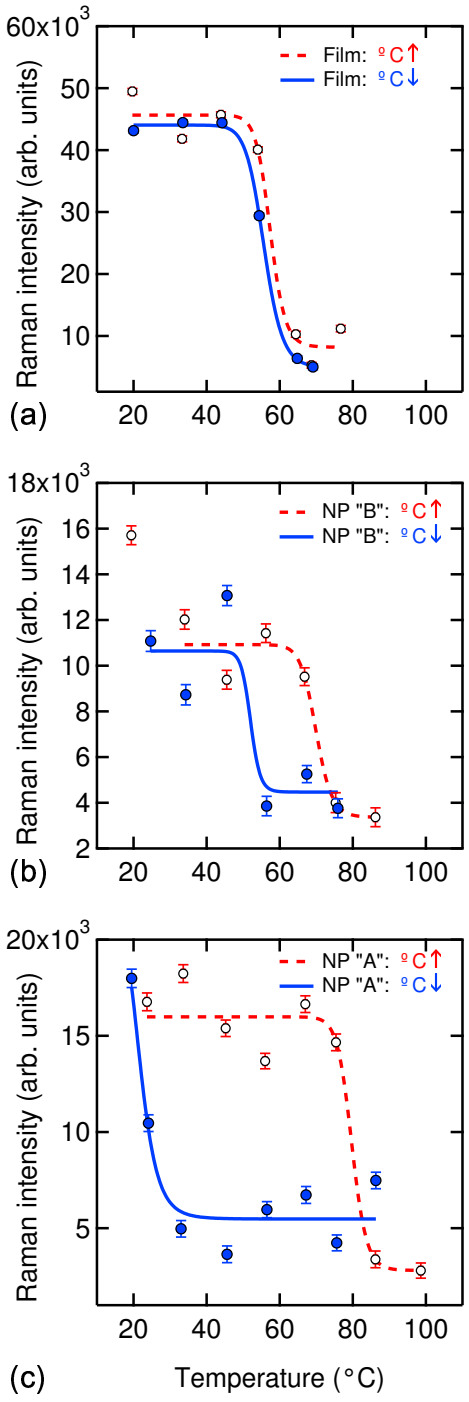

Figure 5.4: Thermal hystereses of the Raman intensity (165–255 cm^{-1}, minus background), for **(a)** witness film, **(b)** nanoparticle "B", and **(c)** nanoparticle "A". Dashed / solid fit line is for the heating (↑) / cooling (↓) half-cycle; one data point in **(b)** is excluded from the fit as an outlier; error bars indicate statistical uncertainty. The hysteresis width is a measure of the "ease" of switching between the low- and high-temperature states.

some amount of overheating above and undercooling below the equilibrium transition temperature, where the free-energy curves of the two phases intersect with a discontinuity in the first derivative (see Section 1.2). At thermodynamic equilibrium, the system occupies one of the two (meta)stable states depending on the transformation history, *i.e.*, whether the temperature has been increasing or decreasing. For example, martensitic structural transformations,[70] a class to which the VO_2 phase transition belongs,[75] take place at two constant temperatures when only a single interface between the two phases is involved (*e.g.*, in single crystals); however, the transition points may vary over a range of temperatures in materials with multiple interfaces, such as polycrystals.[72]

Specifically for VO_2, the sharpness, shape, width, position, and switching ratio of the thermal hysteresis have been shown to depend critically on the quality of the VO_2 material (crystallinity, stoichiometry, impurities);[45,95,203,204] grain size, distribution, and orientation;[46,47,75,79,81] and NP size.[5,9] Considering the statistical characteristics of heterogeneous nucleation of martensitic transformations,[43,44] Lopez *et al.* have proposed an explanation of the increasingly wider hystereses (up to 50 °C) with decreasing NP sizes, as observed in near-infrared transmission through VO_2 NPs implanted into silica.[5] According to the model, a small VO_2 particle has a certain probability of switching phases that depends, for any given temperature, on the availability of "potent defects". These defects are envisioned as stochastically distributed sites where the free-energy barrier is low enough for the new phase to nucleate inside the parent phase. The probability of finding at least one such nucleation site per particle, and hence the probability of transformation, is modelled phenomenologically as a function of particle volume and the temperature-dependent excess driving force[44] (see also Section 1.3.2). A small amount of VO_2 material, such as our NP "A" or "B", would require substantial overheating and undercooling beyond the nominal transition temperature (*i.e.*, excess driving forces) to change from the monoclinic to the tetragonal phase and *vice versa*, thereby exhibiting a wide thermal hysteresis (Figure 5.4b and 5.4c). On the other hand, a contiguous VO_2 film contains many nucleation sites due

to the large accessible volume, so that even relatively small excursions in temperature can initiate the phase transition, resulting in a narrower hysteresis loop (Figure 5.4a).

The above arguments help explain why the Raman hysteresis loops of our NPs are much wider than that of the witness film: The "ease" of switching depends on the presence of nucleation sites, which become more scarce as the volume of VO_2 material involved shrinks. But why is NP "B" much "easier" to switch than NP "A" ($\Delta T_B = 18\pm2$ °C *vs.* $\Delta T_A = 56\pm5$ °C) when both NPs should have the same volume, predetermined by lithographic and deposition conditions? Figure 5.1b offers a possible explanation. The evident differences in surface morphology may indicate that NP "A" constitutes one single-crystal grain, whereas NP "B" possibly contains grain boundaries, dislocations, or other structural imperfections as a result of the post-deposition annealing process, and those can act as potent sites for heterogeneous nucleation of the phase transition, thus yielding a narrower hysteresis for the more "defective" particle. Of course, without direct measurements of the underlying crystallinity of these specific NPs, such reasoning remains speculative though in keeping with the notion of the stochastic nature of the VO_2 phase transition, namely that NPs of a well-defined size do not have a unique T_c but a probability of switching centered at that temperature.[9]

5.4 Summary and outlook

To summarize, we reported the first observations of the phase transition in *individual* VO_2 NPs and the evolution of their Raman response as a function of temperature. In accord with previous results from ensembles of VO_2 NPs,[5,9] the two single NPs studied here exhibited thermal hysteresis loops much wider than that of a companion thin film (Figure 5.4). In fact, NP "A" (Figure 5.1b) produced one of the widest VO_2 hystereses reported to date: $\Delta T_A = 56\pm5$ °C. Such large thermal delays in the monoclinic-tetragonal-monoclinic transition cycles for isolated nanoscale amounts of VO_2 have been attributed to the diminished availability of nucleation sites active at a given temperature as the volume of the

probed material decreases.[5] Various stochastically occurring defects (vacancies, dislocations, untransformed embryonic regions, etc.) can become potent sites for heterogeneous nucleation, so even NPs of identical volumes may transform with different "ease", that is, different hysteresis widths (Figure 5.4b *vs.* 5.4c).

The single-particle measurements reported here afford a direct way to obtain statistical information on the distribution of potent nucleation sites, namely by spatio-thermal confocal mapping of the Raman (or other optical) response of arrays of widely spaced VO_2 nanocrystals of a given nominal size. Armed with many single-NP hystereses and the corresponding particle morphologies or, better still, electron-diffraction patterns,[3,36] one can gain valuable insight into the microscopic, "special-site" origins of the phase transition of this fascinating material.

CHAPTER VI

SIZE-EFFECTS IN THE STRUCTURAL PHASE TRANSITION OF VO_2 NANOPARTICLE ARRAYS STUDIED BY SURFACE-ENHANCED RAMAN SCATTERING

Abstract

Described here is the first experimental application of surface-enhanced Raman scattering (SERS) to the study of the phase transition of vanadium dioxide (VO_2). Using arrays of hybrid gold-capped VO_2 nanoparticles (Au+VO_2 NPs) and a VO_2 film covered with Au islands, we obtained the temperature evolution of the SERS intensity with respect to the amount of accessible VO_2 material across the monoclinic-tetragonal-monoclinic transformation cycle. Overall, we found that the smallest Au+VO_2 NPs required the largest deviations from the bulk transition temperature to complete their phase transition, resulting in the widest thermal hysteresis, while the Au+VO_2 film exhibited the narrowest hysteresis. Although the observed size-dependence agreed with the model of defect-induced nucleation of the VO_2 phase transition, the observed magnitude and change of the hysteresis width with NP size were less pronounced than those in a previous study of elastic light scattering from arrays of bare VO_2 NPs. The discrepancies likely stem from the creation of extrinsic defect sites in the VO_2 material owing to the presence of Au during the high-temperature processing. Finally, we correlated the size-dependence of the measured VO_2 SERS intensity with the scattering efficiency of the Au particles, within the framework of a modified Mie-theory calculation.

6.1 Introduction

6.1.1 Motivation

The present work is an extension of the Raman study of *single* VO_2 NPs presented in Chapter V. Briefly, VO_2 undergoes a temperature-driven metal-semiconductor transition at $T_c \approx 340$ K, which causes profound changes not only in the electronic configuration but also in the crystallographic structure of the material, which switches from a monoclinic (semiconductor) phase (below T_c) to a tetragonal/rutile (metal) phase.[22,23] The single-NP Raman study demonstrated the feasibility of measuring a well-known signature of the structural transition of VO_2—the disappearance of certain Raman-active vibrational modes—but in isolated, nanoscale amounts of VO_2. The potential value of such single-NP measurements exceeds the mere "proof of concept" because they provide a practicable method for gathering particle-by-particle statistics on the "potent" defect sites deemed responsible for nucleating the VO_2 phase transition. As an intermediate step along this route, we set out to investigate the size-dependent properties of *arrays* of VO_2 NPs across their temperature-driven structural transformation.

The interest in size-effects in the VO_2 phase transition is relatively new. Lopez *et al.*[9] studied ordered arrays of VO_2 NPs by incoherent elastic light scattering, and reported size-dependent transition temperatures, as well as an intrinsic variability in the transition temperatures of nominally identical NPs within the same array, which gives rise to intermediate states of increased scattering. Such states of maximum scattered intensity, indicated as points "C" and "G" in Figure 6.1b, arise under conditions of maximum disorder when about half of the NPs in an array have switched from semiconducting to metallic (point "C"), or *vice versa* (point "G"). Regarding the size-dependence of T_c during heating and cooling, the authors found that the hysteresis loops widen as the NP diameters decrease (Figure 6.1c), in qualitative agreement with the model of defect-initiated nucleation of the VO_2 phase transition[5] (see also Section 1.3.2). In view of the still-debated issue of the relative roles of lattice distortion and electron-electron correlations in the mechanism of

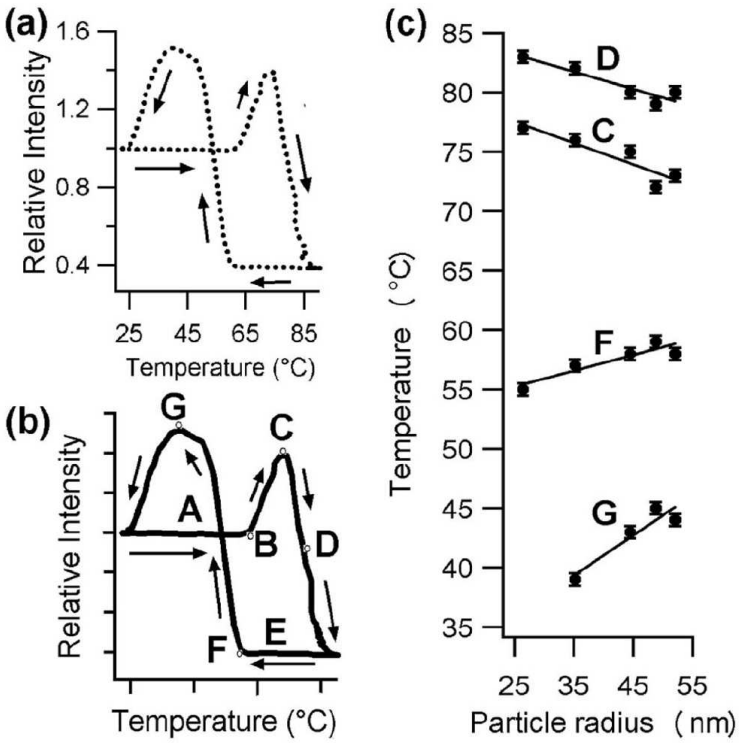

Figure 6.1: **(a)** Temperature evolution of incoherent light scattering at $\lambda = 600$ nm from array of VO_2 NPs. **(b)** Typical hysteresis loop of scattered light from one such array, with indicator points along VO_2 semiconductor-metal-semiconductor phase transition. **(c)** Temperatures of indicator points during a cycle of the VO_2 phase transition as a function of NP size (solid lines are only meant to guide the eye). After Lopez *et al.*[9]

the VO_2 phase transition[1–3,25–32] (see also Section 1.1.3), and because Lopez *et al.*'s light-scattering study[9] probed mainly the electronic response of VO_2 NPs, it is fair to say that the work presented here was partly motivated by curiosity to discover whether probing solely the structural transition of VO_2 NPs (through Raman-active phonon modes) would yield a different size-dependence and possibly shed light on the nature, electronic *vs.* structural, of the elusive "nucleating defects". We shall return to Figure 6.1c in Section 6.3.2.

6.1.2 SERS from hybrid Au+VO_2 NPs

Unfortunately, we were unable to detect any usable Raman signal from arrays of bare-VO_2 NPs of interesting sizes (*i.e.*, diameters of about 100 nm and smaller). A scanning

electron micrograph (SEM) of one such array on a silicon (Si) substrate is shown in Figure 6.2a, and its Raman spectrum in Figure 6.2b. Despite the very long integration time (60 minutes) and relatively large average NP size (110 nm), only Raman peaks belonging to the Si substrate stand out distinctly above the background level. The weak spectral feature just below 200 cm^{-1}, while indeed attributable to the 195-cm^{-1} mode of VO_2, was indistinguishable from noise in the spectra of arrays of smaller VO_2 NPs. In fact, it was not until 125-nm NPs were measured (not shown) that clear, though still weak, VO_2 Raman peaks emerged.

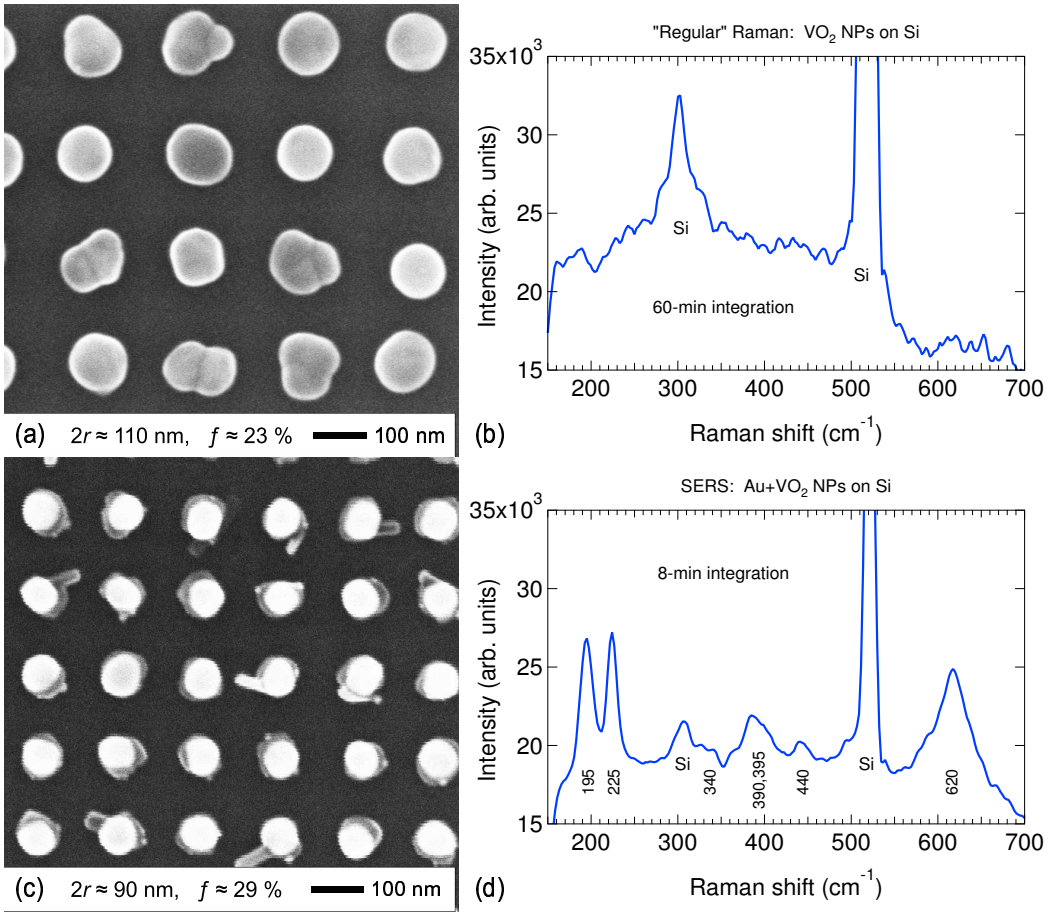

Figure 6.2: Scanning electron micrographs (SEMs) ($2r \equiv VO_2$ NP diameter; $f \equiv$ areal coverage) and room-temperature Raman spectra from arrays of **(a, b)** bare and **(c, d)** Au-capped VO_2 NPs on Si. Note the presence of several strong VO_2 peaks in the Au+VO_2 case, owing to signal enhancement (SERS effect) from the Au caps despite the shorter collection time (8 *vs.* 60 min) and smaller NP sizes (90 *vs.* 110 nm).

Raman scattering is inherently an extremely weak process, with cross-sections per molecule ($\sim 10^{-30}$ cm^2) that are typically 14–15 orders of magnitude smaller than fluorescence cross-sections.[112] In comparison with Raman scattering from bulk materials, thin films, or large particles, the situation becomes progressively less favorable for smaller and smaller NPs, since the reduced volume and elastic scattering efficiency of the latter weaken the interaction with the excitation light even further. Fortunately, the electromagnetic field enhancement associated with the *collective* oscillations of the free electrons—the surface plasmons—of noble metals can be harnessed to greatly increase the interaction strength between an analyte and optical radiation. This notion finds its most prominent realization in the technique of surface-enhanced Raman scattering (SERS). In SERS, the analyte, which may even consist of single molecules, is placed in close proximity (a few nm) or in contact with the signal enhancer (usually made of Ag or Au), which can be a roughened metal substrate, granular metal film, colloidally dispersed or lithographically patterned metal NPs.

In the hope of overcoming the weakness of "regular" Raman scattering from VO_2 NPs, we fabricated hybrid Au+VO_2 nanostructures, as described below (Section 6.2), which consisted of VO_2 NPs "capped" with Au NPs (*e.g.*, see Figure 6.2c). The improvement in signal strength due to the SERS effect was spectacular: for example, the SERS spectrum in Figure 6.2d shows a number of intense VO_2 peaks, especially the two peaks of interest at 195 and 225 cm^{-1}, even though the VO_2 NPs in this array were smaller ($2r_{\mathrm{Au+VO2}} \approx 90$ nm *vs.* $2r_{\mathrm{onlyVO2}} \approx 110$ nm) and the integration time much shorter ($t_{\mathrm{Au+VO2}} = 8$ min *vs.* $t_{\mathrm{onlyVO2}} = 60$ min). Smaller (down to 50 nm) as well as larger (up to 150 nm) hybrid Au+VO_2 NPs also produced distinguishable VO_2 peaks, but invariably of lower intensity than the 90-nm Au+VO_2 NPs. To see why this was so, we recall that the main contribution to signal enhancement in SERS, the electromagnetic effect (as opposed to the "chemical" one), scales roughly with the fourth power of the electric-field enhancement because the Stokes shifts (*i.e.*, vibrational frequencies) of the analyte are usually small enough in comparison with the plasmon bandwidth of the metal, so that the local fields at both the excitation frequency

of the incident radiation and the Stokes frequency of the induced-dipole radiation become enhanced[112,113] (see also Section 2.6.3). Since both of these enhancement factors originate from the interaction of optical radiation with metal nanostructures, the *scattering efficiency* of a field enhancer plays a key role in determining the magnitude of signal enhancement obtainable from a SERS measurement.

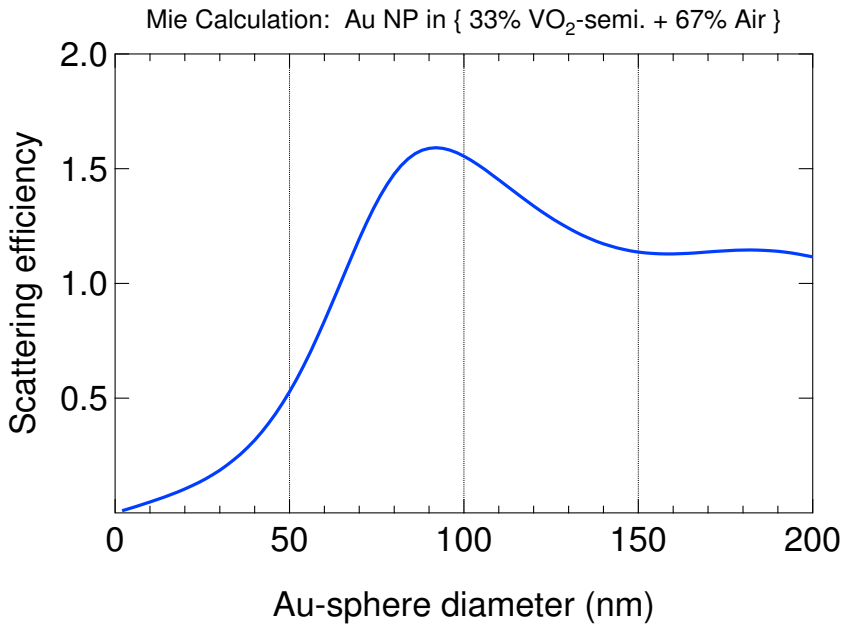

Figure 6.3: Mie-theory calculation (modified for absorbing host medium) of scattering efficiency as a function of particle diameter for Au sphere in composite host medium consisting of $\frac{1}{3}$ VO_2 (semiconducting phase) and $\frac{2}{3}$ Air. Note that the highest efficiency occurs at $2r_{\mathrm{Au}} = 90$ nm, *apparently* (see Section 6.1.2) in accord with the largest measured SERS intensity (cf, Figures 6.9 and 6.10, right panels).

Figure 6.3 shows an analytical calculation, based on the Mie theory of light scattering[120] but modified to account for an absorbing host medium,[119] of the scattering efficiency as a function of size for a spherical Au particle immersed in a composite host medium. The complex permittivity of the host medium consists of weighted contributions of VO_2 and air; the permittivity of Au was obtained from Reference [184], and that of VO_2 from Reference

[57]. The specific choice of 33% VO_2 and 67% air was prompted by a simple geometrical argument: assuming a hemispherical Au "cap" on a flat VO_2 surface, $\frac{1}{3}$ of the cap's surface area lies in contact with VO_2 and $\frac{2}{3}$ with air. Despite using this *ad hoc* assumption in conjunction with a calculation for a sphere, Mie theory predicts the maximum scattering efficiency of such Au NPs to peak precisely at $2r_{\mathrm{Au}} = 90$ nm—apparently in excellent agreement with the strongest SERS signal measured in the present study (Figure 6.2d; see also Section 6.1.2 for a minor correction to this calculation).

6.2 Experimental details

Arrays of Au-capped VO_2 NPs, along with a Au-covered patch of VO_2 film, were fabricated on a Si substrate by means of: **(i)** electron-beam lithography (EBL: 30-kV accelerating voltage, 10-μm beam aperture, 40-pA beam current, 10-mm working distance, 1000 X magnification) in a spin-coated layer of poly(methyl-methacrylate) (PMMA: 100-nm thickness, 950K molecular weight), followed by chemical removal of the exposed areas; **(ii)** pulsed-laser deposition (PLD: KrF excimer laser at $\lambda = 248$ nm, fluence ≈ 3 J·cm^{-2}, V_2O_3 pressed-powder target, O_2 gas at 5 mtorr) of amorphous, sub-stoichiometric vanadium oxide ($VO_{1.7}$, 20-nm thickness); **(iii)** electron-beam evaporation of gold (Au: 15-nm thickness); **(iv)** chemical lift-off of the remaining PMMA and its Au+$VO_{1.7}$ overlayer; **(v)** thermal anneal (450 $^{\mathrm{o}}$C, O_2 gas at 250 mtorr, 30 min) of the resulting Au+$VO_{1.7}$ structures in order to render the VO_2 film patch and NPs stoichiometric and crystalline.[45] Nanoparticles of different sizes were obtained by either defining lithographic areas of given lateral dimensions (mainly for the larger NPs), or by varying the dwell time in "dot exposures"—that is, exposing the PMMA to a greater amount of electron charge in one spot to make a larger NP (*e.g.*, 10/29/48 fC per "dot" for NPs of 50/70/90-nm average diameters). According to the expected NP size, the lattice spacing of the NP arrays was also varied, between 75 and 250 nm, in order to keep the areal coverage approximately constant.

Scanning electron micrographs (SEMs) showing sections of the Au+VO_2 film patch

(Figure 6.8(a, b)) and Au+VO_2 NP arrays (Figures 6.9(a, c, e) and 6.10(a, c, e)) reveal that the Au layer does not wet the VO_2 layer very well, leading to the formation of Au islands on the film patch and "balled-up" Au caps on the VO_2 NPs; moreover, as particle size increases, the Au caps appear to cover less of the surface area of their underlying VO_2 NPs. Another feature peculiar to the morphology of these hybrid NPs, which was absent prior to the thermal anneal (step (v) above), is the finger-like protrusions that extend from some of the NPs or even bridge the gap between a pair of neighboring NPs, especially in arrays of smaller NP sizes and spacings. Judging solely from the contrast in the SEM images, most of the protrusions seem to consist of VO_2 without Au on top.

The arrays were excited using a continuous-wave laser light (He-Ne: $\lambda = 633$ nm, 45-mW output and 8-mW on-sample power), fed through a monomode fiber into an optical microscope operating in confocal-reflection mode, then focused onto the sample with a micro-objective (60 X, NA = 0.80, $1/e^2$ beam spot ≈ 0.5 μm). The scattered light from the Au+VO_2 NPs or film, and from the Si substrate, was collected by the same micro-objective (backscattering geometry), filtered to reduce the elastic-scattering component, and sent through a multimode fiber to a spectrometer equipped with a cooled charge-coupled-device (CCD) detector. The sample temperature was ramped and maintained (± 0.05 K) using a controller unit that supplied power to a resistive heater based on the feedback from a temperature sensor under the heating plate.

Raman measurements were performed at several fixed temperatures, during heating and cooling, as follows: **(1)** the array or film patch of interest was positioned into the laser beam spot using manual micrometers, and imaged onto a CCD camera under concurrent white-light illumination; **(2)** the positioning was further fine-tuned by digital adjustments to the sample stage until two designated sample features coincided with two fixed on-screen markers; **(3)** the focus was visually adjusted by vertical displacement of the microscope head; **(4)** an 8-min Raman spectrum was collected. The sample was then heated up or cooled down, and the measurement sequence repeated at the next temperature point. We

thus obtained the evolution of the Raman response across the structural phase transition of VO_2. Unlike the single-NP experiment (Chapter V), here we measured the collective response as a function of size from *arrays of Au-capped* VO_2 NPs, where the NPs within each array were nominally identical.

6.3 Results and discussion

6.3.1 Peak statistics: Film vs. 90-nm NPs

Let us first compare the Raman response of the VO_2 film covered with Au islands and the response of an array of Au-capped VO_2 NPs (90-nm average diameter). As in Chapter V, we concentrate mainly on the peaks near 195 cm^{-1} and 225 cm^{-1}, which correspond to characteristic vibrational modes of the monoclinic (low-temperature) structure of VO_2 and vanish upon transition into the tetragonal (high-temperature) phase.[195–197,201] These phonon modes play a crucial role in the structural transition of VO_2, since they are associated with the pairing and tilting motions of V–V dimers that map the monoclinic onto the tetragonal lattice configuration.[31]

For the Au+VO_2 film and array of 90-nm NPs, Figure 6.4 shows representative spectra of the two peaks taken at room temperature (monoclinic phase), together with least-squares fits through the data points. Lacking *a priori* reasons to attribute the spectral linewidths to homogeneous (Lorentzian) or inhomogeneous (Gaussian) broadening mechanisms, Gaussian peak profiles were chosen because they fit the data better (*i.e.*, lower chi-square values); in fact, using Voigt functions, which are convolutions of a Lorentzian and a Gaussian,[205] resulted in fits weighted almost entirely in favor of the Gaussian profiles. The overall fits also included polynomial baselines to account for the background signal in the collected spectra. The fit parameters for the two VO_2 peaks, along with the Si-substrate peak near 520 cm^{-1} (*e.g.*, see Figure 6.2d), were obtained at each measured temperature point (heating and cooling) for which the fitting algorithm was able to "autofind" a peak.

The temperature evolutions of the positions and widths of the three peaks (VO_2: 195

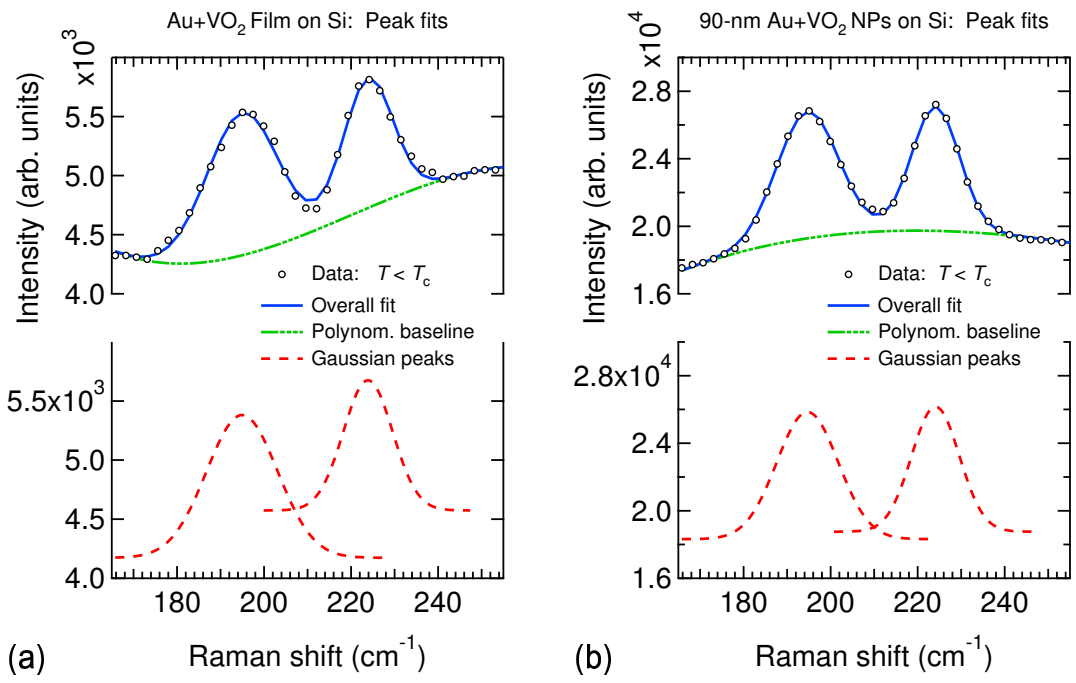

Figure 6.4: **(a)** Least-squares fits to VO_2 Raman peaks (two Gaussians + polynomial baseline) in the monoclinic phase of **(a)** Au+VO_2 film and **(b)** array of 90-nm Au+VO_2 NPs on Si.

cm^{-1} and 225 cm^{-1}; Si: 520 cm^{-1}) are presented in Figure 6.5. Regarding the spectral positions of the VO_2 peaks, a decrease in the Raman shift upon approaching the phase transition temperature—that is, lowering of the vibrational frequencies of the relevant phonon modes—would indicate a softening of the crystal lattice as it transforms from monoclinic to tetragonal. Despite the apparent involvement of the 195 and 225 cm^{-1} A_g-modes in the structural transformation,[31] only one Raman study[195] so far has claimed a spectral shift for either one of these peaks ($\pm$10 cm^{-1} at 195 cm^{-1}), although the authors did not specify whether the shift was positive (mode stiffening) or negative (mode softening). There have been observations[206,207] of a single soft mode at 149 cm^{-1} (up to -15 cm^{-1} shift between 300 K and T_c), while other workers[196,198] have observed no significant shifts of the monoclinic-VO_2 peaks. The data shown here (Figure 6.5(a, b)) suggest a slight softening of the 195-cm^{-1} mode of about 5 cm^{-1} towards higher temperatures (*i.e.*, closer to the tetragonal phase), whereas the positions of the 225-cm^{-1} peak remain unchanged within

the statistical uncertainties of the fits. Apart from those uncertainties, the estimated instrumental resolution of about ± 2 cm^{-1} renders the above -5 cm^{-1} shifts even less significant.

As for the spectral linewidths of the peaks (Figure 6.5(c, d)), the apparent narrowing near T_c, seen more clearly in the NP case, is likely an artifact of the fitting procedure, as automatic peak detection yields the least reliable "finds" right before a peak disappears entirely. Therefore, the highest-temperature fit points for each peak, both during heating and cooling, should be considered the most suspect. Without these, the NP peak widths change very little, while the large uncertainties in the case of the VO_2 film case make it hard to discern a trend. In both cases, however, the absolute width of the 195-cm^{-1} peak room-temperature exceeds that of the 225-cm^{-1}, in qualitative agreement with previously reported Raman spectra of VO_2 (*e.g.*, see Reference [195]).

The most interesting statistic extracted from the least-squares fits to the Raman data was the area under each peak as a function of temperature; the results are plotted in Figure 6.6. Three observations promptly stand out, and are discussed below.

First: In the NP case, the peak at 520 cm^{-1} due to the Si substrate exhibits hysteretic behavior instead of remaining oblivious to the phase transition in the VO_2 material. Furthermore, the Si hysteresis is "reversed" with respect to the VO_2 hysteresis—that is, the total intensity of the Si peak *increases* on heating through the monoclinic-to-tetragonal transition and *decreases* on cooling back into the monoclinic phase of the VO_2 NPs (cf, top panel *vs.* middle or bottom panels in Figure 6.6b). The cause of this behavior becomes clear once we consider the Raman response of tetragonal VO_2. Above T_c, symmetry constraints allow only four Raman-active vibrational modes,[207] which are also rather broad and heavily damped, likely because of interactions with the increased density of free carriers in metallic VO_2.[196] One of these modes results in a high-temperature VO_2 peak centered around 510 cm^{-1}—right underneath the Si-substrate peak at 520 cm^{-1}. As the VO_2 material transforms into the high-temperature phase, this tetragonal-phase mode grows and

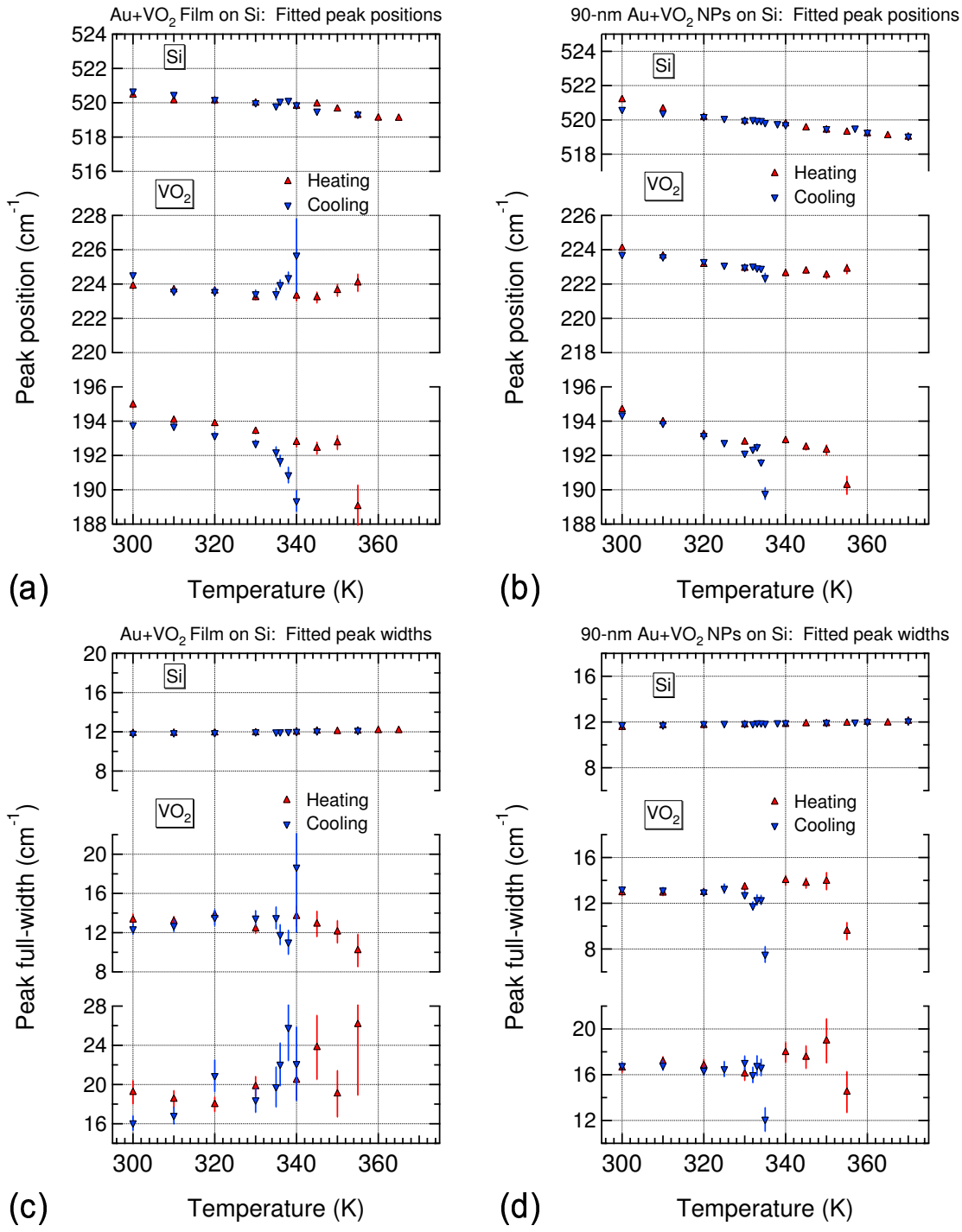

Figure 6.5: Peak statistics as a function of temperature (heating and cooling) for **(a, c)** Au+VO_2 film and **(b, d)** array of 90-nm NPs on Si, obtained from least-squares fits (see Figure 6.4) to the 195-cm^{-1} VO_2 peak (bottom panels), 225-cm^{-1} VO_2 peak (middle panels), and 520-cm^{-1} Si-substrate peak (top panels). For each peak: **(a, b)** full-width at half-maximum, **(c, d)** spectral position.

adds intensity to the Si peak; conversely, the disappearance of the mode towards the low-temperature phase diminishes the total intensity of the Si peak. Considering the different transition temperatures of VO_2 during heating and cooling, the Si peak also shows hysteretic behavior but in the reverse sense compared with the two monoclinic-VO_2 peaks. In the case of the Au+VO_2 film (Figure 6.6a), the temperature evolution of the Si-substrate peak does not seem to follow a clear trend, except near room temperature, where the lack of overlap between the heating and cooling data resembles the corresponding mismatch between the heating and cooling hysteresis branches of the two VO_2 peaks, possibly due to inconsistent focusing and/or power drift of the incident laser.

Second: The non-zero areas (total intensities) of the NP VO_2 peaks exceed their film counterparts by nearly an order of magnitude. Also, the film case lacks a conspicuous hysteresis loop for the Si peak, such as was seen in the NP case. These related observations can be attributed to the much weaker, if any, enhancement of the VO_2 Raman signal due to the Au islands of various shapes and sizes covering the film (Figure 6.8(a, b)), in contrast with the much greater enhancement from the Au NPs (Figure 6.10a)—on-resonance with the incident and scattered light (Figure 6.3). In other words, being critically reliant on size, shape, and surface morphology of the noble-metal structures to boost the *local* electromagnetic fields,[113] the SERS effect enhances the VO_2-NP peaks beyond their film counterparts, while scarcely influencing the signal from the more "remote" Si substrate (*i.e.*, spatially separated from the Au caps by the VO_2 layer).

Third: The NP array yielded VO_2 hysteresis loops that are clearly wider than those of the film patch. The dependence of the hysteresis width on NP size is further investigated in the next section.

6.3.2 Thermal hystereses: Size-dependence and comparison with previous results

With a view to uncovering a potential trend in the VO_2 structural transformation as a function of the amount of probed material, SERS spectra were measured from arrays of

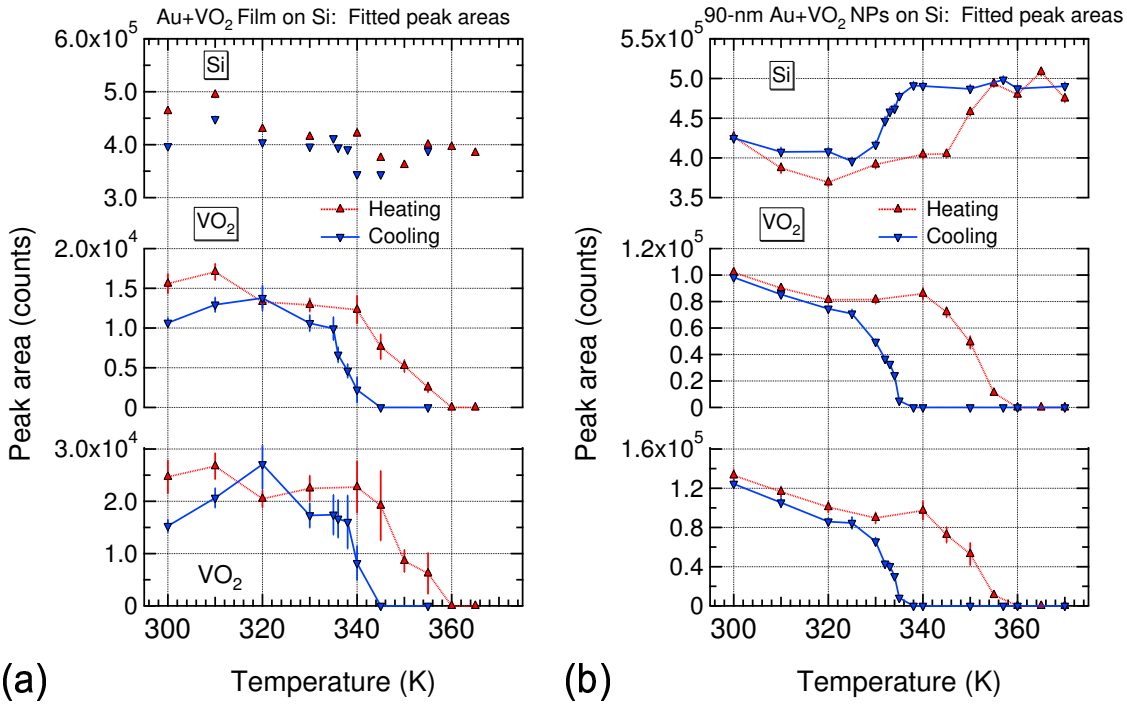

Figure 6.6: Integrated intensities (areas under Gaussian peaks in Figure 6.4) as a function of temperature (heating and cooling) for **(a)** Au+VO_2 film and **(b)** array of 90-nm NPs on Si, obtained from least-squares fits to the 195-cm^{-1} VO_2 peak (bottom panels), 225-cm^{-1} VO_2 peak (middle panels), and 520-cm^{-1} Si-substrate peak (top panels). All lines are only guides for the eye.

Au+VO_2 NPs of different sizes. Contrast analysis of SEM images, portions of which are shown in Figures 6.9(a, c, e) and 6.10(a, c, e), gave the following average diameters of the VO_2 NPs (but not necessarily of the corresponding Au caps): $2r \approx$ 50, 60, 70, 90, 130, 150 nm. For each of the six NP arrays and two spots on the film patch, Raman spectra were collected, as described above (Section 6.2), at ten or so temperature points during heating and about as many during cooling through the VO_2 phase transition. Figure 6.7 examines the region of interest from four such spectra out of the data sets for the smallest and largest NPs, below (300 K) and above (365 K) their transition temperatures upon heating. Once again, the vanishing of the peaks at 195 and 225 cm^{-1} marks the transition from monoclinic to tetragonal VO_2, and *vice versa*. As already noted in Chapter V, the 305-cm^{-1} Si peak decreases in intensity above the VO_2 phase transition owing to the vanishing of

an underlying VO_2 peak around 310 cm^{-1}. The background contribution was removed using an algorithm implementing a rolling-circle spectral filter, which distinguishes between peaks and baselines according to their radii of curvature.[202] Even after background subtraction, however, some intensity would often remain above the calculated baselines within the region of interest (175−245 cm^{-1}), whether due to random noise of small radius of curvature or to spectral features of the Si substrate, such as the one shown near 245 cm^{-1} in Figure 6.7a (top panel). It is because of this remanent intensity that the cumulative counts of the VO_2 peaks differ from zero even at the highest temperature points, well above T_c (*e.g.*, see the bases of the hysteresis loops in Figure 6.9).

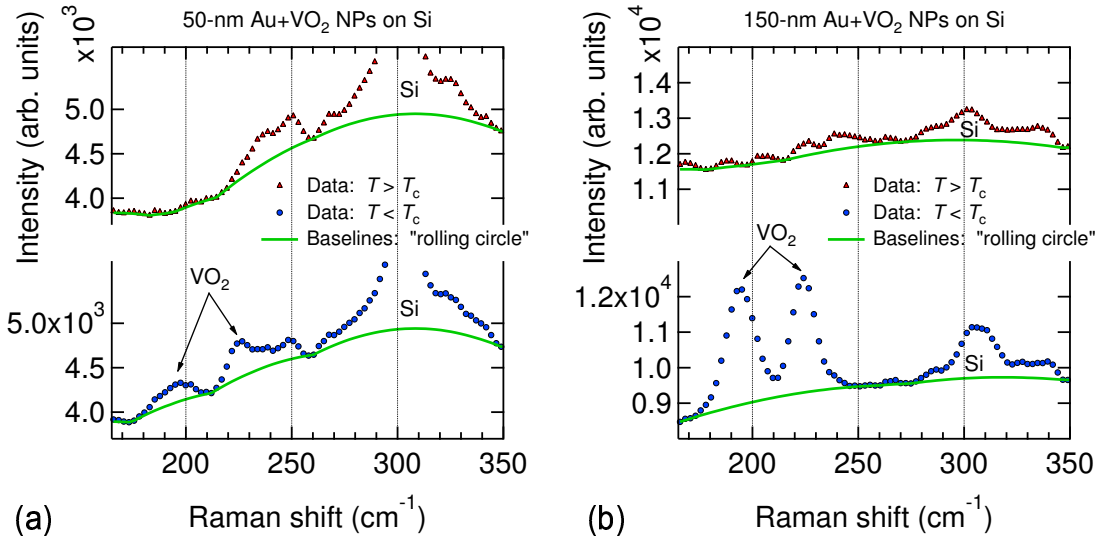

Figure 6.7: Representative SERS spectra from arrays of **(a)** 50-nm and **(b)** 150-nm Au+VO_2 NPs on Si, below and above their respective VO_2 transition temperatures. The solid lines denote the background levels calculated using a "rolling-circle" filter algorithm. The room-temperature (monoclinic) VO_2 peaks vanish in the high-temperature (tetragonal) phase, while features due to the Si substrate remain.

Thermal hystereses of the total above-baseline intensity between 175 and 245 cm^{-1} are presented in Figure 6.8c for one of the film spots; in Figure 6.9(b, d, f) for the 50, 60, 70-nm NPs; and in Figure 6.10(b, d, f) for the 90, 130, 150-nm NPs. The error bar of each

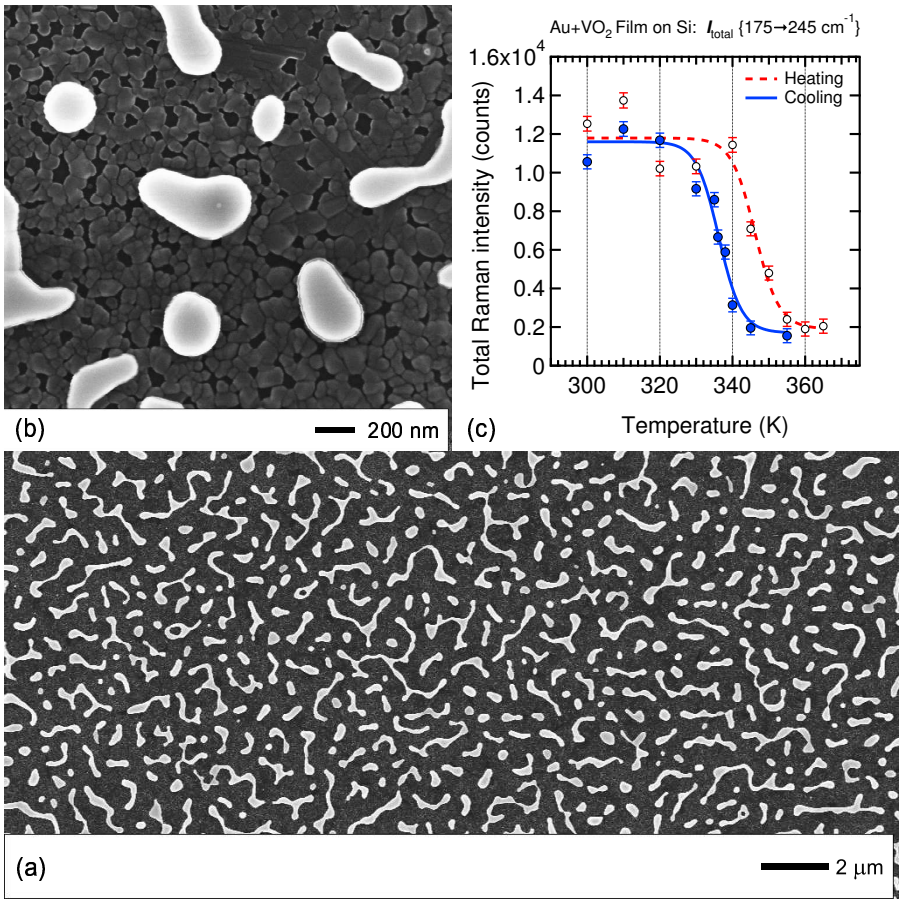

Figure 6.8: **(a, b)** SEM images of Au islands on VO_2 film on Si substrate, and **(c)** thermal hysteresis of SERS intensity of VO_2 peaks, summed between 175 and 245 cm^{-1} after "rolling-circle" background subtraction (see Figure 6.7). The lines are fits to the data points using an empirical sigmoidal function (see Equation 5.1).

data point denotes the uncertainty in determining the total intensity according to counting statistics: $I_{\text{total}} \pm \sqrt{I_{\text{total}}}$. Consequently, the significantly greater *relative* uncertainties for the smallest NP sizes (see Figure 6.9(b, d)) stem from their weaker (that is, less enhanced) Raman signals, as compared to the larger NPs (cf, VO_2 peaks in Figure 6.7a and 6.7b, bottom panels). The lines through the hysteresis data resulted from least-squares fitting with an empirical function of sigmoidal shape (see Equation 5.1), under the added constraint that the low- and high-temperature plateaus (I_{max} and I_{base}) of the heating and cooling branches overlap within the uncertainty of the fit. The main purpose of the fitting procedure was to provide a consistent measure of the transition temperatures for each hysteresis loop,

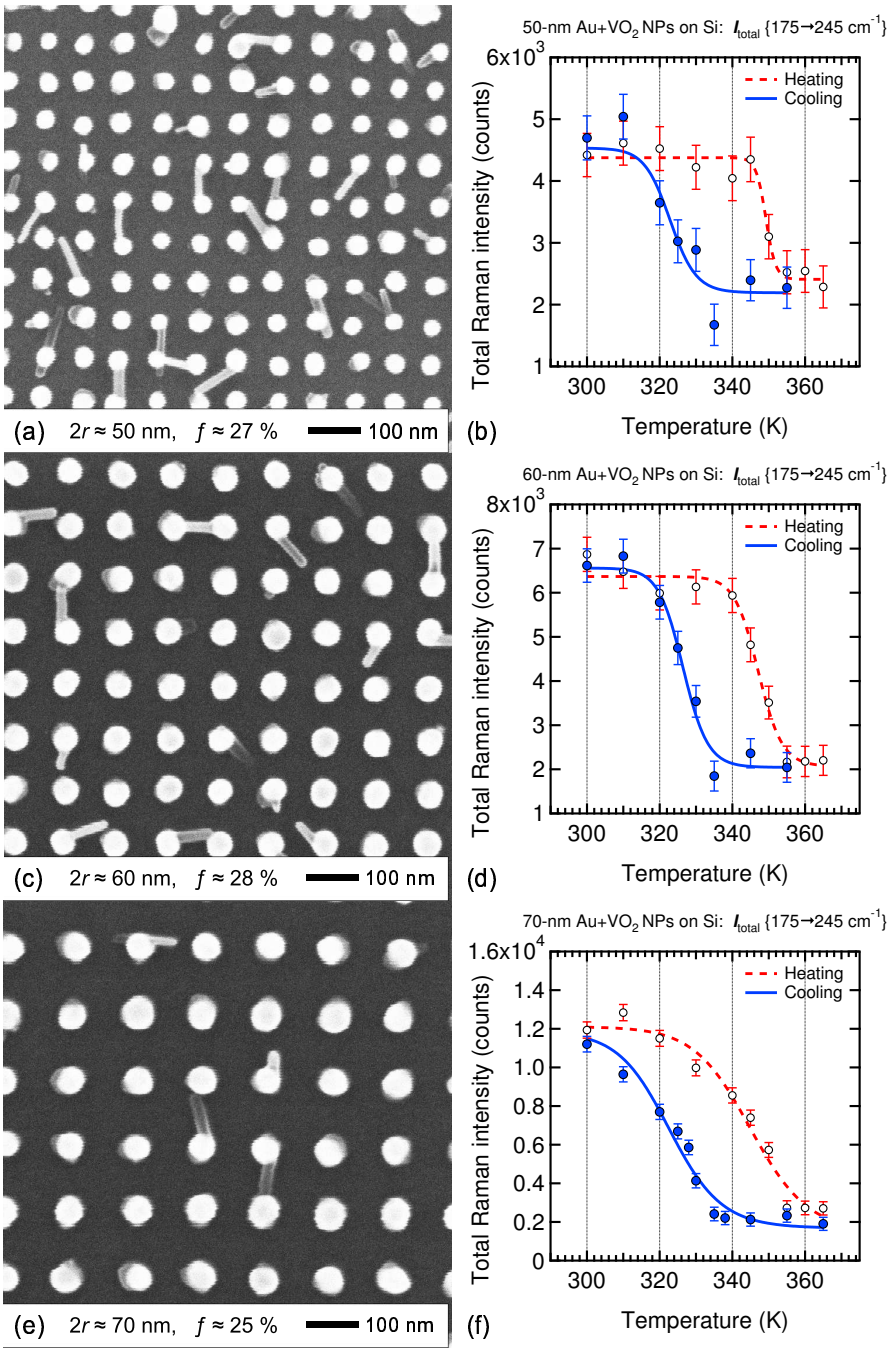

Figure 6.9: SEM images of arrays of Au-capped VO_2 NPs ($2r \equiv VO_2$ NP diameter; $f \equiv$ areal coverage), and thermal hystereses of SERS intensity of VO_2 peaks, summed between 175 and 245 cm^{-1} after "rolling-circle" background subtraction (see Figure 6.7), for $2r$ of **(a, b)** 50 nm, **(c, d)** 60 nm, and **(e, f)** 70 nm. The lines are fits to the data points using an empirical sigmoidal function (see Equation 5.1).

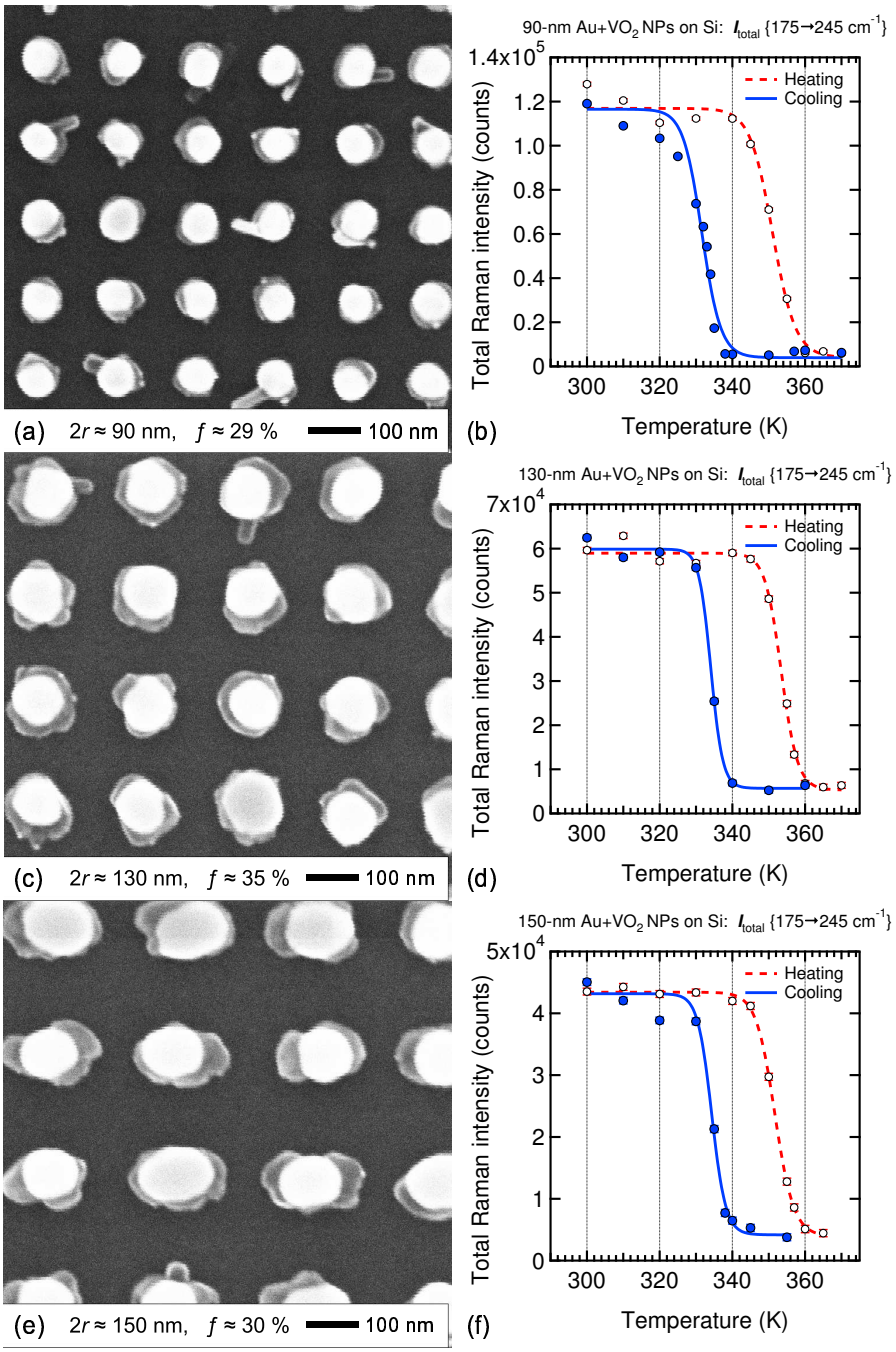

Figure 6.10: SEM images of arrays of Au-capped VO_2 NPs ($2r \equiv$ VO_2 NP diameter; $f \equiv$ areal coverage), and thermal hystereses of SERS intensity of VO_2 peaks, summed between 175 and 245 cm^{-1} after "rolling-circle" background subtraction (see Figure 6.7), for $2r$ of **(a, b)** 90 nm, **(c, d)** 130 nm, and **(e, f)** 150 nm. The lines are fits to the data points using an empirical sigmoidal function (see Equation 5.1).

taken here as the half-maximum points (T_{half} in Equation 5.1) on the corresponding heating and cooling curves. Figure 6.11a summarizes those results for all six NP sizes and two separate spots on the film patch; the error bars here equal $\pm 1\sigma$, as calculated by the fitting routine.

Taking the film as a reference, we can now look for size-dependent trends in the NP data. For instance, most of the NP transition temperatures of the heating branch lie above the T_{c} of either film spot. Assuming that the total Raman intensity of the two VO_2 peaks is directly proportional to the overall amount of monoclinic-phase material, this means that, for example, half of the 130-nm VO_2 NPs would switch from monoclinic to tetragonal at a 7±1 degrees higher temperature than half of the VO_2 material in the film. On the cooling branch, all the NP points lie below the corresponding T_{c} of the film; furthermore, the relative undercooling for the three smallest NP sizes is much more pronounced than their relative overheating. Large undercooling with respect to bulk T_{c}, previously observed in the aforementioned studies of VO_2 NPs implanted into silica[5] (Section 1.3.2) and arrays of VO_2 NPs on Si[9] (Figure 6.1), likely arises from asymmetric shear stress[5] present on transforming from the tetragonal (high-symmetry) back into the monoclinic (low-symmetry) phase, although a quantitative atomic-scale explanation is lacking. The cooling curve in Figure 6.11a then suggests that, for example, half of the 50-nm VO_2 NPs would return to the monoclinic phase at a 13±2 degrees lower temperature than half of the film volume. In VO_2 nanocrystals, such thermal "delays" in switching phases are particularly pronounced because the availability of potent nucleation defects diminishes for smaller transforming volumes of VO_2, so that greater deviations from bulk T_{c} are required to drive the phase transition (see Chapter V, Section 5.3.2).

Before continuing, we ought to consider the possibility of plasmonic heating of the VO_2 NPs by means of light-energy dissipation in the Au caps. For example, Au NPs embedded in ice have been shown to generate localized heat and even melt the surrounding matrix under optical illumination, especially with a photon energy close to the particle-

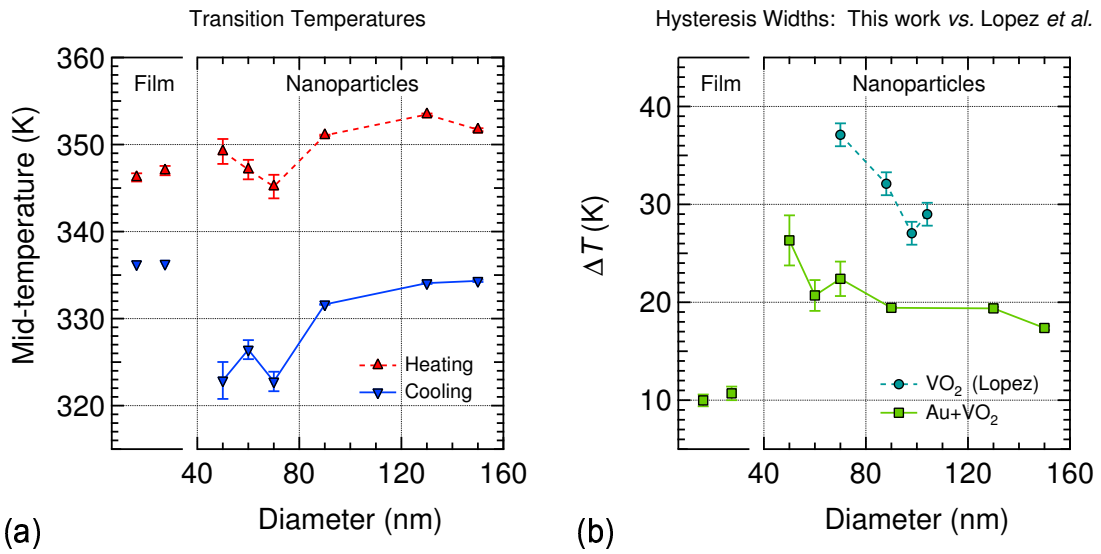

Figure 6.11: **(a)** Transition half-maximum points of heating and cooling branches of SERS hystereses (obtained from sigmoidal fits in Figures 6.8, 6.9, 6.10) for two different spots on the Au+VO_2 film (left panel) and for all six NP sizes (right panel). **(b)** Comparison between hysteresis widths from SERS measurements on Au+VO_2 film (left panel) and NPs (right panel) on Si (this work) and hysteresis widths from light-scattering measurements on VO_2 NPs on Si (after Lopez *et al.*,[9] see Figure 6.1 and text). All lines are only meant to guide the eye.

plasmon resonance.[208] Theoretical analysis of the mechanism of heat generation in a Au NP reveals that the maximum increase in local temperature due to plasmonic heating occurs at the surface of the particle and scales with the square of its radius.[208,209] It is then conceivable that the VO_2 transition temperatures obtained in this study may have been biased by an additional source of heat besides the sample heater. Such an effect would manifest itself as an "artificial" decrease in the observed T_c *in either direction*, since less external energy (as registered by the temperature sensor) would need to be added upon sample heating but more dissipated upon cooling through a full transition cycle. However, neither the heating nor the cooling branch in Figure 6.11a shows a progressive lowering of T_c as the VO_2 NPs (hence, the Au caps) increase in size. Therefore, plasmonic heating of the VO_2 NPs by the Au caps, albeit possible in principle, is not borne out by the present data.

A measure of the intrinsic size-dependence of the phase transition that would remain unaffected by a constant temperature bias is the width of the thermal hysteresis. As mentioned before, a contiguous VO_2 film has a relatively narrow hysteresis (typically ΔT = 10–15 K) because many potent sites for heterogeneous nucleation reside in its large accessible volume, so that relatively small excursions in temperature can initiate the phase transition. On the contrary, smaller amounts of VO_2 material generally require substantial overheating and undercooling (*i.e.*, excess driving forces) to change from the monoclinic into the tetragonal phase and back, thereby exhibiting a wide thermal hysteresis. Figure 6.11b, where the square points are obtained directly from Figure 6.11a, further corroborates this trend: ΔT_{film} = 10.5±0.5 K, whereas $\Delta T_{\text{50nmNPs}}$ = 26.5±2.5 K. Moreover, the hysteresis width shrinks with increasing NP size (*e.g.*, $\Delta T_{\text{150nmNPs}}$ = 17.5±0.5 K), as expected from the model,[5] since an increase in the probed volume per particle should result in a greater average probability that any given NP contains at least one random site capable of heterogeneously nucleating the phase transition.

Also shown in Figure 6.11b (circles) are the hysteresis widths for arrays of VO_2 NPs from the above-mentioned light-scattering experiments of Lopez *et al.*[9] The values were computed from the points in Figure 6.1c as $\Delta T_{\text{Lopez}} = T_{\text{C}} - T_{\text{G}}$. Points "C" and "G" were chosen because they mark the temperatures of maximum disorder in those NP arrays, when about half of all NPs have turned metallic during heating ("C") or semiconducting during cooling ("G") (see also Figure 4d in Reference [9]). In comparison with the present study (Figure 6.11b, squares), Lopez *et al.*'s VO_2 NPs demonstrate a stronger size-dependence both in terms of the magnitude and slope of ΔT. It may be tempting to rationalize these discrepancies as due to probing the two different components of the VO_2 phase transition—electronic (via elastic light scattering) *vs.* structural (via SERS)—but such a statement could be misleading. In hindsight, the Au caps utilized in this study likely play a dual role: above all, to greatly enhance the weak Raman signal from the VO_2 NPs, but also, possibly, to introduce new "potent defects" during the thermal anneal (step (v) in Section 6.2). The

finger-like protrusions mentioned in Section 6.2 give visual clues that the presence of the Au layer does impact the growth of the underlying VO_2 NP; in fact, doping VO_2 films with Au has been shown to reduce the width and sharpness of the hysteresis of the IR transmission.[91] Adding extrinsic defect sites to the ones mandated by the statistics of heterogeneous nucleation[5] would be expected to narrow the hysteresis width and, to some extent, obscure its dependence on particle size. Nevertheless, the present study lends further experimental support to the notion that the size-effect in the VO_2 phase transition is a statistical manifestation of a more fundamental criterion—the presence or absence of nucleating sites active at a given temperature.

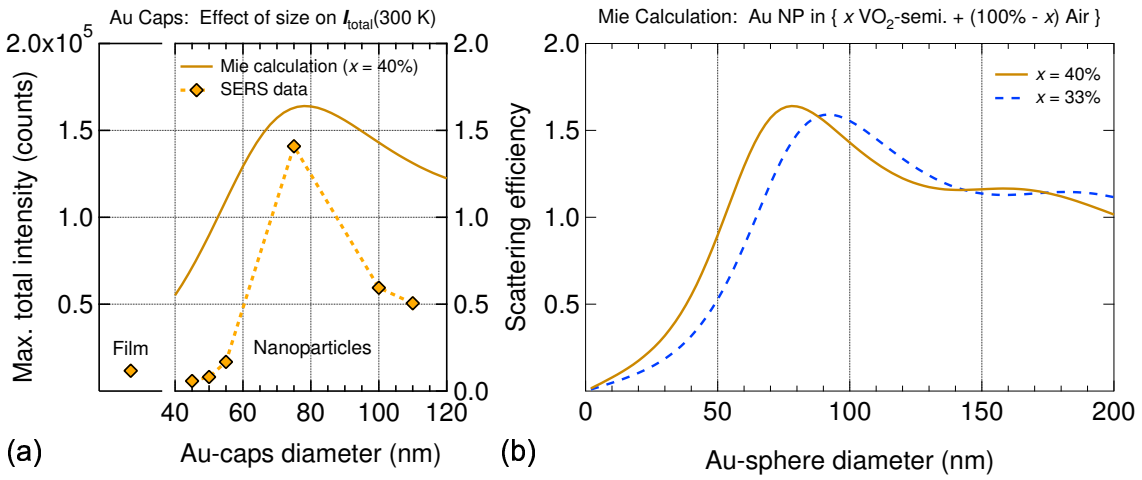

Figure 6.12: **(a)** Total SERS intensity at 300 K (from hysteresis curves in Figures 6.8, 6.9, and 6.10) as a function of size of the Au caps (right panel); dashed line is only a guide for the eye; solid line is one of the Mie calculations shown in **(b)**; the value for the Au+VO_2 film is also shown (left panel). **(b)** Mie-theory calculations (modified for absorbing host medium) of scattering efficiency as a function of particle diameter for Au sphere in composite host medium consisting of $\frac{2}{5}$ ($x = 40\%$) semiconducting-phase VO_2 and $\frac{3}{5}$ Air, compared to the calculation from Figure 6.3. The highest efficiency for $x = 40$ % occurs near $2r_{\mathrm{Au}} = 75$ nm, closely matching the largest measured SERS intensity in **(a)**.

6.3.3 Size-dependence of the SERS intensity

We now briefly return to the SERS effect, which made this study altogether possible (see Figure 6.2), and quantify its dependence on particle size. As mentioned earlier in connection with Figure 6.3, Mie theory predicts the scattering efficiency of a spherical Au NP to peak at $2r_{\mathrm{Au}} = 90$ nm when the particle resides in an effective external medium consisting of 33% VO_2 and 67% air; hence, the 90-nm VO_2 NPs capped with Au hemispheres (Figure 6.10a) were expected to exhibit the strongest enhancement of the VO_2 Raman signal. Indeed, even a cursory glance at the hysteresis maxima reveals this to be the case: cf, I_{total} at 300 K in Figures 6.8c, 6.9(b, d, f), and 6.10(b, d, f). These maxima of the total Raman intensity of the two VO_2 peaks are plotted in Figure 6.12a; the particle sizes here refer to the diameters of the Au caps, which further image analysis (*i.e.*, higher grey-level threshold) determined to be approximately 5 to 40 nm smaller than the underlying VO_2 NPs (*e.g.*, see Figure 6.10e). The strongest SERS signal therefore came from "90-nm VO_2 NPs with 75-nm Au caps atop". It turns out that the Mie calculation in Figure 6.3 requires only a relatively small parameter adjustment—40% instead of 33% VO_2 contribution—to yield a maximum in the Au-NP scattering efficiency at $2r_{\mathrm{Au}} = 75$ nm (Figure 6.12b, also overlaid on the experimental data in Figure 6.12a). This situation (40% VO_2, 60% air) corresponds to a contact angle of less than 90° between the Au caps and the underlying VO_2 layer. Considering the simplifications employed in this calculation, such as spherical Au particles and a weighted average for the optical constants of the host medium, the qualitative agreement between the size-dependence of the measured SERS signal and the size-dependence of the calculated scattering efficiency seems quite encouraging (Figure 6.12a).

6.4 Summary and outlook

We reported the first experimental application of surface-enhanced Raman scattering (SERS) to the study of the phase transition of VO_2. The electromagnetic enhancement of the VO_2 Raman signal, caused by the plasmonic properties of Au particles, was instrumental

to this experiment, since no Raman signal could be obtained from bare VO_2 NPs of sizes less than 125 nm. The structures fabricated on a Si substrate were: **(i)** VO_2 NPs of different diameters (50 to 150 nm), arranged in regular arrays of nominally identical NPs, with each VO_2 NP capped with a somewhat smaller Au particle (45 to 110 nm); and **(ii)** a contiguous VO_2 film covered with disconnected Au islands. On comparing NPs to film, we found that the film required a smaller "driving force" to complete the phase transformation, as evidenced by its much narrower thermal hysteresis. We also observed the trend expected from a model of heterogeneous nucleation of the VO_2 phase transition,[5] namely that the 50-nm VO_2 NPs produced the widest thermal hysteresis (Figure 6.11b), since the smallest volume should have the least statistical likelihood of harboring a potent site for nucleating the phase transition. The size-effect proved less pronounced for the Au+VO_2 NPs studied here than for the bare-VO_2 NPs in Lopez *et al.*'s light-scattering experiment.[9] We offer a heuristic explanation: During high-temperature annealing, the Au metal may contribute extrinsic defects to the VO_2 NPs, thus masking the correlation between size (scarcity of nucleation sites) and hysteresis width (driving force needed to activate latent nucleation sites). Nevertheless, another size effect was clearly evident: The measured SERS intensity scaled according to NP size, peaking for the 75-nm-Au+90-nm-VO_2 NPs (Figure 6.12a), in good agreement with Mie-theory predictions for the scattering efficiency of a Au sphere surrounded by a mixture of VO_2 and air (Figure 6.12b).

The experiment described here can undoubtedly improve the throughput of a confocal Raman mapping measurement such as that proposed at the end of Chapter V: constructing many single-NP Raman hystereses in order to look for a statistical correlation between hysteresis width and VO_2 NP morphology. Ironically, the presence of the Au caps, so crucial in the SERS process, also constitutes the chief drawback of this method, for it remains unknown as to what extent the Au material alters the phase transition properties of VO_2 during the thermal anneal of a Au+VO_2 hybrid nanostructure.

APPENDIX A

VANADIUM SESQUIOXIDE (V_2O_3) THIN FILMS

Abstract

The following information is meant to provide some measure of continuity in our effort to make another material that undergoes a spectacular metal-insulator phase transition: vanadium sesquioxide, V_2O_3. A simple fabrication protocol is presented, along with some of the characterization data used to establish it. The two main steps are: **(i)** room-temperature PLD of amorphous V_xO_y with excess oxygen content, followed by **(ii)** high-temperature annealing in a reducing atmosphere and crystallization to stoichiometric V_2O_3.

1.1 Introduction

V_2O_3 is the other famous oxide of vanadium. First discovered by Föex in 1946, vanadium sesquioxide undergoes a metal-to-insulator transition upon cooling and the reverse transition upon heating through $T_c \approx 150$ K, accompanied by magnetic and crystallographic changes: at room temperature V_2O_3 is a paramagnetic metal with a rhombohedral (corundum) lattice, while the low-temperature phase is an antiferromagnetic monoclinic insulator with a 0.6-eV bandgap.[210] Resistivity jumps by up to 6–7 orders of magnitude,[21,211] infrared (IR) transmission also increases,[212–215] and the first-order nature of the transition gives rise to hysteresis. The V_2O_3 phase transition has long been regarded as a model for the Mott-Hubbard transition mechanism[59,210,216,217] (see also Section 1.1.3), with the monoclinic lattice distortion thought to originate simply from magnetostrictive forces[63] due to the peculiar magnetic ordering[23] below T_c. Unlike the structural transition of VO_2, the change in crystal structure of V_2O_3 is *not* associated with a Peierls instability and unit-cell doubling.[59] However, recent X-ray absorption measurements[218] of the temperature depen-

dence of the local structure have identified a structural *precursor* to the metal-to-insulator transition of V_2O_3, namely a continuous increase in the monoclinic tilt starting well before the onset of the electronic and magnetic transition. These findings suggest that it may be the orbital degrees of freedom that drive the metal-to-insulator transition via changes in hybridization, which are in turn triggered by the monoclinic distortion.[218] Here too, as in the case of VO_2, the web of cause-and-effect links in the transition mechanism of V_2O_3 is yet to be untangled.

Studies devoted to bulk single crystals or thin films of V_2O_3 abound in the scientific literature: according to Imada *et al.*,[23] more than 500 papers on V_2O_3 had been published as of 1998. Yet only a handful of articles[219–225] deal with nanocrystalline V_2O_3—all reporting exclusively on chemical synthesis and/or catalysis; I know of no studies on the phase transition of V_2O_3 nanoparticles (NPs). Observation of the optical switching of V_2O_3 NPs would be more than a scientific "first". Studying nanostructures of another system that behaves like VO_2 in terms of optical changes across the phase transition, and yet differs from VO_2 as regards the roles of the various degrees of freedom involved, can only improve our understanding of how one solid-state phase transforms into another at the nanoscale. In particular, experimental data from "switchable" V_2O_3 NPs would provide a new set of benchmarks for testing the "potent defect" model (see Section 1.3) of the microscopic origins of such solid-solid transformations.

1.2 A V_2O_3 "recipe"

The following deposition and annealing steps were found to yield good-quality V_2O_3 films (∼100 nm) on fused-silica substrates:

• Clean substrate: solvents (TCE, acetone, methanol/IPA, deionized water) and/or UV-ozone treatment.

• Deposit amorphous V_xO_y ($y/x \geq 1.5$) film by room-temperature PLD: V-metal or V_2O_3 pressed-powder target; 300-mJ pulses focused to ~ 0.1 cm^2 on target surface; 15-cm target-

to-substrate distance; 3–5 mtorr O_2.

• Reduce and crystallize deposited film by annealing in tube furnace, *one sample at a time*: **(i)** introduce 1 atm of flowing {4% H_2 + 96% Ar} into vacuum-tight quartz tube, pre-evacuated to 1–5 mtorr (use oil filter with the roughing pump); **(ii)** ramp up furnace temperature to 600 °C at 30 °C/min; **(iii)** dwell at 600 °C for 60 min; **(iv)** turn off heaters and let system cool down to (near) room temperature under flowing gas mix.

When viewed in transmission against white light, a "switchable" V_2O_3 film should look some shade of grey, depending on thickness, but without a tinge of green, brown, or yellow. The acid test, as it were, for good-quality V_2O_3 material is the optical switching in the vicinity of 150 K: sharpness, contrast, and hysteresis of the IR transmission across the metal-insulator transition. The transmission setup used here comprises: **(i)** fiber-coupled light source, either an IR laser at $\lambda = 1330$ nm or a white-light tungsten-halogen lamp; **(ii)** mechanical chopper connected to a lock-in amplifier through a frequency generator; **(iii)** beamsplitter and CDD camera for visual inspection of the interrogated area via reflected and scattered light from the sample surface; **(iv)** one focusing and one collection low-magnification micro-objectives, with the sample in-between; **(v)** pinhole aperture (∼0.5 mm) for stray-light rejection; **(vi)** InGaAs IR detector with responsivity (amp/watt) greater than 10 % for $\lambda = 800$–1700 nm; **(vii)** lock-in amplifier, with input signals from the chopper and the detector, and output of amplified and filtered DC signal proportional to the intensity of the transmitted light. The sample is mounted on a thin copper plate in contact with the heating/cooling pad of a micro-refrigerator assembly, which cools on the principle of expansion of highly pressurized dry N_2 gas inside a series of micrometer-sized capillaries (Joule-Thomson effect) and heats by means of a resistor coil. The assembly is housed in a small optical chamber, continuously pumped to maintain roughing vacuum. The sample temperature is scanned and maintained (±0.05 K) using a controller unit, which supplies power to the resistive heater based on the feedback from a temperature sensor under the heating plate.

1.3 Different annealing temperatures

The first three figures show the effect of annealing temperature on the IR transmission (Figures A.1 and A.3) and X-ray diffraction (XRD) (Figure A.2) of two sets of initially amorphous V_xO_y films on fused-silica (SiO_2) substrates. Upon visual inspection of these data, 600 °C was chosen for further experiments based on somewhat subjective criteria: **(i)** it is at the lower end of the temperature window that yielded films with "good switching", hence reducing the possibility that the (eventual) closely-spaced V_xO_y NPs would diffuse towards one another and coalesce during the anneal; **(ii)** unlike the 925-°C or 850-°C films, the film annealed at 600 °C has (nearly) completed its transition into the insulating state by the lowest measured temperature (85 K); **(iii)** switching contrast is larger for the 65-nm-thick 600-°C film than for its 700-°C counterpart; **(iv)** 600 °C has been popular processing temperature in previous V_2O_3 studies.[212–214]

1.4 Different annealing times and ramp rates

The interesting curve in Figure A.4 is the one for slow ramp-up (3 °C/min) to the final annealing temperature of 600 °C. That particular film likely became sub-stoichiometric ($V_2O_{y<3}$) before it had had a chance to crystallize into V_2O_3. A ramp-up rate of 30 °C/min and a dwell time of 1 hr were chosen for subsequent anneals, since dwell times of 0–4 hr had all produced switchable V_2O_3 films (Figures A.1 and A.4).

1.5 Different PLD target materials

Heeding an apropos observation by Schuler *et al.*[213] that V_2O_3 films grown by reactive e-beam evaporation from a V-metal target or from a sintered V_2O_3 powder exhibited "a drastic difference in quality", the former being the better, we performed depositions from four different PLD targets: V-metal disc from Cerac, inc. (http://www.cerac.com) and pressed-powder discs with nominal compositions of V_2O_3, VO_2, and V_2O_5 from Vin Karola Instruments (http://www.vinkarola.com). While the V and V_2O_3 targets did produce films

with steeper transmission hystereses than those from the other two targets, the differences in quality were hardly drastic (see Figure A.8).

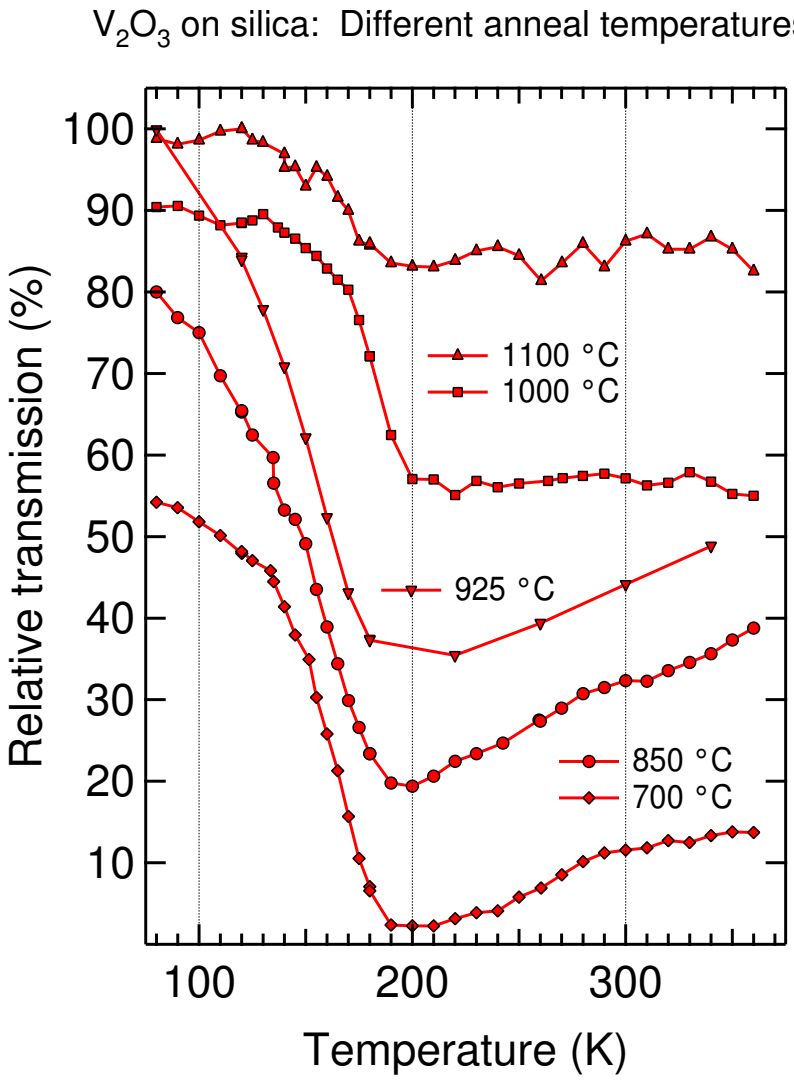

Figure A.1: Relative IR transmission as a function of temperature (heating part of hysteresis cycle) for 140-nm-thick V_2O_3 films on fused silica, H_2-annealed at the indicated temperatures: 1100, 1000, 925, 850, 700 °C. Dwell times: 2 hr, except for the 925-°C film, which was annealed for 4 hr. Illumination sources: white-light lamp for the 925-°C film, and IR laser (λ = 1330 nm) for the rest. The data for each film are normalized to the highest transmission in the low-temperature phase; the curves are offset vertically relative to one another for clarity.

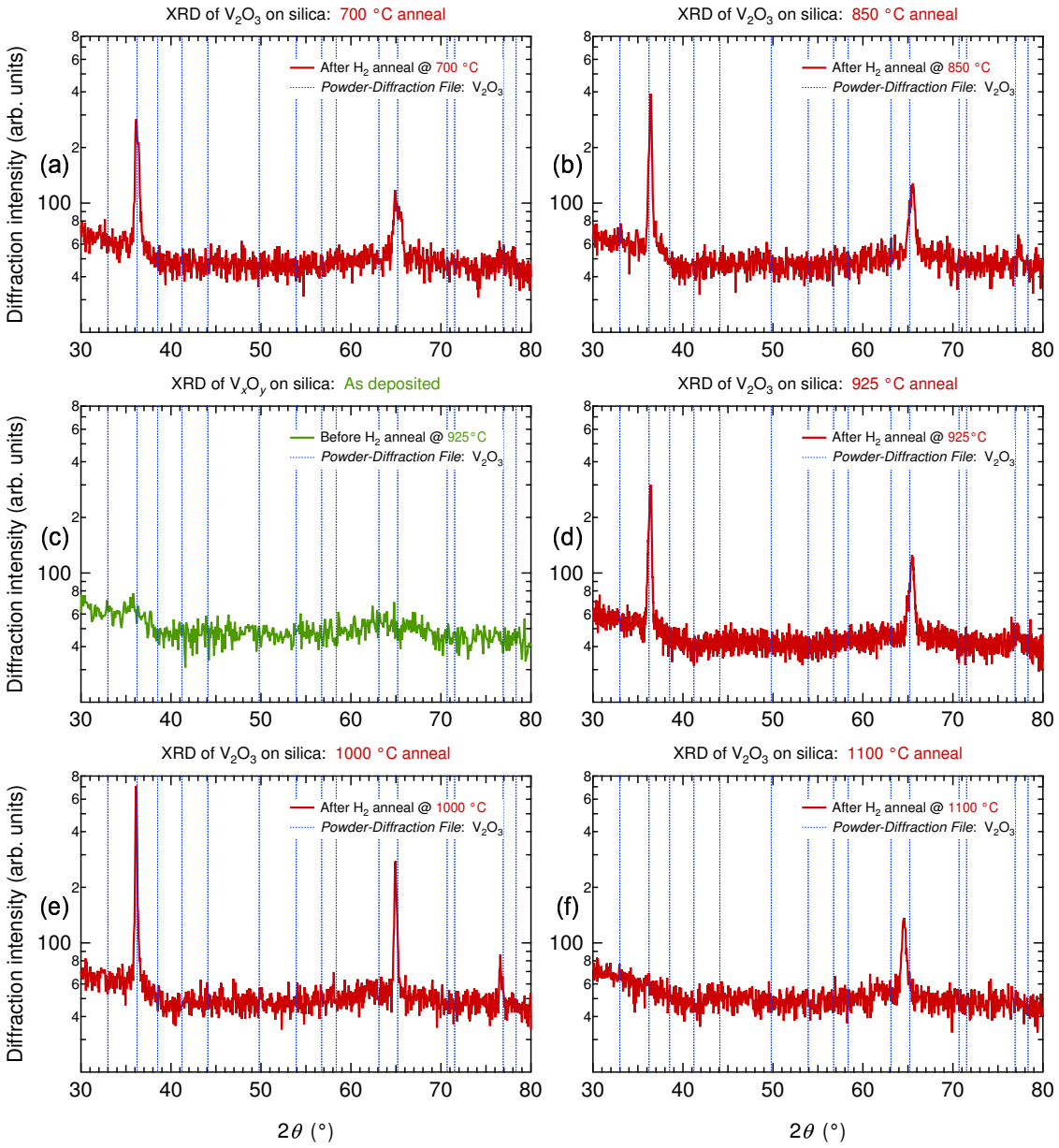

Figure A.2: Room-temperature X-ray diffraction (XRD) θ–2θ scans (Cu–K_α, $\lambda = 1.54$ Å), for the above 140-nm-thick V_2O_3 films on fused silica, H_2-annealed at the indicated temperatures: **(a)** 700 °C; **(b)** 850 °C; **(d)** 925 °C; **(e)** 1000 °C; **(f)** 1100 °C. Part **(c)** shows the XRD scan for the film in **(d)** as deposited, *i.e.*, before annealing at 925 °C. Peaks at the powder-diffraction values (PDF #34-0187) of $2\theta = 36.23°$, $65.193°$, and $76.914°$ correspond to reflections from V_2O_3 planes (1 1 0), (3 0 0), and (2 2 0), respectively.

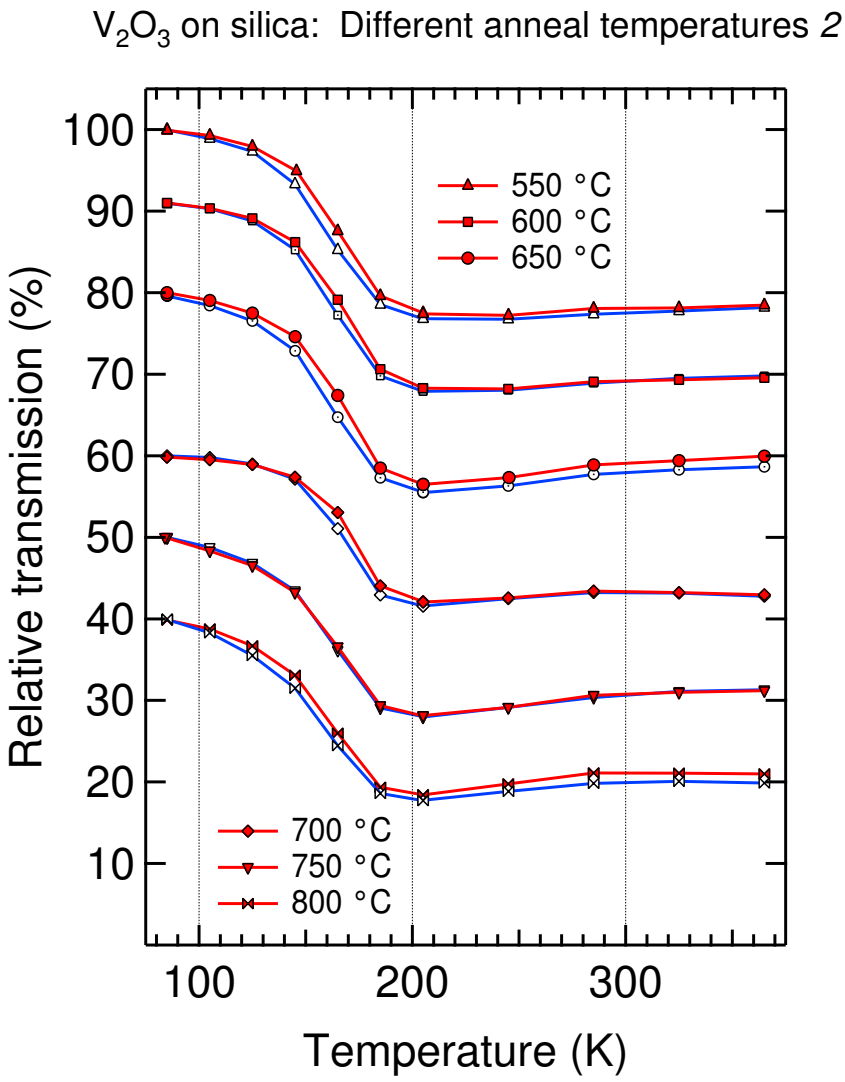

Figure A.3: Relative IR transmission as a function of temperature for 65-nm-thick V_2O_3 films, H_2-annealed at the indicated temperatures: 550, 600, 650, 700, 750, 800 °C. Dwell time: 1 hr. Illumination: white-light lamp. Data for each film are normalized to the highest transmission in the low-temperature phase; the curves are offset vertically relative to one another for clarity. Filled symbols (red lines) correspond to the heating part of the hysteresis cycle, and open symbols (blue lines) to the cooling part.

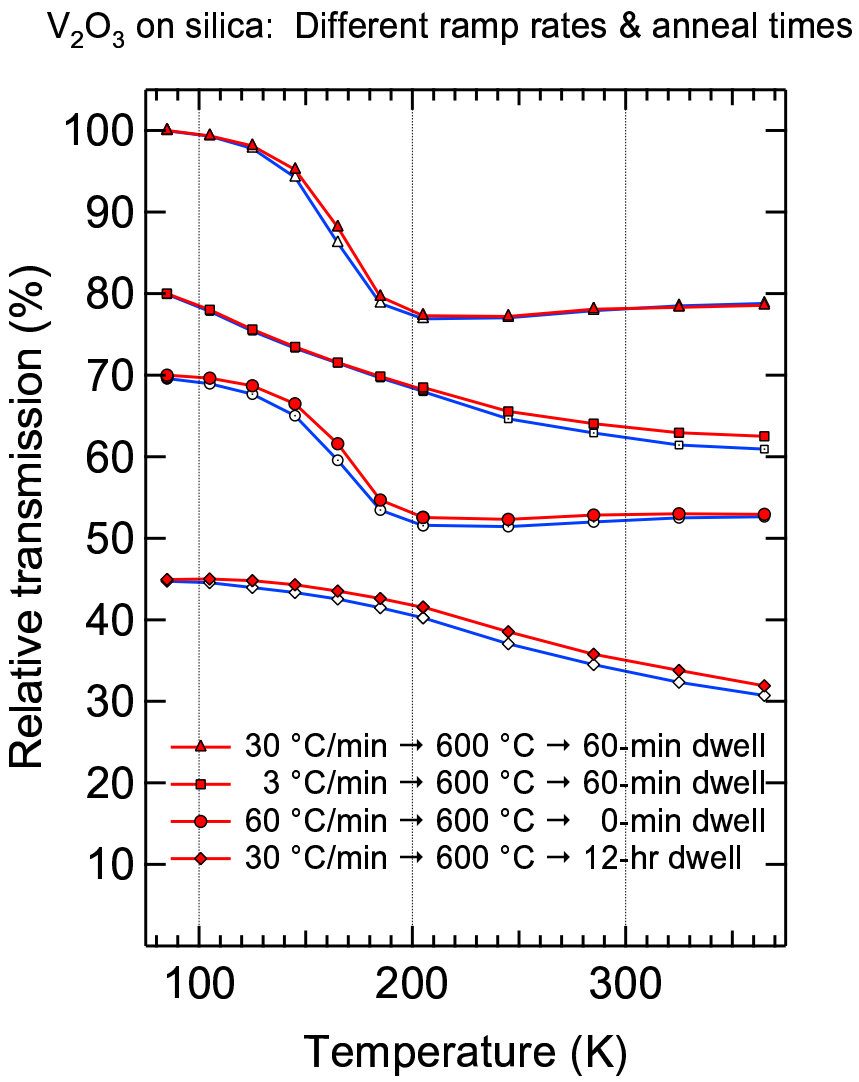

Figure A.4: Relative IR transmission as a function of temperature for 65-nm-thick V_2O_3 films (from the same initial batch as the films in Figure A.3), H_2-annealed by ramping up the temperature to 600 °C at the indicated rates and holding it constant thereafter for the indicated dwell times. Illumination source: white-light lamp. Data for each film are normalized to the highest transmission in the low-temperature phase; the curves are offset vertically relative to one another for clarity. Filled symbols (red lines) correspond to the heating part of the hysteresis cycle, and open symbols (blue lines) to the cooling part.

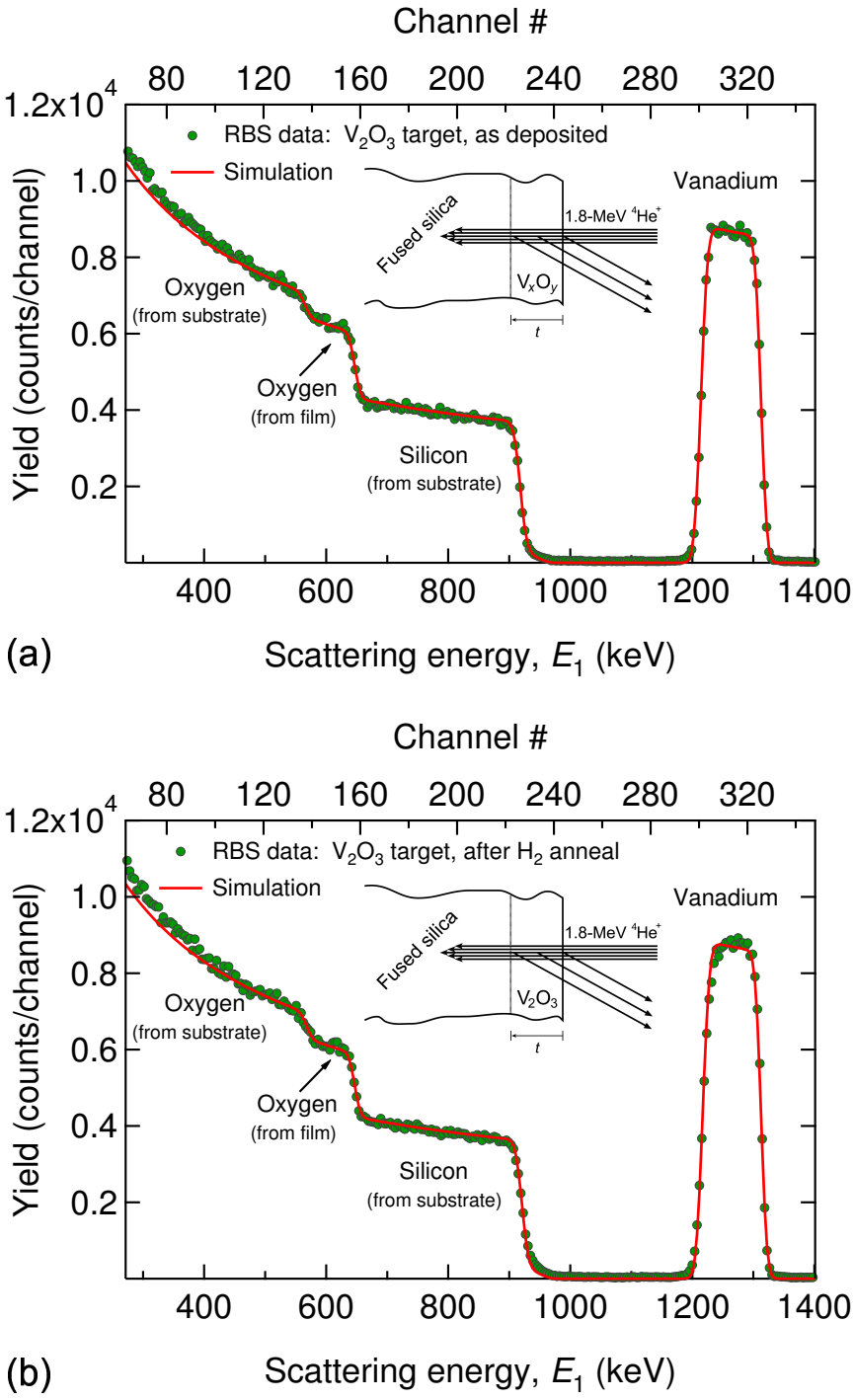

Figure A.5: Example of experimental (circles) and simulated (lines) RBS spectra for vanadium-oxide film on fused-silica (SiO_2) substrate: **(a)** before H_2 anneal (*i.e.*, as deposited); **(b)** after H_2 anneal for 1 hr at 600 °C. The film was grown by room-temperature PLD from a V_2O_3 target in 3 mtorr O_2 background gas. Simulations were performed using the SIMNRA program.[107] *Analysis*: **(a)** $V_2O_{3.12\pm0.01}$, $t \approx 101$ nm; **(b)** $V_2O_{3.03\pm0.01}$, $t \approx 99$ nm.

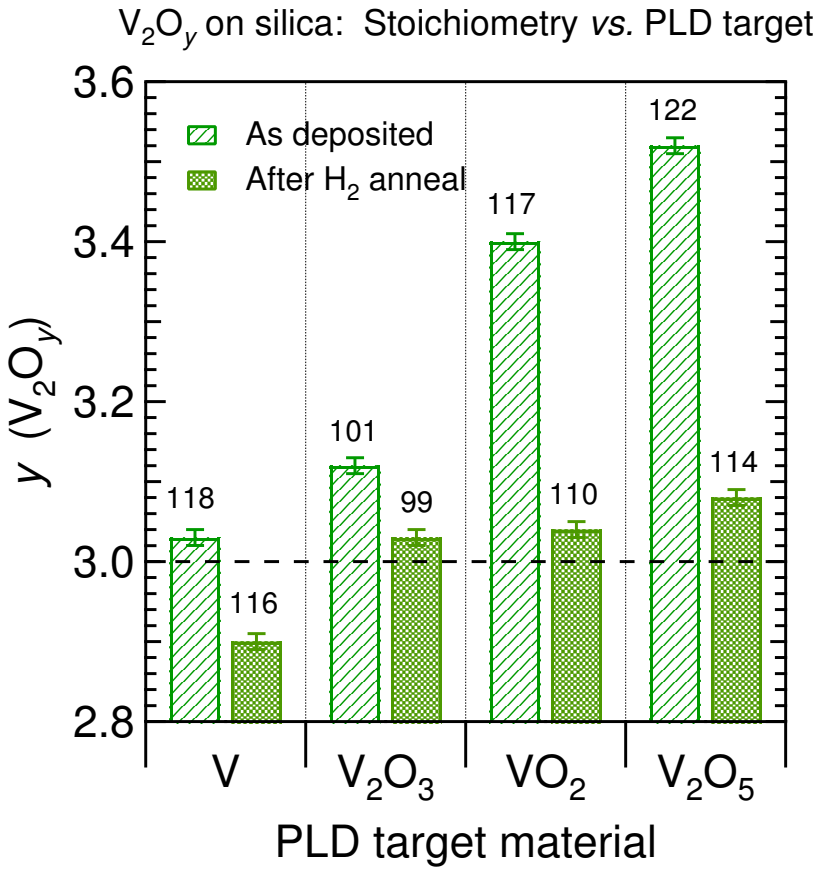

Figure A.6: RBS-measured stoichiometry (see example in Figure A.5), before and after H_2 anneal (1 hr at 600 °C), for vanadium-oxide films deposited from V-metal (in 3 mtorr O_2), V_2O_3 (in 3 mtorr O_2), VO_2 (in vacuum), and V_2O_5 (in vacuum) PLD targets. The number above each bar denotes the thickness in nanometers.

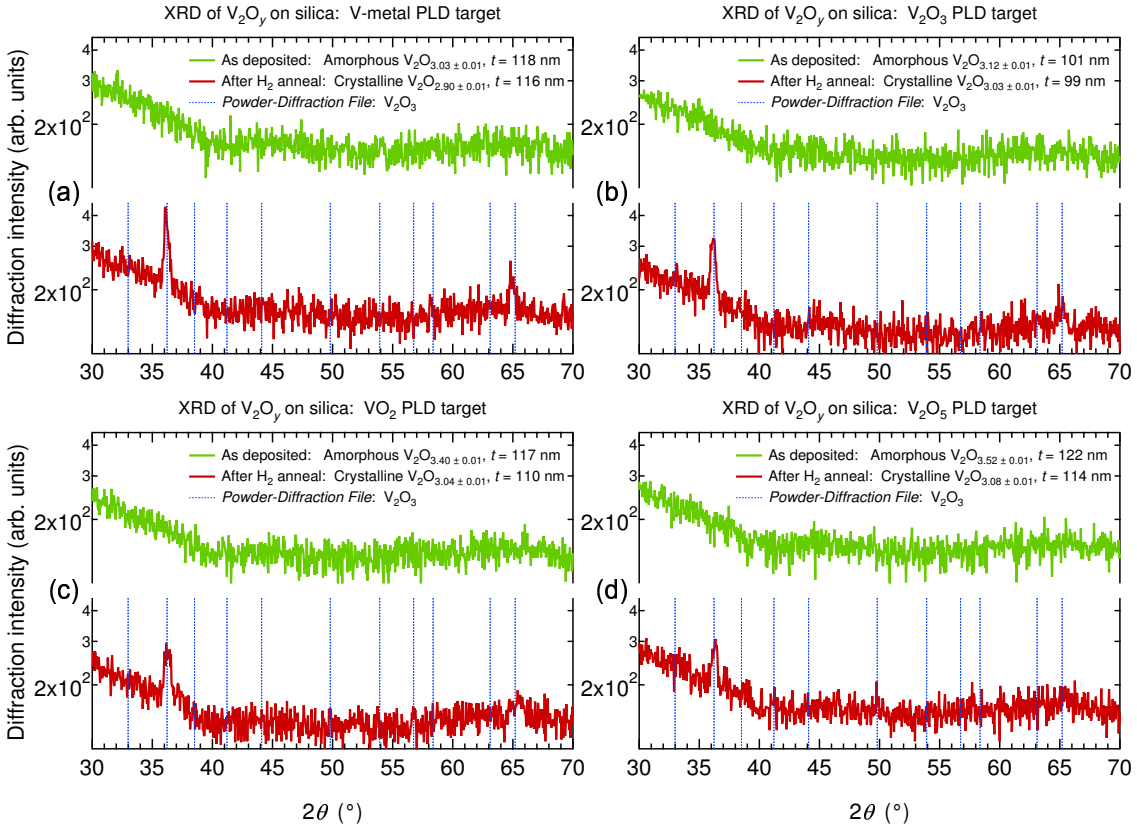

Figure A.7: Room-temperature XRD scans (Cu–K_α, $\lambda = 1.54$ Å), before and after H_2 anneal (1 hr at 600 °C), for vanadium-oxide films deposited from **(a)** V-metal (in 3 mtorr O_2), **(b)** V_2O_3 (in 3 mtorr O_2), **(c)** VO_2 (in vacuum), and **(d)** V_2O_5 (in vacuum) PLD targets. Peaks at the powder-diffraction values (PDF #34-0187) of $2\theta = 36.23°$ and 65.193° correspond to reflections from V_2O_3 planes (1 1 0) and (3 0 0), respectively.

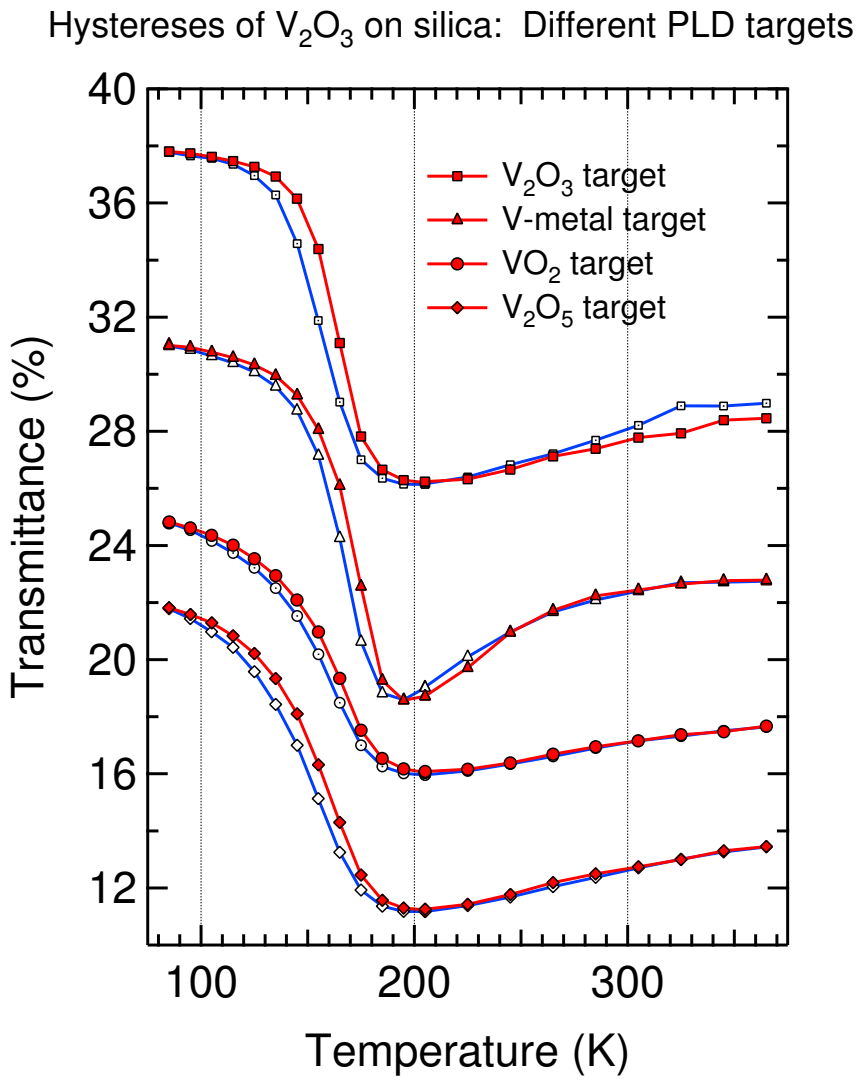

Figure A.8: Optical transmittance for H_2-annealed V_2O_3 films deposited from different PLD target materials. Anneal: 1 hr at 600 °C. Illumination source: white-light lamp. Data for each film are normalized at each temperature point to transmission through the bare fused-silica substrate; the curves are offset vertically relative to one another for clarity. Filled symbols (red lines) correspond to the heating part of the hysteresis cycle, and open symbols (blue lines) to the cooling part.

REFERENCES

[1] C. Kübler, H. Ehrke, R. Huber, R. Lopez, A. Halabica, R. F. Haglund, and A. Leitenstorfer, *Physical Review Letters* **99**, 116401 (2007).

[2] M. M. Qazilbash, M. Brehm, B. G. Chae, P. C. Ho, G. O. Andreev, B. J. Kim, S. J. Yun, A. V. Balatsky, M. B. Maple, F. Keilmann, H. T. Kim, and D. N. Basov, *Science* **318**, 1750 (2007).

[3] P. Baum, D. S. Yang, and A. H. Zewail, *Science* **318**, 788 (2007).

[4] A. Sharoni, J. G. Ramírez, and I. K. Schuller, *Physical Review Letters* **101**, 026404 (2008).

[5] R. Lopez, T. E. Haynes, L. A. Boatner, L. C. Feldman, and R. F. Haglund, *Physical Review B* **65**, 224113 (2002).

[6] T. W. Ebbesen, H. J. Lezec, H. F. Ghaemi, T. Thio, and P. A. Wolff, *Nature* **391**, 667 (1998).

[7] T. J. Kim, T. Thio, T. W. Ebbesen, D. E. Grupp, and H. J. Lezec, *Optics Letters* **24**, 256 (1999).

[8] J. Dintinger, A. Degiron, and T. W. Ebbesen, *MRS Bulletin* **30**, 381 (2005).

[9] R. Lopez, L. C. Feldman, and R. F. Haglund, *Physical Review Letters* **93**, 177403 (2004).

[10] C. X. Wang and G. W. Yang, *Materials Science & Engineering R: Reports* **49**, 157 (2005).

[11] J. G. Lee and H. Mori, *Physical Review Letters* **93**, 235501 (2004).

[12] K. K. Nanda, A. Maisels, F. E. Kruis, H. Fissan, and S. Stappert, *Physical Review Letters* **91**, 106102 (2003).

[13] T. Shibata, B. A. Bunker, Z. Y. Zhang, D. Meisel, C. F. Vardeman, and J. D. Gezelter, *Journal of the American Chemical Society* **124**, 11989 (2002).

[14] T. Shinohara, T. Sato, and T. Taniyama, *Physical Review Letters* **91**, 197201 (2003).

[15] H. J. Mamin, R. Budakian, B. W. Chui, and D. Rugar, *Physical Review Letters* **91**, 207604 (2003).

[16] K. Dick, T. Dhanasekaran, Z. Zhang, and D. Meisel, *Journal of the American Chemical Society* **124**, 2312 (2002).

[17] R. A. Masumura, P. M. Hazzledine, and C. S. Pande, *Acta Materialia* **46**, 4527 (1998).

[18] D. Katz, T. Wizansky, O. Millo, E. Rothenberg, T. Mokari, and U. Banin, *Physical Review Letters* **89**, 199901 (2002).

[19] J. T. Lau, A. Fohlisch, R. Nietubyc, M. Reif, and W. Wurth, *Physical Review Letters* **89**, 057201 (2002).

[20] C. Voisin, D. Christofilos, N. D. Fatti, F. Vallee, B. Prevel, E. Cottancin, J. Lerme, M. Pellarin, and M. Broyer, *Physical Review Letters* **85**, 2200 (2000).

[21] F. J. Morin, *Physical Review Letters* **3**, 34 (1959).

[22] J. B. Goodenough, *Journal of Solid State Chemistry* **3**, 490 (1971).

[23] M. Imada, A. Fujimori, and Y. Tokura, *Reviews of Modern Physics* **70**, 1039 (1998).

[24] P. A. Cox, *Transition metal oxides: An introduction to their electronic structure and properties*, The International Series of Monographs on Chemistry, Clarendon Press; Oxford University Press, Oxford New York, 1992.

[25] A. Zylbersztejn and N. F. Mott, *Physical Review B* **11**, 4383 (1975).

[26] D. Paquet and P. L. Hugon, *Physical Review B* **22**, 5284 (1980).

[27] R. M. Wentzcovitch, W. W. Schulz, and P. B. Allen, *Physical Review Letters* **73**, 3043 (1994).

[28] T. M. Rice, H. Launois, and J. P. Pouget, *Physical Review Letters* **73**, 3042 (1994).

[29] R. M. Wentzcovitch, W. W. Schulz, and P. B. Allen, *Physical Review Letters* **72**, 3389 (1994).

[30] S. Biermann, A. Poteryaev, A. I. Lichtenstein, and A. Georges, *Physical Review Letters* **94**, 026404 (2005).

[31] A. Cavalleri, T. Dekorsy, H. H. W. Chong, J. C. Kieffer, and R. W. Schoenlein, *Physical Review B* **70**, 161102 (2004).

[32] H. T. Kim, Y. W. Lee, B. J. Kim, B. G. Chae, S. J. Yun, K. Y. Kang, K. J. Han, K. J. Yee, and Y. S. Lim, *Physical Review Letters* **97**, 266401 (2006).

[33] A. Cavalleri, M. Rini, and R. W. Schoenlein, *Journal of the Physical Society of Japan* **75**, 011004 (2006).

[34] V. S. Vikhnin, S. Lysenko, A. Rua, F. Fernandez, and H. Liu, *Solid State Communications* **137**, 615 (2006).

[35] S. Lysenko, A. J. Rua, V. Vikhnin, J. Jimenez, F. Fernandez, and H. Liu, *Applied Surface Science* **252**, 5512 (2006).

[36] M. S. Grinolds, V. A. Lobastov, J. Weissenrieder, and A. H. Zewail, *Proceedings of the National Academy of Sciences of the United States of America* **103**, 18427 (2006).

[37] I. Yamashita, H. Kawaji, T. Atake, Y. Kuroiwa, and A. Sawada, *Physical Review B* **68**, 092104 (2003).

[38] A. S. Shirinyan and M. Wautelet, *Nanotechnology* **15**, 1720 (2004).

[39] G. F. Goya, M. Veith, R. Rapalavicuite, H. Shen, and S. Mathur, *Applied Physics A: Materials Science & Processing* **80**, 1523 (2005).

[40] K. Jacobs, J. Wickham, and A. P. Alivisatos, *Journal of Physical Chemistry B* **106**, 3759 (2002).

[41] D. Zaziski, S. Prilliman, E. C. Scher, M. Casula, J. Wickham, S. M. Clark, and A. P. Alivisatos, *Nano Letters* **4**, 943 (2004).

[42] Q. Xu, I. D. Sharp, C. W. Yuan, D. O. Yi, C. Y. Liao, A. M. Glaeser, A. M. Minor, J. W. Beeman, M. C. Ridgway, P. Kluth, I. Ager, J. W., D. C. Chrzan, and E. E. Haller, *Physical Review Letters* **97**, 155701 (2006).

[43] R. E. Cech and D. Turnbull, *Journal of Metals* , 124 (1956).

[44] I. W. Chen, Y. H. Chiao, and K. Tsuzaki, *Acta Metallurgica* **33**, 1847 (1985).

[45] J. Y. Suh, R. Lopez, L. C. Feldman, and R. F. Haglund, *Journal of Applied Physics* **96**, 1209 (2004).

[46] D. Brassard, S. Fourmaux, M. Jean-Jacques, J. C. Kieffer, and M. A. El Khakani, *Applied Physics Letters* **87**, 051910 (2005).

[47] R. A. Aliev, V. N. Andreev, V. M. Kapralova, V. A. Klimov, A. I. Sobolev, and E. B. Shadrin, *Physics of the Solid State* **48**, 929 (2006).

[48] J. Rozen, R. Lopez, R. F. Haglund, and L. C. Feldman, *Applied Physics Letters* **88**, 081902 (2006).

[49] K. Nagashima, T. Yanagida, H. Tanaka, and T. Kawai, *Journal of Applied Physics* **101**, 026103 (2007).

[50] R. Lopez, L. A. Boatner, T. E. Haynes, R. F. Haglund, and L. C. Feldman, *Applied Physics Letters* **79**, 3161 (2001).

[51] R. Lopez, L. A. Boatner, T. E. Haynes, L. C. Feldman, and R. F. Haglund, *Journal of Applied Physics* **92**, 4031 (2002).

[52] R. Lopez, T. E. Haynes, L. A. Boatner, L. C. Feldman, and R. F. Haglund, *Optics Letters* **27**, 1327 (2002).

[53] R. Lopez, J. Y. Suh, L. C. Feldman, and R. F. Haglund, *Symposium Proceedings of the Materials Research Society* **820**, R1.5 (2004).

[54] M. Rini, A. Cavalleri, R. W. Schoenlein, R. Lopez, L. C. Feldman, R. F. Haglund, L. A. Boatner, and T. E. Haynes, *Optics Letters* **30**, 558 (2005).

[55] V. Eyert, *Annalen der Physik* **11**, 650 (2002).

[56] M. M. Qazilbash, K. S. Burch, D. Whisler, D. Shrekenhamer, B. G. Chae, H. T. Kim, and D. N. Basov, *Physical Review B* **74**, 205118 (2006).

[57] H. W. Verleur, A. S. Barker, and C. N. Berglund, *Physical Review* **172**, 788 (1968).

[58] S. Shin, S. Suga, M. Taniguchi, M. Fujisawa, H. Kanzaki, A. Fujimori, H. Daimon, Y. Ueda, K. Kosuge, and S. Kachi, *Physical Review B* **41**, 4993 (1990).

[59] M. M. Qazilbash, A. A. Schafgans, K. S. Burch, S. J. Yun, B. G. Chae, B. J. Kim, H. T. Kim, and D. N. Basov, *Physical Review B* **77**, 115121 (2008).

[60] S. Lysenko, V. Vikhnin, F. Fernandez, A. Rua, and H. Liu, *Physical Review B* **75**, 075109 (2007).

[61] C. Kittel, *Introduction to solid state physics*, Wiley, New York, 7th edition, 1996.

[62] J. Spalek, Superconductivity mechanisms, in *Encyclopedia of Modern Physics*, edited by R. A. Meyers and S. N. Shore, pp. 679–716, Academic Press, San Diego, 1990.

[63] T. M. Rice and D. B. McWhan, *IBM Journal of Research and Development* **14**, 251 (1970).

[64] N. F. Mott, *Reviews of Modern Physics* **40**, 677 (1968).

[65] J. Hubbard, *Proceedings of the Royal Society of London. Series A, Mathematical and Physical Sciences* **276**, 238 (1963).

[66] A. I. Buzdin and L. N. Bulayevskii, *Uspekhi Fizicheskikh Nauk* **131**, 495 (1980).

[67] J. M. Tomczak and S. Biermann, *Journal of Physics: Condensed Matter* **19**, 365206 (2007).

[68] M. W. Haverkort, Z. Hu, A. Tanaka, W. Reichelt, S. V. Streltsov, M. A. Korotin, V. I. Anisimov, H. H. Hsieh, H. J. Lin, C. T. Chen, D. I. Khomskii, and L. H. Tjeng, *Physical Review Letters* **95**, 196404 (2005).

[69] C. Kübler, H. Ehrke, A. Leitenstorfer, R. Lopez, A. Halabica, and R. F. Haglund, Ultrafast Conductivity and Lattice Dynamics of Insulator-Metal Phase Transition in VO2 Studied via Multi-Terahertz Spectroscopy, in *Joint 31st Int'l Conference on Infrared and Millimeter Waves and 14th Int'l Conference on Terahertz Electronics (IRMMW-THz'06)*, Shanghai, China, 2006.

[70] C. N. R. Rao and K. J. Rao, *Phase transitions in solids: an approach to the study of the chemistry and physics of solids*, McGraw-Hill, New York, 1978.

[71] C. N. Berglund and H. J. Guggenheim, *Physical Review* **185**, 1022 (1969).

[72] J. Ortín, A. Planes, and L. Delaey, Hysteresis in Shape-Memory Materials, in *The Science of Hysteresis*, edited by G. Bertotti and I. D. Mayergoyz, volume 3, pp. 467–553, Elsevier, London, 2005.

[73] L. Delaey, Diffusionless Transformations, in *Phase Transformations in Materials*, edited by G. Kostorz, pp. 583–654, Wiley-VCH, Weinheim; New York; Chichester, new edition, 2001.

[74] P. C. Clapp, *Journal de Physique IV* **5**, 11 (1995).

[75] I. A. Khakhaev, F. A. Chudnovskii, and E. B. Shadrin, *Fizika Tverdogo Tela* **36**, 1643 (1994).

[76] H. S. Choi, J. S. Ahn, J. H. Jung, T. W. Noh, and D. H. Kim, *Physical Review B* **54**, 4621 (1996).

[77] F. J. Perez-Reche, E. Vives, L. Manosa, and A. Planes, *Physical Review Letters* **8719**, 195701 (2001).

[78] D. Maurer, A. Leue, R. Heichele, and V. Müller, *Physical Review B* **60**, 13249 (1999).

[79] J. Narayan and V. M. Bhosle, *Journal of Applied Physics* **100**, 103524 (2006).

[80] L. A. L. de Almeida, G. S. Deep, A. M. N. Lima, H. F. Neff, and R. C. S. Freire, *Ieee Transactions on Instrumentation and Measurement* **50**, 1030 (2001).

[81] V. A. Klimov, I. O. Timofeeva, S. D. Khanin, E. B. Shadrin, A. V. Ilinskii, and F. Silva-Andrade, *Technical Physics* **47**, 1134 (2002).

[82] R. A. Aliev and V. A. Klimov, *Physics of the Solid State* **46**, 532 (2004).

[83] R. A. Aliev, V. N. Andreev, V. A. Klimov, V. M. Lebedev, S. E. Nikitin, E. I. Terukov, and E. B. Shadrin, *Technical Physics* **50**, 754 (2005).

[84] W. Haidinger and D. Gross, *Thin Solid Films* **12**, 433 (1972).

[85] Y. Muraoka and Z. Hiroi, *Applied Physics Letters* **80**, 583 (2002).

[86] G. Xu, P. Jin, M. Tazawa, and K. Yoshimura, *Applied Surface Science* **244**, 449 (2005).

[87] E. Kusano and J. A. Theil, *Journal of Vacuum Science & Technology A: Vacuum Surfaces and Films* **7**, 1314 (1989).

[88] V. A. Klimov, I. O. Timofeeva, S. D. Khanin, E. B. Shadrin, A. V. Il'inskii, and F. Silva-Andrade, *Semiconductors* **37**, 370 (2003).

[89] F. Beteille and J. Livage, *Journal of Sol-Gel Science and Technology* **13**, 915 (1998).

[90] W. Burkhardt, T. Christmann, B. K. Meyer, W. Niessner, D. Schalch, and A. Scharmann, *Thin Solid Films* **345**, 229 (1999).

[91] E. Cavanna, J. P. Segaud, and J. Livage, *Materials Research Bulletin* **34**, 167 (1999).

[92] F. C. Case, *Journal of Vacuum Science & Technology A: Vacuum Surfaces and Films* **2**, 1509 (1984).

[93] F. C. Case, *Journal of Vacuum Science & Technology A: Vacuum Surfaces and Films* **7**, 1194 (1989).

[94] A. Leone, A. M. Trione, and F. Junga, *IEEE Transactions on Nuclear Science* **37**, 1739 (1990).

[95] P. Jin, S. Nakao, and S. Tanemura, *Nuclear Instruments & Methods in Physics B: Beam Interactions with Materials & Atoms* **141**, 419 (1998).

[96] L. B. Lin, T. C. Lu, Q. Liu, Y. Lu, and X. D. Feng, *Surface & Coatings Technology* **158**, 530 (2002).

[97] F. Beteille, L. Mazerolles, and J. Livage, *Materials Research Bulletin* **34**, 2177 (1999).

[98] C. Petit, J. M. Frigerio, and M. Goldmann, *Journal of Physics-Condensed Matter* **11**, 3259 (1999).

[99] K. Y. Tsai, T. S. Chin, H. P. D. Shieh, and C. H. Ma, *Journal of Materials Research* **19**, 2306 (2004).

[100] I. Karakurt, J. Boneberg, P. Leiderer, R. Lopez, A. Halabica, and R. F. Haglund, *Applied Physics Letters* **91**, 091907 (2007).

[101] J. E. Mahan, *Physical vapor deposition of thin films*, Wiley, New York; Chichester, 2000.

[102] O. Svelto, S. Longhi, G. D. Valle, S. Kück, G. Huber, M. Pollnau, and H. Hillmer etc., Lasers and Coherent Light Sources, in *Springer Handbook of Lasers and Optics*, edited by F. Träger, pp. 583–936, Springer, New York, 2007.

[103] N. D. Bassim, P. K. Schenck, E. U. Donev, E. J. Heilweil, E. Cockayne, M. L. Green, and L. C. Feldman, *Applied Surface Science* **254**, 785 (2007).

[104] C. A. Volkert and A. M. Minor, *MRS Bulletin* **32**, 389 (2007).

[105] P. Rai-Choudhury, *Handbook of Microlithography, Micromachining, and Microfabrication*, volume 1, SPIE Optical Engineering Press; Institution of Electrical Engineers, Bellingham, Wash., USA London, UK, 1997.

[106] T. L. Alford, L. C. Feldman, and J. W. Mayer, *Fundamentals of nanoscale film analysis*, Springer, New York; London, 2007.

[107] M. Mayer, *SIMNRA (ver. 5.02)*, http://www.ipp.mpg.de/∼mam, 2004.

[108] K. Iizuka, *Elements of photonics*, Wiley Series in Pure and Applied Optics, Wiley, New York, 2002.

[109] WITec, *AlphaSNOM Manual*, WITec Wissenschaftliche Instrumente und Technologie GmbH, 2002.

[110] M. Fox, *Optical properties of solids*, Oxford Master Series in Condensed Matter Physics, Oxford University Press, Oxford; New York, 2001.

[111] G. Brooker, *Modern classical optics*, Oxford University Press, Oxford, 2003.

[112] L. Novotny and B. Hecht, *Principles of Nano-Optics*, Cambridge University Press, 2006.

[113] S. A. Maier and H. A. Atwater, *Journal of Applied Physics* **98**, 011101 (2005).

[114] U. Kreibig, M. Gartz, A. Hilger, and H. Hovel, *Optical investigations of surfaces and interfaces of metal clusters*, volume 4, JAI Press, Inc., Stanford, 1998.

[115] K. L. Kelly, E. Coronado, L. L. Zhao, and G. C. Schatz, *Journal of Physical Chemistry B* **107**, 668 (2003).

[116] J. D. Jackson, *Classical electrodynamics*, Wiley, New York, 3rd edition, 1999.

[117] M. L. Sandrock and C. A. Foss, *Journal of Physical Chemistry B* **103**, 11398 (1999).

[118] G. Mie, *Annalen der Physik* **25**, 377 (1908).

[119] I. W. Sudiarta and P. Chylek, *Journal of the Optical Society of America A* **18**, 1275 (2001).

[120] H. C. van de Hulst, *Light Scattering by Small Particles*, Dover Publications, Inc., New York, 1981.

[121] M. B. Cortie, A. Dowd, N. Harris, and M. J. Ford, *Physical Review B* **75**, 113405 (2007).

[122] L. R. Hirsch, R. J. Stafford, J. A. Bankson, S. R. Sershen, B. Rivera, R. E. Price, J. D. Hazle, N. J. Halas, and J. L. West, *Proceedings of the National Academy of Sciences of the United States of America* **100**, 13549 (2003).

[123] J. M. Brockman, B. P. Nelson, and R. M. Corn, *Annual Review of Physical Chemistry* **51**, 41 (2000).

[124] E. U. Donev, J. Y. Suh, F. Villegas, R. Lopez, R. F. Haglund, and L. C. Feldman, *Physical Review B* **73**, 201401 (2006).

[125] J. Y. Suh, E. U. Donev, R. Lopez, L. C. Feldman, and R. F. Haglund, *Applied Physics Letters* **88**, 133115 (2006).

[126] A. Bianconi, S. Stizza, and R. Bernardini, *Physical Review B* **24**, 4406 (1981).

[127] Y. N. Xia and N. J. Halas, *MRS Bulletin* **30**, 338 (2005).

[128] G. Xu, Y. Chen, M. Tazawa, and P. Jin, *Journal of Physical Chemistry B* **110**, 2051 (2006).

[129] E. A. Coronado and G. C. Schatz, *Journal of Chemical Physics* **119**, 3926 (2003).

[130] M. Maaza, O. Nemraoui, C. Sella, A. C. Beye, and B. Baruch-Barak, *Optics Communications* **254**, 188 (2005).

[131] W. Rechberger, A. Hohenau, A. Leitner, J. R. Krenn, B. Lamprecht, and F. R. Aussenegg, *Optics Communications* **220**, 137 (2003).

[132] J. Y. Suh, E. U. Donev, D. W. Ferrara, K. A. Tetz, L. C. Feldman, and R. F. Haglund, *Journal of Optics A: Pure and Applied Optics* , 055202 (2008).

[133] M. D. McMahon, R. Lopez, R. F. Haglund, E. A. Ray, and P. H. Bunton, *Physical Review B* **73**, 041401 (2006).

[134] S. Wang, D. F. P. Pile, C. Sun, and X. Zhang, *Nano Letters* **7**, 1076 (2007).

[135] C. A. Foss, G. L. Hornyak, J. A. Stockert, and C. R. Martin, *Journal of Physical Chemistry* **98**, 2963 (1994).

[136] J. Grand, P. M. Adam, A. S. Grimault, A. Vial, M. L. De la Chapelle, J. L. Bijeon, S. Kostcheev, and P. Royer, *Plasmonics* **1**, 135 (2006).

[137] K. H. Su, Q. H. Wei, X. Zhang, J. J. Mock, D. R. Smith, and S. Schultz, *Nano Letters* **3**, 1087 (2003).

[138] T. R. Jensen, M. L. Duval, K. L. Kelly, A. A. Lazarides, G. C. Schatz, and R. P. Van Duyne, *Journal of Physical Chemistry B* **103**, 9846 (1999).

[139] J. J. Mock, D. R. Smith, and S. Schultz, *Nano Letters* **3**, 485 (2003).

[140] P. B. Johnson and R. W. Christy, *Physical Review B* **6**, 4370 (1972).

[141] S. Link and M. A. El-Sayed, *Journal of Physical Chemistry B* **103**, 4212 (1999).

[142] H. Bethe, *Physical Review* **66**, 163 (1944).

[143] C. J. Bouwkamp, *IEEE Transactions on Antennas and Propagation* **AP18**, 152 (1970).

[144] H. Liu and P. Lalanne, *Nature* **452**, 728 (2008).

[145] C. Liu, V. Kamaev, and Z. V. Vardeny, *Applied Physics Letters* **86**, 143501 (2005).

[146] A. Krishnan, T. Thio, T. J. Kima, H. J. Lezec, T. W. Ebbesen, P. A. Wolff, J. Pendry, L. Martin-Moreno, and F. J. Garcia-Vidal, *Optics Communications* **200**, 1 (2001).

[147] E. Hendry, M. J. Lockyear, J. Gómez-Rivas, L. Kuipers, and M. Bonn, *Physical Review B* **75**, 235305 (2007).

[148] E. U. Donev, J. Y. Suh, R. Lopez, L. C. Feldman, and R. F. Haglund, *Advances in OptoElectronics* , 739135 (2008).

[149] S. G. Tikhodeev, A. L. Yablonskii, E. A. Muljarov, N. A. Gippius, and T. Ishihara, *Physical Review B* **66**, 045102 (2002).

[150] A. Roberts, *Journal of the Optical Society of America A: Optics Image Science and Vision* **4**, 1970 (1987).

[151] A. Liebsch, *Physical Review Letters* **71**, 145 (1993).

[152] W. L. Barnes, *Journal of Optics A: Pure and Applied Optics* **8**, S87 (2006).

[153] H. Raether, *Springer Tracts in Modern Physics* **111**, 1 (1988).

[154] W. L. Barnes, A. Dereux, and T. W. Ebbesen, *Nature* **424**, 824 (2003).

[155] A. V. Zayats, L. Salomon, and F. de Fornel, *Journal of Microscopy* **210**, 344 (2003).

[156] H. F. Ghaemi, T. Thio, D. E. Grupp, T. W. Ebbesen, and H. J. Lezec, *Physical Review B* **58**, 6779 (1998).

[157] D. S. Kim, S. C. Hohng, V. Malyarchuk, Y. C. Yoon, Y. H. Ahn, K. J. Yee, J. W. Park, J. Kim, Q. H. Park, and C. Lienau, *Physical Review Letters* **91**, 143901 (2003).

[158] P. Lalanne, J. C. Rodier, and J. P. Hugonin, *Journal of Optics A: Pure and Applied Optics* **7**, 422 (2005).

[159] E. Popov, M. Neviere, S. Enoch, and R. Reinisch, *Physical Review B* **62**, 16100 (2000).

[160] S. Enoch, E. Popov, M. Neviere, and R. Reinisch, *Journal of Optics A: Pure and Applied Optics* **4**, S83 (2002).

[161] T. Thio, H. F. Ghaemi, H. J. Lezec, P. A. Wolff, and T. W. Ebbesen, *Journal of the Optical Society of America B: Optical Physics* **16**, 1743 (1999).

[162] L. Martin-Moreno, F. J. Garcia-Vidal, H. J. Lezec, K. M. Pellerin, T. Thio, J. B. Pendry, and T. W. Ebbesen, *Physical Review Letters* **86**, 1114 (2001).

[163] S. A. Darmanyan and A. V. Zayats, *Physical Review B* **67**, 035424 (2003).

[164] W. L. Barnes, W. A. Murray, J. Dintinger, E. Devaux, and T. W. Ebbesen, *Physical Review Letters* **92**, 107401 (2004).

[165] H. J. Lezec and T. Thio, *Optics Express* **12**, 3629 (2004).

[166] G. Gay, O. Alloschery, B. V. De Lesegno, C. O'Dwyer, J. Weiner, and H. J. Lezec, *Nature Physics* **2**, 262 (2006).

[167] G. Gay, O. Alloschery, B. V. de Lesegno, J. Weiner, and H. J. Lezec, *Physical Review Letters* **96**, 213901 (2006).

[168] G. Gay, O. Alloschery, J. Weiner, H. J. Lezec, C. O'Dwyer, M. Sukharev, and T. Seideman, *Physical Review E* **75**, 016612 (2007).

[169] P. Lalanne and J. P. Hugonin, *Nature Physics* **2**, 551 (2006).

[170] F. Kalkum, G. Gay, O. Alloschery, J. Weiner, H. J. Lezec, Y. Xie, and M. Mansuripur, *Optics Express* **15**, 2613 (2007).

[171] G. Gay, O. Alloschery, J. Weiner, H. J. Lezec, C. O'Dwyer, M. Sukharev, and T. Seideman, *Nature Physics* **2**, 792 (2006).

[172] F. J. Garcia-Vidal, S. G. Rodrigo, and L. Martin-Moreno, *Nature Physics* **2**, 790 (2006).

[173] P. Lalanne, J. P. Hugonin, M. Besbes, and P. Bienstman, *Nature Physics* **2**, 792 (2006).

[174] J. Weiner and H. J. Lezec, *Nature Physics* **2**, 791 (2006).

[175] A. Degiron and T. W. Ebbesen, *Journal of Optics A: Pure and Applied Optics* **7**, S90 (2005).

[176] C. Genet, M. P. van Exter, and J. P. Woerdman, *Optics Communications* **225**, 331 (2003).

[177] M. Sarrazin and J. P. Vigneron, *Physical Review E* **68**, 016603 (2003).

[178] M. Sarrazin, J. P. Vigneron, and J. M. Vigoureux, *Physical Review B* **67**, 085415 (2003).

[179] A. Degiron, H. J. Lezec, W. L. Barnes, and T. W. Ebbesen, *Applied Physics Letters* **81**, 4327 (2002).

[180] K. L. van der Molen, F. B. Segerink, N. F. van Hulst, and L. Kuipers, *Applied Physics Letters* **85**, 4316 (2004).

[181] A. Hessel and A. A. Oliner, *Applied Optics* **4**, 1275 (1965).

[182] F. J. Garcia de Abajo, *Reviews of Modern Physics* **79**, 1267 (2007).

[183] J. E. Stewart and W. S. Gallaway, *Applied Optics* **1**, 421 (1962).

[184] E. D. Palik, *Handbook of optical constants of solids*, Academic Press Handbook Series, Academic Press, Orlando, 1985.

[185] W. Bogaerts, P. Bienstman, D. Taillaert, R. Baets, and D. De Zutter, *IEEE Photonics Technology Letters* **13**, 565 (2001).

[186] A. Degiron, H. J. Lezec, N. Yamamoto, and T. W. Ebbesen, *Optics Communications* **239**, 61 (2004).

[187] A. Cavalleri, C. Tóth, C. W. Siders, J. A. Squier, F. Ráksi, P. Forget, and J. C. Kieffer, *Physical Review Letters* **87**, 237401 (2001).

[188] M. F. Becker, A. B. Buckman, R. M. Walser, T. Lepine, P. Georges, and A. Brun, *Applied Physics Letters* **65**, 1507 (1994).

[189] M. F. Becker, A. B. Buckman, R. M. Walser, T. Lepine, P. Georges, and A. Brun, *Journal of Applied Physics* **79**, 2404 (1996).

[190] K. C. Kam and A. K. Cheetham, *Materials Research Bulletin* **41**, 1015 (2006).

[191] J. Park, I. H. Oh, E. Lee, K. W. Lee, C. E. Lee, K. Song, and Y. J. Kim, *Applied Physics Letters* **91**, 153112 (2007).

[192] F. Guinneton, L. Sauques, J. C. Valmalette, F. Cros, and J. R. Gavarri, *Journal of Physics and Chemistry of Solids* **62**, 1229 (2001).

[193] S. Q. Xu, H. P. Ma, S. X. Dai, and Z. H. Jiang, *Journal of Materials Science* **39**, 489 (2004).

[194] S. A. Pauli, R. Herger, P. R. Willmott, E. U. Donev, J. Y. Suh, and R. F. Haglund, *Journal of Applied Physics* **102**, 073527 (2007).

[195] K. Hyun-Tak, C. Byung-Gyu, Y. Doo-Hyeb, K. Gyungock, K. Kwang-Yong, L. Seung-Joon, K. Kwan, and L. Yong-Sik, *Applied Physics Letters* **86**, 242101 (2005).

[196] R. Srivastava and L. L. Chase, *Physical Review Letters* **27**, 727 (1971).

[197] M. Pan, J. Liu, H. M. Zhong, S. W. Wang, Z. F. Li, X. H. Chen, and W. Lu, *Journal of Crystal Growth* **268**, 178 (2004).

[198] G. I. Petrov, V. V. Yakovlev, and J. Squier, *Applied Physics Letters* **81**, 1023 (2002).

[199] J. C. Parker, *Physical Review B* **42**, 3164 (1990).

[200] H.-T. Yuan, K.-C. Feng, X.-J. Wang, C. Li, C.-J. He, and Y.-X. Nie, *Chinese Physics* , 82 (2004).

[201] P. Schilbe, *Physica B: Condensed Matter* **316**, 600 (2002).

[202] N. N. Brandt, O. O. Brovko, A. Y. Chikishev, and O. D. Paraschuk, *Applied Spectroscopy* **60**, 288 (2006).

[203] C. H. Griffiths and H. K. Eastwood, *Journal of Applied Physics* **45**, 2201 (1974).

[204] C. L. Xu, X. Ma, X. Liu, W. Y. Qiu, and Z. X. Su, *Materials Research Bulletin* **39**, 881 (2004).

[205] D. Dragoman and M. Dragoman, *Optical characterization of solids*, Springer, Berlin; New York, 2002.

[206] R. R. Andronenko, I. N. Goncharuk, V. Y. Davydov, F. A. Chudnovskii, and E. B. Shadrin, *Physics of the Solid State* **36**, 1136 (1994).

[207] P. Schilbe and D. Maurer, *Materials Science and Engineering A: Structural Materials Properties Microstructure and Processing* **370**, 449 (2004).

[208] H. H. Richardson, Z. N. Hickman, A. O. Govorov, A. C. Thomas, W. Zhang, and M. E. Kordesch, *Nano Letters* **6**, 783 (2006).

[209] A. O. Govorov, W. Zhang, T. Skeini, H. Richardson, J. Lee, and N. A. Kotov, *Nanoscale Research Letters* **1**, 84 (2006).

[210] G. A. Thomas, D. H. Rapkine, S. A. Carter, A. J. Millis, T. F. Rosenbaum, P. Metcalf, and J. M. Honig, *Physical Review Letters* **73**, 1529 (1994).

[211] S. Yonezawa, Y. Muraoka, Y. Ueda, and Z. Hiroi, *Solid State Communications* **129**, 245 (2004).

[212] F. C. Case, *Journal of Vacuum Science & Technology A: Vacuum Surfaces and Films* **9**, 461 (1991).

[213] H. Schuler, S. Grigoriev, and S. Horn, *Materials Research Society Symposium Proceedings* **474**, 291 (1997).

[214] B. Sass, C. Tusche, W. Felsch, N. Quaas, A. Weismann, and M. Wenderoth, *Journal of Physics: Condensed Matter* **16**, 77 (2004).

[215] P. A. Metcalf, S. Guha, L. P. Gonzalez, J. O. Barnes, E. B. Slamovich, and J. M. Honig, *Thin Solid Films* **515**, 3421 (2007).

[216] D. B. McWhan and J. P. Remeika, *Physical Review B* **2**, 3734 (1970).

[217] D. B. McWhan, A. Jayaraman, J. P. Remeika, and T. M. Rice, *Physical Review Letters* **34**, 547 (1975).

[218] P. Pfalzer, G. Obermeier, M. Klemm, S. Horn, and M. L. denBoer, *Physical Review B* **73**, 144106 (2006).

[219] S. Guimond, M. Abu Haija, S. Kaya, J. Lu, J. Weissenrieder, S. Shaikhutdinov, H. Kuhlenbeck, H. J. Freund, J. Dobler, and J. Sauer, *Topics in Catalysis* **38**, 117 (2006).

[220] Y. Jiang, S. Decker, C. Mohs, and K. J. Klabunde, *Journal of Catalysis* **180**, 24 (1998).

[221] N. Pinna, M. Antonietti, and M. Niederberger, *Colloids and Surfaces A: Physicochemical and Engineering Aspects* **250**, 211 (2004).

[222] C. V. Ramana, S. Utsunomiya, R. C. Ewing, and U. Becker, *Solid State Communications* **137**, 645 (2006).

[223] Z. H. Yang, P. J. Cai, L. Y. Chen, Y. L. Gu, L. Shi, A. W. Zhao, and Y. T. Qian, *Journal of Alloys and Compounds* **420**, 229 (2006).

[224] K. F. Zhang, J. S. Guo, C. H. Tao, X. Liu, H. L. Li, and Z. X. Su, *Chinese Journal of Inorganic Chemistry* **21**, 1090 (2005).

[225] K. F. Zhang, X. Z. Sun, G. W. Lou, X. Liu, H. L. Li, and Z. X. Su, *Materials Letters* **59**, 2729 (2005).